Modelling the Drying Behaviour of Liquids Deposited by Inkjet Printing into Surface Structures for OLED Manufacture

Chris Johnson

Submitted in accordance with the requirements for the degree of
Doctor of Philosophy

The University of Leeds
School of Mechanical Engineering

September, 2019

Abstract

For the manufacture of OLED displays, it is vital for the various layers of material to be as uniform as possible in order to optimise display quality, product lifetime and energy consumption.

However, an experimental investigation into the drying of a droplet containing OLED material deposited into a pixel-shaped well by inkjet printing showed a tendency to form a protuberance, or accumulation, of fluid and material in centre of the well, characterised as a ‘W-shaped’ profile. Experiments also showed that ‘M-shaped’ profiles developed in some cases, with an accumulation of fluid and material near the walls of the well, and very little in the centre. In order to produce efficient OLED displays, with uniform layers of deposited material, a ‘U-shaped’ profile is desirable, where the majority of the material is distributed evenly across the base of the well.

In this work, a numerical model is developed to simulate the evaporation of an axisymmetric droplet from within a well in order to better understand the physical mechanisms behind these experimentally observed droplet profiles.

The model is based upon the Arbitrary Lagrangian-Eulerian approach and the Finite Element Method (FEM) with local evaporation rates coupled to the free surface, giving the model the ability to produce non-spherical cap droplet profiles, representing a considerable advantage over the “Classical model”, and is thoroughly verified and validated against published numerical, analytical and numerical works.

Studies of evaporation rate, surface tension, viscosity, thermocapillary and solutocapillary effects, bank structure depth, angle and aspect ratio, and the effect of having the viscosity and mass flux dependent on the concentration of a solute are conducted.

It was found that the formation of a central protuberance is due to the ability of the flows from the centre of the droplet to maintain the radial outwards flows caused by enhanced evaporation at the contact line. When the outwards flows are sustained, a U-shaped profile will occur, and when they cannot, fluid in the intermediate region of the droplet will not be replenished, leading to a thinning of that region, and a W-shaped profile developing. This was the case in droplets with high evaporation rates, low surface tension or high viscosity, with a critical aspect ratio of the well of 30. M-shaped profiles were only seen with a surface tension gradient across the droplet surface intended to simulate the solutocapillary effect.

Investigation was also carried out into the impact of a concentration-dependent viscosity, in which a novel oscillatory behaviour was observed in the protuberance height at increasing evaporation rates.

Declaration

The candidate confirms that the work submitted is his own and that appropriate credit has been given where reference has been made to the work of others.

This copy has been supplied on the understanding that it is copyright material and that no quotation from the thesis may be published without proper acknowledgement.

The right of Chris Johnson to be identified as Author of this work has been asserted by him in accordance with the Copyright, Designs and Patents Act 1988.

Acknowledgements

I would like to thank my supervisors during this research, Dr Mark Wilson and Dr Krzysztof Kubiak at the University of Leeds and Dr Dan Walker at Merck Chemicals Ltd., who have been extremely valuable in guiding the direction and contents of this Thesis.

I would also like to thank the University of Leeds, Merck Chemicals Ltd., and the EPSRC for providing hardware and software, technical support and funding.

Finally, I would like to thank my family for encouraging and supporting me through this research, and especially Jenna, who has been a constant source of motivation, inspiration and reassurance.

Thank you all.

Nomenclature

Bo	Bond number
C	Heat capacity, J/(kg·K)
Ca	Capillary number
c_{sat}	Saturation concentration, mol/m^3
cv	Vapour concentration, mol/m^3
D	Diffusion coefficient, m^2/s
E	Relative evaporation rate
F	Volume force vector, m/s
g	Acceleration due to Gravity, m/s^2
G	Moisture source, kg/(m^3·s)
g_{evap}	Evaporative flux, kg/(m^2·s)
H	Relative humidity
H_c	Mean Curvature of the Droplet Surface
h	Height of droplet, mm
J	Vapour flux, kg/(m^2·s)
k	Thermal conductivity, W/(m·K)
K	Evaporation rate, m/s
Kn	Knudsen number
L	Characteristic length, mm
La	Laplace number
L_C	Capillary Length, mm
Mf	Mass flux, kg/(m^2·s)
M_v	Molar mass of vapour, kg/mol
n	Normal vector, m/s

Oh	Ohnesorge number
p	Pressure, Pa
Q	Heat source, W/m^3
Q_p	Work done by pressure changes, W/m^3
Q_{vd}	Viscous dissipation, W/m^3
R	Contact line radius, mm
r_1 , r_2	Principal Radii of Curvature of the Droplet, mm
S_F	Step Function
T	Temperature, K
t	Time, s
u	Velocity vector, m/s
v	Characteristic velocity, m/s
V	Volume of droplet, m^3
We	Weber number

Greek Letters

μ	Viscosity, Pa·s
γ	Interfacial tension, N/m
θ	Contact angle, rad
λ	Mean free path of vapour, mm
ρ	Density, kg/m^3
σ	Surface tension, N/m

List of Abbreviations

ALE	Arbitrary Lagrangian Eulerian
AR	Aspect Ratio
BDF	Backwards Differentiation Formula
CAH	Contact Angle Hysteresis
ENO	Essentially Non-Oscillatory
EQE	Electroluminescence Quantum Efficiency
FEA	Finite Element Analysis
FEM	Finite Element Method
FPA	4,4,4-Trifluorobutylphosphoic acid
IMF	Initial Mass Fraction
ITO	Indium Tin Oxide
LB	Lattice Boltzmann
LCD	Liquid Crystal Display
LS	Level Set
OLED	Organic Light Emitting Diode
OVPD	Organic Vapour Phase Deposition
PDE	Partial Differential Equation
PF	Phase Field
SAM	Self-Assembled Monolayer
VOF	Volume of Fluid
VTE	Vacuum Thermal Evaporation
WENO	Weighted Essentially Non-Oscillatory

Contents

List of Figures

Chapter 1:
Introduction

1.1 Motivation

Organic light emitting diode (OLED) displays are currently being heralded as “the Holy Grail for picture purists everywhere” [What HIFI? Magazine, 2015] due to their ability to display absolute black and infinite contrast ratios, as well as brighter, more vibrant images and extremely fast response times of less than 0.1ms, whilst also being thinner, lighter and more energy efficient than comparable LCD displays.

However, the principle issues with OLED devices are the high cost of mass manufacture due to being mainly produced via vacuum thermal evaporation (VTE) or organic vapour phase deposition (OVPD) [Robbliard, 2015], and product lifetime issues relating to the blue pixel deteriorating faster than the red and green pixel, which could lead to colour imbalances [LEDinside, 2013].

The issue of manufacture cost may be tackled by applying traditional inkjet printing techniques into a bank structure already formed upon a substrate. This has the potential to drastically reduce the cost of OLED devices, and ensure they become a viable large-scale alternative to LCD.

In order to produce an OLED display via inkjet printing, several layers of specialised deposit must be laid down sequentially into a bank structure, which forms the overall shape of each sub-pixel. However, as these layers dry, the polymer within the solution is deposited in a distinctive ‘coffee-ring’ pattern at the base of the bank structure and up the bank walls. This leads to a device with sub-optimal performance in almost all key areas: display quality, product lifetime and energy consumption, with the reason for this deposition being unknown.

This chapter provides background information on OLED operation and manufacture, describes challenges in the application of inkjet techniques, and presents the aims and objectives of this research.

1.2 OLED Operation and Device Structure

The basic operation of an OLED device involves a small voltage being applied across the device, which causes the cathode to inject electrons and the anode to inject holes into the intermediate layers of the device. When an electron and a hole recombine in the emissive layer, a high-energy molecular state known as an exciton is formed. In order to return to a less active state, this exciton releases a photon of light, which passes back through the transparent anode and out the front of the device [Tsujimura, 2012], as shown in Figure 1.1.

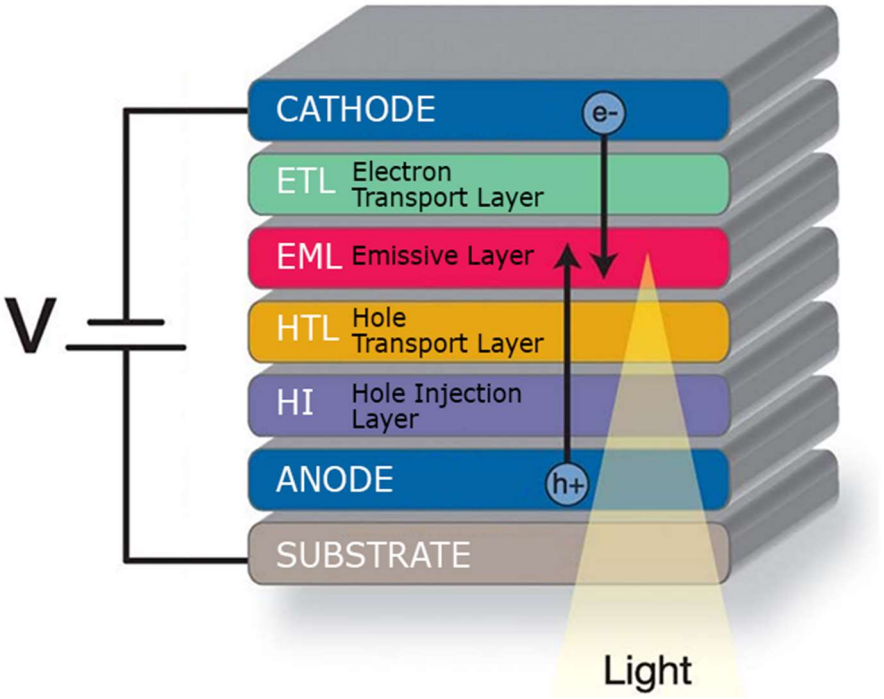

Figure 1.1: Structure of an OLED device [Solvay, n.d.].

Whilst the operating principle of an OLED device is relatively straightforward, the production of such devices is extremely difficult due to the various layers being only around 100nm thick, and needing to be perfectly uniform to produce a consistent luminance across the individual pixel and the entire screen [Chesterfield, 2011].

Also, as seen in Figure 1.1, multiple layers must be produced sequentially in order to maintain controllable, efficient light emission. This means that any non-uniformity in the first layers to be deposited will be magnified throughout subsequent layers, leading to a very poor quality device in terms of display quality, product lifetime and energy consumption [Doust, 2011]. It is therefore paramount that every layer must be as flat and uniform as possible.

1.3 Current OLED Display Manufacturing Techniques

Before discussing the intricacies of the problem of interest in this research, it is necessary to understand the shortcomings of the current methods of producing OLED screens.

1.3.1 Vacuum Thermal Evaporation

Vacuum thermal evaporation (VTE) consists of heating the OLED material to the point at which it evaporates into a vapour, and then pumping this vapour onto a substrate through a shadow mask, as seen in Figure 1.2. This shadow mask prevents material being deposited onto certain areas of the substrate, thereby producing the geometry of the individual pixels [Tsujimura, 2012].

VTE allows for the precise control of layer thickness, but material can flake off the cool walls of the vacuum chamber and cause inclusions within the next layer of OLED material. In addition, this technique lacks the finesse required to control uniformity over a large area [Robbliard, 2015] and is extremely wasteful in terms of material utilisation, due to 75-85% of the material being deposited on the shadow mask [Hamer, 2014].

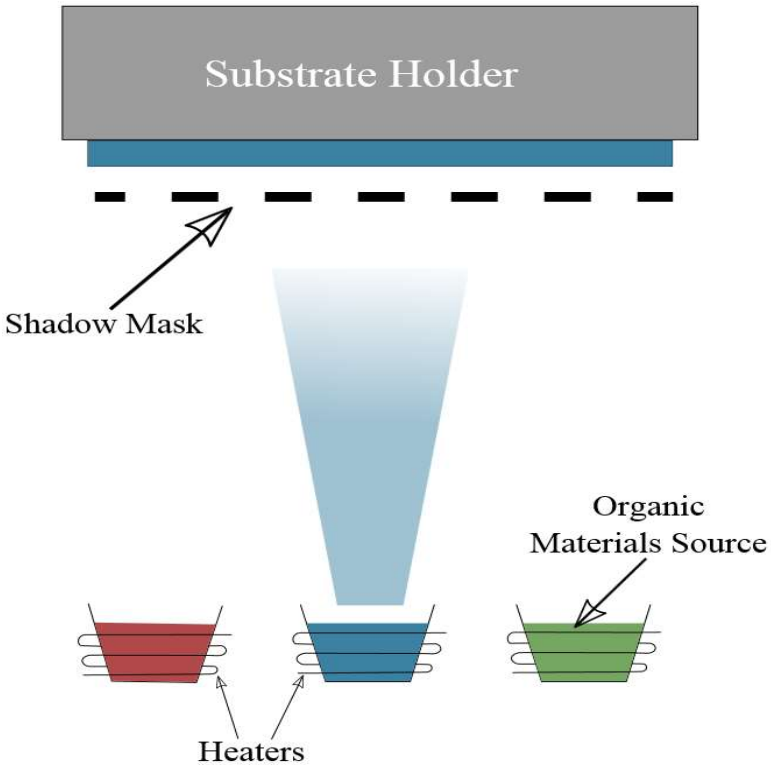

Figure 1.2: VTE operation in OLED production [Handrigan, 2011].

1.3.2 Organic Vapour Phase Deposition

Building upon the technology of VTE, organic vapour phase deposition (OVPD) works by thermally evaporating the OLED material into a hot gaseous stream, which is pumped onto a cold substrate, whereby condensation occurs and forms a thin film upon the surface. The geometry of the deposition is governed by a shadow mask, as with VTE [Burrows et al, 1995], and is illustrated in Figure 1.3.

This method can produce accurate, uniform depositions over a large substrate area very rapidly and without inclusions, due to the internal surfaces being heated [Benziger Group, n.d.]. However, the capacity for this technique to be up-scaled to mass production is not cost-effective, due to the very low material utilisation inherent in a technique employing a shadow mask to control the pattern of deposition [Matheson, 2015]. In addition, the heated internal surfaces can cause issues, such as damage to the OLED device and deformation of the shadow mask, both due to radiant heat [Tsujimura, 2012].

Although it is currently regarded as unsuitable for large-scale production, development continues in OVPD technology in a bid to increase capacity, quality and material utilisation [Long et al, 2006 & Hamer, 2014 & Schwambera, 2006 & Kreis, 2012].

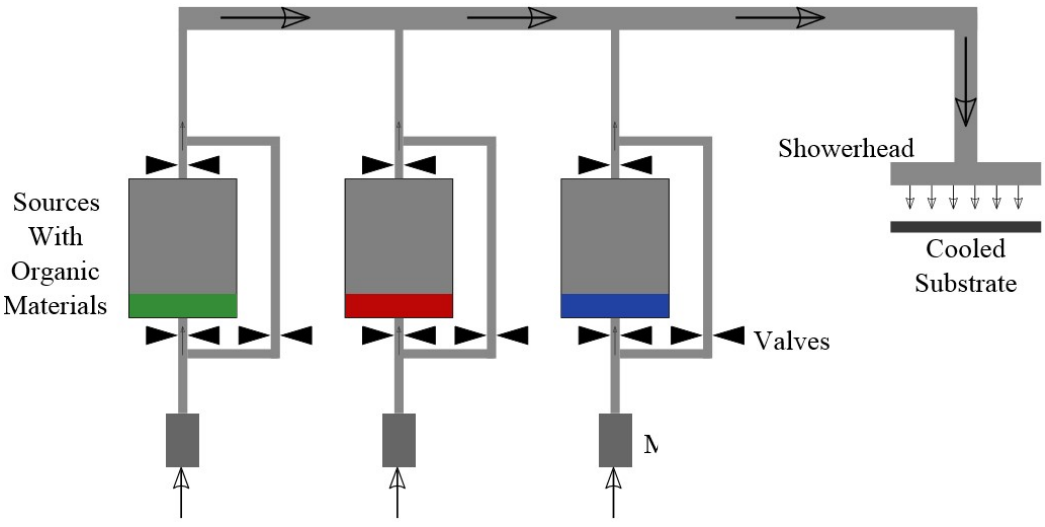

Figure 1.3: OVPD operation in OLED production [Liza, 2013].

1.4 Inkjet Printing for OLED Manufacture

Drop-on-demand inkjet printing offers a method for removing the troublesome shadow mask from the OLED manufacturing process. This is done by precisely depositing the OLED material in solution into a bank structure on the substrate, as shown in Figure 1.4, which enables extremely high material utilisation, and therefore the lowest possible manufacturing cost [Strasser, 2014/b]. Inkjet methods also allow for superior manufacturing capacity, and does not directly contact the substrate, so cannot cause any deformation of the bank structure or previously deposited layers [Villani et al, 2009].

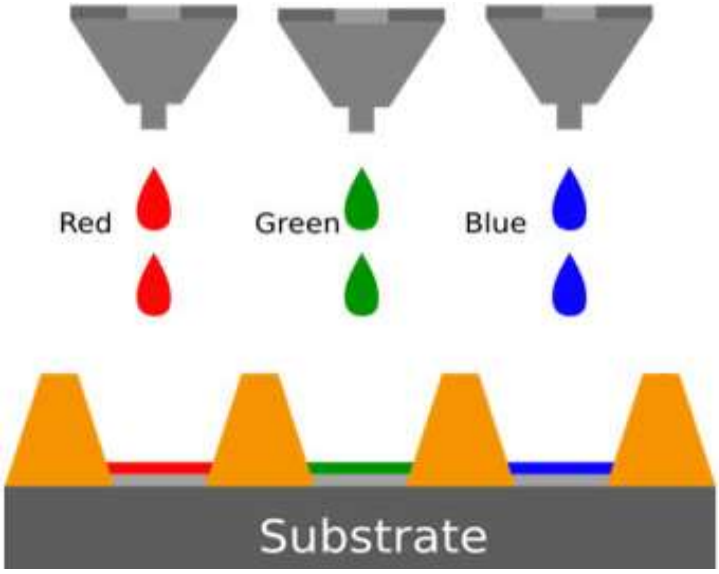

Figure 1.4: Inkjet printing into a bank structure [Strasser, 2014/a].

The printing head can be actuated by many mechanisms, the most common being piezoelectric and thermal.

In a piezoelectric print head, droplets of ink are formed and ejected by the electrically-induced deformation of a piezoelectric crystal. This deformation creates a pressure wave due to a small volume change in the piezoelectric actuator, and this pressure wave moves towards the nozzle to eject the droplet of ink, as shown in Figure 1.5a [Maleki and Bertola, 2020].

In the case of a thermally-actuated print head, the temperature of the ink solution is increased using a heating element located near the nozzle. This causes a small volume of ink to evaporate and form a bubble of ink vapour, which provides the jetting force to expel a droplet from the nozzle, as shown in Figure 1.5b. As this method of print head actuation relies on the evaporation of a volume of ink, it necessitates the inclusion of a volatile

component within the ink, such as water or a short-chain alcohol [Maleki and Bertola, 2020].

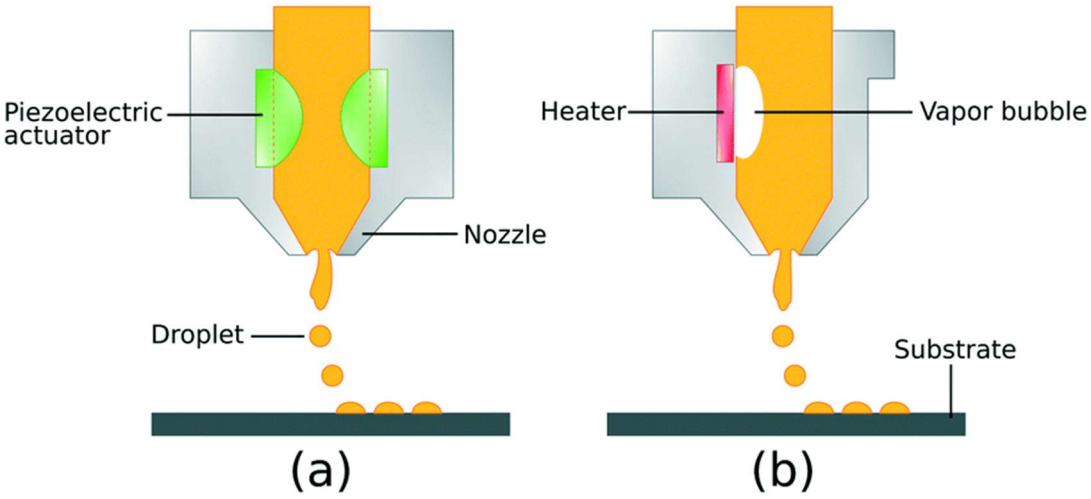

Figure 1.5: Schematic diagram showing the (a) piezoelectric and (b) thermal actuation of an inkjet print head [Maleki and Bertola, 2020].

In contrast, piezoelectric print heads are suitable for use with a far wider variety of ink solvents, as the formation and ejection of the droplet of ink are based on the ink volume change determined by the fluctuation of the piezoelectric membrane. In addition, the ejection rate and volume of the ejected droplets can be precisely controlled via regulating the working voltage applied to the piezoelectric crystal, without the need for altering the temperature of the ink. Due to these advantages, piezoelectric print heads are favoured in inkjet-printed OLED production [Maleki and Bertola, 2020].

With both piezoelectric and thermally-actuated print heads, uniformly-sized droplets of as small as 240nm in diameter can be produced. This allows very high accuracy of ink volume and deposition into the bank structure [Castrejón-Pita et al, 2013].

Regardless of how the print head is actuated, during the printing process the fluid forms a droplet which is connected to the nozzle by a ‘ligament’ of fluid. If the printing is performed correctly, this ligament will pinch-off at the droplet end and retract back into the aperture, producing a spherical droplet, as seen in Figure 1.6a. However, if the ligament pinches off at the nozzle end, the volume of the ligament will join the droplet leading to a larger volume droplet than intended being printed, as seen in Figure 1.6b. The ligament may also pinch-off at both the droplet and nozzle ends and will then form one or more smaller ‘satellite’ droplets that will fall to the substrate

separately from the main droplet, as shown in Figure 1.6c. It is also possible for the ligament not to pinch-off at all, and draw the droplet back up into the print head, causing not only the current droplet but the next one as well to misfire, as seen in Figure 1.6d [Morrison and Harlen, 2010].

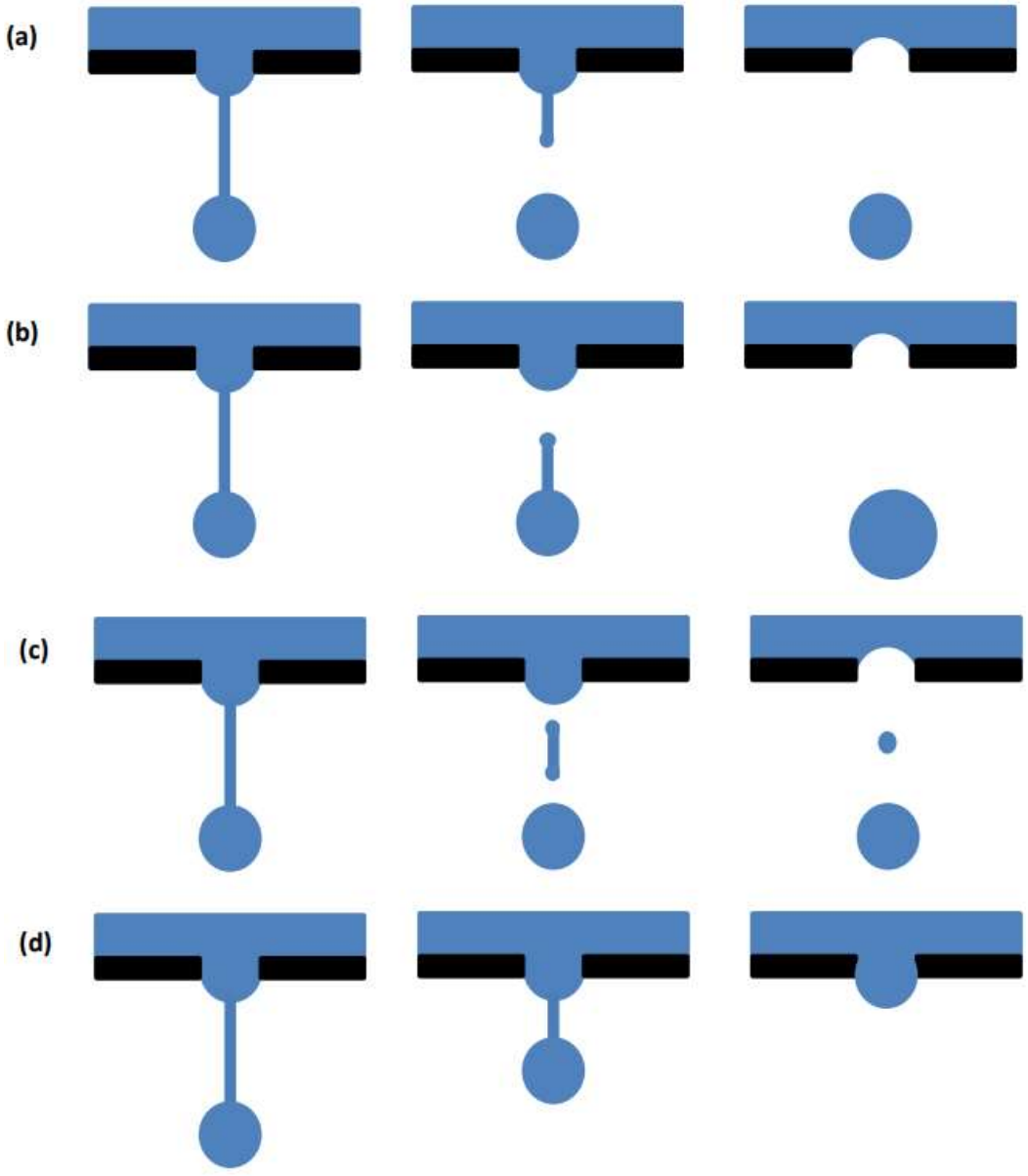

Figure 1.6: A schematic diagram illustrating the different drop break-off modes that can occur in drop-on-demand printing: (a) represents the ideal droplet formation where pinch-off occurs at the droplet, (b) represents pinch-off at the top of the ligament, (c) represents the generation of a satellite droplet and (d) represents a misfiring droplet [Kazmierski, 2018].

Despite the manufacturing advantages of inkjet printing over VTE and OVPD, there are several inherent issues that must be addressed.

Firstly, the active OLED material must be held in a low-viscosity solution in order to pass through the print head [Merklein et al, 2019], and this leads to a very low material to droplet volume ratio. This can lead to issues with delivering the correct amount of material into the pixel, as the volume of the solvent required can be substantially larger than the volume of the pixel trough.

Secondly, the drying of the solvent tends to produce non-uniform deposits of the OLED material. This research shall attempt to understand this particular issue.

Finally, excessively high drop delivery speed can cause splashing onto the surrounding bank structure, whilst low droplet velocity hampers overall production throughput [Castrejón-Pita et al, 2013].

1.5 Issues Currently Experienced Using Inkjet Techniques

The drying of OLED solutions in a bank structure is a multiscale process, and so the issues being addressed must be divided into local and global subcategories.

As mentioned in Section 1.2, achieving a flat, uniform film of OLED material within the pixel is critically important for device performance in terms of display quality, product lifetime and energy consumption, but, as stated in Section 1.4, this has proved very difficult to achieve with inkjet techniques. The OLED material tends to be deposited up the sides of the bank structure, rather than solely at the bottom in flat, uniform layers, and the reason for this is currently unclear, and will be investigated in subsequent chapters.

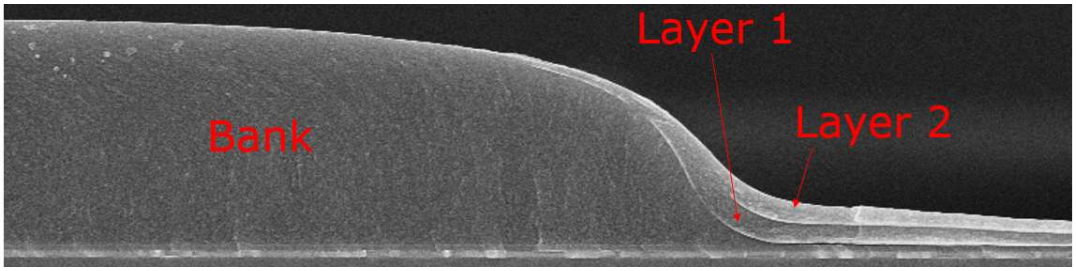

Figure 1.7: OLED material deposited on the side of the bank structure [Tan, 2016].

As can be seen in Figure 1.7, the vertical depth of the Layer 1 is around 2μm on the side of the bank structure, whereas the required depth, and that achieved in the centre of the pixel, is only approximately 60nm. It is also clear that Layer 2 cannot be deposited in a flat film, as it must follow the previously laid down and incorrect profile of Layer 1.

The physics of this issue are further complicated by the extremely high aspect ratio of the pixel, with a depth of only around 2μm, but a length of around 200μm, as shown in Figure 1.8.

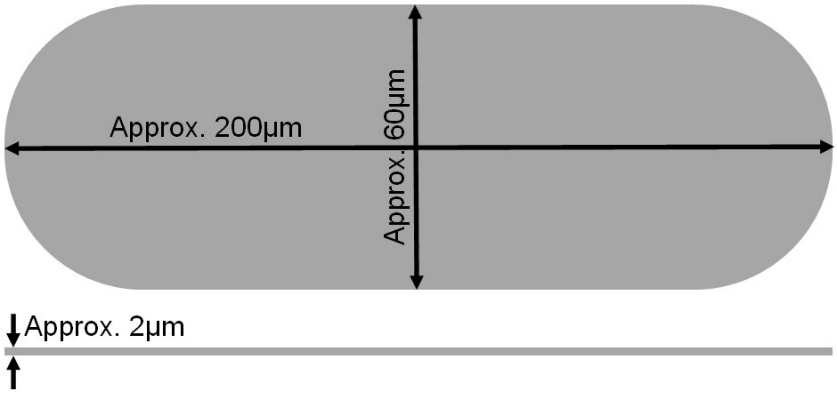

Figure 1.8: Schematic diagram of an OLED pixel.

In addition to ensuring that each individual pixel is uniform, the array of thousands of pixels must also be uniform to produce a high quality display. As the OLED solutions dry, the evaporative flux of each pixel interferes with its neighbours and this can cause non-uniformity of deposit on a global scale, as discussed in Section 2.4.4.

1.6 Research Aims and Objectives

The aim of this research is to understand the dynamics of interface deformation of a drying OLED droplet in a bank structure, by way of numerical modelling, to predict the behaviour of drying OLED solutions and the deposits left behind. This model was then validated against experimental data acquired at Merck Chemicals Ltd, with the intention of providing insight into optimising the OLED production process.

In order to achieve this aim, and after consideration of the literature shown in Chapter 2, this research has been divided into three primary objectives:

1. Model droplet evaporation from a flat substrate:
    a. Model local evaporation due to diffusion.
    b. Relate local evaporation to free surface deformation.
    c. Relate deformation of the free surface to internal flows within the droplet.
    d. Validate against theoretical and experimental works.
2. Expand model to include a bank structure geometry:
    a. Validate the model against experimental works.
    b. Consider the effects of varying evaporation rate, surface tension, viscosity and thermocapillary and solutocapillary effects on droplet drying profile.
    c. Investigate the impact of bank depth, aspect ratio and angle for straight-sided, curved and ‘S-shaped’ bank structures.
3. Expand model to include a concentration-dependent viscosity:
    a. Consider the influence of the initial concentration of a solute on the drying profile of the droplet.
    b. Investigate the impact of varying the bank depth and evaporation rate at different initial solute concentrations.

1.7 Thesis Outline

This thesis has been organised into the following chapter structure:

Chapter 1 is a discussion of the motivation, aims and objectives for the research, a brief explanation of OLED operating principles, current manufacturing techniques and the benefits and issues involved in using inkjet printing techniques.

Chapter 2 consists of a comprehensive literature review of the subject area, covering background concepts and definitions, previous analytical, numerical and experimental investigations into the evaporation of droplets from both flat surfaces and from within a bank structure, and critically evaluating the benefits and shortcomings of several previously proposed methodologies.

Chapter 3 contains the governing equations and boundary conditions that will be applied in the model developed for this thesis, as well as a general overview of the Finite Element Method.

Chapter 4 serves as a verification of the model against published literature for the vapour concentration gradient in the atmosphere surrounding the droplet, the evaporative flux from the free surface and the internal flows generated by said evaporation.

Chapter 5 incorporates a bank structure into the model, with the studies on the effects of varying the evaporation rate, surface tension, viscosity, incorporating thermocapillary and solutocapillary effects and the impact of various bank structure geometries.

Chapter 6 includes the addition of a viscosity value that is dependent on the concentration of a solute within the droplet, with studies on the effects of varying the initial concentration, evaporation rate and different bank structure geometries.

Chapter 7 concludes the thesis with a discussion of all current findings and further work that could build upon the model proposed here.

Chapter 2:
Literature Review

2.1 Introduction

This chapter will cover the various methods of performing fluid mechanics simulations numerically, wettability and evaporation phenomena previously studied, the techniques, benefits and shortcomings of theoretical works that are to be built upon by this research, and experimental works that will be used to validate any subsequent numerical results.

2.2 Background Concepts and Definitions

2.2.1 Surface Tension and Contact Angles

In order to fully understand the physics of the highly complex system of an OLED solution drying in a surface structure, it is necessary to first establish the principles of how liquids behave when in contact with a solid substrate, both in terms of surfaces and interfaces. This is categorised under the topic of wettability.

A cornerstone of the subject of wettability is the study of surface tension, which has been researched extensively since Tome III of *Traite de Mécanique Celeste* was published by Laplace in 1802. Surface tension has been a key feature of many important recent developments, such as fluid lenses [Varioptic, 2010], capillary self-alignment [Zhou, 2006], capillary motors [Takei, 2013] and droplet micro-bearings [Yoxall et al, 2012].

Surface tension arises from the cohesive forces between like molecules. As the molecules at a liquid/gas interface cannot adhere to molecules on all sides, they are more strongly attracted to other molecules on the interface. This forms a film upon the surface of the liquid, which requires more energy to pass an object through than to pass it through the rest of the liquid body when it is submerged. This cohesive force is also responsible for the curvature of droplets, as the liquid attempts to minimise its surface area [Nave, 2016].

The contact angle refers to the angle at which the liquid/gas interface meets the solid surface, and defines the wettability of the contact through the use of Young's Equation:

$$cos\theta = \frac{\gamma_{SG} - \gamma_{SL}}{\gamma_{LG}} \tag{2.1}$$

where γ_{LG} is the liquid-gas surface tension, and γ_{SL} and γ_{SG} are the solid-liquid and solid-gas interfacial tensions respectively, and are illustrated in Figure 2.1.

If $\theta = 0$ there is complete wetting, $0 < \theta < 180°$ there is partial wetting and if $\theta = 180°$ there is no wetting.

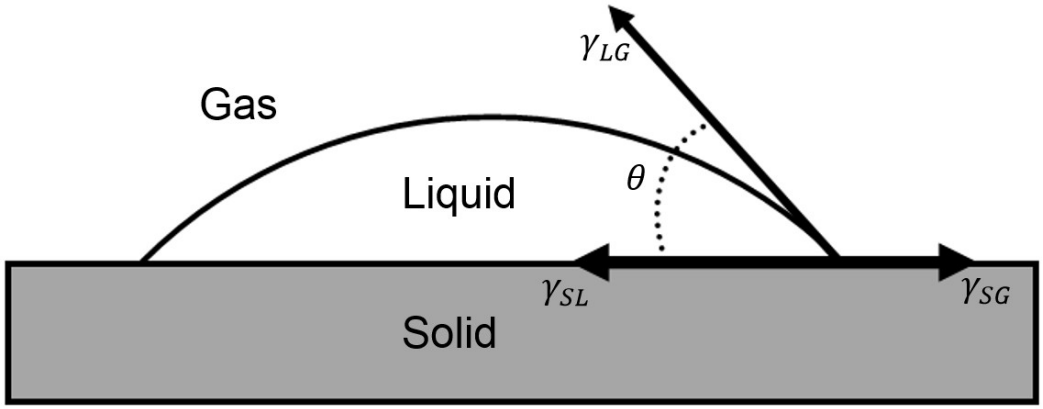

Figure 2.1: Young's Equation parameters.

In reality, the solid surface will always possess a certain level of heterogeneity and so will not conform exactly to Young's Equation. This means that a range of contact angles may be present, with values between the limits of the advancing (θ_A) and receding (θ_R) static contact angles.

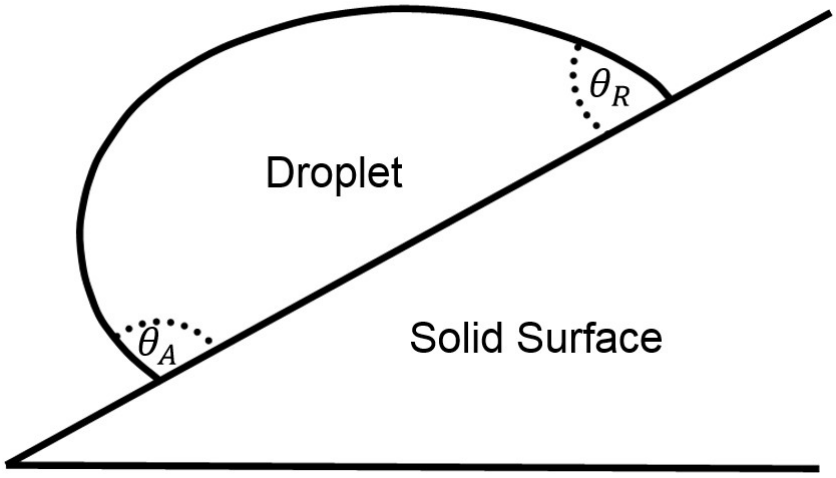

Figure 2.2: Contact angle hysteresis on an inclined solid surface.

It is important to note that the droplet is static on the inclined surface, and so is only intended to show the maximum θ_A and θ_R for that liquid on that surface. The droplet will begin to move only if $\theta > \theta_A$ at the front of the droplet or $\theta < \theta_R$ at the rear of the droplet.

Due to this heterogeneity, it is necessary to study contact angle hysteresis (CAH), which is defined as $\theta_A - \theta_R$. CAH is best demonstrated if a droplet is placed on an inclined surface, as shown in Figure 2.2, the droplet will not slide down the solid surface until a critical incline angle has been reached. The effect of surface heterogeneity is vitally important when considering a drying solution, as it has been shown to lead to the coffee-ring effect [Eral et al, 2013], discussed in Section 2.4.3.

2.2.2 Surface Treatments for OLED Manufacture

As the contact angle is dependent upon the interaction of the solid and liquid, surface treatments can be applied to alter the relative difference in energy between the two, and therefore change the contact angle to increase wettability (becoming more hydrophilic) or decrease wettability (becoming more hydrophobic). This is particularly useful on the scale of microfluidics, as in the case of an OLED pixel, as surface tension effects dominate those of gravity [De Coninck, 2016].

There are three main types of surface treatment for altering the surface characteristics of the indium tin oxide (ITO) coated glass anode: wet, dry or a combination of the two. In wet methods, substrates are treated with several chemical treatments to form a new radical on the surface to modify the properties of the ITO and dry treatments use physical methods such as mechanical polishing, annealing and plasmas to clean the surface and to improve surface roughness and surface composition. Unsurprisingly, the combination method consists of a wet treatment followed by a dry treatment, such as an acid wash and a plasma treatment [Katam, 2014].

For purely altering the wettability of the ITO, a plasma coating method is applied. This is usually performed with an oxygen plasma treatment method [Wu et al, 1997], which consists of placing the ITO in a vacuum chamber, and introducing oxygen at a very low pressure. This oxygen is then subjected to a very powerful electrical charge, which removes any contaminants from the ITO surface and increases wettability [Tantec, n.d.].

Oxygen plasma methods have been shown by Wu et al [1997] to greatly increase the efficiency of OLED devices, being responsible for a 50% reduction in drive voltage, increased Electroluminescence Quantum Efficiency (EQE) by a factor of 4 and a much higher drive current can be applied to increase maximum brightness. The lifetime of the OLED device was also increased by two orders of magnitude.

However, recently oxygen plasma methods have been enhanced by self-assembled monolayer (SAM) adsorption methods. This method functions by taking an ITO substrate that has already been subjected to an oxygen plasma treatment and soaked in a solution of ethanol and 4,4,4-Trifluorobutylphosphoic acid (FPA) before being baked to ensure complete chemical bonding. The ITO is then sonicated in an ethanol and trimethylamine solution, rinsed with pure ethanol and then dried by a stream of nitrogen [Yu et al, 2012]. It was found that the addition of SAM adsorption

increased the stability of the work function (i.e. the energy required to remove an electron) and driving voltage during operation, and so increased device lifetime [Yu et al, 2014].

It was found by Patil et al. [2016] that varying the wettability of a substrate, along with temperature and inclusion of colloidal particles, greatly influences the deposition pattern of material onto that substrate, from uniform to strongly ring-shaped deposits.

In addition to changing wettability, surface treatments can increase the stability of OLED devices through reducing oxygen deficiency within the ITO films and indium ingress into the OLED layers, caused by ITO degradation due to high temperature. These issues can be greatly reduced through the use of UV ozone cleaning and oxygen plasma treatment, which also improve OLED performance by reducing surface roughness and increasing work function [Zhou, 2007].

The inclusion of buffer layers, such as carbon, between the ITO and the OLED material can also improve performance through reduced indium diffusion [Zhou, 2007].

2.2.3 Dimensionless Numbers Related to Surface Tension

There are several dimensionless numbers associated with surface tension that are used to represent the relative strengths of different phenomena, such as viscosity, gravity and kinetic energy.

An important dimensionless value when considering surface tension is the Weber number, We defined as

$$We = \frac{\rho v^2 L}{\sigma} \tag{2.2}$$

where ρ is the fluid density, v is the characteristic velocity of the fluid, L is a characteristic length and σ is the surface tension. This value is the ratio between the inertial forces and the surface tension forces, and indicates whether the kinetic or surface tension energy is dominant.

Another commonly used dimensionless number is the Bond number, Bo found by

$$Bo = \frac{\Delta\rho g L^2}{\sigma} \tag{2.3}$$

where $\Delta\rho$ is the difference in density between the liquid and surrounding fluid (i.e. air) and g is the acceleration due to gravity. The Bond number represents the ratio of gravitational forces to the surface tension.

The Ohnesorge number, Oh represents the ratio of viscous force to inertial and surface tension forces and is defined as

$$Oh = \frac{\mu}{\sqrt{\rho\sigma L}} \tag{2.4}$$

Liquids with an Ohnesorge number in the range 0.1 to 1 are considered 'jettable' in inkjet printing [Derby, 2010].

The Laplace number, La represents the relationship between surface tension and momentum transport inside a fluid:

$$La = \frac{\sigma\rho L}{\mu^2} = Oh^{-2} \tag{2.5}$$

The final dimensionless number to be discussed in this section is the capillary number, Ca, which relates the effect of viscous drag forces against surface tension forces at a liquid-gas interface, such as the surface of a droplet

$$Ca = \frac{\mu v}{\sigma} \tag{2.6}$$

2.3 Initial Geometry of the Droplet

The impact of the droplet onto the substrate during inkjet printing causes the droplet to transition from a spherical droplet into a spherical cap upon the substrate.

A small viscous droplet whose largest dimension is much smaller than the capillary length, L_C, will take the shape of a spherical cap, where

$$L_C = \sqrt{\frac{\sigma}{\rho g}} \tag{2.7}$$

The shape of the droplet can also be determined by Bo and Ca, as these represent the ratio of gravitational forces to surface tension, and the ratio of viscous forces to surface tension forces respectively.

However, as $Bo \ll 1$ and $Ca \ll 1$ for all solvents studied in subsequent chapters, surface tension forces will dominate. For example, the solvent anisole, with a droplet diameter of 200μm and an internal flow rate of 20 x 10^{-6} m/s, as measured by Kazmierski [2018], has a Bond number of 1 x 10^{-2} and a capillary number of 6 x 10^{-7}. Therefore, as anisole is very typical of the solvents studied in this work, the initial geometry of the droplets before evaporation will always be assumed to be a spherical cap on a flat surface.

In the case of droplets evaporating from a bank structure, the assumption will be that the droplet will initially be pinned to the top of the bank structure, as seen in the experimental data in Figures 2.13 and 2.14. The droplets will also initially have constant mean curvature, due to the surface tension forces being initially dominant. The mean curvature across the droplet surface, H_c, is given by

$$H_c = \frac{1}{2}\left(\frac{1}{r_1} + \frac{1}{r_2}\right) \tag{2.8}$$

where r_1 and r_2 are the principal radii of curvature of the droplet.

2.4 Droplet Evaporation from Flat Surfaces

An understanding of various evaporation phenomena is essential for this research, as the goal of achieving a flat film of OLED material at the bottom of a trough geometry depends heavily on the flow behaviour of the evaporating solvent.

Evaporation is the process by which a solvent molecule transitions from a liquid phase to a vapour phase across an interface, in this case the droplet surface. The rate of evaporation is governed by four factors [Dobson et al., 2008]:

- Temperature, as molecules with a higher thermal energy are more likely to pass through the interface.
- Surface area of the droplet as a larger area can exchange more molecules between phases.
- Wind speed across the surface of the liquid, as this carries molecules away from the droplet reducing the vapour pressure and allowing more molecules to pass through the interface.
- Relative humidity of the vapour, as the less vapour there is in the atmosphere compared to the saturation concentration, the faster evaporation can occur.

Once a molecule has passed through the interface into the atmosphere, it can be carried away from the droplet surface by either diffusion, convection or ballistically.

Diffusion-driven evaporation occurs when there is a concentration gradient in the vapour phase allowing vapour to move from an area of high concentration at the droplet surface to an area of lower concentration further into the atmosphere. If the atmosphere becomes saturated with vapour, evaporation will cease. For the case of OLED-scale droplets evaporating under typical manufacturing temperatures and at ambient atmospheric pressure, evaporation is always governed by diffusion.

If convection is neglected, the vapour concentration is determined by a two-dimensional version of Fick's Second Law:

$$\frac{dc}{dt} = D\nabla^2 c \tag{2.9}$$

where D is the diffusion coefficient of the vapour in the atmosphere, c is the vapour concentration and t is time.

Ballistic evaporation is induced by low atmospheric pressure surrounding the droplet, causing the vapour molecules to travel many times the size of the droplet before encountering other molecules. This means that there is very little chance of the molecule returning to the droplet surface, as is often the case in diffusion-driven systems, and so accounts for greatly increased evaporation rates. A system that has entered a ballistic evaporation state is identified by the Knudsen number, Kn being greater than 1 from

$$Kn = \frac{\lambda_p}{R_c} \tag{2.10}$$

where λ_p is the mean free path of the vapour and R_c is the contact radius [Trusler, 2011]. Ballistic evaporation is only typically achieved via vacuum drying techniques.

The evaporation of a sessile droplet has been an area of intensive research in recent years, and the following sub-sections will investigate the applicability and usefulness of several different methods that have been employed.

The overwhelming proportion of numerical studies on droplet evaporation have utilised the axisymmetric system, whereby half of the droplet is represented in 2D, and then is rotated around an axis of symmetry to give 3D results. This greatly reduces the complexity and computational effort required to generate results, whilst having few negative repercussions on accuracy [Brutin and Starov, 2018]. All papers subsequently mentioned will have used the axisymmetric system, unless otherwise stated.

Nguyen & Nguyen [2012] studied the evaporation of sessile droplets of ethanol with a fixed base radius (i.e. pinned) on a flat surface, both numerically and experimentally. It was shown that the two-thirds power dependence of the transient droplet volume on time is appropriate for determining the droplet lifetime by linearly extrapolating limited experimental data within the pinning mode, and that the dependence of the squared transient radius of the droplet base on time is good for determining the droplet lifetime by linearly extrapolating the limited experimental data within the depinning mode. The theoretical predictions produced showed that the evaporation by natural diffusion of sessile droplets within the depinning mode takes longer than the evaporation of pinned droplets with the same volume. It was also found that droplets on a moderately hydrophobic surface evaporate more slowly than on a hydrophilic surface, except for when it is on

a superhydrophobic surface, where the contact angle is larger than about 150°.

On the subject of evaporation from flat surfaces, there are excellent review papers from Erbil [2012], who provides an in-depth overview of the evaporation of micrometre and millimetre sized spherical and sessile droplets (representing appropriate length scales for the current work), and Gurrala et al. [2021], who provides a fantastic review of the state-of-the-art of experimental, analytical, and computational techniques used to study the evaporation dynamics of binary sessile droplets. Both of these review papers offer a great deal of background information into the overall subject area of sessile droplet evaporation, and several studies that are discussed in subsequent Sections and Chapters are featured therein, however much of the work included in these reviews cannot be included in this work due to the need to focus on the study at hand.

2.4.1 Classical Model

One of the most well-known papers on this subject is by Hu and Larson [2002], which studied the evaporation of a pinned sessile droplet of water on a flat glass substrate, experimentally, analytically and numerically using Finite Element Analysis (FEA). The droplet was considered to be pinned for the entire evaporation process, as experimental observations found that with a contact angle below 90° the contact line remained pinned for the first 90-95% of the total drying time, with the contact line only moving with a very low contact angle in the final stage of drying.

The method used to calculate the evaporation rate was based on eq. (2.11). As the water is evaporating into ambient air, the vapour concentration distribution is non-uniform, with the vapour concentration, c at the droplet surface was assumed to be equal to the saturation vapour concentration, c_v. Far away from the surface, the vapour concentration was considered to be equal to the ambient vapour concentration Hc_v, where H was the relative humidity of ambient air. This difference in vapour concentration, $c_v(1-H)$ drove the evaporation of water into the air, according to the quasi-steady diffusion equation

$$\nabla^2 c = 0 \tag{2.11}$$

At each time step, the loss of water was determined from the product of the total evaporation rate integrated over the droplet surface and the time step.

The new droplet volume was therefore calculated from the solvent loss and the previous droplet volume, with the droplet surface being derived from

$$V(t) = \frac{\pi h(0,t)[3R^2 + h^2(0,t)]}{6} \tag{2.12}$$

where $V(t)$ is the volume of the droplet, $h(0,t)$ is the droplet height as a function of time and R is the contact line radius.

There was close agreement between experimental and FEM results, proving that whilst this model may lack several important features required of a comprehensive model of droplet evaporation (i.e. thermal considerations, local evaporation rates, etc.), it does accurately predict the evolution of droplet height and, if the spherical cap assumption holds true, droplet surface profile through time. The FEM results were also compared to experimental results by Birdi et al. [1989] and Rowan et al. [1995], and to an analytical solution by Lebedev [1965], agreeing closely in all cases.

Building on previous work by Picknett and Bexon [1977] and Deegan et al. [2000/b], this work by Hu and Larson is a keystone in the development of droplet evaporation models, being cited by over 700 articles since its publication. The impressive agreement of the experimental and FEM results show that this modelling methodology is very effective for droplets that maintain a spherical cap throughout the drying process, and provides a robust study to compare future results against, hence being commonly known as the ‘classical model’. A droplet will maintain a spherical cap if the droplet has $Bo < 1$, as the surface tension forces dominate the gravitational forces [Berthier, 2013].

However, there are several shortcomings with the classical method, chiefly that the droplet has to maintain a spherical cap, so cannot produce W- or M-shaped profiles as observed in OLED droplets by Kazmierski [2018] (See Section 2.5). Also, the evaporation rate is global across the entire droplet surface rather than local, so it cannot produce the radial outward flows, or simulate the effect of bank structures or other droplets on local evaporation rate. In addition, the internal flows are not considered in this model, and so the extent of the coffee-ring effect cannot be acquired. Finally, there is no temperature consideration, so the effects of evaporative cooling are neglected.

2.4.2 Thermal Effects

During evaporation, latent heat is removed from the surface of the droplet by a process known as evaporative cooling. This occurs because the molecules that are escaping the liquid to become vapour during the evaporation process require a high amount of energy to pass through the interface region, and therefore only molecules with particularly high energy levels manage to vaporise. This means that lower energy molecules remain in the liquid, and, as temperature is a direct measure of molecular energy, the liquid is therefore cooled [AP Physics, n.d.].

Ward & Duan [2004] found that temperature drop increases proportionally with evaporation rate, and Sefiane et al [2009] found that evaporative cooling is increased on a substrate with a lower thermal conductivity and also at lower atmospheric pressures, as is to be expected.

Raghupathi & Kandlikar [2016] studied the effect of the contact line on heat transfer during evaporation of droplets, and divided the region near the contact line into four sub-regions. The first is the ‘adsorbed’ region nearest the contact line, where strong attractive forces between the substrate and liquid prevents evaporation, and therefore heat transfer, and causes a relatively flat film to form. Moving inwards from the contact line, next is the ‘transition’ region, where the attractive forces are significantly reduced due to low disjoining pressure, leading to high levels of evaporative cooling. The next two regions, the ‘intrinsic meniscus’ and ‘micro-convection’ regions are usually grouped together as the collective ‘macro’ region, where heat flux is reduced due to the rapidly thickening film layer. Dhavaleswarapu et al [2007] found that 95% of heat transfer in the vicinity of the contact line occurs in the ‘transition’ region, even though it only accounts for around 30% of the interface, as seen in Figure 2.3. This is not of great importance to the current work, but could be utilised in future, more detailed investigations of the behaviour near the contact line in an evaporating OLED droplet.

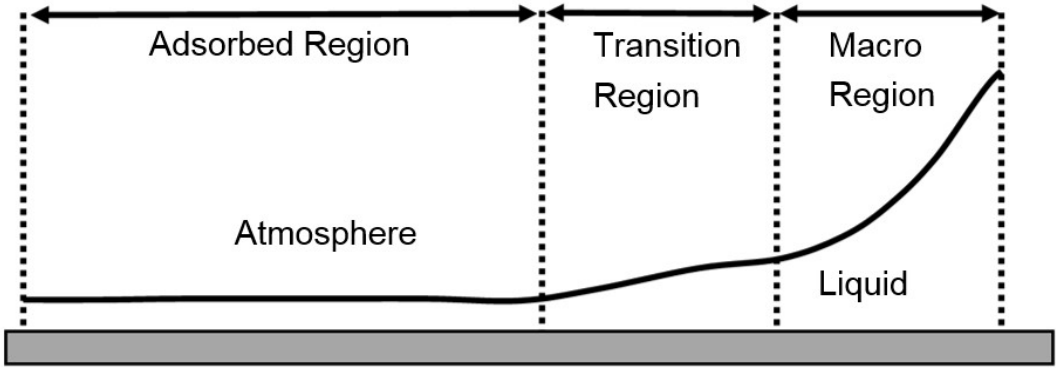

Figure 2.3: Heat transfer regions near the contact line.

In order to expand on the classical model, evaporative cooling was considered by Sefiane et al. [2009], with the temperature of the droplet, substrate and atmosphere being continuous. The saturation concentration around the droplet was an increasing function of temperature, approximated quartically in $T_a - T$ by

$$c_{sat}(T) = \sum_{i=0}^{4} \alpha_i (T_a - T)^i \tag{2.13}$$

where T_a and T are the temperature of the atmosphere and droplet respectively, c_{sat} is the saturation concentration and the coefficients α_i for $i = 0, \dots, 4$ were $\alpha_0 = 1.93 \text{ x } 10^{-2}$, $\alpha_1 = 1.11 \text{ x } 10^{-3}$, $\alpha_2 = 2.77 \text{ x } 10^{-5}$, $\alpha_3 = 3.8 \text{ x } 10^{-7}$ and $\alpha_4 = 2.66 \text{ x } 10^{-9}$ and were calculated from data on the specific volume of water vapour stated by Raznjevic [1995].

It was identified from Figure 2.4 that a linear approximation is sufficient for a temperature drop of less than 20K, but any larger decrease would require the use of the quartic approximation.

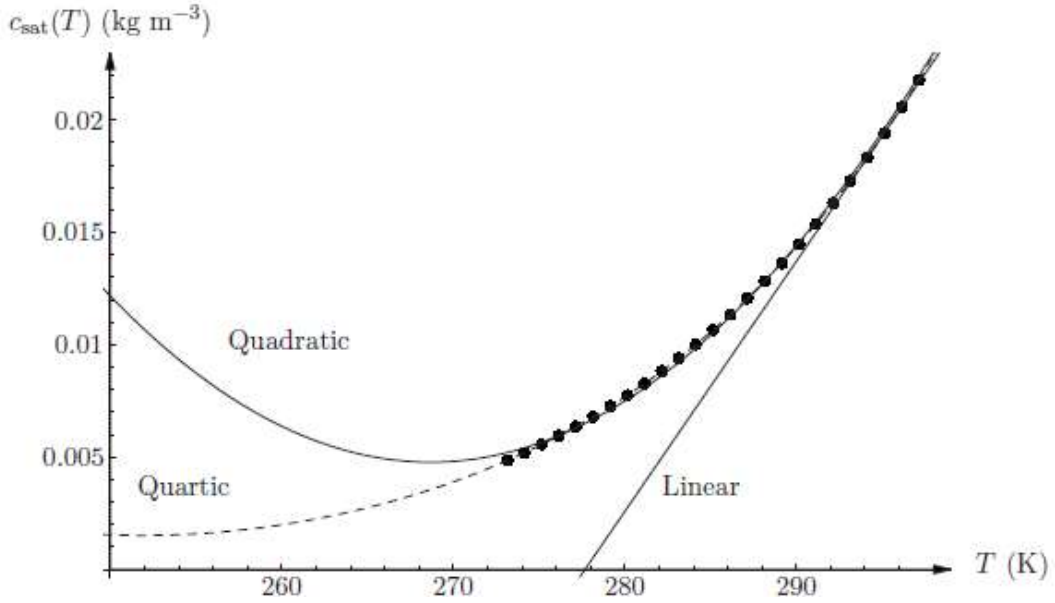

Figure 2.4: Variation of saturation concentration of vapour, $c_{sat}(T)$ with temperature, T. The linear, quadratic and quartic approximations are shown, with the data given by Raznjevic [1995] being shown by the bold dotted line [Sefiane et al., 2009].

However, there are issues with this model, as it assumes a spherical cap linked to a droplet volume decrease each time step, and so cannot represent changing droplet profiles. It also assumes constant viscosity, density, surface tension, thermal conductivity, atmospheric pressure and atmospheric temperature, which in reality would be variable.

Starov & Sefiane [2009] studied the effect of evaporative cooling and heat transfer from the substrate on droplet evaporation. They found that the highest level of evaporative cooling occurs near the contact line, as is to be expected as that is where the evaporation rate is highest. Counterintuitively however, this region was also the hottest across the entire droplet surface, as heat transfer with the substrate was most efficient in this region.

David, Sefiane and Tadrist [2007] conducted an experimental investigation into the evaporation of sessile droplets on substrates with various thermal properties, finding that evaporation rate is influenced by substrate thermal properties and that the droplet experiences a cooling effect when the substrate is thermally insulating. Increasing droplet evaporation amplified the influence of substrate thermal properties. This was expanded upon and confirmed by Dunn et al. (2009).

Numerical and experimental work by Lopes et al. [2013] investigated the effect of thermal properties of substrates on the evaporation rate of sessile

water droplets on a layer of polystyrene atop glass or silicone substrates, in order to ensure the same wettability. It was shown experimentally that silicone, which has a higher thermal conductivity, accelerated droplet evaporation by 10%. Numerical analysis showed this was due to the transient heat transport affecting local temperature distribution at the liquid-gas interface, and therefore the evaporation rate.

A good example of a comprehensive study into thermal effects is by Hu and Wu [2015], which built upon works by several authors including Birdi, Vu and Winter [1989] who found that droplet mass decreased linearly with time by measuring the weight of evaporating water droplets on un-heated glass substrates. Crafton and Black [2004] demonstrated that both contact angle and droplet volume decreased non-linearly with time on heated aluminium and copper substrates. Sobac and Brutin [2012] found via experiment that thermally-linked mechanisms, such as buoyancy-induced convection and evaporative cooling, become increasingly important factors in the evolution of contact angle and droplet volume as the temperature of the substrate increased.

Hu and Wu [2015] considered vapour diffusion in the air, evaporative cooling at the liquid-air interface, conjugate heat transfer in the substrate, liquid and air, and both buoyancy-induced and Marangoni convections in both the liquid and air domains, all on heated and unheated substrates. They found that when the evaporation time and droplet volume are normalized by the lifetime and initial volume respectively, the evolution of contact angle and normalized volume of pinned droplets with an initial contact angle $\theta_0 = \pi/2$ follow the same respective patterns, which are independent of base radius, substrate temperature and ambient humidity.

2.4.3 Internal Flows within the Droplet

During the evaporation of a sessile droplet (i.e. a droplet upon a flat surface) with a pinned contact angle of less than 90°, there is an outward radial flow due to a higher evaporation rate at the contact line than at the peak of the meniscus. This is due to the curvature of the droplet surface and impermeability of the substrate leading to a steep vapour concentration gradient near the contact line, as seen in Figure 2.5. In order to maintain the spherical shape of the droplet, as determined by surface tension, a flow must occur from the centre of the droplet towards to perimeter [Gelderblom, 2013], leading to the coffee-ring effect.

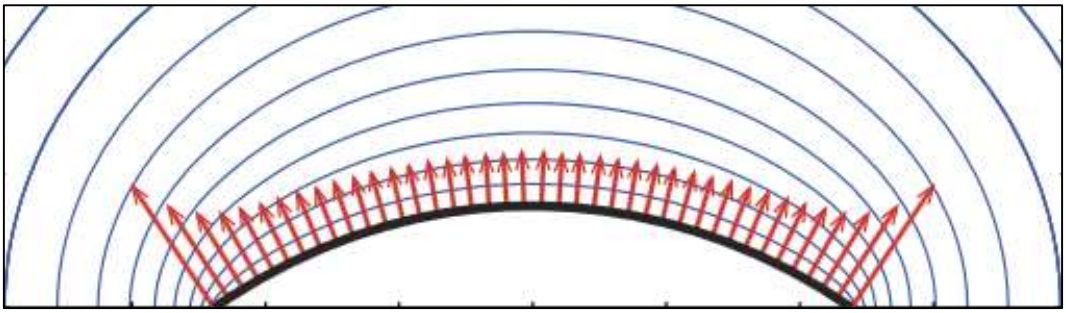

Figure 2.5: Schematic of an evaporating sessile drop, where the red arrows represent the magnitude of local mass flux and the blue contour lines are the vapour concentration in the atmosphere [Sáenz et al, 2017].

The coffee-ring effect describes the phenomenon of a drying droplet containing colloidal material and with a pinned contact line to form a ring shaped deposit, rather than a uniform film, as seen in Figure 2.6. It is currently believed that this is the cause of the deposition of OLED material up the side walls of the bank structure [Eales et al, 2015/b], in addition to the pinning of the ink on the upper surface of the bank structure, as visible in Figure 1.6.

Figure 2.6: Development of the coffee-ring effect [Breinlinger, n.d.].

The mechanism of the coffee-ring effect was first understood by Deegan et al [1997, 2000/a, 2000/b] as the higher evaporation rate at the contact line leads to a radial flow which transported material towards the contact line. Here it accumulated and pinned the contact line, ensuring that further material was deposited in the same region and formed a ring of almost all the material around what was the edge of the droplet. It was also found that other factors which usually govern fluid flow in droplets, such as surface tension gradients, solute diffusion, electrostatic and gravity effects, were negligible in ring formation [Deegan, 1997].

As stated by Deegan et al [1997], three conditions are required to facilitate the coffee-ring effect: a non-volatile solute, outwards flow and a pinned contact line. The contact line may be pinned by surface roughness, adsorption of the non-volatile component or by the deposition of large particles in the vicinity of the contact line [Eales et al, 2015/a]. The

deposition of material at the contact line is referred to as ‘self-pinning’, as a slight coffee-ring effect causes the contact line to pin due to the deposition of material along the edge of the contact line, leading to more widespread material transport to the perimeter of the droplet [Weon & Je, 2013].

The Marangoni effect serves as a counter measure to the radial outflow described above and exists when there is a difference in surface tension at the liquid-vapour interface. The direction of fluid flow is from an area of low surface tension to an area of higher surface tension [Meggs, 2011]. This means that, due to the increased evaporation at the contact line, the surface tension is lower at the contact line, and this causes a flow along the curvature of the meniscus and back towards the centre of the droplet, directly opposing the radial outwards flow.

The difference in local surface tension may be caused by variance in concentration, whereby it is known as the solutocapillary effect, or by thermal variance, when it is referred to as the thermocapillary effect, but both can coexist in the same system [Nakajima et al, 2003]. The total variation in surface tension is found by

$$d\sigma = \frac{\partial \sigma}{\partial T} dT + \frac{\partial \sigma}{\partial c} dc \tag{2.14}$$

where σ is the surface tension, T is the temperature and c is the concentration [COMSOL, 2017/a]. The relationship between temperature and surface tension, as it pertains to the current work, is explored in Section 3.4.5.

The solutocapillary effect is best illustrated by the ‘tears of wine’ research performed by James Thomson and then by Carlo Marangoni in 1865. They investigated the phenomena of wine seeming to run down the inside of a glass long after the wine had been poured in. Marangoni solved this mystery by realising that the alcohol within the wine evaporates faster than the water, and therefore the concentration of alcohol is lower at the three-phase contact line between the wine, glass and atmosphere, where the slight meniscus has a relatively high ratio of surface area to volume. This concentration gradient causes a surface tension (denoted as γ in Figure 2.7) gradient causing the meniscus to move up the wall of the glass, forming a film on the glass wall and increasing the surface tension gradient further. At a critical point, gravity takes effect and the wine runs back down the inside of the glass, forming the ‘tears of wine’ phenomena [Costa, 2015].

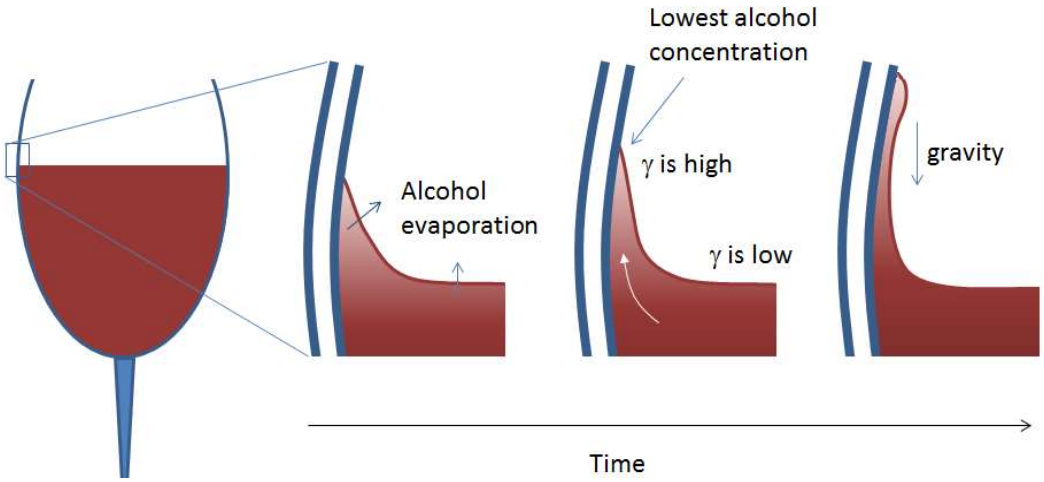

Figure 2.7: The solutocapillary effect on wine [Costa, 2015].

The thermocapillary effect is caused by localised temperature variance across the liquid-vapour interface. As a warmer vapour phase will contain more liquid molecules, due to enhanced local evaporation, the energy penalty of a liquid molecule moving to the interface is reduced and so, therefore, is the local surface tension, leading to a Marangoni flow [Bush, 2010].

As a droplet containing a diluted solute loses solvent to the atmosphere during evaporation, the concentration of the solute will increase, which will in turn increase the viscosity eventually leading to the solvent becoming immobile. This was studied by Ozawa et al. [2005], who found that changing the evaporation rate and initial solute concentration had a profound effect on the drying profile of droplets. Cases with high initial concentration and low evaporation rate generated deposits with a dip in the centre and cases with low initial concentration and high evaporation rates produced much flatter deposits. This work was expanded by Tarasevich et al. [2011], who reduced the mass flux of solvent with the increasing volume fraction of the solute to match experimental data, rather than having a linear evaporation rate as previously used by Ozawa et al. [2005].

2.4.4 Interacting Droplets

As an OLED device must contain many pixels in very close proximity to each other, it may not be entirely representative of reality to model just one pixel on its own, as the concentration field produced by evaporation of the ink in one pixel is affected by the overlapping concentration field of neighbouring pixels. This is further complicated in the case of OLEDs for display

purposes, as the red, green and blue inks may dry at different rates, and so will be affected surrounding pixels differently from all sides.

Pradhan & Panigrahi [2015] studied the phenomena of two colloidal droplets drying in close proximity to each other. It was found that less deposit was made in a coffee-ring at the point at which they were closest together, and this was shown experimentally and numerically to be caused by interference to the evaporative flux. In a single droplet, the evaporative flux is even around the contact line, so the coffee-ring is of a uniform thickness. When two droplets are adjacent, the vapour concentration of the atmosphere between the droplets becomes saturated, and so evaporation is lower in that area. This causes less radial outwards flow, and so less ring-shaped deposit, as seen in Figure 2.8.

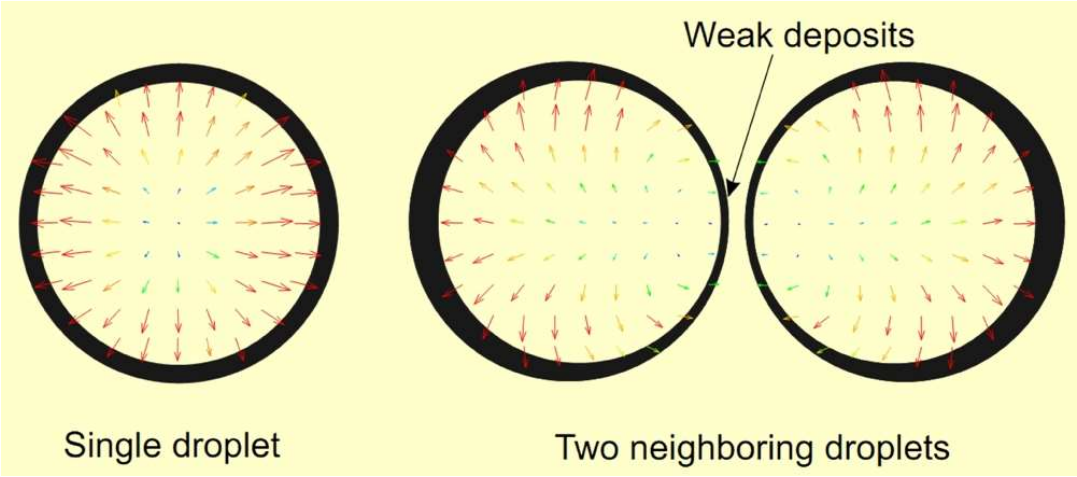

Figure 2.8: Deposition pattern of interacting droplets [Pradhan & Panigrahi, 2015].

Pradhan & Panigrahi [2016] expanded their research on the effect of droplets drying in close proximity by studying the evaporation of two droplets of a binary mixture (aqueous NaCl solution) numerically and experimentally. They found that the presence of an adjacent evaporating droplet influences the evaporative flux on the droplet surface, concentration field inside the droplet and the internal convection pattern inside a droplet, as seen in Figure 2.9. It was also shown that there is a reduction in the evaporative flux from the droplet surface leading to lower salt concentration inside the droplet in the proximity region between the two droplets compared to the remaining region, and that the influence of an adjacent evaporating droplet on the evaporative flux distribution, salt concentration and the velocity vector field reduces with increasing distance between the droplets, eventually leading to single droplet behaviour at a sufficiently large separation distance.

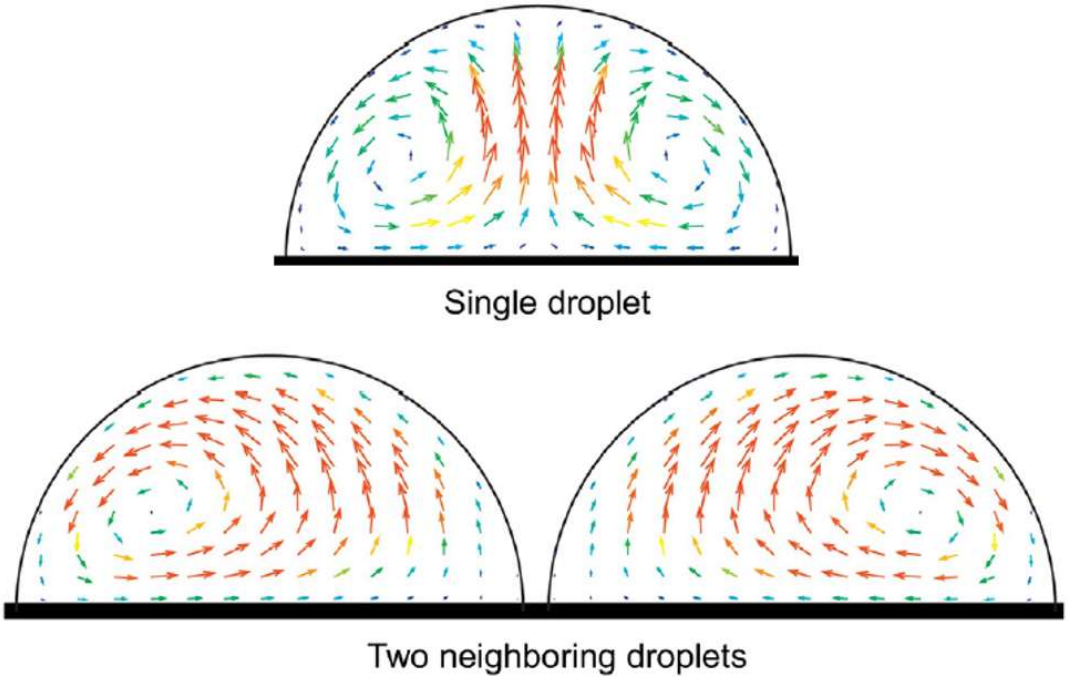

Figure 2.9: Internal flows of interacting droplets [Pradhan & Panigrahi, 2016].

2.4.5 Effect of Atmosphere and Vacuum Drying

Sefiane et al [2009] studied the effect of the atmosphere on the evaporation of a pinned droplet, covering the impact of various ambient gases, pressures and substrate materials. They showed, both mathematically and experimentally, that reducing atmospheric pressure increases the diffusion coefficient of vapour in the atmosphere and therefore the evaporation rate, and that the ambient gas also affects the evaporation rate, as seen in Figure 2.10.

Currently, OLED manufacturer Kateeva use a high-purity nitrogen environment in the production of inkjet-printed OLED devices, as this prevents contamination from oxygen and moisture and so maximise device performance and lifetime [Madigan at al., 2015].

The process of vacuum drying exploits this enhanced evaporation due to lower ambient pressure and can drastically increase production throughput of inkjet produced devices and reduce oxygen and moisture contamination [CPI, n.d.]. However, a high vacuum must be used and this can lead to the issues outlined in Section 1.5.

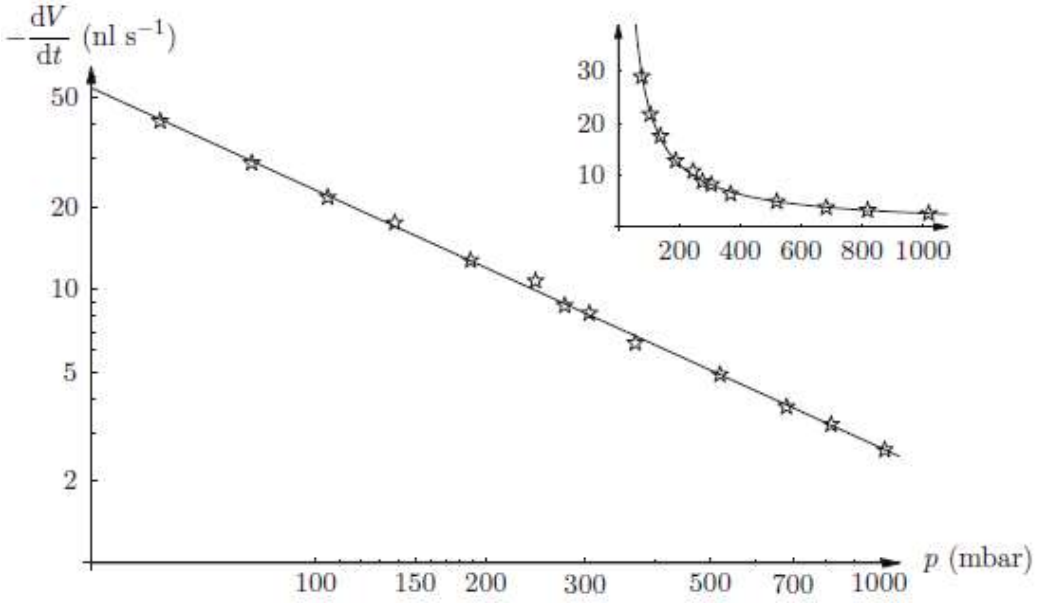

Figure 2.10: Experimental results showing the effect of atmospheric pressure on the evaporation rate of a sessile water droplet in a pure nitrogen atmosphere. Insert: The same results on a linear, rather than logarithmic, scale. [Sefiane, 2009].

2.4.6 Effect of Additives within Formulated Inks

The presence of nano-sized particles within the evaporating liquid, which OLED inks must contain to be printed in the micro-sized bank structures shown in Figure 1.7, were shown by Zhong, Crivoi and Duan [2015] to increase thermal conductivity and viscosity, and to change evaporation behaviour when compared to solvents containing no nanoparticles. The degree to which these changes occurred was largely due to the size and geometry of the nanoparticles present.

Zhong, Crivoi and Duan [2015] also observed experimentally a wide range of evaporation rates of sessile droplets containing nanoparticles, with the evaporation rate dependant on whether the nanoparticles were hydrophobic or hydrophilic, nanoparticle concentration, nanoparticle deposition patterns, contact angle dynamics and the various interactions between the nanoparticles, the liquid and the substrate.

Trokhymchuk et al. [2001] and Wasan, Nikolov and Moudgil [2005] had also observed the same impacts of the presence of nanoparticles on evaporation rate, and found that the nanoparticles increased the internal pressure within

the sessile droplet due to the attraction between particles, which lead to increased spreading across the substrate.

The effects of nanoparticles within a sessile droplet on the contact angle was conducted by Vafaei et al [2006], and found that increasing the nanoparticle concentration, increased the contact angle and the evaporation rate. However, Sefiane and Bennacer [2009] observed that introducing aluminium nanoparticles into a sessile droplet of ethanol reduced the evaporation rate, which was likely attributable to the nanoparticle deposits at the contact line leading to a longer period of the droplet remaining pinned. The relationship between the radii of the sessile droplet and the nanoparticles and the pinning-depinning cycles of the contact line was investigated experimentally by Shmuylovich et al. [2002], and was found to be stochastic.

Dan et al. [2011] and Darwich et al. [2011] studied the deposition formation of nanoparticles during the drying of a sessile droplet, and found that the capillary force was responsible for the horizontal movement of the nanoparticles, and Van der Waals forces were responsible for the deposition of the nanoparticles onto the substrate.

Fukai et al. [2014] studied the evaporation of a droplet of anisole containing polystyrene spheres deposited by inkjet printing onto a flat surface, both numerically by a Lagrangian finite element method and experimentally. This numerical model considered heat transfer between the droplet, substrate and air domains, and thermal and solutal Marangoni flows. It was found that the migration of the solute towards the contact line was almost finished by the time a thin liquid film had formed and so a ring-shaped deposit developed on the periphery of the dried film. It was also found that a high viscosity decreases the velocity of the outward flow, resulting in no generation of a ring-shaped deposit, which agreed with empirical results.

The effect of nanoparticle size on the pattern of deposition was also studied experimentally by Chon et al. [2007] and Zhong, Xie and Duan [2016], who observed that whilst all nanoparticle sizes generated some form of ring-shaped deposit, the smaller nanoparticles tend to be more evenly distributed across the substrate, whereas larger nanoparticles tend to form a more extreme ring-shaped deposit, as seen in Figure 2.11.

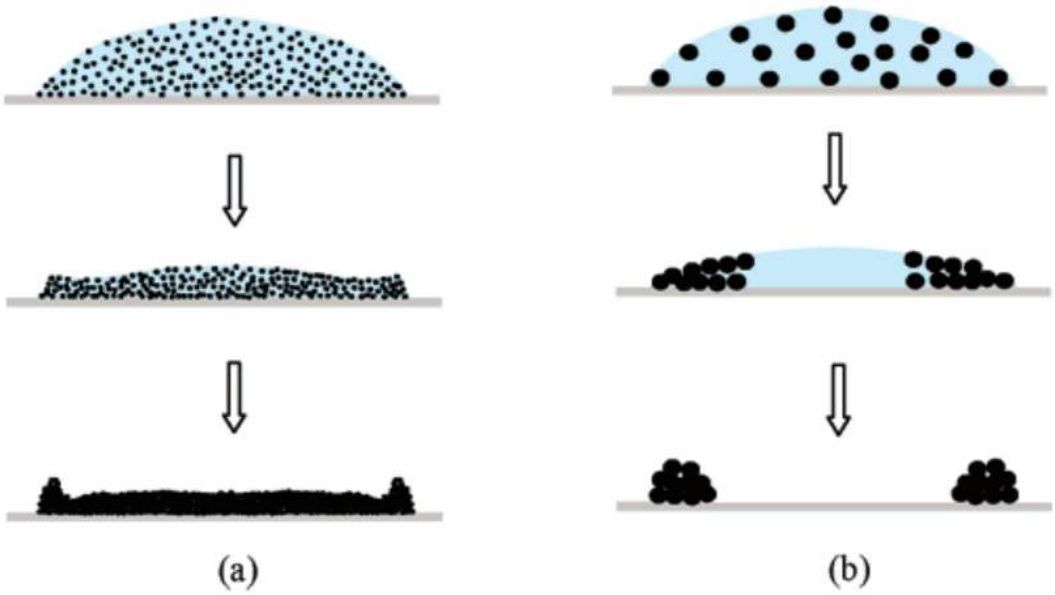

Figure 2.11: Schematic illustration of the evaporation and final deposition pattern of a sessile droplet containing (a) smaller nanoparticles and (b) larger nanoparticles [Chon et al., 2007].

The influence of hydrophilic and hydrophobic substrates on the deposition patterns of polymer latex was studied experimentally by Uno et al. [1998]. It was found that hydrophilic substrates induced adsorbtion towards the contact line, which was kept pinned throughout the drying process, creating a ring-shaped deposit. Hydrophobic substrates did not pin the contact line, due to no adsorbtion in the early stages of evaporation, and once a critical concentration was reached, aggregation occurs and adsorbtion produces tiny spots upon the substrate. This is shown in Figure 2.12.

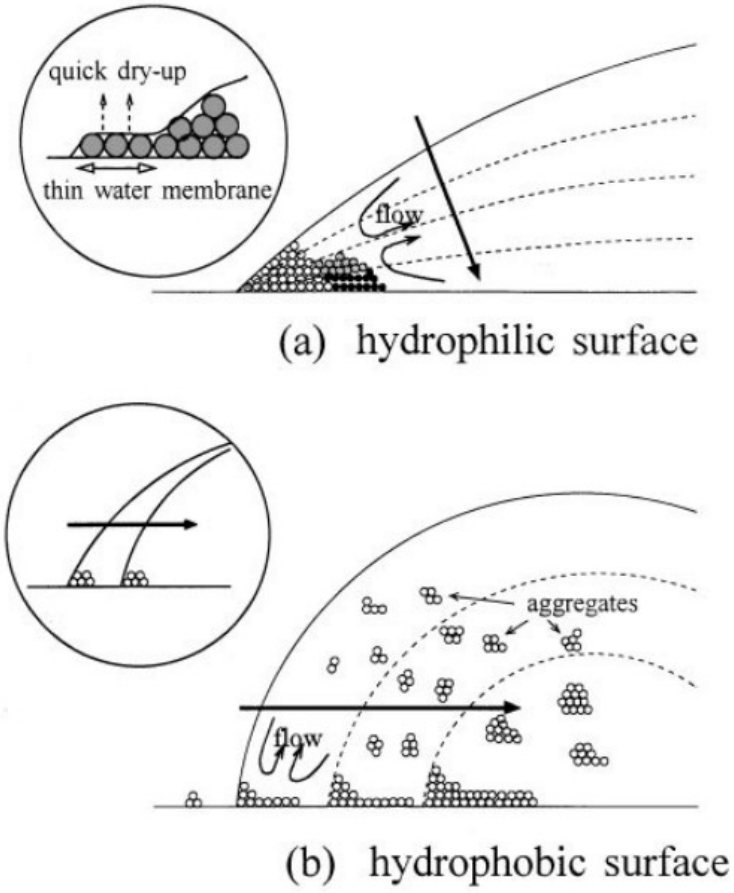

Figure 2.12: Schematic illustration of the deposition patterns of polymer latex on (a) hydrophilic substrates and (b) hydrophobic substrates [Uno et al., 1998].

The effects of the presence of hydro-soluble polymer additives was studied experimentally by Cui et al. [2012], who found that these additives enable the contact line to remain unpinned, due to the increased viscosity and Marangoni flows preventing suspended particles from reaching the contact line. This lead to a uniform distribution of the particles across the substrate.

Wray et al. [2014 & 2015] produced a comprehensive numerical model that simulated the effect of an electric field on the evaporation of a sessile droplet containing nanoparticles on a heated substrate, and it was found that careful manipulation of the electric field can control the formation of the ring-shaped deposits.

Sefiane [2010] conducted experimental investigations into various liquids containing various concentrations of nanoparticles at various substrate temperatures ranging from 20 to 80°C, and found that the evaporative behaviour of the droplet is dependent on the concentration of nanoparticles, the nanoparticle material, and the hydrophobicity of the substrate.

2.4.7 Evaporation of Multi-Component Droplets

The evaporation of multi-component droplets was studied extensively by Diddens et al. [2017/a] who extended a mathematical model for the drying of sessile droplets, based on the lubrication approximation, to binary mixture droplets, with the specific intention of applying this model to inkjet printing applications. This required generalising an established vapor diffusion-limited evaporation model to multi-component mixtures, where the different evaporation rates of the liquid components generate a composition gradient at the liquid-air interface. The model considered the composition-dependence of mass density, viscosity, surface tension, mutual diffusion coefficient and thermodynamics. They then used this model to study the evaporation of both water-glycerol and water-ethanol droplets, finding that in both cases the enhanced evaporation of the more volatile component near the contact line induces a surface tension gradient, which drives a Marangoni flow and can lead to a deviation from the spherical cap shape for flat droplets, and as a consequence of the Marangoni flow, the more volatile component is replenished at the liquid-air interface.

In water-glycerol droplets, the internal flows ceased due to the very high viscosity increase and, due to the low mutual diffusion coefficient, the entrapped water that remained was less able to reach the liquid-air interface and evaporate. This was in contrast to water-ethanol droplets, where the surface tension gradient was more pronounced and the viscosity value remained small, enabling the Marangoni flows to be maintained until almost all of the ethanol had evaporated. This was in good agreement with experimental studies conducted by Bennacer and Sefiane [2014] and Zhong and Duan [2016].

Diddens [2017] then went on to model the evaporation of a sessile multi-component droplet axisymmetrically using the finite element method, and comprised the coupled processes of mixture evaporation, multi-component flow with composition-dependent fluid properties and thermal effects for water–glycerol and water–ethanol droplets. This model used a spherical cap assumption, so that the equation for the free interface did not need to be solved. The vapor diffusion in the gas phase was used to determine the evaporation rates of both components, and due to preferential evaporation, a composition gradient was induced which drove complex flows via the composition dependence of the liquid properties. This flow then affected the

liquid composition and the temperature, which was also coupled via the latent heat of evaporation and the Antoine equation to the evaporation rates.

It was found that in water–glycerol droplets, the solutal Marangoni flow changed its direction when a droplet evaporated that had an initial contact angle above 90°. During the final stages of evaporation, the Marangoni flow ceased due to the increased viscosity and the slow evaporation of the remaining water, which was entrapped in an almost pure glycerol shell, which agreed with experimental findings by Shin, Jacobi and Stone [2016].

Whilst investigating the evaporation of a water–ethanol droplet, it was shown that the evaporation of the more volatile component could lead to a rapid decrease in the interface temperature, and due to this cooling, the ambient vapor of the less volatile component could initially condense on the droplet. The solutal Marangoni effects initially drove a chaotic flow in the water–ethanol droplet, which rapidly changed to a regular thermal Marangoni flow once almost all ethanol had evaporated.

Diddens et al. [2017/b] studied the ‘Ouzo effect’, which describes how Ouzo will turn from a transparent miscible liquid to a milky-white coloured emulsion when water is added. This effect can also be triggered by the preferential evaporation of ethanol in an evaporating sessile Ouzo drop, leading to a highly complex drying process with multiple phase transitions [Tan et al., 2016]. Due to the enhanced evaporation near the contact line, the nucleation of oil droplets starts at the contact line, which results in an oil ring encircling the droplet, with oil droplets being advected through the Ouzo drop by a rapid solutal Marangoni flow.

The evaporation of increasingly more complex mixtures from pure water, through a binary water–ethanol mixture, to the ternary Ouzo mixture consisting of water, ethanol and anise oil was investigated experimentally and numerically, via the finite element method, both axisymmetrically and in full 3D. This built upon the aforementioned work by Diddens [2017], and found good agreement between the numerical predictions and the experimental data for both a pure water droplet and a binary water–ethanol droplet. The numerical simulation for the ternary Ouzo droplet initially showed good agreement, including the onset of oil nucleation, but predicted a faster evaporation rate of the remaining water residual than seen in the experiments. This difference was attributed to the presence of the oil ring, which represented a geometric deviation from the typical spherical cap shape, and which was not included in the model.

2.5 Droplet Evaporation from Non-Uniform Surfaces

Kazmierski [2018] investigated the drying processes that occur within droplets deposited into a bank structure by way of experiment. The movement of particles was investigated within the droplet during drying and t the profile of the droplet surface was tracked with interferometry. This work covered square, circular and round-end rectangle shaped OLED pixels, and this review shall only concentrate on the circular bank structure results, as this is directly relevant to the case of a droplet modelled axisymmetrically.

Particle tracking experiments showed that the internal flows of droplets evaporating in bank structures are very similar to those previously observed in droplets drying on flat substrates, as described in Section 2.4.3.

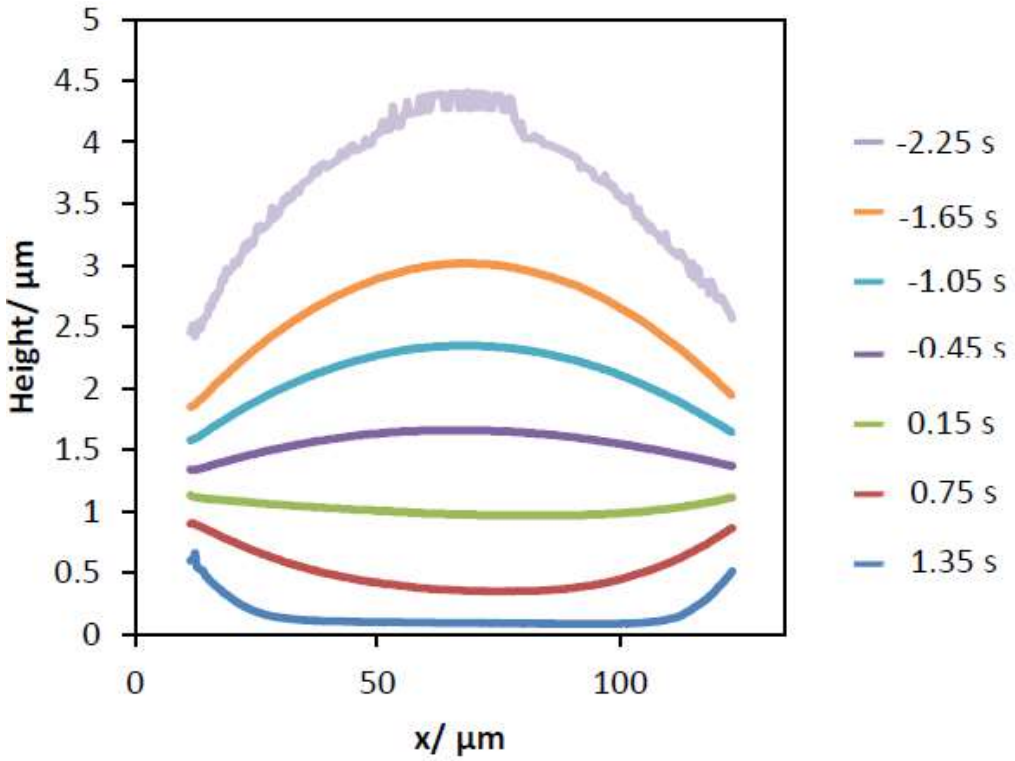

Figure 2.13: Cross-section profile of a methyl anisole droplet during evaporation from a circular well [Kazmierski, 2018].

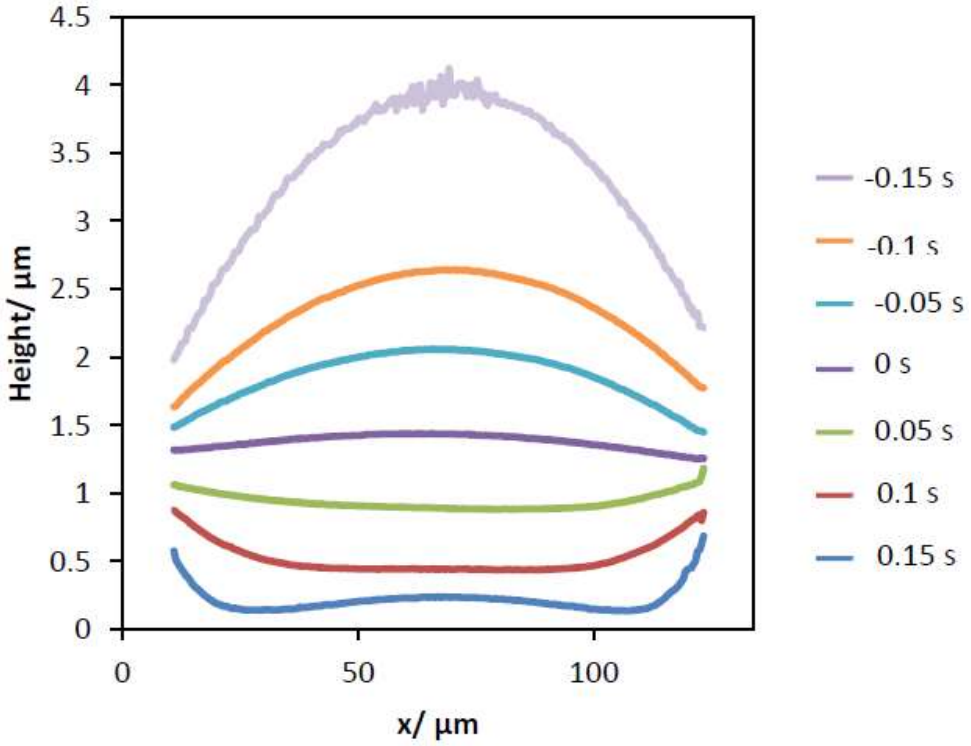

Figure 2.14: Cross-section profile of an anisole droplet during evaporation from a circular well [Kazmierski, 2018].

In Figures 2.13 and 2.14, t = 0 represents the moment at which the centre of the droplet is level with the top of the bank structure, and the edges of the bank structure are located at x = 0 and x = 134µm (i.e. the edges of the chart). Interference from the bank structure meant that data could not be reliably collected any closer to the edges than is shown.

It was found that the droplet remained pinned at the wall top for the duration of the drying process, with less volatile solvents, such as methyl benzoate, mesitylene, dimethyl anisole and methyl anisole, producing U-shaped profiles, as seen in Figure 2.13, whereas more volatile solvents, such as anisole, produced W-shaped profiles, as seen in Figure 2.14. It was identified that the biggest factor in generating a W-shaped profile is the rate of evaporation, whether that be a more volatile solvent evaporating under normal conditions, or a less volatile solvent drying under enhanced evaporation conditions, such as increasing the extraction of vapour via vacuum.

An M-shaped profile was intermittently seen in o-xylene tests in circular wells, with the only plausible explanation being seen as the presence of surface stress arising from a surface tension gradient. The surface tension driven flows coupled with the capillary flows from the curvature of the drop

surface overcame the relatively fast evaporation rate of o-xylene and prevented a protuberance appearing and creating an M-shaped profile.

As mentioned in Section 2.4.3, surface tension gradients (i.e. the Marangoni effect) can arise from either thermal or solutal causes. As evaporation is higher near the contact line, evaporative cooling is more extreme in this region, and thus increases the surface tension near the contact line relative to the centre of the droplet. The effect of evaporative cooling generated by a fast evaporating fluid, such as o-xylene, may be sufficient to produce a large enough Marangoni flow to generate an M-shaped profile. In addition, contamination of the solvent may produce a solutal Marangoni effect to generate an M-shaped profile, but neither of these possibilities were supported by direct evidence. This phenomena will be studied in detail in Section 5.2.7, in order to elucidate the cause of this unexpected behaviour.

In order to determine the effect of OLED material on the surface tension of the solvents, solutions were made at concentrations of 2-8% by weight of active material, and the surface tension were measured for comparison against pure solvents. All solvents showed an increase in surface tension with increasing concentrations of active material, although not linearly. Due to the higher evaporation at the contact line, active material is transported to the edge of the droplet and this increased local concentration increases the surface tension and leads to the M-shaped profiles observed.

The difference in the levels of enhanced drainage between the slower and faster evaporating solvents could be due to the amount of time the material has to diffuse through the droplet during drying. The faster drying solvents, namely anisole, methyl anisole and mesitylene, did not have time for the material to average horizontally across the droplet, leading to higher concentrations and therefore surface tension at the contact line, producing Marangoni flows. Slower drying solvents, such as dimethyl anisole and methyl benzoate, did have time for the material to average horizontally and therefore did not generate any Marangoni flows due to the active material.

In an industrial setting, OLED pixels dry in a vacuum chamber to increase the evaporation rate, and therefore increase manufacturing output. Mokeba et al [1997] and Holyst et al [2015] showed that in a vacuum chamber evaporation changes from diffusion control to ballistic control as pressure drops. Once the mean free path exceeds the length scale of the drop, any vapour immediately moves away from the drop surface, and evaporation is no longer higher at the contact line than in the centre of the drop. This

reduces enhanced drainage from the centre of the droplet, so an M-shaped profile is less likely to occur, and the processes controlling the deposition of material are evaporation rate and pinning of the droplet at the wall tops.

Plots produced from experiments performed at Merck Chemicals Ltd., where the drying speed was controlled by the pressure in the vacuum chamber, clearly showed that in a vacuum the evaporation rate determines the deposition pattern, with slow drying droplets forming a U-shaped profile, and a fast drying droplet produces a W-shaped profile, much akin to single solvents without active material drying at atmospheric pressure.

Eales et al [2015/b] investigated the impact of trough geometry on film formation for P-OLED displays, and found that increasing the depth or the gradient of the walls increased the coffee-ring effect. The reasons for this were twofold. First, a larger film thickness takes longer to reach the concentration at which the viscosity renders the fluid immobile and outward flow can continue for a greater period of time, transporting more material to form a coffee-ring. Second, the incline of the walls aids the outwards flow, and so an increased gradient will increase material transport to the edge of the pixel.

These results were found through the use of a thin film lubrication approximation in a 2D axisymmetric model, which assumes that the vertical forces are negligible compared to the horizontal forces, due to the very high aspect ratio of the trough. Whilst this is a reasonable assumption for a very thin film droplet, by Eales' own admission it is not realistic for "thick droplets in deep troughs", with the lubrication approximation only effective in the case

$$Re = \frac{\rho E R}{\mu} \ll 1 \tag{2.15}$$

where *Re* is the Reynolds number, ρ is the liquid density, *E* is the vertical velocity of the fluid, *R* is the radius of the droplet and μ is the viscosity of the fluid. However, it is not stated at which point this model will lose accuracy, and so it would be more useful, realistic and reliable to use a model which does not employ the lubrication approximation, despite this model being considerably more complex.

2.6 Advanced Computational Models of Evaporating Droplets

Due to the shortcomings of the classical model described in Section 2.4.1, several so-called ‘comprehensive’ models have been developed which incorporate many more variables.

An example of a comprehensive model is Hu and Wu [2015], as mentioned in Section 2.4.2, which considered vapour diffusion in the air, evaporative cooling at the liquid-air interface, conjugate heat transfer in the substrate, liquid and air, and both buoyancy-induced and Marangoni convections in both the liquid and air domains, all in pined droplets on heated and unheated substrates. The model was validated against experimental work by Sobac and Brutin [2012], with a relative difference of less than 4% for the total drying time.

This study assumed that droplet evaporation is dominated by vapour transport in the air domain and that droplet evaporation can be considered quasi-steady, as the droplets studied had a radius of 1mm and therefore took around 100s to dry completely, however this assumption may not hold true for much smaller, faster drying droplets on the scale of OLED pixels.

The local normal vapour flux, $J(r)$ was established through

$$J(r) = -D\nabla c \cdot \mathbf{n} + (\mathbf{n} \cdot \mathbf{u})c \tag{2.16}$$

where $\mathbf{n}$ is the unit normal vector at the liquid-air interface and $\mathbf{u}$ is the velocity vector. A global evaporation rate was used by integrating the local vapour flux over the whole droplet surface, therefore assuming that the droplet maintained a spherical cap,

$$\dot{V}(\theta) = \frac{dV}{dt} = --\frac{2\pi}{\rho}\int_0^R J(r)\sqrt{1+\left(\frac{\partial h}{\partial r}\right)^2}\, rdr \tag{2.17}$$

where V is the droplet volume, π is the contact angle, ρ is the liquid density, R is the base radius of the droplet, and h and r are the height and radial coordinates of the droplet surface respectively. This method is both efficient and accurate in a sessile droplet on a flat substrate, where a spherical cap is assumed to always be maintained, but would fail to represent the W- and M-shaped profiles observed by Kazmierski [2018] when a bank structure is present.

Yang, Hong and Cheng [2014] studied the role of liquid and substrate thermophysical properties in an evaporating sessile droplet, and calculated the mass flux through

$$M_f = \mathbf{n} \cdot (-D\nabla c + \mathbf{u} \cdot c) \cdot M_v \tag{2.18}$$

where M_f is the local mass flux and M_v is the molar mass of the vapour. This mass flux was then applied to the computational mesh by

$$\mathbf{u}_{mesh} = \left(\mathbf{u}_{\boldsymbol{l}} \cdot \mathbf{n} + \frac{M_f}{\rho_l}\right)\mathbf{n} \tag{2.19}$$

where $\mathbf{u}_{mesh}$ is the velocity of the mesh, $\mathbf{u}_l$ is the velocity of the liquid and ρ_l is the density of the liquid. This meant that the droplet surface moved according to the local mass flux at that mesh element, rather than globally, so that the surface was ‘free’ to achieve any profile shape imposed by the input variables. Hence, U-, W- and M-shaped droplet profiles can all be represented in this method, making it ideal for studying the evaporation of droplets from a bank structure at OLED scales.

This model was further added to by Chen et al [2017], who included natural convection of both heat and mass transfer.

2.7 Conclusions

It is clear from the research reviewed above that previous studies, whilst often matching closely with experimental data and some containing a comprehensive range of variables, there is a gap in the literature on modelling the effect of a bank structure on the deposition pattern of material onto the substrate.

Experimental work by Kazmierski [2018] showed that different solvents produce either U-, W- or M-shaped drying profiles, with U- and W-shaped profiles being attributed to slower or faster drying solvents respectively. M-shaped profiles were only seen sporadically with o-xylene, with the introduction of thermal or solutal Marangoni flows seen as the only possible cause, but without direct evidence.

The widely-used classical method must maintain a spherical cap and so cannot represent the changes in the free surface demonstrated experimentally by Kazmierski [2018], only expresses the evaporative flux globally across the entire droplet surface, and does not consider internal flows or thermal considerations. Evaporative cooling was included into the classical model by Sefiane et al [2009], but the other above-mentioned issues persisted.

Due to these shortcomings, several comprehensive models have been proposed, with a model by Yang, Hong and Cheng [2014] having the ability to match the local evaporation to the local deformation of the mesh in order to allow various droplet drying profiles to be produced, dependent on input variables.

In terms of the stated aims and objectives of this work, outlined in Section 1.6, there is considerable literature surrounding the topic of drying sessile droplets on flat substrates, allowing for detailed validation against theoretical and experimental works. There is far less available literature on the drying of droplets from a bank structure however, and therefore there must be a heavy reliance on the work of Kazmierski [2018] for experimental data to validate the current model against.

The current gap in the knowledge base for droplets drying in a bank structure which is apparent from the literature, will enable the current work to explore a barely studied area of science, and to generate some truly novel results. The most appropriate method of achieving this that was gleamed from the literature is to apply a model similar to Yang, Hong and Cheng

[2014] to a geometry including a bank structure. Further justification for the use of this method in the current work can be found in Section 3.2.

Chapter 3:
Modelling Methodology

3.1 Introduction

Modelling a problem is an extremely efficient way of studying the effect of changing variables within a system. For example, studying the effect of viscosity on drying profiles of an OLED solution experimentally could be difficult to accomplish, however if a model validated against current OLED solutions was used, the effect of changing one parameter could be studied easily. Modelling a problem also allows a feature to be studied in isolation, such as the vapour concentration field around the droplet or the velocity and temperature fields, which is impossible to study to the same degree experimentally.

3.2 Selection of Modelling Method

Before the specifics of modelling the problem of a droplet containing OLED material drying in a bank structure can be addressed, the fundamental operation of various modelling techniques must be understood.

There are two types of modelling that can be applied to such a problem: analytical and numerical. Analytical modelling, also known as mathematical modelling, treats the problem as one that can be described by a mathematical function. This means that they can generate insightful results relatively quickly, but for droplets containing complex fluids, especially those containing soluble and insoluble solid material, a full mathematical analysis leading up to a completely dried pattern, is extremely difficult, if not impossible [Zhang et al., 2019].

Numerical modelling techniques on the other hand provide far more detailed results and allow for the manipulation of all parameters independently, meaning that any “what if” scenario can be addressed. Unexplained results can be examined more closely than the analytical method and, as the numerical method allows for the variation of individual parameters, their effect on the final material deposition can be studied. Despite numerical methods requiring considerable computational effort and so taking more time to produce results, it is the most desirable technique for the present case.

There are several numerical methods for solving two-phase flow problems with interface-capturing, such as diffuse-interface models like the Phase Field (PF) and Lattice Boltzmann (LB) methods, the Eulerian formulation-based Volume of Fluid (VOF) and Level Set (LS) methods, a Lagrangian formulation method and the Arbitrary Lagrangian-Eulerian (ALE) method.

Diffuse interface models, such as the PF and LB methods, enable the modelling of interfacial forces as continuum forces, meaning that forces and discontinuities at the interface are smoothed by distributing them over thin, numerically resolvable layers. Diffuse-interface models for multiphase Navier-Stokes flow are computationally less taxing than solving the exact equations, as calculations can be done on fixed grids, with the diffuse interfaces able to propagate through the grids, whereas the sharp-interface equations usually require adaptive, interface fitting grids. Interface fitting grids, such as those used in the ALE method, are not useful for flows where the phases split or coalesce, but these flows can be calculated by using diffuse-interface flow models [Jacqmin, 1999].

In the PF method, the interfacial layer is governed by a phase field variable, rather than the interface being tracked directly between the two fluids, with the surface tension force added as a body force to the Navier-Stokes equations by way of multiplying the chemical potential of the system and the gradient of the phase field variable. The evolution of the phase field variable is governed by the Cahn-Hilliard equation, which is a 4th-order PDE, but is decomposed by the PF method into two second-order PDEs. The Cahn-Hilliard equation convects the fluid interface and ensures that the total energy of the system diminishes correctly. The PF method is therefore more mathematically complex than the LS method, where the fluid interface is simply advected with the flow field [COMSOL, 2021].

PF methods possess several advantages over the VOF approach, such as PF models allowing the use of standard advection techniques and so can be implemented in 3D more easily, and it is relatively straightforward to generate phase-field numerical implementations that are dissipative of energy and free of parasitic flows. However, the PF interface structure is vital to determine interface energy and surface tension, and due to the need to calculate this structure, numerical PF interfaces have to be artificially wide. These are usually four to eight cells wide, representing several orders of magnitude thicker than the actual interface. These wide interfaces worsen other issues of the PF method, such as curvature dependent solubilities, as these are proportional to interface thickness. In addition, more robust anti-diffusion is required for these wider interfaces to prevent distortion through advective straining. The artificially thick interface tends to generate spurious velocities in and around the interface, and dealing with large density ratios (such as modelling both water and air) is challenging. There is also a tendency in PF models for droplets to evaporate even when they should not [Jacqmin, 1999].

The LB method is useful in fluid flow applications including interfacial dynamics and complex boundaries, as the LB method is based on microscopic models and mesoscopic kinetic equations, whereas conventional numerical schemes depend on discretizations of macroscopic continuum equations, [Chen and Doolen, 1998].

The foundation of the LB method is to capture the physics of micro- or mesoscopic processes via simplified kinetic models, so that the macroscopic average matches the macroscopic equations. Using simplified kinetic models for macroscopic fluid flows operated on the premise that the

macroscopic dynamics of a fluid is simply an extension of the collective behaviour of many microscopic particles in the system, and that the macroscopic behaviour will largely not be sensitive to the nuanced details seen at microscopic level. [Kadanoff, 1986].

The use of simplified versions of the kinetic equation, removes the complexity of solving the full kinetic equations, such as the full Boltzmann equation, and also avoids having to track each particle individually, as in computationally expensive molecular dynamics simulations. Even though the LB method is founded on a particle-by-particle basis, the primary focus is to replicate averaged macroscopic behaviour of the system. Using the kinetic equation gives the LB method many of the advantages of molecular dynamics, such as clear physical pictures and easy implementation of boundary conditions [Chen and Doolen, 1998].

The kinetic-based approach of the LB method can be distinguished from other numerical methods in three key ways [Chen and Doolen, 1998]:

1. The convection operator of the LBM in phase space is linear, which is a feature that is used in kinetic theory and contrasts with the non-linear convection terms in other methods that utilise a macroscopic outlook. Simple convection in combination with a relaxation process allows non-linear macroscopic advection to be revered via multi-scale expansions.
2. The incompressible Navier-Stokes equations can be obtained in the LB method, and the pressure of the LB method is calculated using an equation of state. In methods that employ direct numerical simulation of the incompressible Navier-Stokes equations, the pressure satisfies a Poisson equation with velocity strains acting as sources, often causing numerical difficulties that have to be treated with iteration or relaxation tools.
3. The LB method utilizes a minimal set of velocities in phase space. In traditional kinetic theory using the Maxwell-Boltzmann equilibrium distribution, the averaging process requires data from the whole velocity phase space. Due to the LB method using only one or two speeds and a few moving directions, the transformation relating the microscopic distribution function and macroscopic quantities is made far simpler and consists of simple arithmetic calculations.

Despite the advantages that the LB method offers, it still suffers the same drawbacks as the PF method, namely the artificially thick interface also tends to produce spurious velocities in and around the interface, dealing with large density ratios is again difficult, and the tendency remains for droplets to evaporate when they should not. Additionally, in the LB method, it can be

difficult to match experimental parameters, as the fluid properties are linked to the lattice size.

The VOF method is based upon the fraction function C, which is a scalar function defined as the volume of a computational cell. Every cell tracks the volume fraction of each, and one set of momentum equations is applied to all fluids. If a cell contains no traced fluid, $C = 0$, if the cell is entirely full of traced fluid, $C = 1$, and if there is a fluid interface within the cell, C has a value between 0 and 1. As C is a discontinuous function, its value will jump from 0 to 1 when the cell moves fully into a traced fluid, and the point at which the value of C changes fastest represents the normal direction of the fluid interface. As the free-surface is distributed over the span of a cell, rather than being sharply defined, local grid refinements have to be conducted in cells where $0 < C < 1$ in order maintain accuracy. However, the location and mean curvature of the interface cannot be calculated precisely, as the interface position has to be interpreted using the discrete VOF values of the cells around the interface. [Chen and Raad, 1997].

The VOF method, which is commonly used with the finite volume approach to solve the Navier-Stokes equations, is able to handle large deformations in the free surface, including break-up and coalescence, but as the interface needs to be reconstructed, it would be extremely difficult to apply the complicated boundary conditions needed to simulate a drying sessile droplet. It is possible to do the VOF method without performing reconstructions, by having a surface tension force represented by a volume force, but this makes the interface numerically more diffuse [Tanguy and Berlemont, 2005].

In the LS method, a zero contour of a signed distance is used to represent the interface, known as the LS function. The LS function can be identified by iso-lines or iso-surfaces in 2D and 3D respectively, with negative values referring to one of the fluids, positive values referring to the other, and a zero value identifying the location of the interface. A differential equation for the level set function governs the movement of the interface, and advection is typically found through the use of essentially non-oscillatory (ENO) or weighted essentially non-oscillatory (WENO) methods. In order to keep the level set function as a signed distance function, a reinitialization process is required. LS methods will automatically account for topological changes and it is straightforward to achieve a high order of accuracy, by selecting an ENO

or WENO scheme with the desired order of accuracy [Olsson and Kreiss, 2005].

The primary limitation of LS methods is that they are not conservative, and can lose or gain mass, which is physically incorrect [Tornberg and Enhquist, 2000]. In an attempt to improve mass conservation of the LS method, Sussman and Puckett [2000] combined of the LS and VOF methods, to maintain the mass conservation of the VOF method whilst using a LS function to better approximate the curvature. In this case, a colour function was required and had to be advected, and due to discontinuity of this function across the interface, a great deal of care had to be taken to advect this function correctly. Due to this, it is difficult to avoid oscillations for any greater than two order advection schemes, and hence this loses much of the simplicity of the original LS method.

Enright et al. [2002] also addressed the issue of mass conservation of LS methods, and proposed a hybrid of the LS method and a marker particles method to improve accuracy, particularly in under-resolved regions. However, this also negated the original simplicity of the LS method.

Ultimately, the LS method generally provides a more accurate determination of the interface than the VOF method, but introduces serious issues regarding the conservation of mass [Olsson and Kreiss, 2005].

In the Lagrangian method, the governing equations are formulated in a Lagrangian grid, where the mesh nodes always coincide with the material particles and so make it possible to track the free surface automatically. However, the numerical realization is far more complex and time-consuming than a Eulerian method, and the whole computational domain has to be frequently re-meshed [Zhang & Chen, 2007]. There is also an issue regarding this methods ability to deal with large deformation, which do not have an impact in sessile droplet, but may become a factor when the surface becomes more deformed in the later stages of geometries that include a bank structure.

The ALE formulation method combines the benefits of both Eulerian and Lagrangian methods, meaning that it can represent the droplet evaporation problem without having to make the concessions of being quasi-steady or assuming a spherical cap. It can also account for complex contact line dynamics during droplet evaporation, such as pinning and de-pinning, and describes the interface, interfacial flux and interfacial stress more precisely than the VOF or LS methods. In addition, it allows for much greater

deformation than the Lagrangian method, whilst reducing the need for frequent re-meshing.

The key advantage of the ALE approach, implemented through the Finite Element Method, is that the interface is precisely defined at all times, with the computational mesh being fitted to it and forming the interface. This makes it much easier to apply complicated boundary conditions and avoid spurious currents. In addition, the zero-thickness interface is a much closer approximation to a real interface, and there are no difficulties in having large density ratio. The disadvantages of the ALE method are inability to deal with topological changes such as break-up, coalescence or coming into contact with the boundary (as is seen in subsequent chapters) and, compared to the VOF method, greater computational resources are required. However, as the current research is only concerned with the behaviour up to the point of touchdown, the benefits outweigh these disadvantages.

The ALE formulation does also has issues with the moving mesh, as will be discussed in Section 3.3.4, but this was considered to be manageable within the scope of the current investigation being carried out.

It is therefore clear that the ALE method, applied numerically by the Finite Element Method described in Section 3.3, should be used for modelling the evaporation of a droplet in a bank structure, as it allows for the vast array of interconnecting equations required to accurately represent an evaporating droplet, and the liquid/gas interface can be sharply defined in order to apply specific parameters, such as variable surface tension, which other methods cannot achieve. This was also the method selected for use by Yang, Hong and Cheng [2014], was established in Section 2.6 as the most applicable method to be applied to the problem being modelled here.

3.3 Finite Element Method

3.3.1 Introduction

The Finite Element Method (FEM) is a general technique for numerical solution of differential and integral equations, and was introduced in the late-1950s for solving partial differential equations (PDEs) in structural engineering. At this time, it was regarded as a generalisation of earlier methods in structural engineering for beams, frames and plates, where the structure was sub-divided into small parts, so-called finite elements, with known simple behaviour. The FEM was developed during the 1960s and 70s into a general method for the numerical solution of PDEs and integral equations, and has since been applied to almost all areas of science and engineering [Johnson, 2009].

For this research, the FEM will be applied through the use of the COMSOL Multiphysics 5.4 software package.

3.3.2 Process Steps of FEM

The basic process steps of the FEM are as follows [Sastry, 2017]:

1. *Discretisation*: the given domain is divided into a number of finite elements, with the points of intersection referred to as nodes. All of the elements and nodes are assigned a number.
2. *Derivation of element equations*: A function, u, that may be the dependent variable in a PDE (such as temperature, pressure, etc.) can be approximated by a function u_h, using linear combinations of base functions according to eq. (3.1) and (3.2).

   $$u \approx u_h \tag{3.1}$$

   For the given differential equation, a variational formulation is constructed over a typical element with n nodes, with the element equations obtained by substituting a typical dependent variable, say

   $$u = \sum_{i=1}^{n} u_i \psi_i \tag{3.2}$$

   into the variational formulation, where u_i represents the coefficients of the functions that approximate u with u_h. After choosing ψ_i, the interpolation functions, the element matrices are computed.
3. *Assembly*: The next step is the assembly of the element equations so that the total solution is continuous. When this is done, the entire system takes the form

$$K\mathbf{u}' = \mathbf{F}' \tag{3.3}$$

where K is the assemblage property matrix, and $\mathbf{u}'$ and $\mathbf{F}'$ are column vector containing unknowns and external forces.

4. *Boundary conditions*: The above system of equations is modified using the boundary conditions of the problem.
5. *Solution of the equations*: The system is solved by any standard technique.

In the FEM, the continuous function over each of the elements is approximated by a suitable piecewise polynomial, and to obtain a better approximation, one need not use higher-order polynomials as in other methods, but can simply use a finer sub-division (i.e. increase the number of elements).

3.3.3 Time-Dependence in FEM

In order for the FEM to be used in a time-dependent problem, such as a drying droplet, a time-stepping scheme must be applied.

For the problem of a drying OLED droplet the Backwards Differentiation Formula (BDF) time-stepping algorithm was used, which is an implicit solver that uses backward differentiation formulas with order of accuracy varying from one to five depending on the requirements of the particular physics models to be solved. This means that a high order will be used when possible, and a lower order will automatically be employed when necessary to obtain stability, but at the risk of potentially damping high frequencies. In COMSOL Multiphysics 5.4, the BDF solver is the default transient solver for transport applications, as it offers extra robustness over other methods such as the Generalised Alpha Method [COMSOL, n.d.].

In this application, the BDF solver has free time-stepping, meaning that larger or smaller time-steps can be taken as required to satisfy the specified tolerances. The solver will try to take as large a time-step as possible, but will reduce the time-step size when necessary if the solution starts to vary rapidly in time [COMSOL, n.d.].

3.3.4 Element Types in FEM

Within FEM there are many ways to define the elements, some of which are shown in Figure 3.1. Figure 3.1a depicts the most common element types in

2D linear functions, with the elements expressed as functions of the positions of the nodes (i.e. x, in 2D, and x,, in 3D).

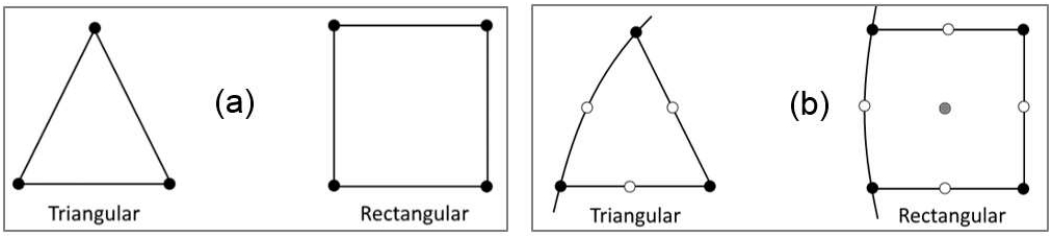

Figure 3.1: Depiction of 2D linear (a) and quadratic (b) mesh elements [COMSOL, 2017/b].

The corresponding second-order (quadratic) elements are illustrated in Figure 3.1b. These elements have the ability to follow curved boundaries whilst another edge of the element represents a flat boundary, this is essential for a droplet being modelled on a flat surface, but all edges can also represent curved boundaries, which is essential in modelling certain bank structure geometries.

However, quadratic elements have a tendency to become 'inverted' in applications with moving boundaries, as in a drying droplet, which causes the entire simulation to fail. Therefore, the more computationally robust linear elements will be used in these simulations, with the mesh greatly refined along the curved free surface of the droplet to match the curvature as closely as possible whilst maintaining a useable number of elements. This is explored in the mesh independence study in Section 4.2.

3.3.5 Error Estimation

As FEM gives an approximate solution to the mathematical model equations, the difference between the solution to the numerical equations and actual solution, also known as the error, e is

$$e = u - u_h \tag{3.4}$$

The error can often be estimated before the numerical equations are solved, known as an *a priori* error estimate, which can be used to predict the convergence order of the applied FEM. However, an *a priori* estimate can only be found for simple problems, and often contain unknown constants which make quantitative predictions impossible. An *a posteriori* estimate uses the approximate solution, along with other approximations to related problems, to estimate the norm of the error.

3.3.6 Mesh Convergence

Mesh convergence is a method that compares approximate solutions obtained for different meshes. In an ideal situation, a very fine mesh approximation could be taken as an approximation to the actual solution, so the error for approximation of coarser meshes can be evaluated as

$$e = u_{h1} - u_h \tag{3.5}$$

However, in reality, computing a far finer mesh than is required can be difficult, so the finest mesh approximation is often used. The convergence can be estimated from the change in solution for each mesh refinement, and the change will be smaller in each mesh refinement if the approximate solution is in a converging area, and therefore closer and closer to the real solution [COMSOL, 2017/b].

Generally, the relative error will decrease with decreasing element size and increasing element order (i.e. the order of the basis functions). However, increasing the number of elements in a given area or increasing the element order will increase accuracy at the expense of increased computation, so a balance between accuracy and computing time must be struck.

After computing a solution to the numerical equations, *a posteriori* local error estimates can be used to create a denser mesh where the error is large. A second approximate solution may then be computed using the refined mesh [COMSOL, 2017/b].

3.4 Governing Equations and Boundary Conditions

3.4.1 Coordinate System and Computational Domains

The geometry of the model was laid out axisymmetrically, as shown in Figure 3.2. This image is only to be considered a guide to the general construction of the geometry with specific dimensions, droplet shapes and bank structures provided in the relevant subsequent sections.

A cylindrical coordinate system is used with the z-axis representing the domain height and the r-axis denoting the radius from the axis of symmetry.

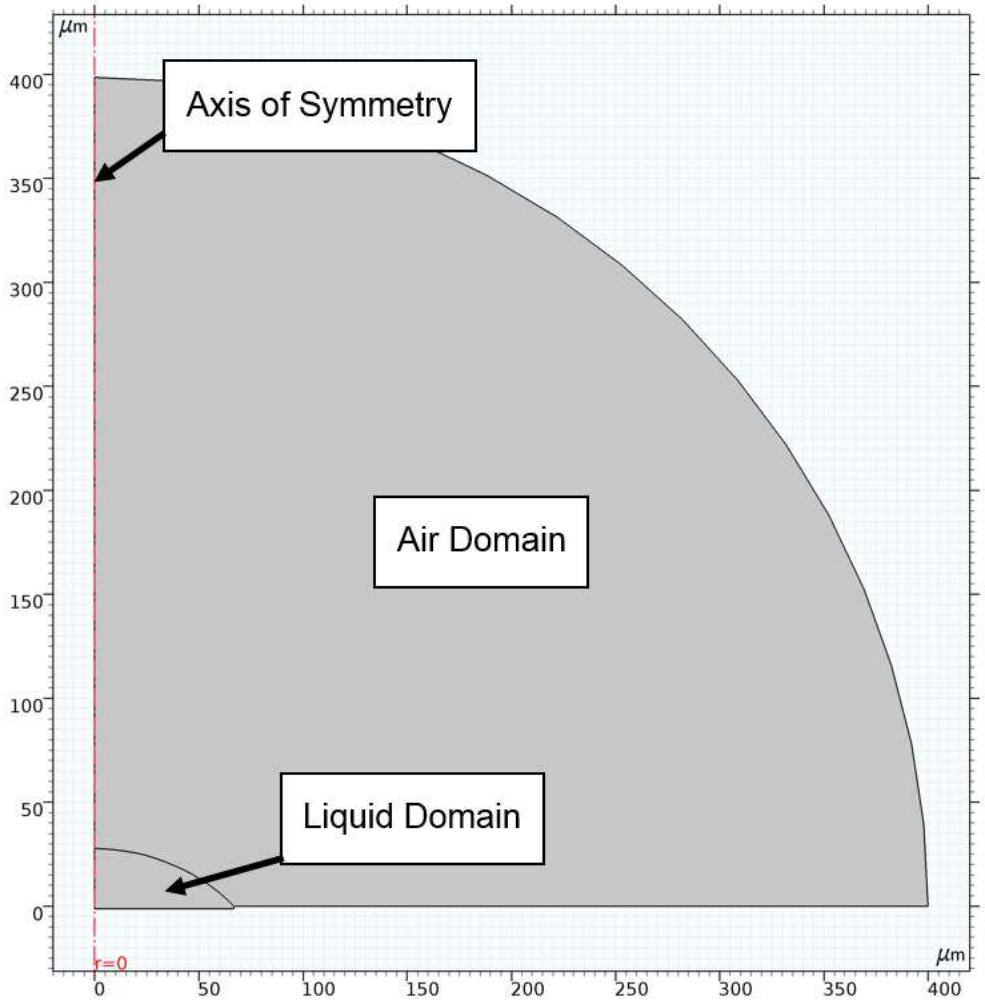

Figure 3.2: Model geometry layout.

The fluid flow is modelled in both the liquid and air domains, the vapour concentration is modelled only in the air domain, heat transfer is modelled in the liquid and air domains, and occasionally in the substrate upon which the liquid and air domains reside (not pictured), and the free surface that separates the liquid and air domains moves in respect to time.

The mathematical details of the models and the coupling between the domains are given in subsequent sub-sections.

3.4.2 Vapour Concentration and Thermal Modelling

In order to represent evaporation, the value for the mass flux from the droplet surface was derived from two interconnected physics models known in COMSOL as Heat Transfer in Moist Air and Moisture Transport in Air.

The heat transfer in the liquid and air domains is governed by the equations

$$\rho C_p \frac{\partial T}{\partial t} + \rho C_p \mathbf{u} \cdot \nabla T + \nabla \cdot \mathbf{q} = Q + Q_p + Q_{vd} \tag{3.6}$$

$$\mathbf{q} = -k \nabla T \tag{3.7}$$

where ρ is the density, C_p is the heat capacity at constant pressure, $\mathbf{u}$ is the velocity field from the moving mesh model discussed in Section 3.4.3, T is the temperature, k is the thermal conductivity, Q is the heat source, Q_p is the work done by pressure changes and Q_{vd} is the viscous dissipation.

The moisture transport in the air domain was governed by the equations

$$M_v \frac{\partial c_v}{\partial t} + M_v \mathbf{u} \cdot \nabla c_v + \nabla \cdot \mathbf{g} = G \tag{3.8}$$

$$\mathbf{g} = M_v D \nabla c_v \tag{3.9}$$

$$c_v = \phi c_{sat} \tag{3.10}$$

where M_v is the molar mass of vapour, c_v is the vapour concentration, G is the moisture source, D is the vapour diffusion coefficient in air, ϕ is the relative humidity and c_{sat} is the saturation concentration.

The initial temperature of the air and liquid domains is set at 293.15K unless otherwise stated, and the substrate was considered to be insulated thermally and to moisture according to

$$-\mathbf{n} \cdot \mathbf{q} = 0 \tag{3.11}$$

$$-\mathbf{n} \cdot \mathbf{g} = 0 \tag{3.12}$$

The outer edge of the air domain was considered to have a moisture content ϕ and be an open boundary with conditions

$$T = T_0 \text{ if } \mathbf{n} \cdot \mathbf{u} < 0 \tag{3.13}$$

$$-\mathbf{n} \cdot \mathbf{q} = 0 \text{ if } \mathbf{n} \cdot \mathbf{u} \geq 0 \tag{3.14}$$

The droplet surface was designated a boundary heat source according to

$$-\mathbf{n} \cdot \mathbf{q} = Q_b \tag{3.15}$$

where Q_b is a latent heat source and also considered a wet surface governed by

$$-\mathbf{n} \cdot \mathbf{g} = g_{evap} \tag{3.16}$$

$$g_{evap} = M_v K(c_{sat} - c_v) \tag{3.17}$$

where g_{evap} is the evaporative flux and K is the evaporation rate factor.

This method allows the model to record the local evaporative flux, which will enable the deformation of the droplet surface locally, and provide more realistic results than those provided by a model that utilised a spherical cap assumption, such as Hu and Larson [2002].

The evaporation rate, K is set to remain at 1 for all subsequent simulations, with the evaporation rate being varied by the step function described in Section 4.2.2. This was done for no reason other than the preference of the author, as both values are applied to the evaporative flux in mathematically identical ways, so changing one rather than the other has no impact on the evaporative flux generated.

In simulations where the substrate is at a constant temperature, the heat transfer between the substrate and the droplet was governed by the simple equation $T = T_0$ where T_0 was a defined substrate temperature on the relevant boundary.

3.4.3 Fluid Flow and Free Surface Conditions

The equations governing the fluid flow in both the liquid and air domains are the Navier-Stokes and continuity equations,

$$\rho \frac{\partial \mathbf{u}}{\partial t} + \rho(\mathbf{u} \cdot \nabla)\mathbf{u} = \nabla \cdot [-p\mathbf{I} + \mu(\nabla \mathbf{u} + (\nabla \mathbf{u})^T)] + \mathbf{F} \tag{3.18}$$

$$\nabla \cdot \mathbf{u} = 0 \tag{3.19}$$

where μ is the viscous stress tensor and $\mathbf{F}$ is the volume force vector, and the initial values are set to $u_r = 0$, $u_z = 0$ and $p = 0$, where p is the pressure.

These equations are solved in the FE method using a computational mesh that is fitted to the shape of the droplet and deforms as the free surface changes shape according to the local evaporative flux, the implementation of which is described in Section 3.4.4.

The outer edge of the air domain is still considered to be an open boundary according to

$$[-\rho\mathbf{I} + \mu(\nabla\mathbf{u} + (\nabla\mathbf{u})^T)]\mathbf{n} = -f_0\mathbf{n} \tag{3.20}$$

where f_0 is the normal stress and equal to 0. The substrate is also considered to be a wall with no slip by $\mathbf{u} = 0$. On the droplet surface (designated a 'fluid-fluid interface' in COMSOL) the following boundary conditions on the velocity and stress apply:

$$\mathbf{u}_1 = \mathbf{u}_2 \tag{3.21}$$

$$\mathbf{n}_1 \cdot \mathbf{T}_1 - \mathbf{n}_1 \cdot \mathbf{T}_2 = \sigma(\nabla_t \cdot \mathbf{n}_1)\mathbf{n}_1 - \nabla_t\sigma \tag{3.22}$$

$$\mathbf{u}_1 = \mathbf{u}_2 + M_f\left(\frac{1}{\rho_1} - \frac{1}{\rho_2}\right)\mathbf{n}_1 \tag{3.23}$$

Where $\mathbf{u}_1$ and $\mathbf{u}_2$ are the flow velocities in fluids 1 and 2 respectively, σ is the surface tension coefficient and M_f is the mass flux.

3.4.4 Implementation of the Moving Mesh

The term 'moving mesh' refers to the deformation of the computational mesh over time, as the droplet evaporates and loses mass to the surrounding atmosphere. The purpose of using a moving mesh system is that the mesh does not need to be generated for each configuration of the free surface, instead the software perturbs the mesh nodes so that they conform to the mesh boundaries.

Within COMSOL, physics can be formulated in either the 'spatial' or the 'material' frame, as shown in Figure 3.3. The spatial frames refers to the fixed, global coordinate system, and in the context of the ALE formulation, the spatial coordinate system is fixed but the spatial coordinates of each mesh node can change over time, hence the overall designation as a 'moving' mesh. The material frame is a coordinate system that identifies the material points by their spatial coordinates in some reference configuration, and so can be used to view the mesh as it deforms.

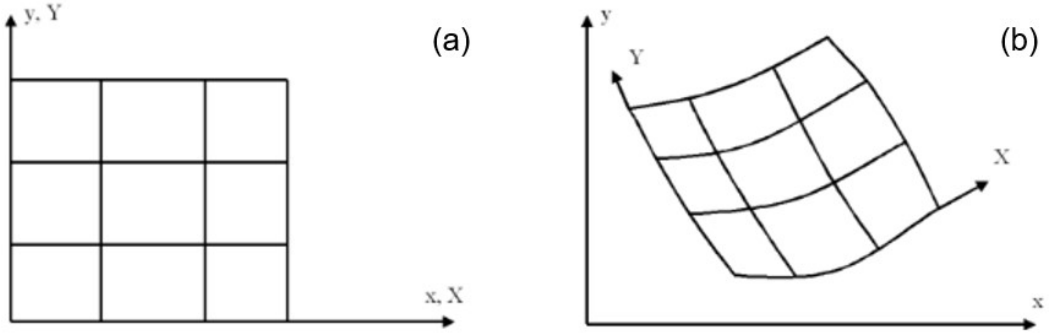

Figure 3.3: An example of an un-deformed mesh in the spatial frame (x, y) shown in (a) and a deformed mesh in the material frame (X, Y) shown in (b) (COMSOL, 2017/c).

The displacement of the free surface is updated in response to the local evaporation rate g_{evap} according to the equation

$$\mathbf{u}_{mesh} = (\mathbf{u}_1 \cdot \mathbf{n}_1) - \frac{M_f}{\rho_1}\mathbf{n}_1 \tag{3.24}$$

$$M_f = g_{evap,r}\mathbf{n}_r + g_{evap,z}\mathbf{n}_z \tag{3.25}$$

There are prescribed mesh displacements on the axis of symmetry of $r = 0$, and on the substrate and outer edge of the air domain of $t_1 = 0$ and $n = 0$, meaning that there is no movement normal to these boundaries.

The movement of the interior nodes (i.e. those not on the free surface) is controlled by propagating the moving boundary displacement through the liquid and air domains to obtain a smooth mesh deformation everywhere. This is done by treating the domain as an elastic material, and solving appropriate PDEs for the mesh displacements with boundary conditions given by the movement of the boundaries. The chosen smoothing model in this case was Yeoh with a stiffening factor of 10. This was selected as it allows the largest displacement of boundaries before the mesh elements become inverted, when compared to other smoothing models. (COMSOL, 2017/d).

The quality of the mesh created by the smoothing equations can deteriorate at large mesh deformations, potentially causing convergence issues or leading to inverted mesh elements where an element is essentially warped to the extent that it is ‘inside-out’. This is an issue inherent to using the ALE formulation, but can be negated by re-meshing, the process of generating a new mesh for the region covered by the overly-deformed mesh, which allows the solver to continue to run by deforming the new mesh. This was not an issue experienced in the simulations conducted for this work, but could be an essential consideration for those carrying out future work, perhaps

studying droplets evaporating in bank structures with a much lower aspect ratio.

As the free surface approaches the touchdown point, the point at which the free surface is almost in contact with the substrate, the mesh becomes extremely deformed and the time step size is automatically reduced, so a stop condition was imposed when the time step fell below a certain predetermined value. The value of this stop condition was determined by conducting a sweep of various values on a model of water drying within a bank structure, and the effect on the final height at the centre of the droplet (i.e. at the line of axisymmetry), with the results shown in Figure 3.4.

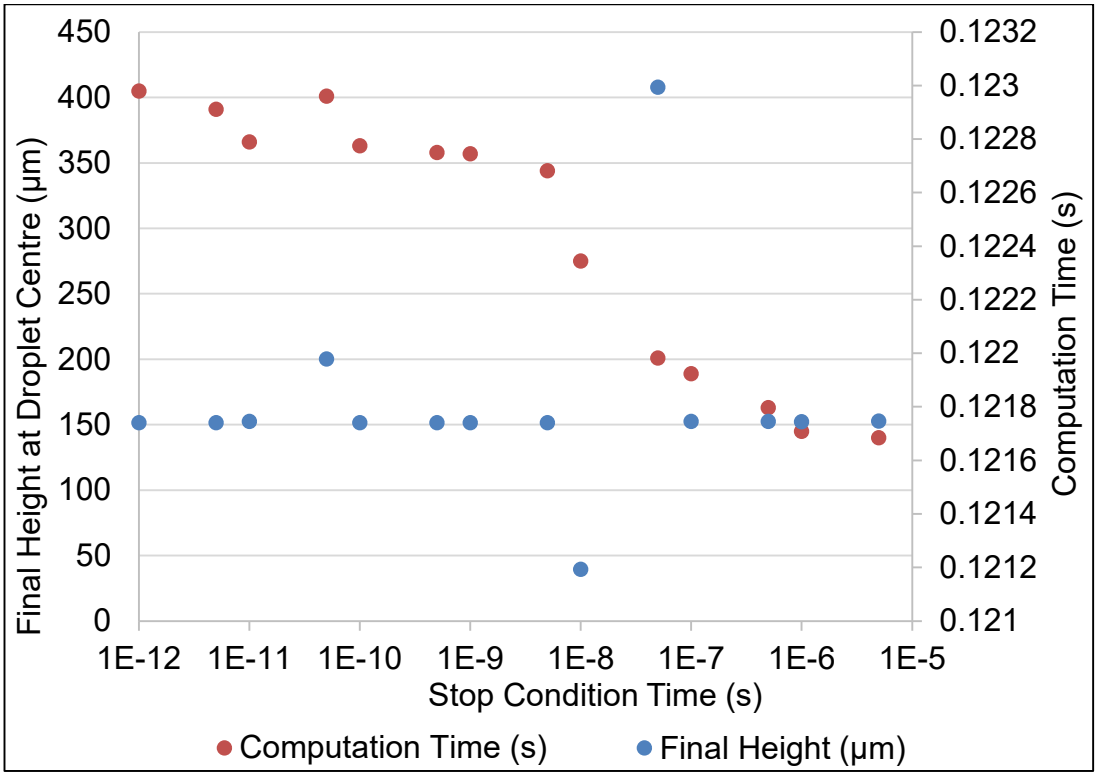

Figure 3.4: Plot of the results of a study into the effect of the time-based stop condition on final droplet height.

From Figure 3.4, it was determined that the most appropriate minimum time step for a stop condition was 1 x 10^{-6}s for most solvents, as this was small enough to not impact the final result, as all of the physics being investigated in this work will have already occurred when the free surface reaches the touchdown point, but also meant that the simulations conclude in far less time. Simulations with a stop condition at 1 x 10^{-5}s, or greater, did not compute. For exceptionally fast evaporating models, like those seen in Section 5.2.2, the minimum time step for the stop condition was reduced to avoid the possibility of an impact on the final droplet profile.

3.4.5 Thermocapillary Flows

In order to model the effects of thermocapillary flows, a function for the change in of water with regard to temperature had to be used, and incorporating this kind of function is made easier by the nature of the FE approach compared to other methods. Such a function was formulated by Vargaftik, Volkov and Voljak [1983], based on an exhaustive study of published tables for the surface tension of water, of the form

$$\sigma = B\left[\frac{T_c - T}{T_c}\right]^{\mu}\left[1 + b\left(\frac{T_c - T}{T_c}\right)\right] \tag{3.26}$$

where values B = 0.2358N/m, b = -0.625, μ = 1.256 and T_c is a critical temperature of 647.15K. This equation replaced the surface tension term in eq. (3.22). and is plotted in Figure 3.5.

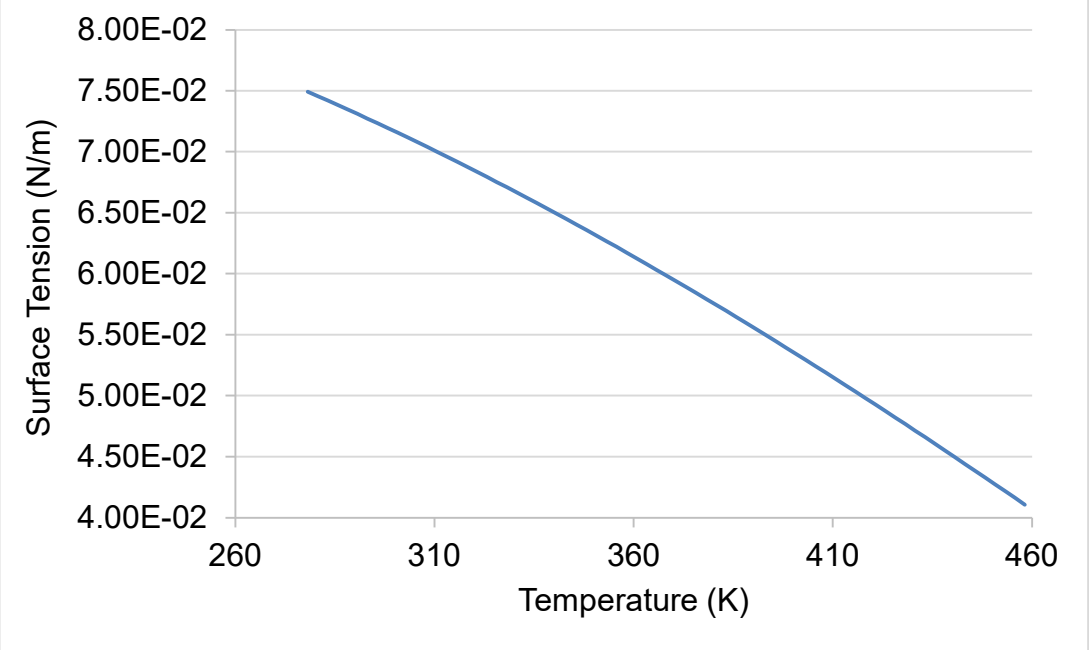

Figure 3.5: Plot of surface tension against temperature based on eq. (3.26).

Chapter 4:
Evaporation of a Sessile Droplet on a Flat Surface

4.1 Introduction

This chapter will seek to verify and validate the modelling methodology outlined in Chapter 3 for a droplet on a flat substrate, as research into sessile droplets has been conducted to a far greater extent over many years, and is very well understood compared to droplets evaporating from a bank structure.

The method for obtaining the vapour concentration, free surface deformation and internal flows in an isothermal system will be compared against work by Hu and Larson [2002], and models considering evaporative cooling, substrate heat transfer and the thermocapillary effect will be verified against work by Yang, Hong and Cheng [2014].

4.2 Isothermal Case

In order to be compared to the work conducted by Hu and Larson [2002], who did not consider evaporative cooling, the model was converted to be isothermal by simply changing the heat source to $Q = 0$, and disabling the heat transfer model for the substrate entirely. The thermal considerations will be included in Section 4.3.

To match the parameters set out by Hu and Larson, the droplet was resized to have a radius R of 1mm, an initial droplet height h_0 of 0.364mm, D = 26.1mm^2/s, H = 0.4 and T = 25°C.

In the work by Hu and Larson, the air domain was set to be 20 times the radius of the droplet, however due to tests shown in Figure 4.7 in Section 4.2.2, the air domain in this model was set to be 80 times the size of the droplet.

Hu and Larson found that any fewer than 10,000 mesh elements provided inaccurate evaporation rate results, so to determine an appropriate mesh sizing for this model, a mesh independence study was carried out, with the results shown in Figure 4.1.

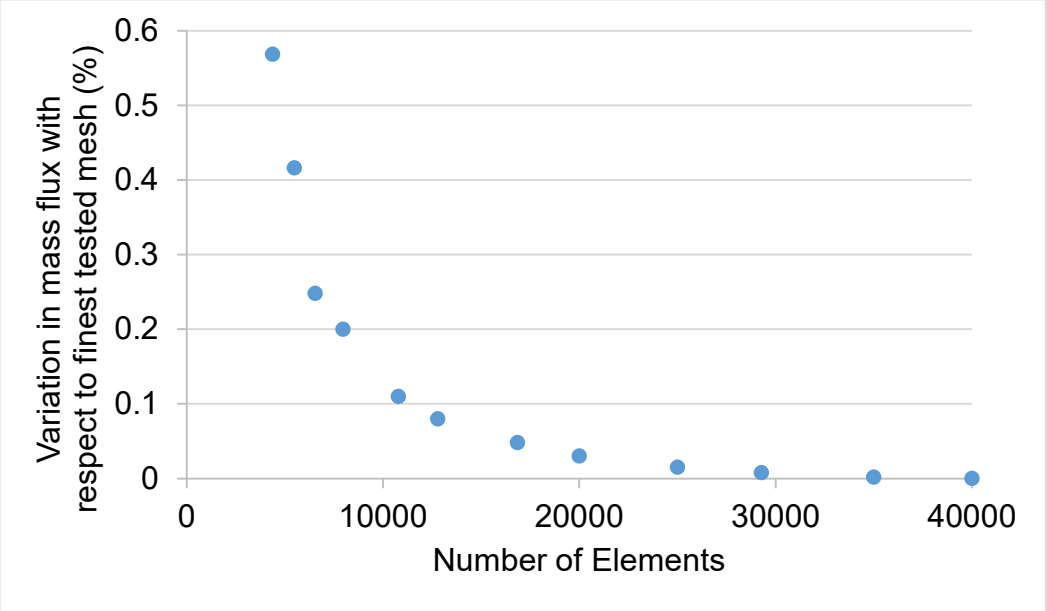

Figure 4.1: Plot of mesh independence study results, showing the variation in mass flux with respect to the finest mesh tested against the total number of elements.

The mass flux in Figure 4.1 was taken at t=1s from the topmost point of the droplet in order to ensure the data could be compared reliably for different meshes. A maximum element size of 5μm was imposed along the droplet

surface, as this would allow the complex movement of the free surface to be tracked closely, with the mesh size in the bulk of the liquid and air domain being determining the total number of elements presented in Figure 4.2.

From the results of the mesh independence tests, it was determined that a minimum of 10,000 elements provided the best compromise between accuracy and computational load, with only a 0.1% variation from the finest mesh tested, and so would be used for all simulations replicating the geometry of Hu and Larson.

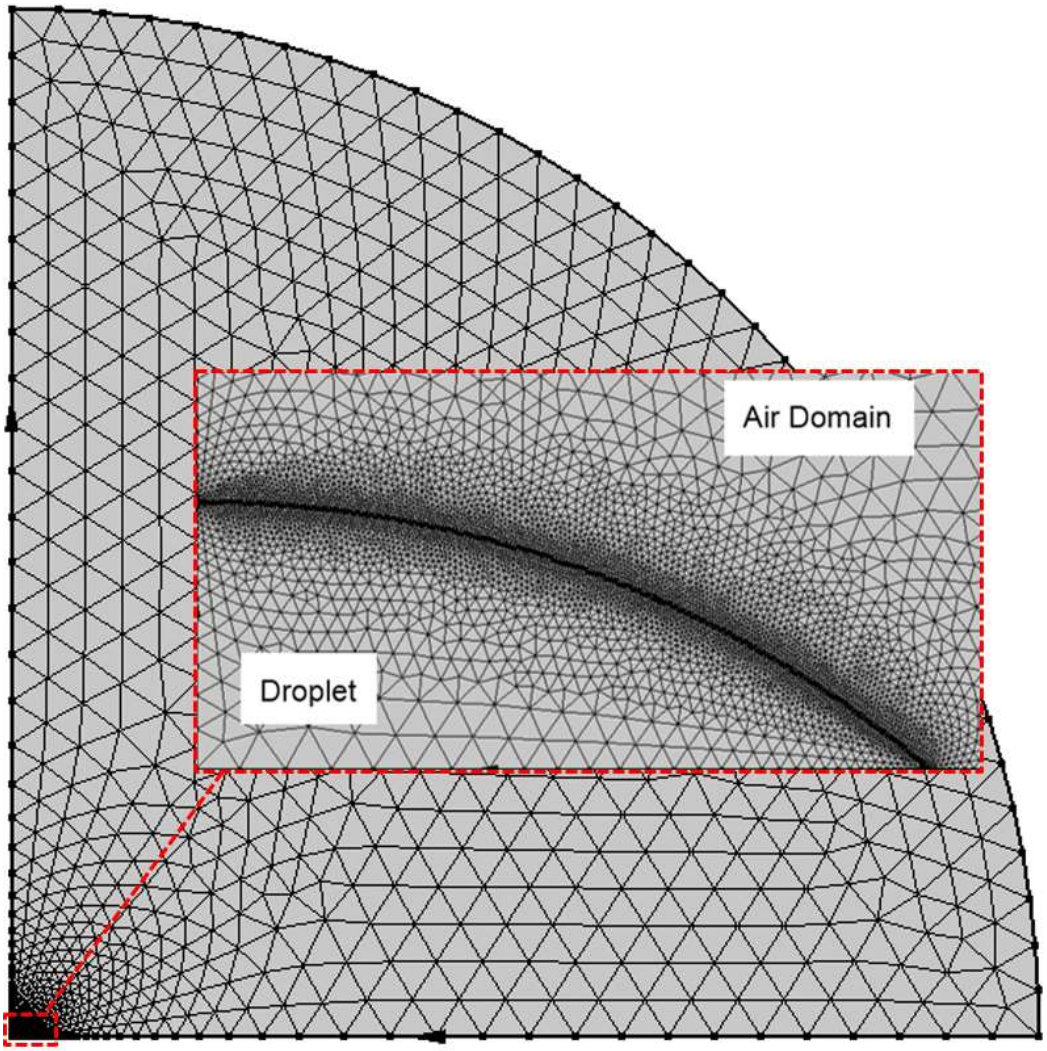

Figure 4.2: Meshed geometry with 11,022 elements, a maximum element size of 5μm along the free surface and an air domain 80 times the radius of the droplet.

4.2.1 Vapour Concentration

From the above parameters, a c_{sat} value of 2.32 x 10^{-8} g/mm^3 was calculated from

$$c_{sat} = \left(\frac{P_{sat}(T)}{R_{const}T}\right) M_{water} \tag{4.1}$$

$$P_{sat} = 610.7 \text{ x } 10^{7.5\frac{T-273.15}{T-35.85}} \tag{4.2}$$

where P_{sat} is the saturation pressure, R_{const} is the universal gas constant and M_{water} is the molar mass of water, which was used in the comprehensive model proposed by Yang, Hong and Cheng [2014]. It is worth noting that the Hu and Larson model required this value be inputted manually, which they retrieved from the CRC Handbook [Weast & Astle, 1982] as 2.32 x 10^{-8} g/mm^3. Calculating this value seems a considerable improvement over previous methods, with the increased simplicity of not having to find a c_{sat} value manually, especially for more obscure solvents.

The resulting vapour concentration gradients shown in Figure 4.3, match the Hu and Larson results (shown in Figure 4.4) closely, both in terms of the value of the vapour concentration at points across the air domain and the overall diffusion pattern with higher evaporation nearer the contact line due to the curvature of the droplet surface and impermeability of the substrate leading to a steep vapour concentration gradient near the contact line, as discussed in Section 2.4.3.

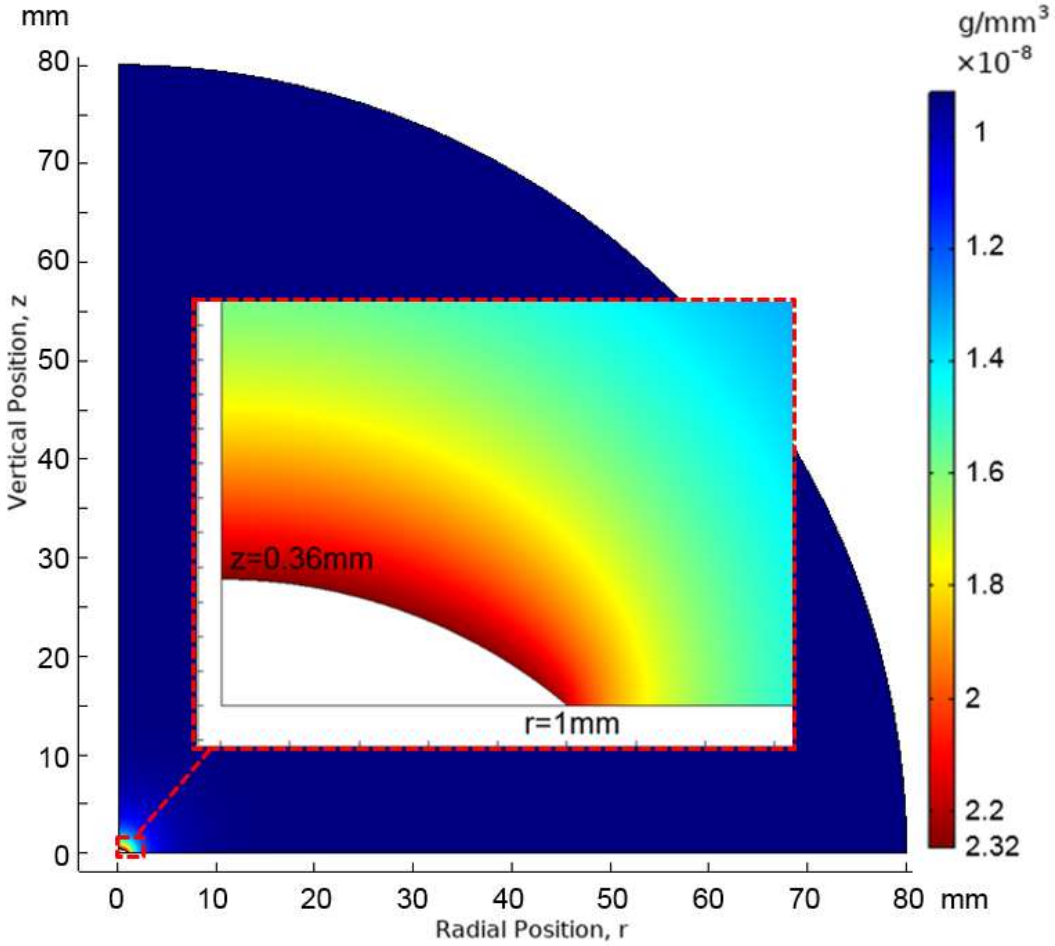

Figure 4.3: Plot of the vapour concentration for the isothermal case at t=1s, where the c_{sat} value of 2.32 x 10^{-8} g/mm^3 was calculated from eq. (4.1) and eq. (4.2).

Figure 4.3 was taken at t=1s, as this allowed the simulation to begin before a reading was made, this was essential because the initial conditions of the model stipulated a saturation concentration at the free surface and ambient concentration throughout the atmosphere, meaning that a short period of time had to elapse for the higher concentration at the free surface to diffuse into the surrounding atmosphere.

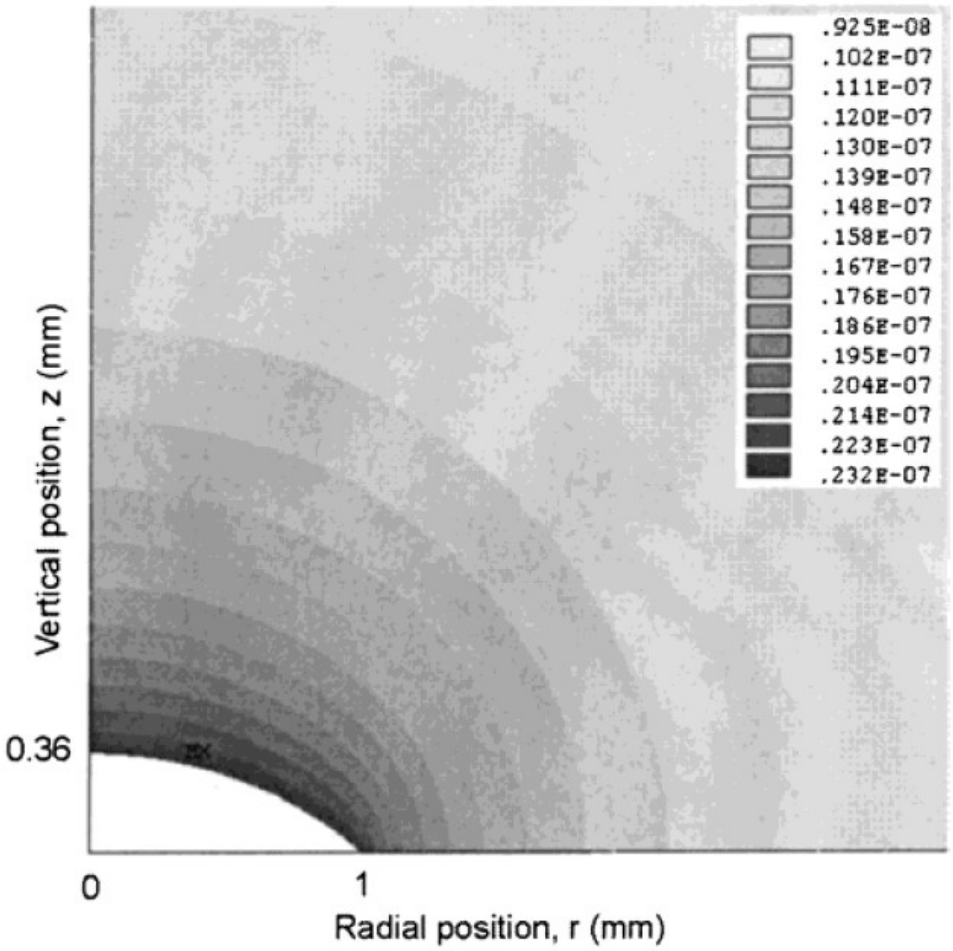

Figure 4.4: Plot of the vapour concentration from Hu and Larson [2002], where the c_{sat} value of 2.32 x 10^{-8} g/mm^3 had to be looked up from the 1982 CRC Handbook.

4.2.2 Free Surface Deformation

Building on the work set out above, the diffusion-driven mass flux model was coupled to the free surface deformation model as outlined in Section 3.4.3. A step function was included in this model in order to allow the simulation to run without error, as the mass flux at the contact line was unrealistically high and lead to inverted mesh elements at this point. This was due to the vapour concentration contour lines having extreme curvature near the contact line as they transitioned from the edge of the droplet to the impermeable substrate, causing the mass flux to tend towards infinity at this point. A step function was therefore applied along the free surface, which reduced the mass flux to zero near the contact line, and removed this error. This was implemented into eq. (3.25) as

$$M_f = S_F \left(g_{evap,r}\mathbf{n}_r + g_{evap,z}\mathbf{n}_z\right) \tag{4.3}$$

where S_F is the step function. As mentioned in Section 3.4.2, varying the step function amplitude is mathematically identical to changing the evaporation rate, K in eq. (3.17).

An example of the form of the step function is shown in Figure 4.5. A transition zone of 0.1 with 2 continuous derivatives was used in all subsequently mentioned step functions, as this gave a smooth transition between the stepped values and therefore minimised the risk of the transition causing issues within the computational mesh.

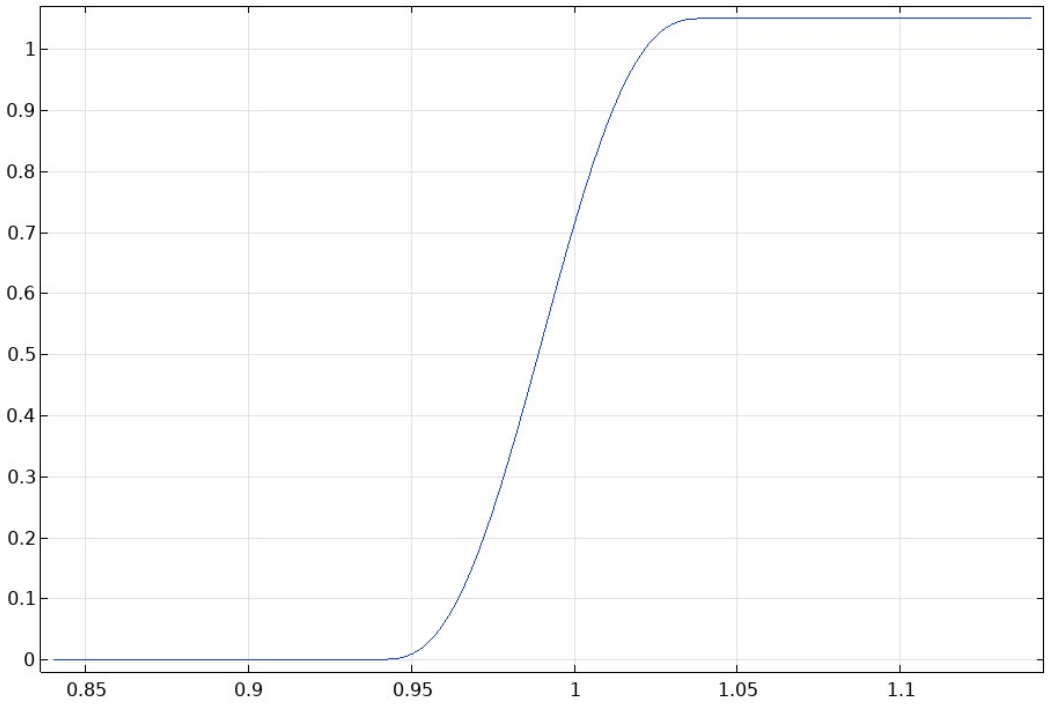

Figure 4.5: Step function S_F with an amplitude of 1.05, at a transition point of 0.99, a transition zone size of 0.1 and 2 continuous derivatives.

There are two feasible methods of employing a step function in this case:

1. As set percentage of the droplet surface, where the step function multiplied all fluxes by 1, up to a certain percentage along the droplet surface towards the contact line, where it was then multiplied by 0, which removed the numerical error.
2. As a set distance from the contact point, inside of which the mass flux would be multiplied by 0, and the rest of the surface would be unaffected.

The droplet height was tracked against time, and the comparison against Hu and Larson's numerical results are shown in Figure 4.6, where the percentage-based step function was set to 1 for 95% of the droplet surface

and the distance-based step function was set to 1 for all but the 0.05μm closest to the contact line.

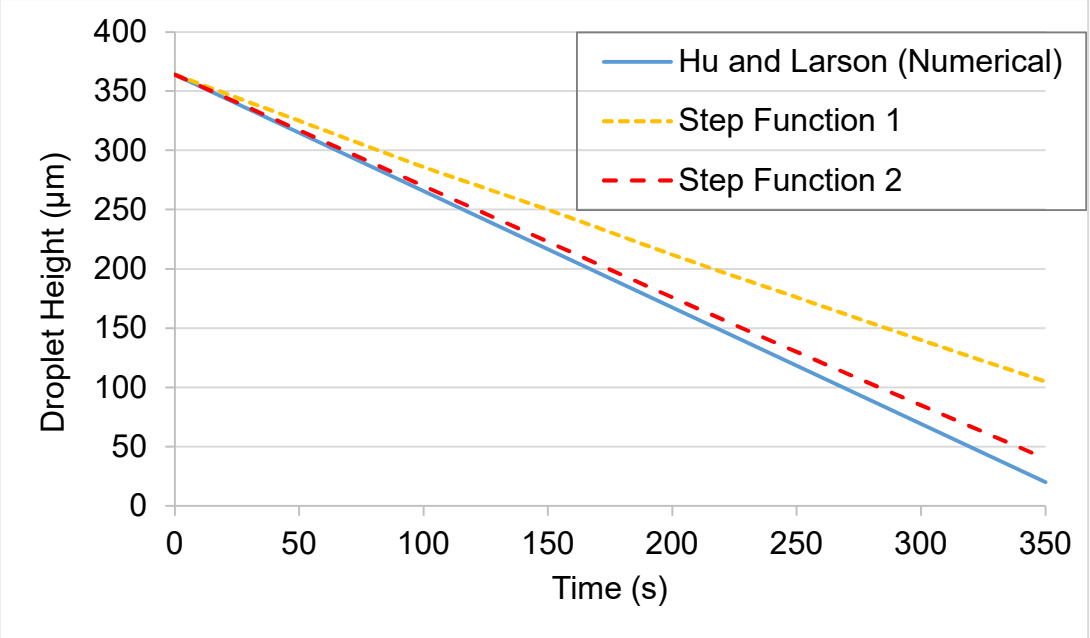

Figure 4.6: Plot of droplet height (μm) against time (s) for the isothermal model with un-tuned step functions and Hu and Larson [2002].

The effect of the size of the air domain relative to the size of the droplet was tested, with the results shown in Figure 4.7, which shows that an air domain 80 times the size of the droplet represents the best compromise between computation load and accuracy, as the variation in droplet height at t=350s is only 0.6% compared to a relative domain size of 100. Therefore, all subsequent simulations will use an air domain with a radius 80 times that of the droplet.

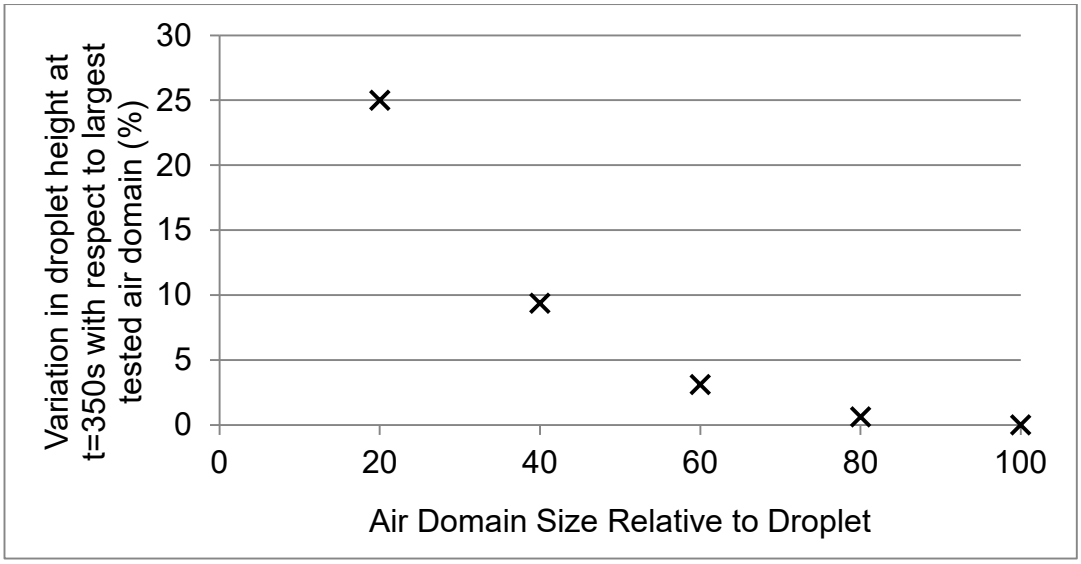

Figure 4.7: Plot of the variation in droplet height at t=350s with respect to the largest tested air domain against the size of the air domain relative to the droplet.

From Figure 4.6, it is clear that the isothermal model slightly underestimates the evaporation rate compared to Hu and Larson's numerical findings. The step functions were therefore tuned to match the results more closely, with the distance-based method set to an amplitude of 1.05 over the entire surface except the 0.01µm closest to the contact line. The results for the tuned step function is presented in Figure 4.8, with the values derived from multiple tests into final results and computational errors with the selected values shown being found to represent the best balance between accuracy, the likelihood of the simulation running successfully and computation time.

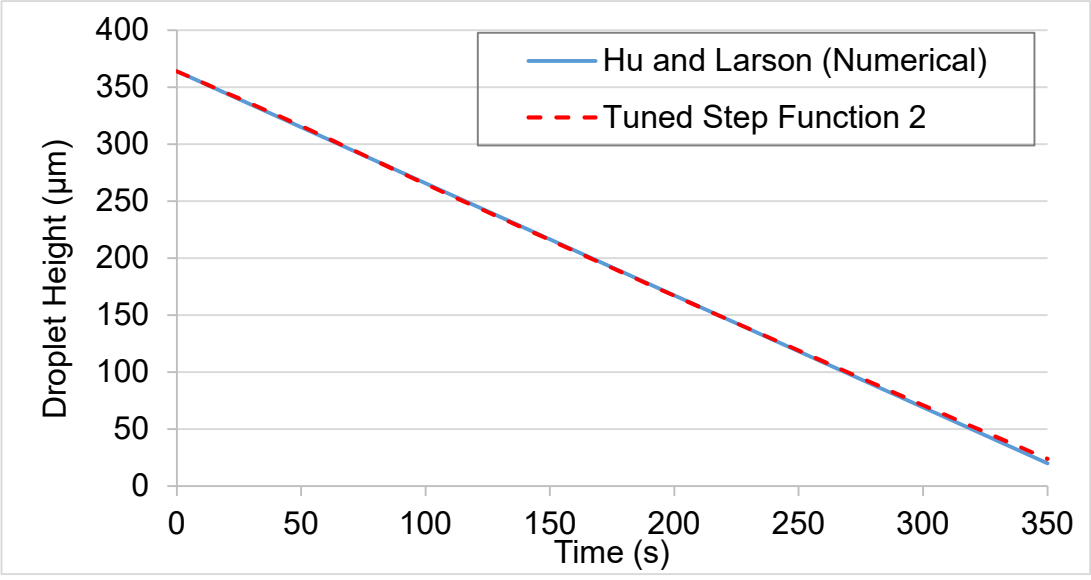

Figure 4.8: Plot of droplet height (µm) against time (s) for the isothermal model with tuned step function 2 and Hu and Larson [2002].

The distance-based method for applying the step function will be used for all subsequent models, in order to account for the model underestimating the diffusive flux, at a value of 1.05 at all but the 0.01μm nearest to the contact line, as it will create a fixed and consistent value regardless of the profile of the droplet surface. Clearly, a percentage-based approach would incorporate slight changes in the location of where the mass flux is not applied depending on the curvature of the free surface, which is best avoided.

In order to confirm the accuracy of this tuned step function, the conditions used for experimental work by Hu and Larson were reproduced in the isothermal model, with a droplet radius of 0.85mm and an initial droplet height of 0.329mm. Hu and Larson measured the droplet height at various radii and at different times to establish the droplet surface, assuming a spherical cap was always maintained, which is a reasonable assumption on a flat substrate. The results for both the isothermal model and the experimental work by Hu and Larson are shown in Figure 4.9.

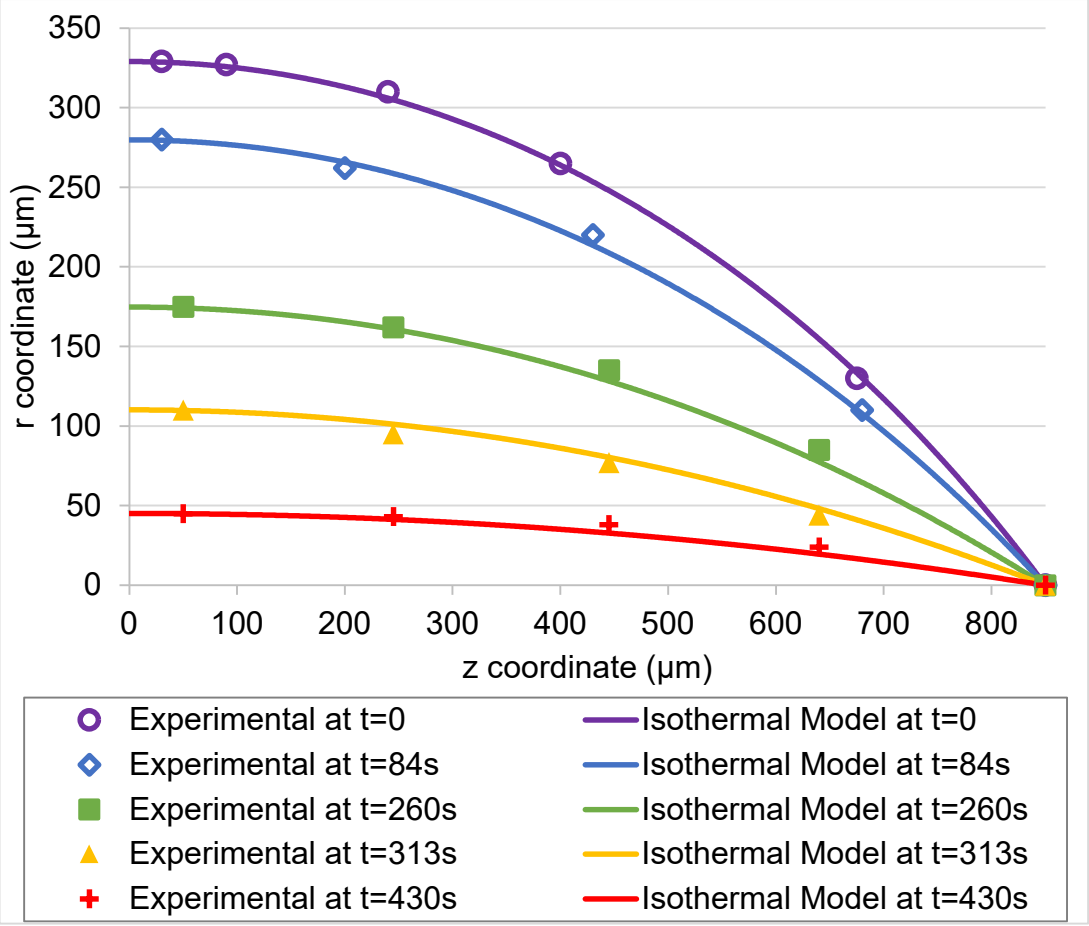

Figure 4.9: Plot of droplet profiles from the isothermal model and experimental droplet heights from Hu and Larson [2002] at various times.

It is clear from Figure 4.9 that the results from the isothermal model match those produced experimentally by Hu and Larson, validating that the model is indeed accurate. The slight deviations between the data plots is most likely due to the difficulties associated with experimentally measuring the height of a droplet at various radii at set times.

4.2.3 Internal Flows

As mentioned in Section 2.4.3, the enhanced evaporation at the contact line leads to a radial outwards flow, which produces the coffee-ring effect. Figure 4.10 demonstrates the ability of the isothermal model to represent this effect. It is also clearly visible that as the droplet height decreases, there is less propensity to vertical flows and only radial outwards flows remain, as was expected from the literature. Unfortunately, there is no data provided by Hu and Larson [2002] for the internal flows, so no direct comparison can be made.

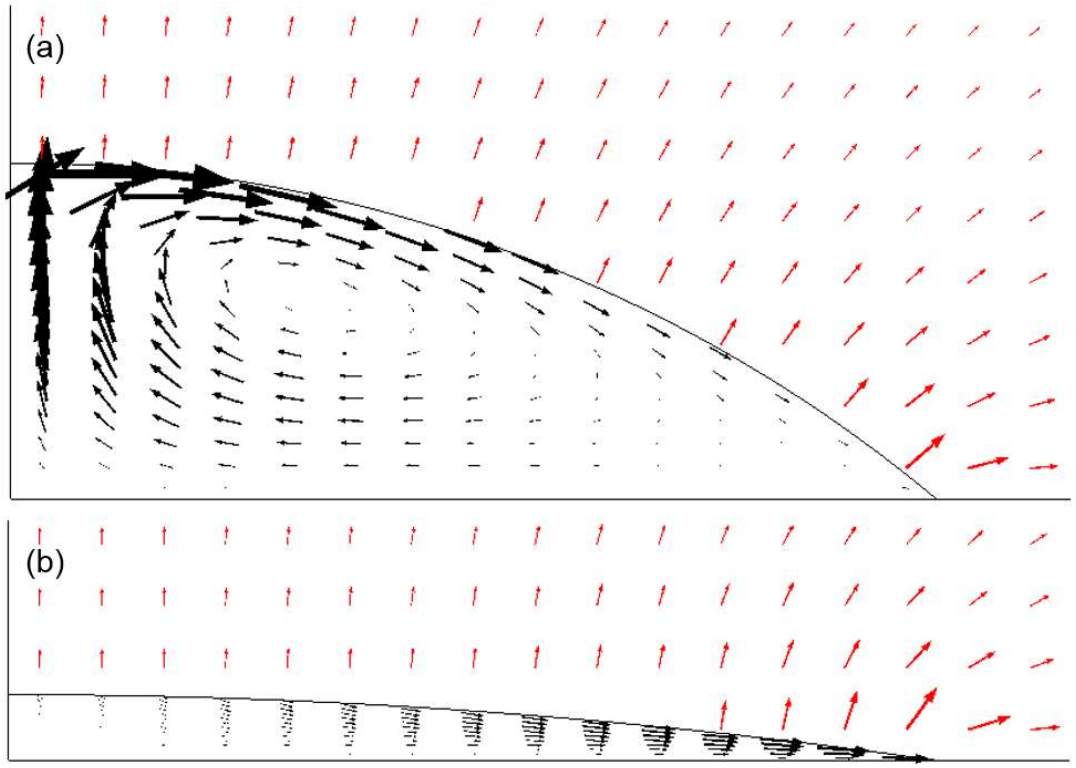

Figure 4.10: Plot of the velocity field in black and the evaporative flux in red at t=1s (a) and t=300s (b), for the isothermal model.

This section has clearly demonstrated that the isothermal model is capable of showing the radial outwards flows being induced by enhanced evaporation at the contact line, as has been shown in numerous previous experimental and theoretical works.

4.3 Thermal Considerations

4.3.1 Evaporative Cooling and Substrate Heat Transfer

In order to study the effects of evaporative cooling on the results, the heat source at the droplet surface was re-established, allowing the transfer of heat from the droplet to the atmosphere during evaporation, and the heat transfer between the droplet and substrate discussed in Section 3.4.2 was also enabled.

To match the parameters set out by Yang, Hong and Cheng [2014], who built upon the works of Hu and Larson [2002] to include thermal considerations, the droplet was resized to have a radius R of 1.415mm, an initial droplet height h_0 of 0.66mm, and the air domain was re-sized to be 40 times the size of the droplet. Other values were H = 0.5, T_{amb} = 22°C and substrate temperature T_s = 40°C. These parameters were selected by Yang, Hong and Cheng [2014] to match experimental work by Girard, Antoni and Sefiane [2008]. The cooling effect of the droplet on the substrate was not included in this investigation, and so the substrate temperature was considered to be constant.

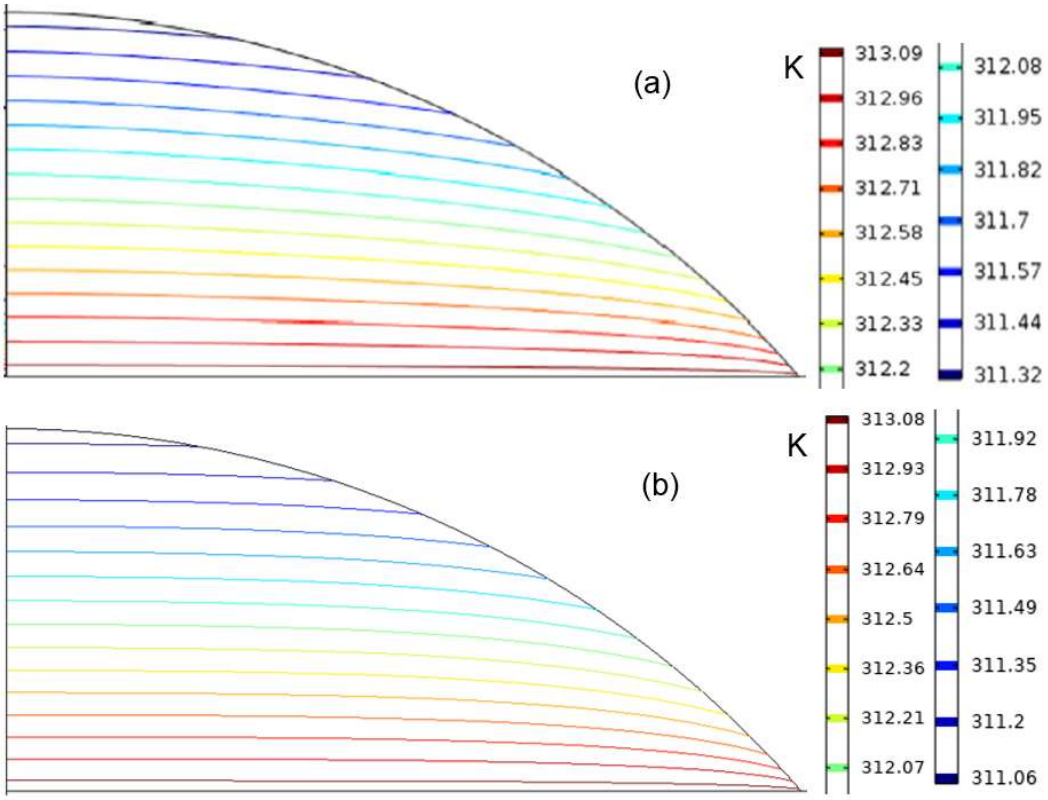

Figure 4.11: Plot of the temperature contours at t=5s of Yang, Hong and Cheng [2014] (a) and the current model including evaporative cooling and heat transfer from the substrate (b).

Figure 4.11 shows a close similarity between the current model and published data with regards to the propagation of heat through the droplet from the substrate and the effects of evaporative cooling. The difference of 0.26K between the coldest points in the two models is considered to be acceptable variation.

Figure 4.12 shows how the velocity field inside the droplet flows towards the contact line as is to be expected from the literature, but there is very little recirculation towards the centre of the droplet like that seen in Figure 4.10a. The flow pattern differs slightly between the results of Yang, Hong and Cheng [2014] and the current model, with the present model generating more flow further into the bulk of the droplet and less along the free surface. The velocity field at contact line has very similar values between the two models, with a variation of approximately 1%.

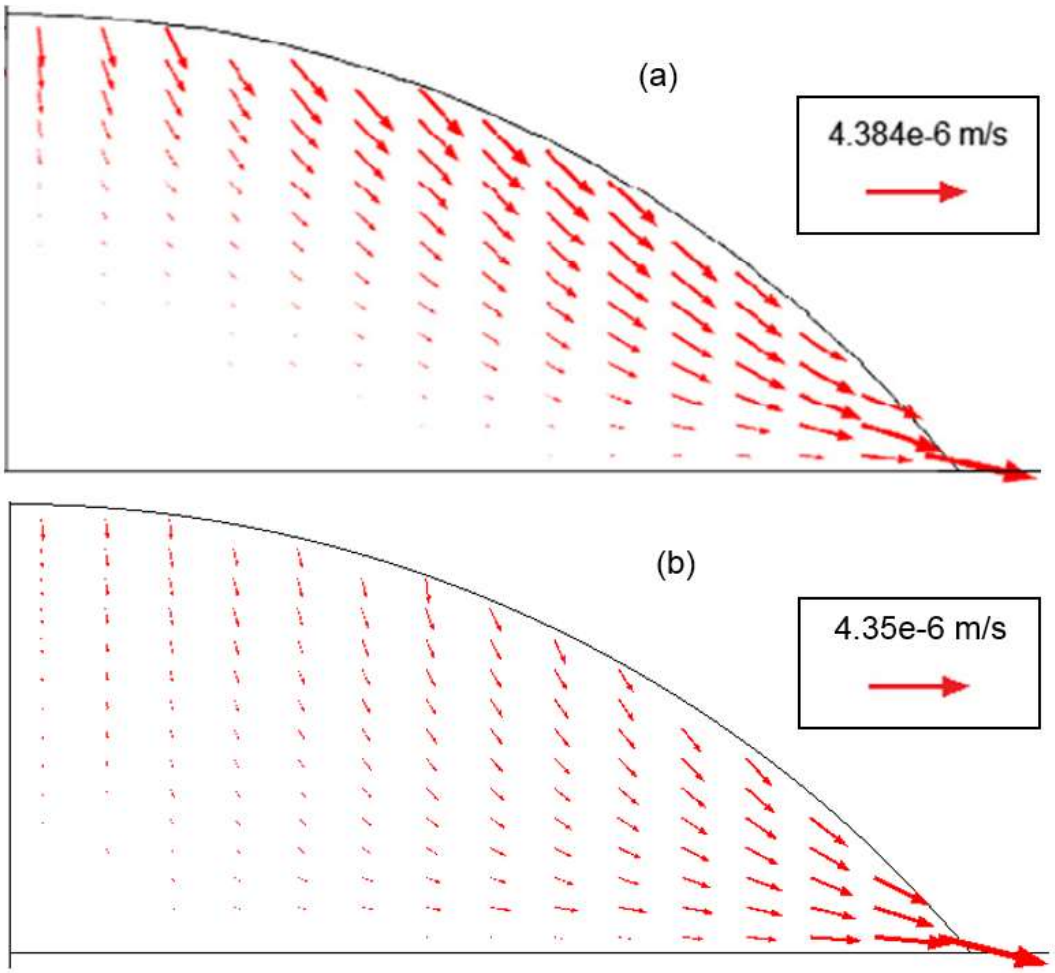

Figure 4.12: Plot of the velocity field inside droplet at t=5s of Yang, Hong and Cheng [2014] (a) and the current model including evaporative cooling and heat transfer from the substrate (b).

Figure 4.13 shows the velocity field in the gas phase, with the results from Yang, Hong and Cheng [2014] showing the majority of the flow occurring near the contact line where the evaporation rate is highest, which was expected from previous studies. The results from the current model shows largely the same effect, but the flow at the top of the droplet is noticeable too, which may be attributable to the lesser outwards flow along the contact line shown in Figure 4.12b. The velocity field at contact line again has very similar values between the two models, with a variation of approximately 1.5%.

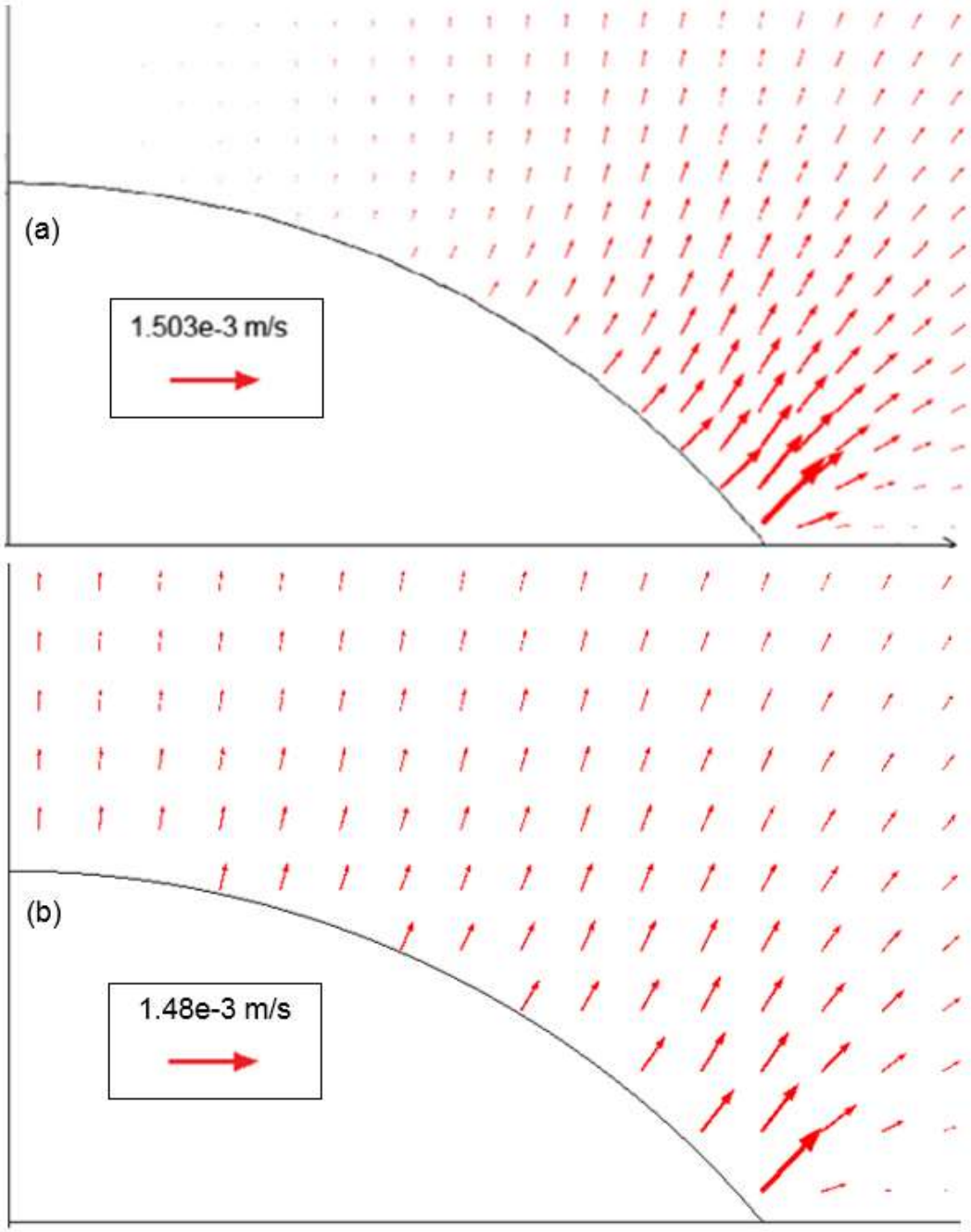

Figure 4.13: Plot of the velocity field in the gas phase at t=5s of Yang, Hong and Cheng [2014] (a) and the current model including evaporative cooling and heat transfer from the substrate (b).

The results generated for the evaporative cooling and substrate heat transfer in this section demonstrate the ability of the current model to show how temperature changes across the droplet during evaporation. The resulting velocity fields are in broad agreement with the literature by Yang, Hong and Cheng [2014] with the maximum velocity value in the droplet differing by 1% and in the atmosphere by 1.5%, although the current model slightly under-predicts the internal flow along the free surface and slightly over-predicts the

velocity field towards the centre of the droplet compared to Yang, Hong and Cheng [2014].

There is no need to investigate this difference further at this time, as this model is simply a stepping stone towards the inclusion of thermocapillary flows, as discussed in the Section 4.4.

4.3.2 Evaporative Cooling Without Substrate Heat Transfer

In order to demonstrate the capability of the current model to accurately represent evaporative cooling further, the model and geometry used in Section 4.3.1 was modified to remove the heat transfer from the substrate.

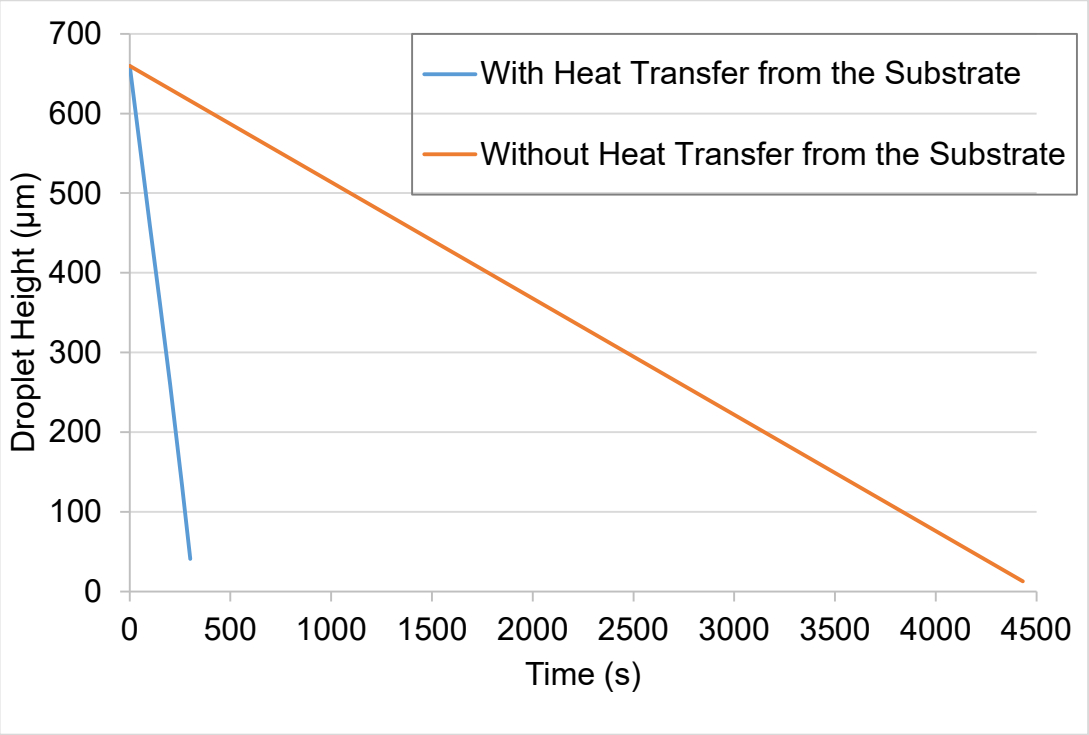

Figure 4.14: Plot of the droplet height (μm) against time (s) for the current model including evaporative cooling, and with or without heat transfer from the substrate.

It is clear from Figure 4.14 that removing the heat transfer from the substrate drastically reduces the evaporation rate of the droplet due to the lower overall temperature of the droplet, as would be expected from the literature. The droplet now has a temperature profile, shown in Figure 4.15, that directly relates to the evaporative cooling rather than the thermal distribution being dominated by the heat transfer from the substrate. The temperature is lower at the contact line, where the evaporation rate is highest and therefore

the evaporative cooling is also at a maximum. This is also in-line with what would be expected from previous literature.

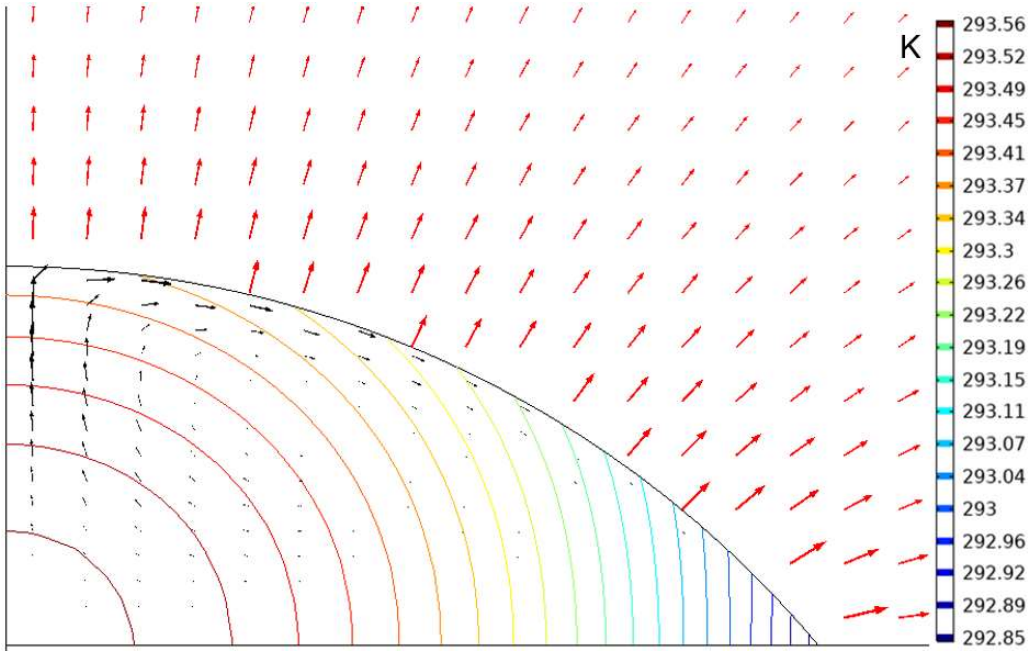

Figure 4.15: Plot of the temperature contours, evaporative flux in red and velocity field in black for the current model including evaporative cooling but without heat transfer from the substrate at t=5s.

This section has shown that heat transfer from the substrate greatly affects the total evaporation time of a sessile droplet, and that artificially removing it to leave only evaporative cooling to affect the temperature of the droplet leads to lower temperatures at the contact line, where the evaporation is highest.

4.4 Thermocapillary Flows

4.4.1 Thermocapillary Flows with Heat Transfer from the Substrate

As discussed in Section 2.4.3, thermocapillary flows are caused by localised temperature variance across the liquid-vapour interface generating a surface tension difference and therefore liquid flow along the surface.

For these simulations, all parameters are kept the same as Section 4.3.1 above, with the exception of the surface tension coefficient, as described in Section 3.4.5.

As is clear from Figure 4.16, once the thermocapillary effect is included in the current model, it agrees even more closely with the temperature distribution throughout the droplet than Figure 4.11, with the same highest temperature of 313.1K, a difference of only 0.13K between the lowest temperatures and near identical contour lines for the thermal distribution.

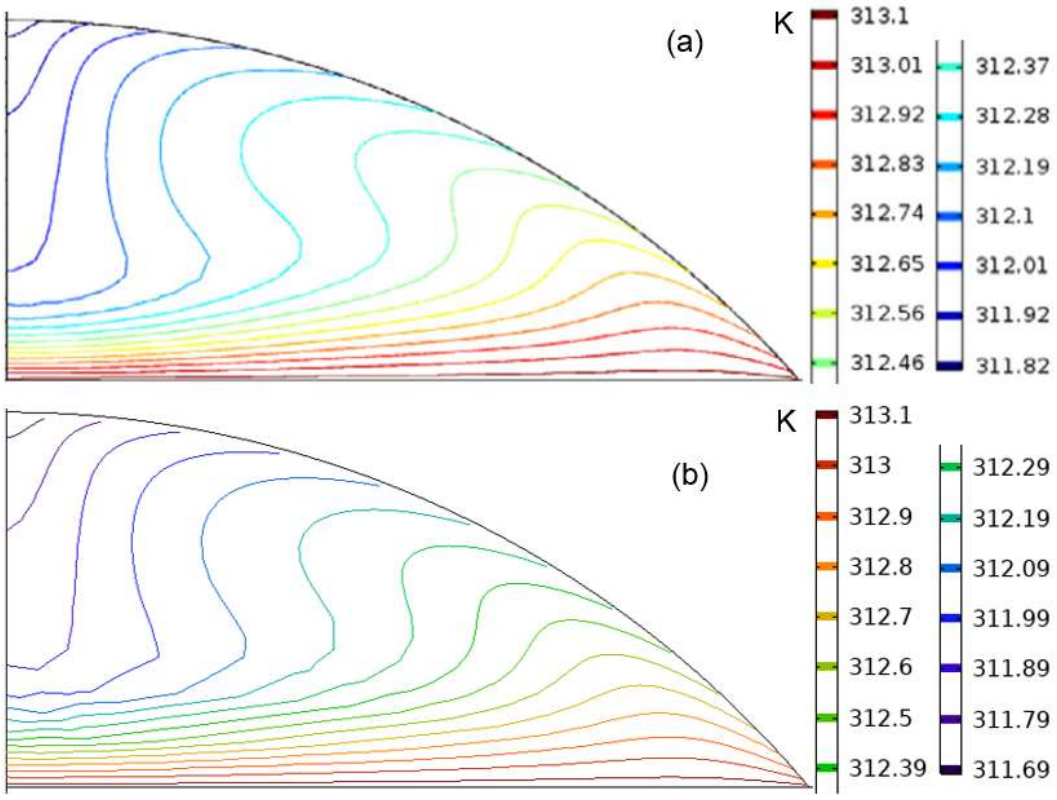

Figure 4.16: Plot of the temperature contours at t=5s of Yang, Hong and Cheng [2014] (a) and the current model including thermocapillary effects and heat transfer from the substrate (b).

The difference in the contour plots between the model with and without the thermocapillary effect is due to the velocity field shown in Figure 4.17 facilitating the higher temperature at the substrate to be transferred up and away from the contact line.

Figure 4.17 shows that the flows inside the droplet are now entirely reversed compared to the model without thermocapillary effects seen in Section 4.3.1, and the direction of internal flows match closely with the results published by Yang, Hong and Cheng [2014]. The current model now underestimates the velocity field slightly compared to published data, but only by approximately 3.5% and so is considered close enough to be useful moving forward.

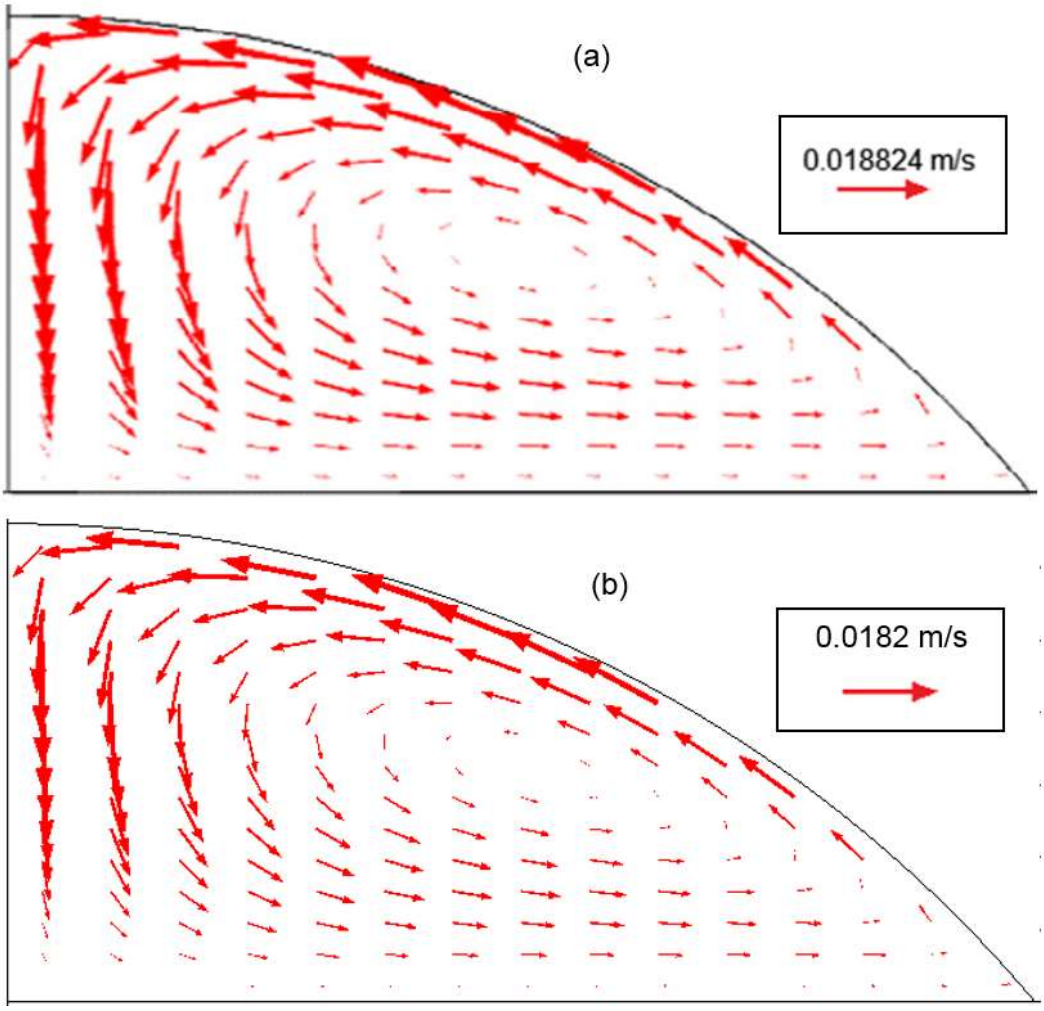

Figure 4.17: Plot of the velocity field inside droplet at t=5s of Yang, Hong and Cheng [2014] (a) and the current model including thermocapillary effects and heat transfer from the substrate (b).

Also, the velocity field in the air domain, as shown by Figure 4.18, is entirely different from when there was no thermocapillary effect with the flow running

along the droplet surface away from the contact line. This is caused by the shear stress applied across the fluid-fluid interface from the moving liquid inside the droplet, and hence the maximum values of the velocity fields in Figures 4.17 and 4.18 are the same.

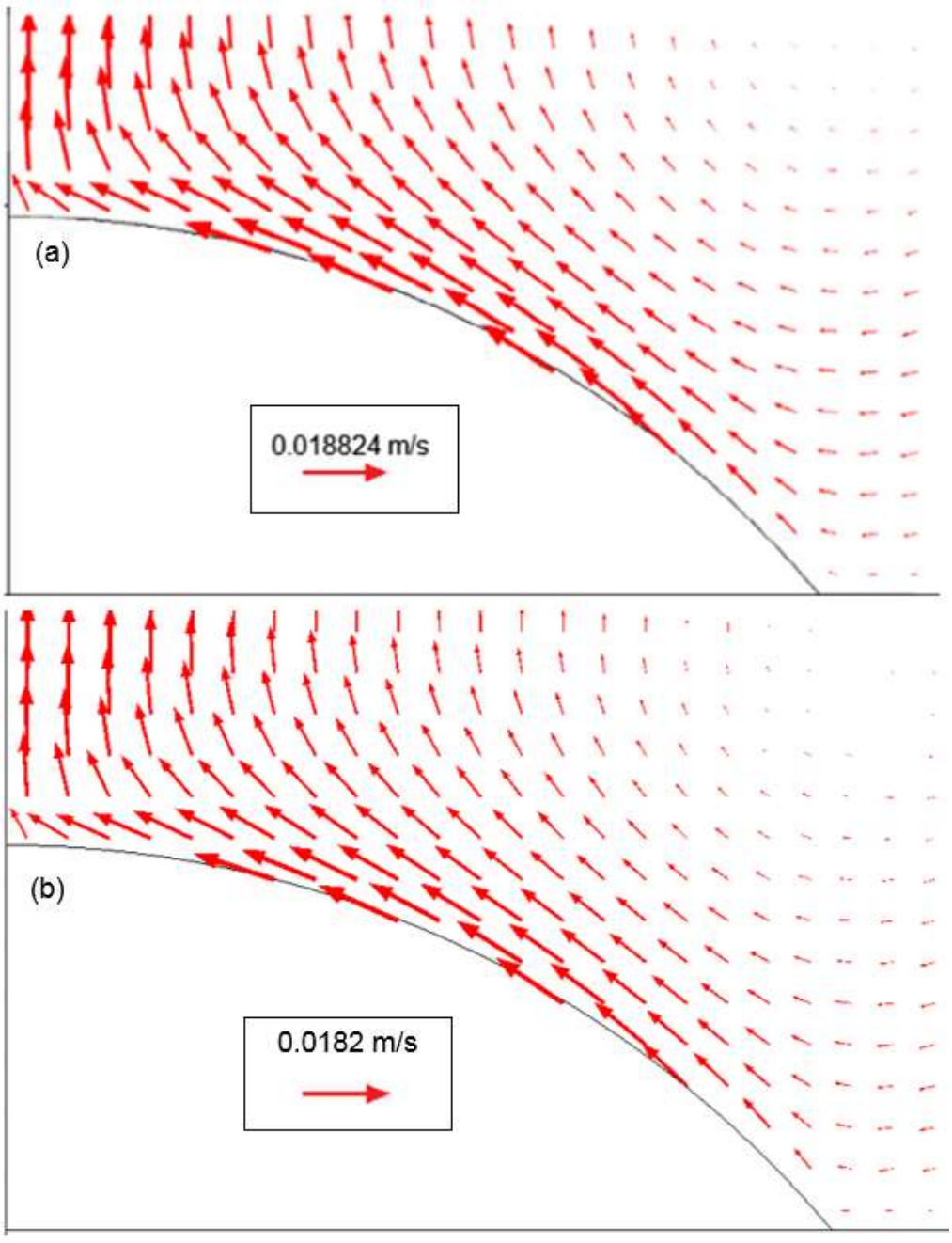

Figure 4.18: Plot of the velocity field in the gas phase at t=5s of Yang, Hong and Cheng [2014] (a) and the current model including thermocapillary effects and heat transfer from the substrate (b).

This section has shown that the current model can demonstrate the inclusion of thermocapillary flows with heat transfer from the substrate to

closely match published literature for the temperature field within the droplet, and to reasonably match the velocity fields both in the droplet and the surrounding air domain with a variance of 3.5%.

4.4.2 Thermocapillary Flows without Heat Transfer from the Substrate

As with Section 4.3.2, the heat transfer from the substrate was removed in order to see the effect this would have on the drying time, internal flows and temperature distribution throughout the droplet.

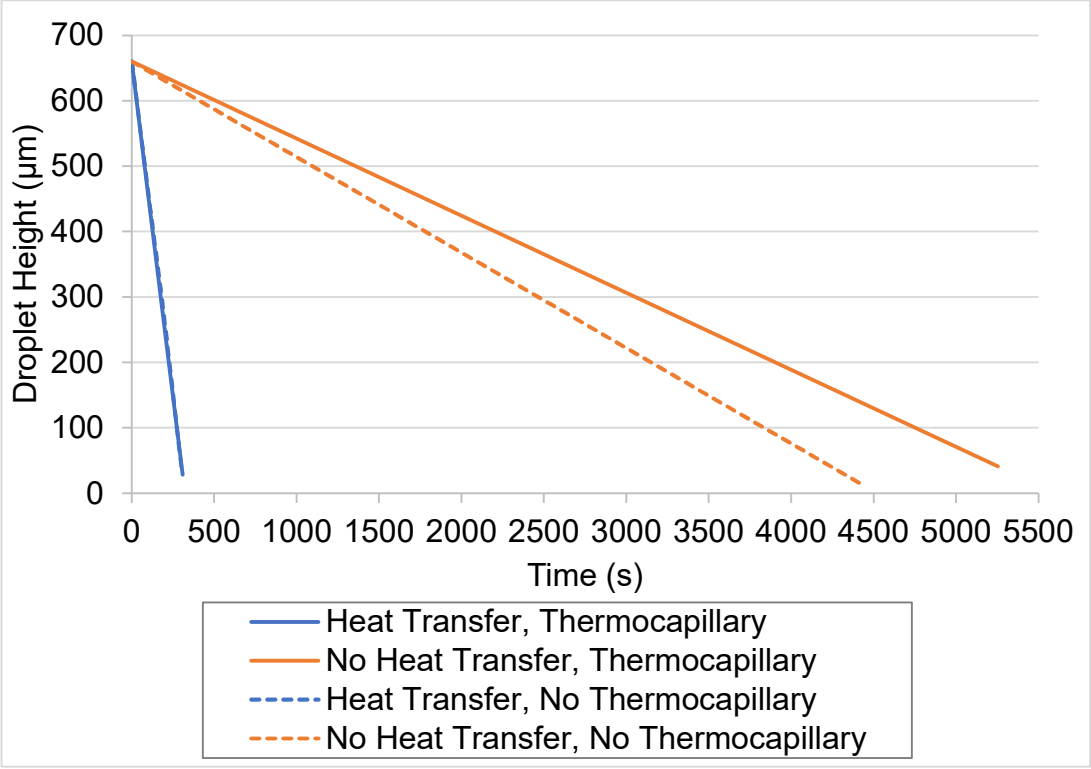

Figure 4.19: Plot of the droplet height against time for the model with or without heat transfer from the substrate, and with or without thermocapillary flows.

Figure 4.19 shows that without the heat transfer from the substrate, the droplet evaporated far more slowly than when it is being heated by the substrate, as a cooler droplet will obviously evaporate more slowly than a warmer one due to the molecules having less energy to break through the free surface. Figure 4.19 also shows that the influence of the thermocapillary effect on the overall drying time of the droplet is minimal.

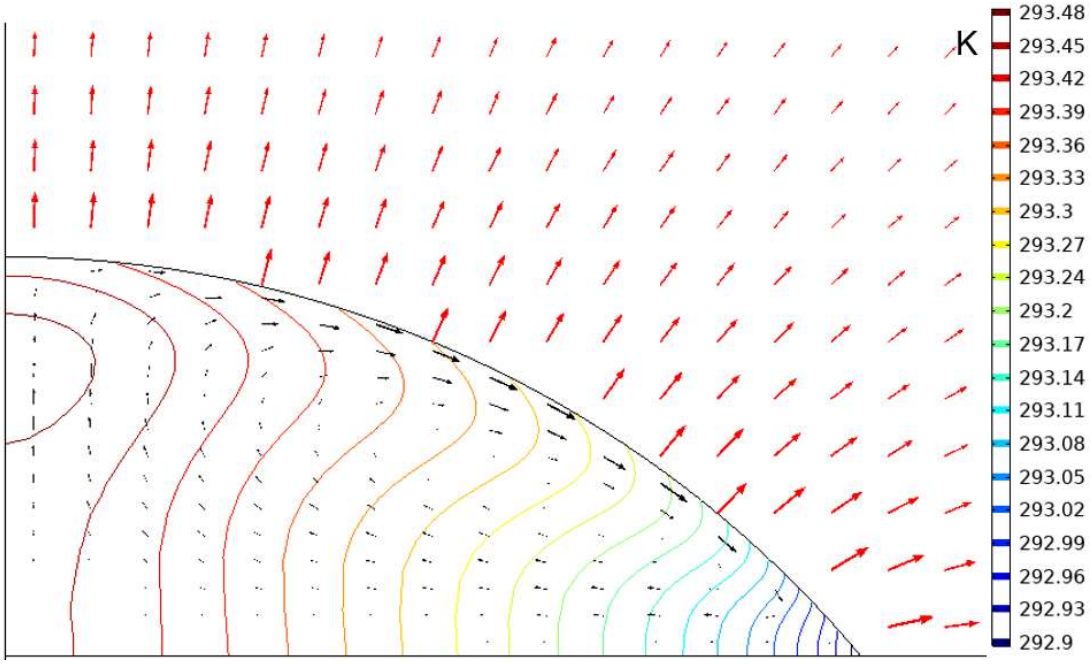

Figure 4.20: Plot of the temperature contours, evaporative flux in red and velocity field in black for the current model including evaporative cooling but without heat transfer from the substrate, with thermocapillary flows at t=5s.

Figure 4.20 shows that the internal flows along the surface are towards the contact line, whereas when the droplet was being heated by the substrate, the flow was towards the centre of the droplet, as seen in Figure 4.17. This was due to the temperature now being lower at the contact line than in the centre, as the substrate is not heating the droplet so evaporative cooling can determine the temperature distribution. This outwards flow along the surface carried warmer liquid towards the contact line and the recirculation flows carry cooler liquid back towards the centre of the droplet, explaining the distorted thermal contours compared to Figure 4.15.

A total drying time of around 5500s, as seen in Figure 4.19, is considerably longer than that typically seen of a 1.415mm droplet drying, but when the lack of heat transfer from the substrate and evaporative cooling is considered, it is not unreasonable to assume that the very low energy available within the droplet would considerably hamper the evaporation rate. In addition, an evaporating droplet that is perfectly insulated from a substrate is essentially impossible to test experimentally, so validating this particular scenario is extremely difficult.

This section has shown that the removal of the heat transfer from the substrate increases total evaporation time when thermocapillary flows are

included, even more so than when thermocapillary flows are not included, as shown in Section 4.3.2.

4.5 Verification and Validation with Other Solvents

In order to increase the robustness of the verification and validation of the current model, in this section it will be compared to other experimental and numerical studies of the drying of droplets of liquids other than water, which are closer in properties to those used in OLED production.

Fukai et al. [2014] studied the evaporation of a droplet of anisole containing polystyrene spheres deposited by inkjet printing onto a flat surface, both numerically by a Lagrangian finite element method and experimentally. This numerical model considered heat transfer between the droplet, substrate and air domains, and thermal and solutal Marangoni flows.

The equations used for modelling solvents other than water are identical to those stated in Chapter 3, but the model would be solved for dry air (i.e. there would be no water vapour present, but the vapour of the solvent would be used instead).

The current model was modified to use the material properties of anisole, with σ = 34.96 x 10^{-3}N/m [Yaws, 1999], μ = 1.001 x 10^{-3}Pa.s [Yaws, 1999], ρ = 990kg/m^3 [Yaws, 1999] and D = 7.29 x 10^{-6}m^2/s [Yaws, 2009]. , with the results for the change in droplet volume over time shown in Figure 4.21.

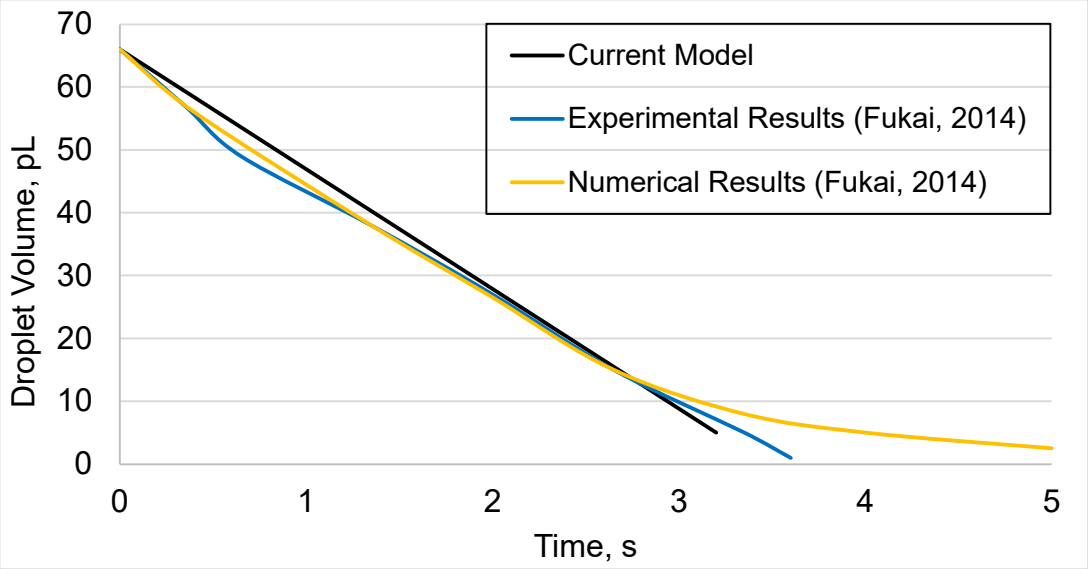

Figure 4.21: Plot of droplet volume against time for the current model and the experimental and numerical results of Fukai et al. [2014] for anisole.

Figure 4.21 clearly shows that the current model closely matches the experimental data by Fukai et al. throughout the duration of the drying

process. There is also a close match with the numerical model employed by Fukai et al., up to a droplet volume of 15pL, where the numerical results by Fukai et al. take around 1.8s longer to reach a stopping point, which for all results is in the 2-5pL range. This is likely due to the presence of the polystyrene spheres, which will greatly reduce the evaporation rate at low droplet volumes. However, as the purpose of this section is to verify and validate that the current model is accurate in predicting the evaporation rate of solvents other than water, this is acceptable, as the polystyrene spheres will have had minimum impact on the evaporation rate at all but the lowest droplet volumes.

Nguyen & Nguyen [2012] studied the evaporation of sessile droplets of ethanol with a fixed base radius (i.e. pinned) on a flat surface, both numerically and experimentally. Whilst they were able to produce a power law to predict the theoretical lifetime of a droplet, the experimental results obtained will be focussed on in this work.

The current model was modified to use the material properties of ethanol, with σ = 22.4 x 10^{-3}N/m [Serras-Pereira, 2008], μ = 1.095 x 10^{-3}Pa.s [Engineering Toolbox, 2021/a] and ρ = 785kg/m^3 [Engineering Toolbox, 2021/b] and D = 11.81 x 10^{-6}m^2/s [Lugg, 1968], with the results for the change in droplet volume over time shown in Figure 4.22 below.

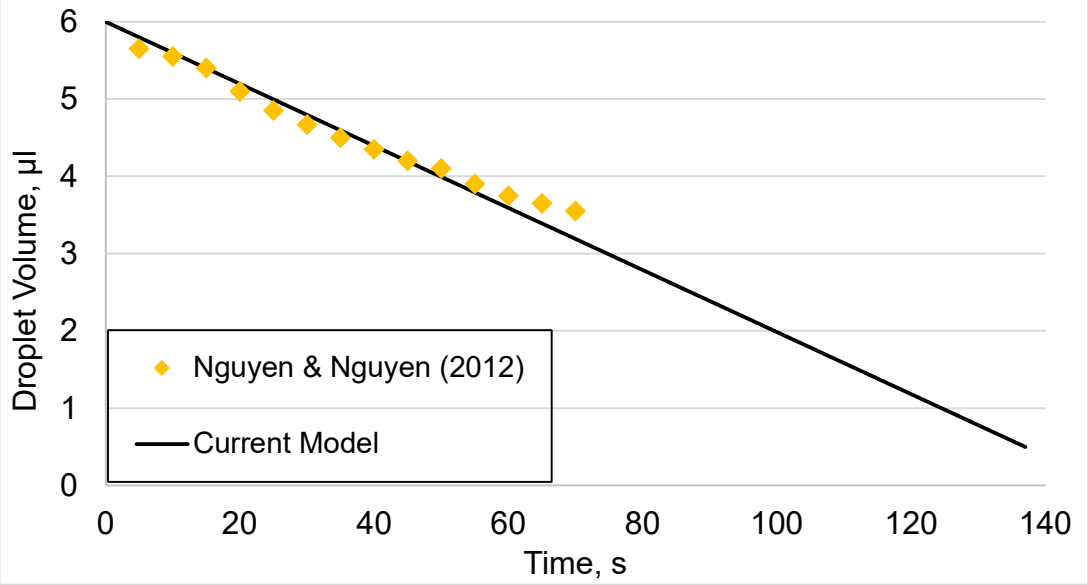

Figure 4.22: Plot of droplet volume against time for the current model and the experimental results of Nguyen & Nguyen [2012] for ethanol.

Figure 4.22 shows a good agreement between the experimental work conducted by Nguyen & Nguyen and the current model. The experimental data was only recorded for the 5.6 - 3.6µl range, but there is clearly a reasonably close resemblance to the results from the current model in that range.

This section has shown that the current model is capable of predicting the change in volume over time for solvents other than water to a reasonable accuracy, and has therefore added credibility to any future results.

4.6 Conclusions

The purpose of this chapter has been to verify and validate the current model against published literature that included data from numerical, analytical and experimental methods.

Comparison of the current model to numerical and experimental work by Hu and Larson [2002] has proven it capable of delivering accurate results for the concentration gradients in the gas domain and the deformation of the free surface, while comparison against Yang, Hong and Cheng [2014] validated the ability of the current model to predict evaporation-driven radial outwards flows to an accuracy of 1-1.5%, evaporative cooling to within 0.13-0.26K, and thermocapillary flows to within 3.5%.

These results mean that a high level of confidence in the accuracy and reliability of the model can be carried forwards into subsequent chapters.

The impact of removing the heat transfer from the substrate was also studied in this chapter, with the model without heat transfer from the substrate having a far slower evaporation rate due to the molecules having less energy to break free of the droplet surface, showing radial outwards flows throughout due to the combination of the higher evaporation rate at the contact line, reinforced by the thermocapillary effect.

Finally, the current model was compared against numerical and experimental works for solvents other than water, namely anisole [Fukai, 2014] and ethanol [Nguyen and Nguyen, 2012], showing that the current model can accurately replicate the evaporation of other solvents, if the correct data for parameters such as diffusion coefficient, density, surface tension and viscosity are known.

Chapter 5:
Evaporation from a Bank Structure

5.1 Introduction

This chapter will cover the inclusion of the bank structure to the previously described model, which represents the main novel aspect of this entire research.

Firstly, the experimental work conducted by Kazmierski [2018] described in Section 2.5 will be replicated in an attempt to confirm or refute the mechanism proposed by that work for the internal flows and drying profile. A study of various bank structure depths and angles will then be tested to discover the impact on drying profiles, and the model will then be compared to a study by Eales et al. [2015/b] in order to study the effects of more complex, curved bank structures like those used in OLED production. This chapter concludes with suggestions for how to generate flat, uniform deposits for optimal OLED production.

5.2 Investigation of Experimental Work

As the experimental work by Kazmierski [2018] showed some interesting behaviour with regards to the drying profile of droplets in a bank structure such as U-, W- and M-shaped profiles, as seen in Figure 5.1, an investigation was carried out into the possible causes.

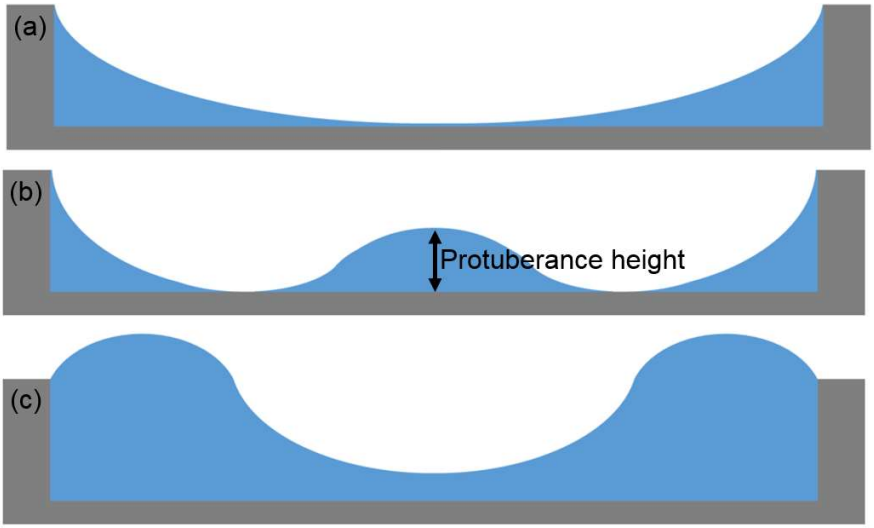

Figure 5.1: Schematic diagram of U-shaped (a), W-shaped (b) and M-shaped (c) droplet profiles.

According to Kazmierski [2018], the key factor in determining the shape of the droplet profile is the evaporation rate, with faster drying solvents developing W-shaped profiles and slower drying solvents developing U-shaped profiles. The cause of M-shaped profiles was hypothesised to be the thermocapillary flows generated preventing a protuberance from forming.

Therefore, this section will consist of parametric studies of evaporation rate, surface tension and viscosity to determine the cause of these differing drying profiles, analysis of the associated internal dynamics and comparison against the experimental work previously undertaken. The model used in this chapter is the same as outlined in Chapters 3 and 4, but with the addition of a bank structure to the model geometry.

To match the experimental work by Kazmierski [2018], the bank structure had a radius of 67μm and a depth of 1.3μm, and an initial droplet height of 27.5μm was deemed a reasonable starting point as all behaviour directly affecting the final surface profile will occur far beneath this point. The angle of the bank in a circular well is not detailed in the experimental work, and is only described as “gently sloping” so a nominal distance in the r-direction of

2μm from the base of the slope to the top was chosen, which equates to an angle of 33°. The contact point between the droplet surface and the substrate was pinned at 0.02μm from the top of the bank, as this allowed the computational mesh to move without the complications imposed by having the droplet surface in contact with the sharp angle at the top of the bank. The starting curvature of the droplet was based upon a spherical cap that intersected the axis of axisymmetry and the bank structure in the locations described above. The geometry is shown in Figure 5.2.

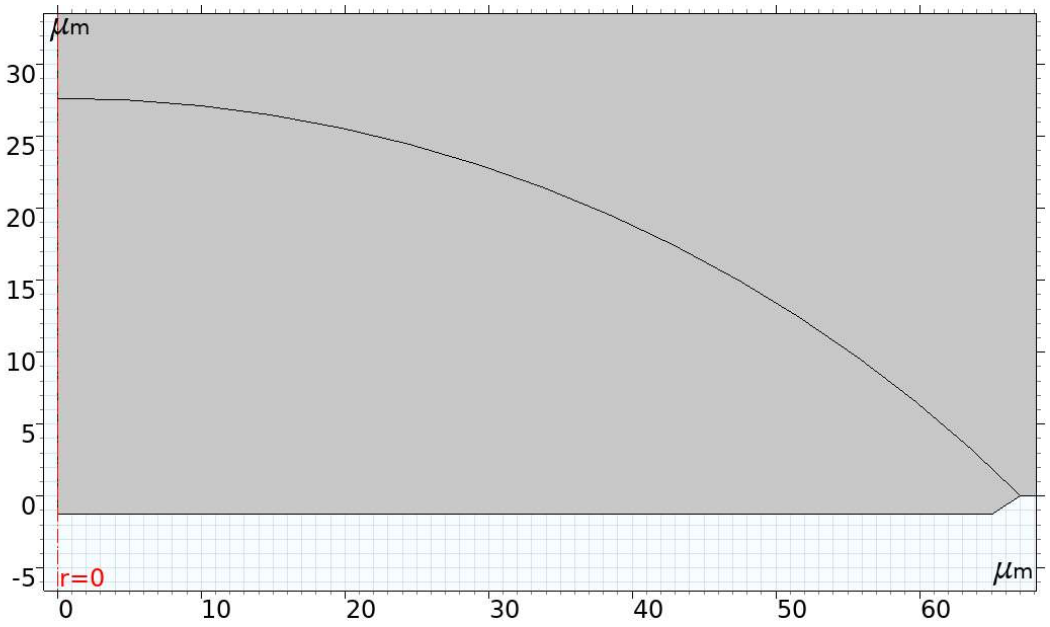

Figure 5.2: Geometry for investigation of Kazmierski [2018].

5.2.1 Model Validation Against Experimental Work in a Bank Structure

Following the thorough validation of the current model against experimental work for evaporation on a flat surface, this section will seek to validate the model against experiments by Kazmierski [2018] for evaporation from a bank structure. These would all be conducted using the circular bank structure geometry described in Section 5.2.

The current model was modified to use the material properties of anisole, with σ = 34.96 x 10^{-3}N/m [Yaws, 1999], μ = 1.001 x 10^{-3}Pa.s [Yaws, 1999], ρ = 990kg/m^3 [Yaws, 1999] and D = 7.29 x 10^{-6}m^2/s [Yaws, 2009]. In the experimental work, anisole produced a distinct W-shaped profile, as seen in Figure 5.3, as did the current model, seen in Figure 5.4.

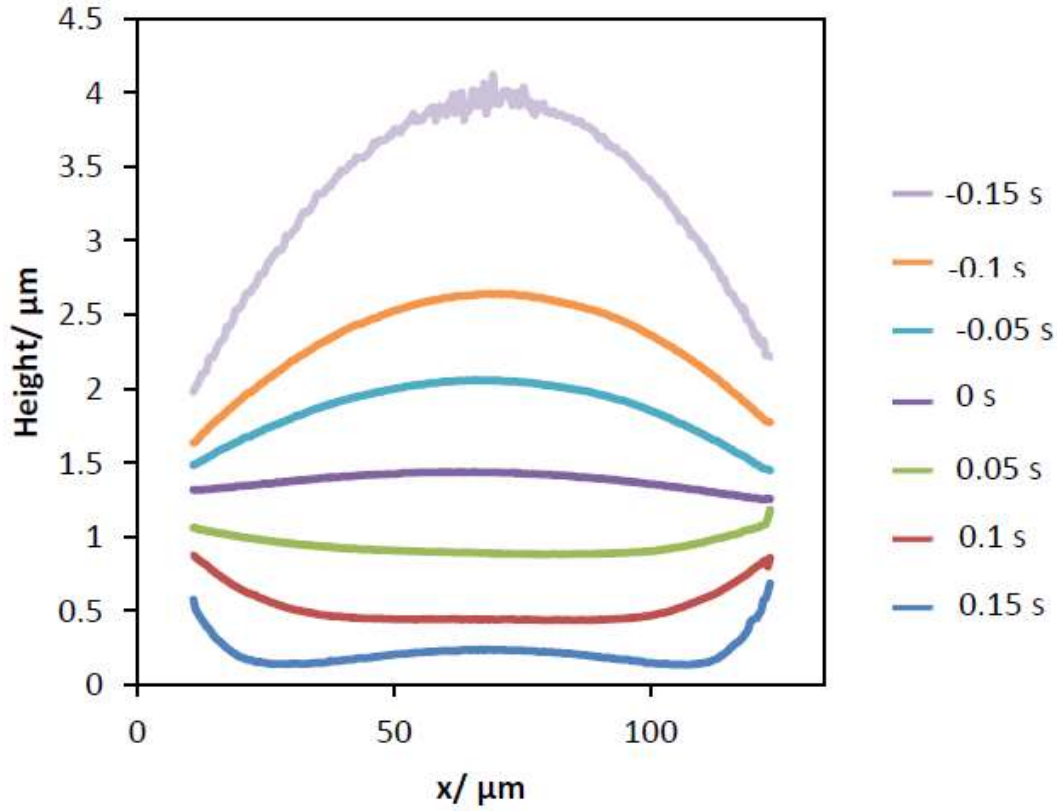

Figure 5.3: Cross-section profile of an anisole droplet during evaporation from a circular well [Kazmierski, 2018].

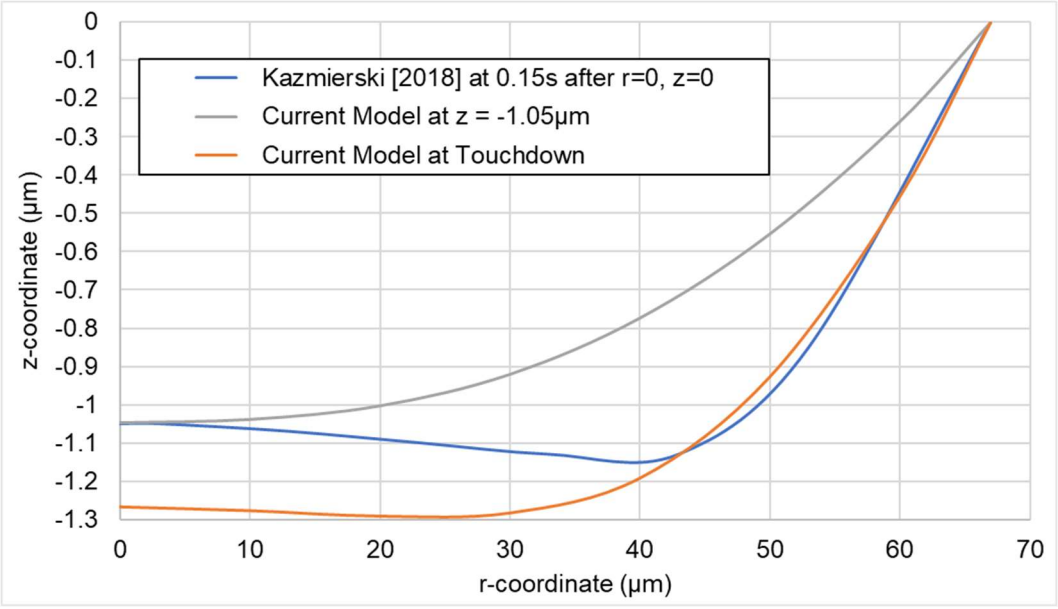

Figure 5.4: Plot of the droplet profile for anisole from experiments by Kazmierski [2018] and from the current model.

As can be seen in Figure 5.4 above, both the experimental results and the current model produced slightly different protuberance heights, with the

experiment showing a 0.08μm protuberance height, when compared to the lowest point of the profile (z = -1.13μm at r = 43μm), and the numerical model showing a 0.032μm protuberance height, albeit at touchdown.

It is worth noting that due to the limitations of the ALE method, the touchdown point actually occurs around 2-5nm from the surface of the substrate for simulations that include a bank structure. All future references to the touchdown point will include this 2-5nm allowance, even when it is not specifically stated.

The primary difference between the experiment and the simulation is the droplet profile as it passes the height of the bank structure at z=0. While the experiment clearly shows a W-shaped profile at this point, the numerical model predicts that it will still be U-shaped. The possible reasons for this are severalfold. Firstly, the experimental data clearly has some variation within it, as the curves shown in Figure 5.3 are not symmetrical, suggesting some level of error is present, particularly away from the centre of the droplet. Secondly, the experimental data was taken at set times, and so was taken some time before touchdown occurred, unlike the model. Thirdly, the presentation of the experimental data uses quite thick lines that necessitate a certain level of interpretation when trying to extract exact points along the curves for comparison. In this case the centre of the line on the right-hand half of the graphs was used for comparison to the simulations. Finally, Figure 5.46 below shows that there was considerable variation with the experimental results attained for anisole.

Of course another potential cause of this variation on the droplet profiles could be inaccuracy within the model, and so further simulations were conducted to compare against experimental results for the evaporation of 4-methyl anisole, the experimental data for which is shown in Figure 5.5.

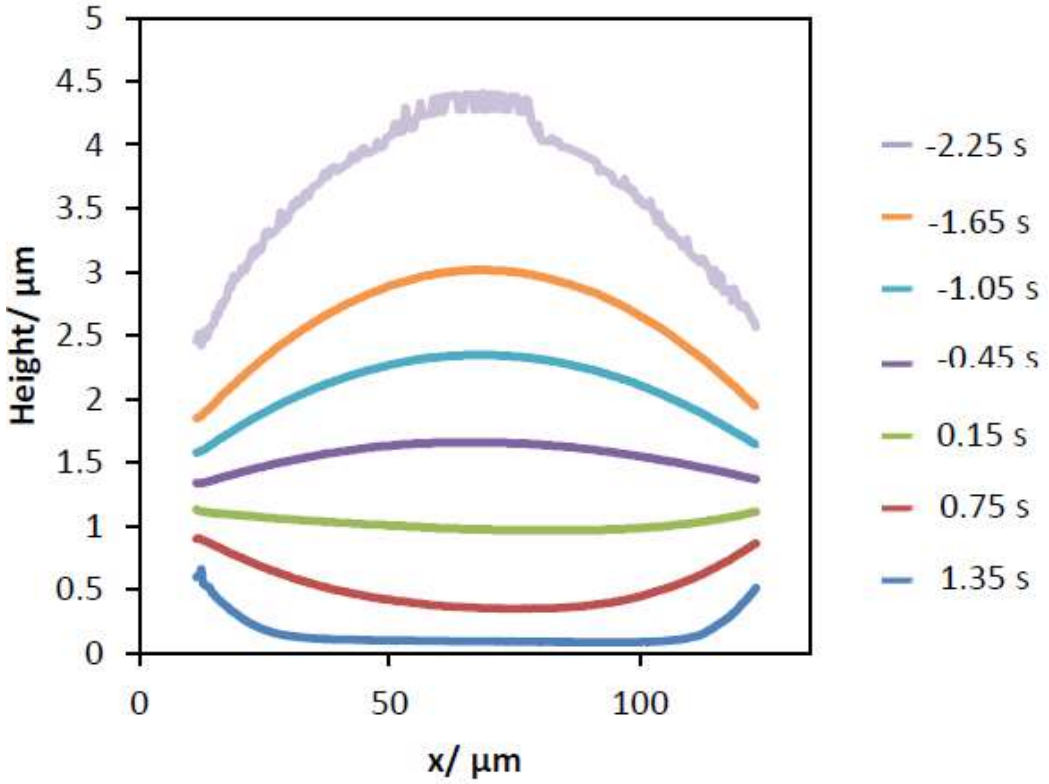

Figure 5.5: Cross-section profile of a methyl anisole droplet during evaporation from a circular well [Kazmierski, 2018].

For this simulation the physical parameters used for methyl anisole were σ = 32.88 x 10^{-3}N/m [Kazmierski, 2018], μ = 0.814 x 10^{-3}Pa.s [ECHA, 2021] and ρ = 971kg/m^3 [Kazmierski, 2018].

There was no data available for the diffusion coefficient for methyl anisole, however, as this depends on molecular size and shape, it is reasonable to base the D value on the diffusion coefficient of similar molecules. There are two solvents that have similar size and shape of molecule as methyl anisole for which there was diffusion coefficient data available, these being p-ethylphenol and 2,5-xylenol, both members of the same $C_8H_{10}O$ family as 4-methyl anisole.

These two solvents both have the methyl groups directly opposite each other in the aromatic ring (i.e. the benzene ring). The ‘p-‘ in p-ethylphenol stands for ‘para’ indicating that the two methyl groups sit directly opposite each other in the benzene ring, as they do in 4-methyl anisole, making p-ethylphenol a reasonable choice.

In addition, as there are 6 carbon atoms in the ring, compounds with numbers differing by 3 will be opposite. 4-methyl anisole is also known as 1-methoxy-4-methylbenzene, with the 1 and 4 indicating that the substituent

methyl groups are at positions 1 and 4 (i.e. directly opposite each other in the benzene ring), therefore 2,5-xylenol might also be a good approximation for the diffusion coefficient. The structural similarities of these compounds can be seen in Figure 5.6.

4-methyl anisole	p-ethylphenol	2,5-xylenol
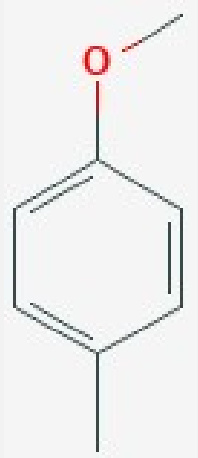	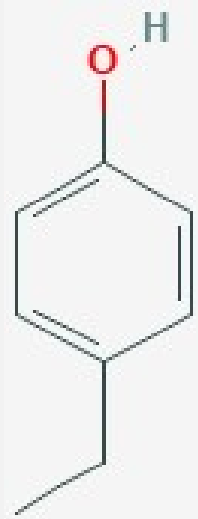	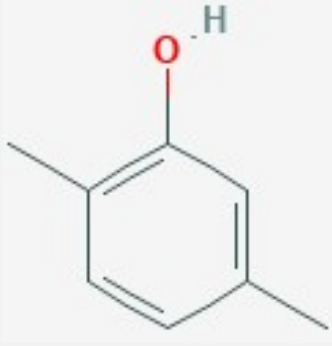

Figure 5.6: Table showing the molecular structures of 4-methyl anisole, p-ethylphenol and 2,5-xylenol.

As the diffusion coefficient in air of p-ethylphenol is 6.58 x $10^{-6}m^2/s$ and is 6.64 x $10^{-6}m^2/s$ for 2,5-xylenol, it is reasonable to assume that D = 6.6 x $10^{-6}m^2/s$ for 4-methyl anisole.

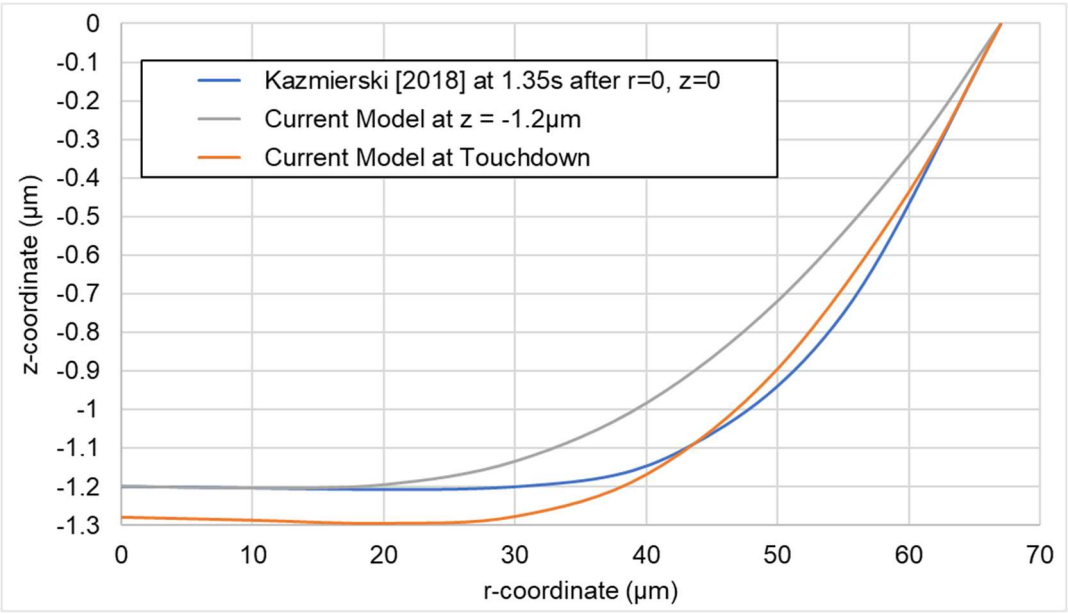

Figure 5.7: Plot of the droplet profile for methyl anisole from experiments by Kazmierski [2018] and from the current model.

Figure 5.7 shows that the numerical model predicts a slight W-shaped profile, with a protuberance height of 0.022μm at touchdown, whereas the experimental data has no protuberance height at z = -1.2μm. However, it is evident from Figure 5.5, that there is plenty of scope for the experimental results to show a protuberance being generated, but data was not collected at a point that could show it. The data for the droplet profile at the distance from the bottom of the bank structure that experimental data was recorded at shows a similar U-shape, but with the curve upwards towards the pinned top of the bank being more gradual and starting at around r = 18μm, rather than r = 33μm for the experiment.

The same issues persist with the available experimental data as with the results for anisole, namely asymmetric droplet profiles, data only recorded at set times and not at touchdown and the use of overly thick lines in the images which could potentially lead to inaccurate readings.

It has been established above that the droplet profile is broadly similar between the results from the current model and the experimental data, with anisole producing a W-shaped profile and methyl anisole generating a U-shaped profile at the same droplet height at which the experimental data was recorded. The current model was then modified to use the physical properties of anisole (as above), methyl anisole (as above), mesitylene (σ = 28.05 x 10^{-3}N/m, μ = 0.916 x 10^{-3}Pa.s, ρ = 861kg/m^3 and D = 6.63 x 10^{-6}m^2/s [Kazmierski, 2018]) and o-xylene (σ = 29.6 x 10^{-3}N/m, μ = 0.747 x 10^{-3}Pa.s, ρ = 876kg/m^3 and D = 7.27 x 10^{-6}m^2/s [Kazmierski, 2018]) in order to compare the numerical results to experimental results from Kazmierski [2018] for protuberance heights at various evaporation rates.

It was decided that one experimental result for o-xylene at an evaporation rate of 8.8μm, shown in Figure 5.46, should be omitted from this graph, as it was so far removed from the other o-xylene results, that it was almost certainly an erroneous measurement. In addition, only the o-xylene experiments that generated U- or W-shaped profiles are included below, and not the experiments that resulted in M-shaped profiles, as the simulations performed did not generate an M-shaped profile with the current physical parameters.

The evaporation rates for each of the solvents was set at the same value as those recorded by Kazmierski, so the only variation would be in the protuberance height generated. This was done to allow as straightforward of a comparison as possible to identify the accuracy of the current model to

generate realistic protuberance heights with realistic solvent parameters. This was implemented in COMSOL through the use of the K parameter seen in eq. (3.17).

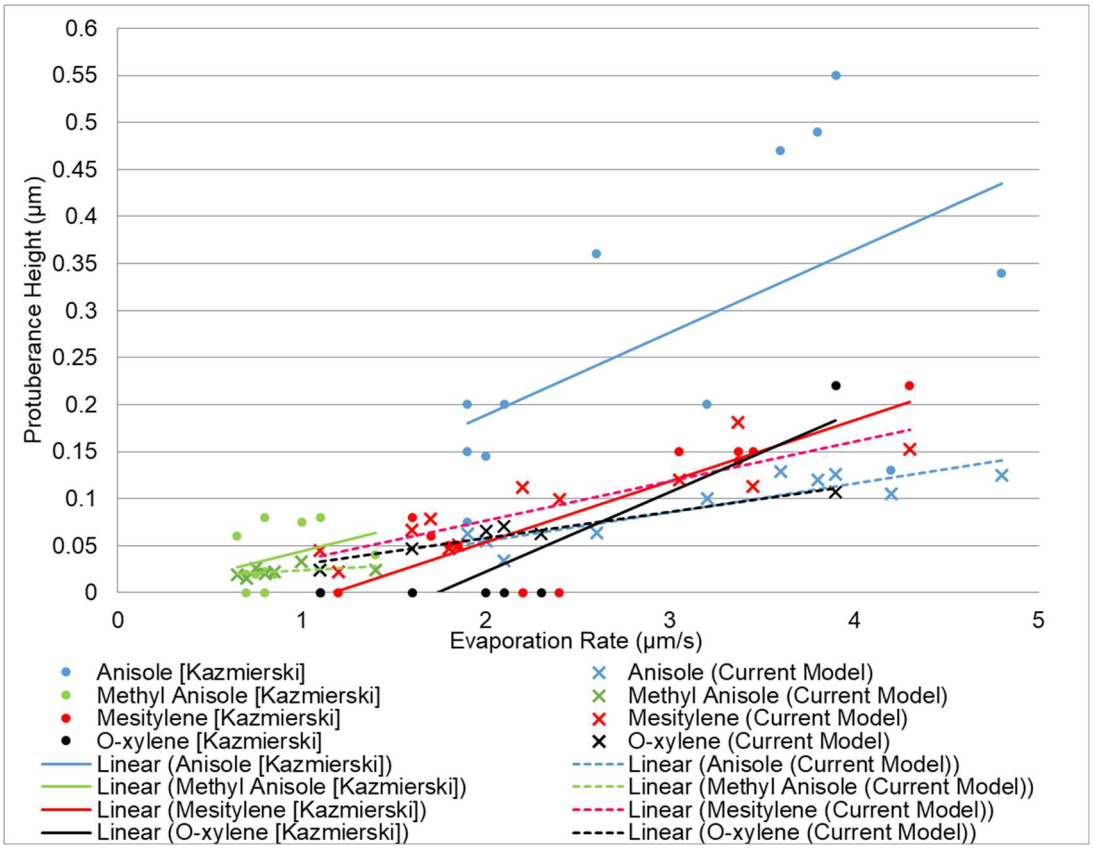

Figure 5.8: Plot of protuberance height against evaporation rate attained experimentally [Kazmierski, 2018] and numerically with the current model for anisole, methyl anisole, mesitylene and o-xylene.

The computational results shown in Figure 5.8 for mesitylene show a decent agreement with the experimental data. There is a 0.045μm overvaluing of the protuberance height at the lowest evaporation rate, and a 0.067μm undervaluing of the protuberance height at the highest evaporation rate, but the linear trendline shows that the general tendency is very similar, with protuberance height gradually increasing with increased evaporation rate.

Figure 5.8 shows that the current model generated a protuberance height at all the evaporation rates studied therein for o-xylene, and shows a steady increase in protuberance height with evaporation rate, as with mesitylene. In this instance, the trendlines do not match as closely as they did for mesitylene, but the trendline for the experimental data is greatly affected by the protuberance height value at an evaporation rate at 3.9μm/s, the only

value that actually showed any generation of a W-shaped profile. This is likely due to the various drying profiles of o-xylene occurring “randomly” [Kazmierski, 2018], especially in circular bank structures, where U-, W- and M-shaped profiles all occurred at various evaporation rates, as shown in Figure 5.46. This suggests discrepancies during the collection of the experimental data in circular bank structures, and Kazmierski does say that it is “reasonable to conclude that pure o-xylene drying within wells with no external influences gives dimple formation”, which is in line with the above simulations. Unfortunately, all of the data used to reach this conclusion was conducted in square bank structures and so cannot be replicated in this study.

The numerical and experimental results for anisole shown in Figure 5.8 show the greatest discrepancy of the three solvents studied. The computations showed a near-linear increase in protuberance height with evaporation rate, and whilst the experimental data demonstrated the same overall trend, both the protuberance height and the spread of the data within it were far greater. This is the clearest visualisation yet of the error that can occur with experimental works conducted at this small length scale, as an evaporation rate of 1.9μm/s generated protuberance heights of 0.075μm, 0.15μm and 0.2μm for the same solvent under the same experimental conditions. This makes it not possible to judge the accuracy of the numerical model for the amplitude of the protuberance height at various evaporation rates, but it does show a broadly general agreement with the correlation between evaporation rate and protuberance height.

Figure 5.8 shows that the current model slightly under-predicts the protuberance height at certain evaporation rates for methyl anisole. Methyl anisole dried in a much narrower range of evaporation rates than the other solvents that were experimentally studied, but still resulted in the same general trend as all the other solvents, with increasing evaporation rate leading to increasing protuberance height.

This section has demonstrated that the current model is broadly capable of replicating the experimental results generated by Kazmierski [2018]. This is somewhat clouded by the lack of experimental data at the touchdown point, so some comparisons between the experimental and numerical results, particularly for the comparison of the droplet profiles shown in Figures 5.3 and 5.5, must rely on a certain amount of extrapolation. Whilst this is clearly not an ideal validation of the current model for solvents in a bank structure, it

is sufficiently in-depth to justify continuing to use this model in subsequent chapters.

5.2.2 Effect of Evaporation Rate

In order to test the effect of differing evaporation rates on droplet drying profiles, the surface tension for all simulations was set to the value of water at 7.28 x 10^{-2}N/m, the humidity to 0.5 and the ambient air and substrate temperature to 22°C in accordance with the experimental conditions.

The evaporation rate was controlled by varying the step function amplitude, discussed in Section 4.2.2, which will now be referred to as a relative evaporation rate, E, with water representing E=1 at a step function amplitude of 1.05 across all of the free surface except the 0.01μm nearest the contact line, as discussed in Section 4.2.2. This will allow for the simple manipulation of the evaporation rate in subsequent simulations and enable straightforward comparison of various evaporation rates to that of water. As previously mentioned in Sections 3.4.2 and 4.2.2, this is mathematically identical to changing the evaporation rate factor K in eq. (3.17), and was chosen by the author entirely due to preference and for ease during the set-up of the simulations. In essence, if E=0.5, the simulated solvent will have half the evaporation rate of water, and if E=2, the solvent would evaporate twice as quickly as water.

The relationship between E and drying time is shown in Figure 5.9, where the protuberance height and drying time was taken at the point that the simulation ended, namely, when the mesh became too deformed in the droplet domain to continue computation, and henceforth referred to as the ‘touchdown’ point. This typically occurred at a droplet thickness of approximately 2-5nm, with the slight error that this method produces having to be accepted as the FEM cannot operate if there is contact between the free surface and the substrate. However, due to the very small distance between the free surface and the substrate at the point at which the simulation fails, the error produced is negligible.

For these tests, the surface tension was to remain constant, regardless of temperature, which negated thermocapillary flows entirely. The drying time was defined as the physical time taken from the start of the simulation to the point at which the simulation ceased due to mesh deformation.

These simulations clearly showed that higher evaporation rates induce W-shaped profiles with lower evaporation rates generating U-shaped profiles, as shown in Figure 5.10.

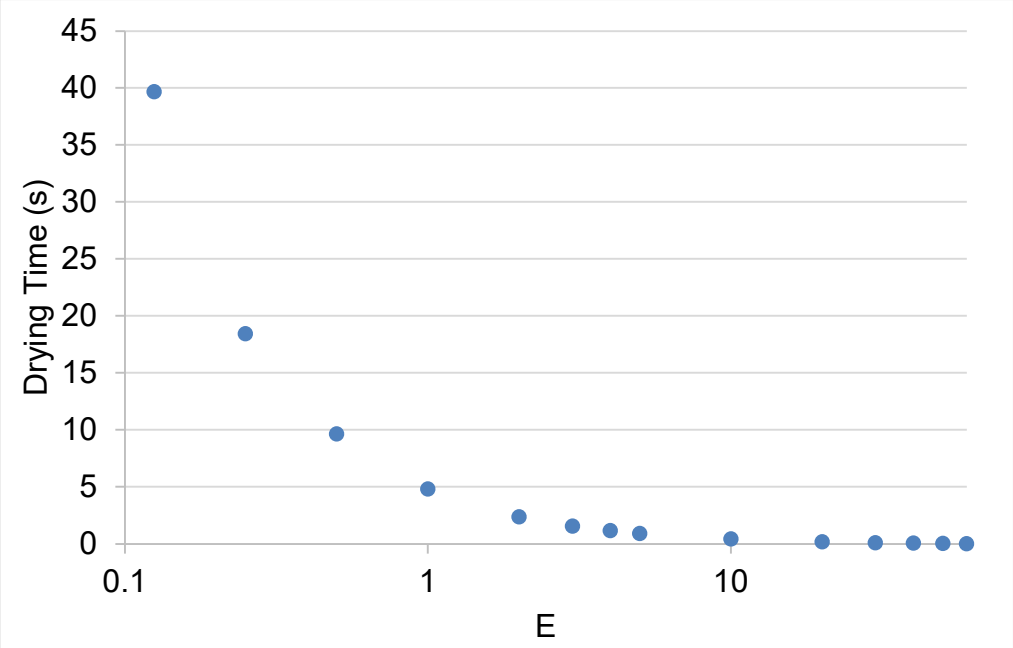

Figure 5.9: Plot of drying times for various E values.

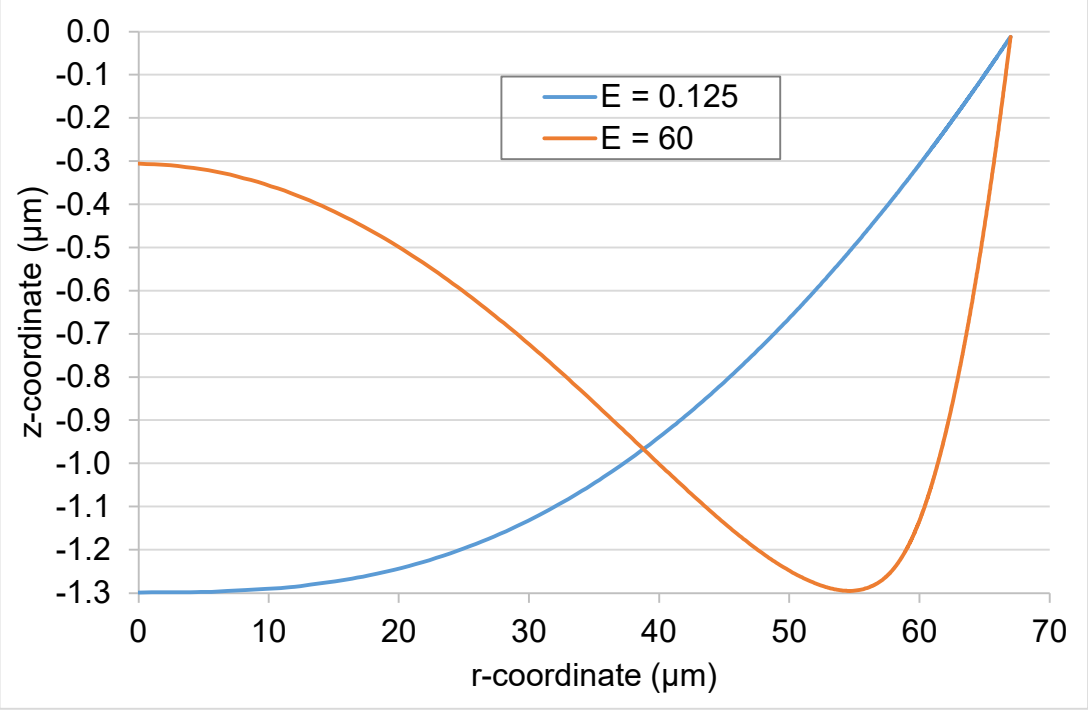

Figure 5.10: Plot of the droplet profile at final output for E values of 0.125 and 60.

The protuberance height was then plotted against E to produce Figure 5.11, which shows a very clear correlation between evaporation rate and protuberance height, with a shift from U- to W-shaped profiles above a relative evaporation rate of approximately 1 (i.e. the evaporation rate of water). .

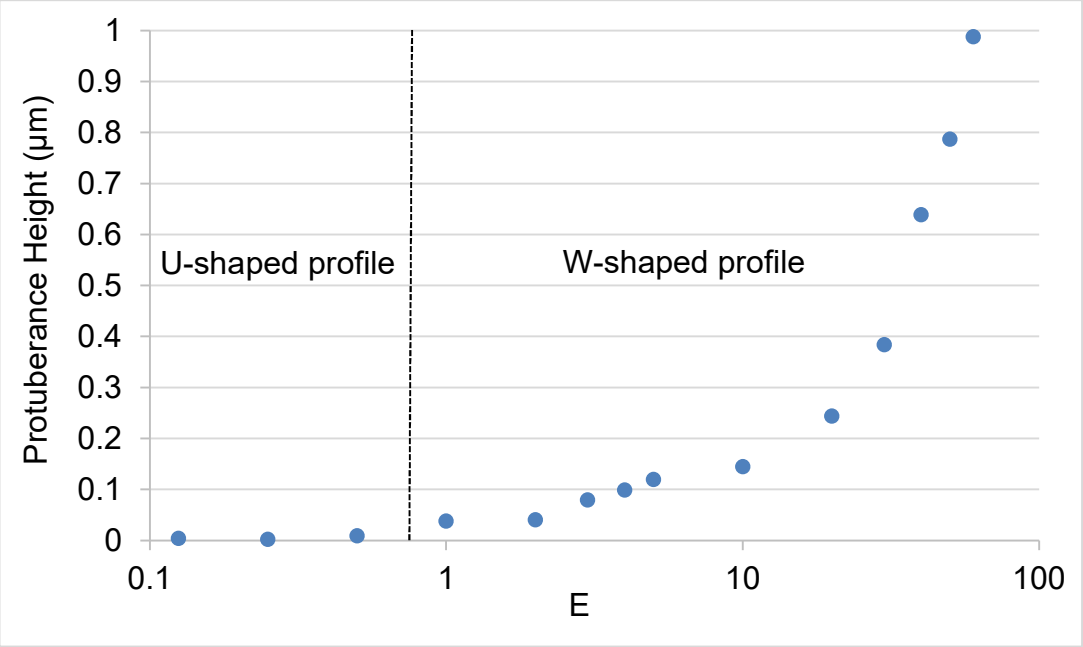

Figure 5.11: Plot of protuberance height against E, on a logarithmic axis, for a constant surface tension of 7.28 x 10^{-2}N/m.

In the case of a very slow evaporating droplet, with E=0.125, the direction of the internal flows during the initial stages of evaporation were unexpected, with a combination of radial outwards flow from the centre of the droplet and internal flows from the contact line converging at approximately 18µm from the droplet centre, as shown in Figure 5.12. This was caused by the very low evaporation rate not being able to generate substantial outwards flows, and allowing the surface tension to govern the internal flows to maintain a very slowly shrinking spherical cap.

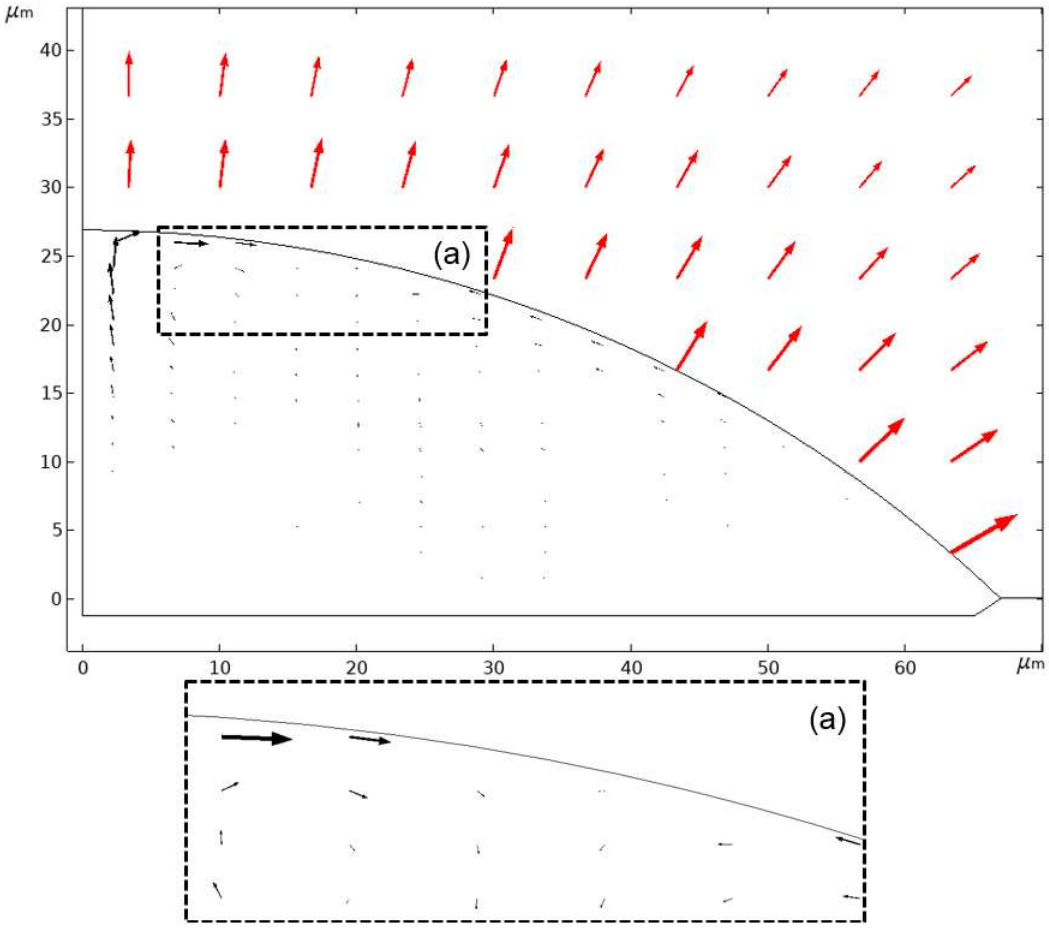

Figure 5.12: Plot of the velocity field in black and the evaporative flux in red for E=0.125 at t=1s.

As the droplet surface passed the top of the bank structure at t=37.5s, the velocity field switched to become entirely outwards flows, as this minimised the area of the free surface due to surface tension and the pinned contact line. The free surface then continued to move towards the substrate with a U-shaped profile until the touching down in the centre of the well at t=39.7s, as shown in Figures 5.13 and 5.14.

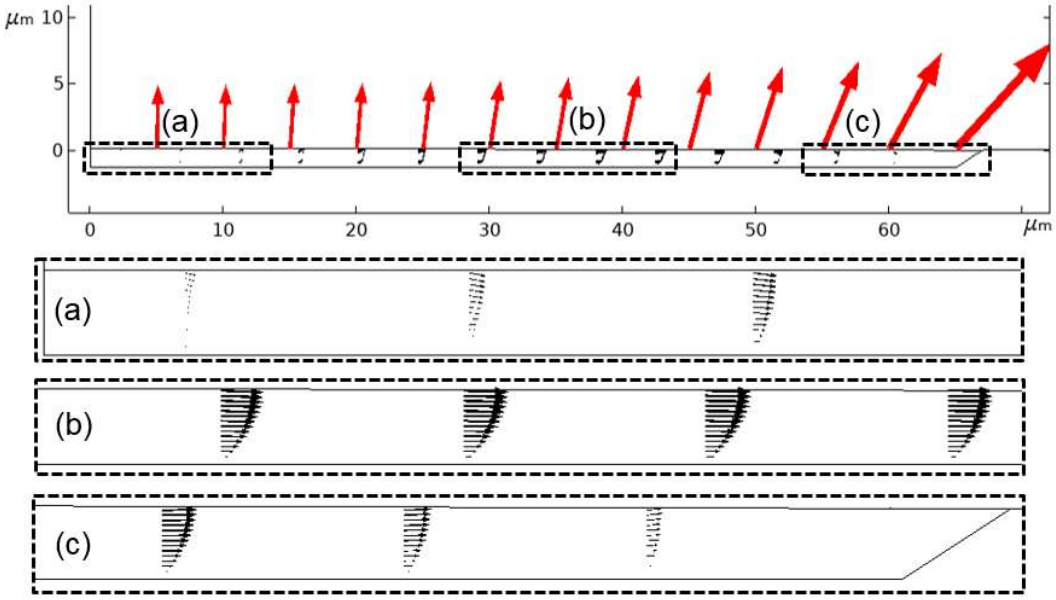

Figure 5.13: Plot of the velocity field in black and the evaporative flux in red for E=0.125 at t=37.5s.

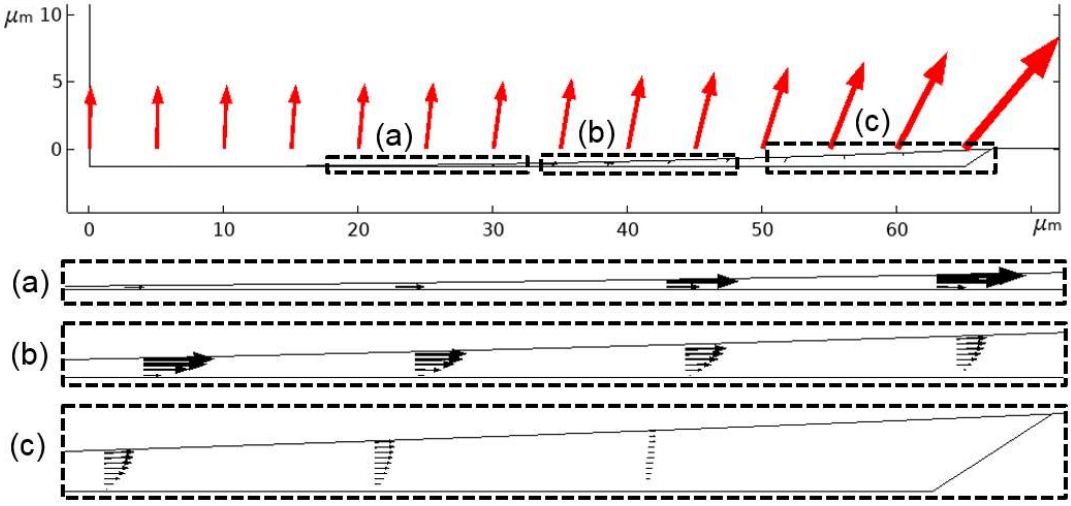

Figure 5.14: Plot of the velocity field in black and the evaporative flux in red for E=0.125 at t=39.7s.

The fast drying model, with E=60, generated strong radial outwards flows from the initial stages of drying due to the very high mass flux at the contact line, as shown in Figure 5.15.

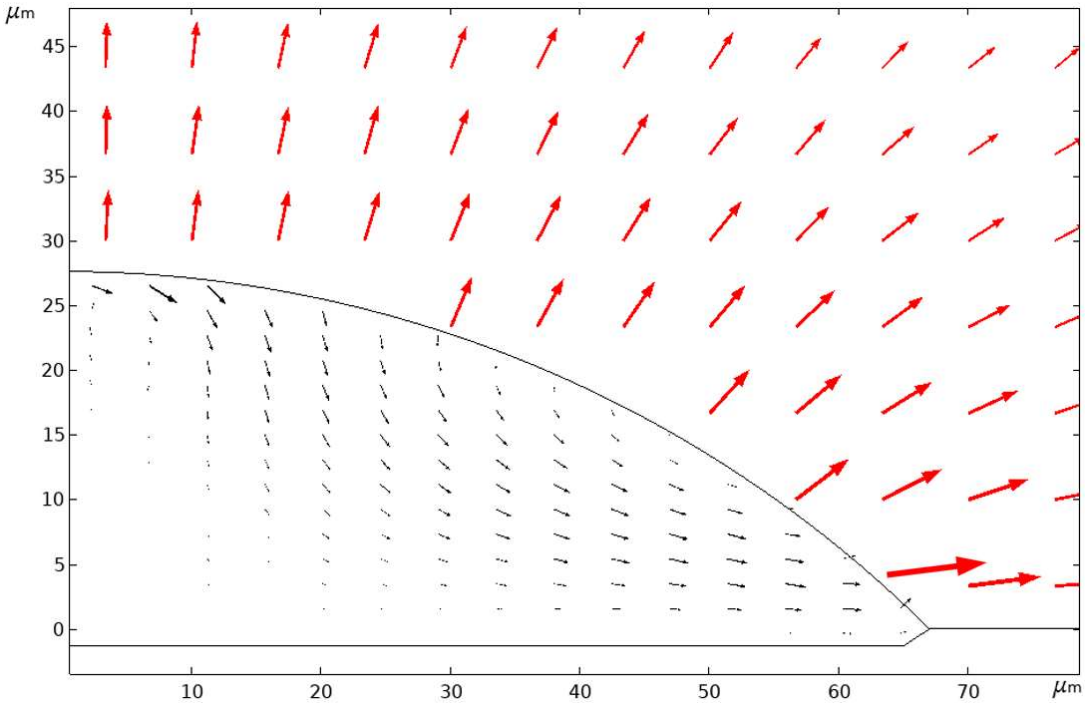

Figure 5.15: Plot of the velocity field in black and the evaporative flux in red for E=60 at t=0.0001s.

However, when the free surface passes the top of the bank structure at 0.017s, the surface tension could not maintain a spherical cap due to the rapid drainage velocity from the intermediate region of the droplet between approximately 40 - 60μm from the droplet centre, which could not be sufficiently replenished by flow from the centre of the droplet, as shown in Figure 5.16. This caused a thinning in that intermediate region that lead to a W-shaped profile, shown in Figures 5.17 and 5.18, at which point there is near zero flow from the centre of the droplet to the touchdown point due to this region of the droplet now being essentially a separate droplet with a very low contact angle.

It is worth noting that as this is an axisymmetric system, at larger radii, the surface area of a small section of the free surface is greater, and hence represents more mass loss. It is also worth noting that all flows are radial and not simply 2D.

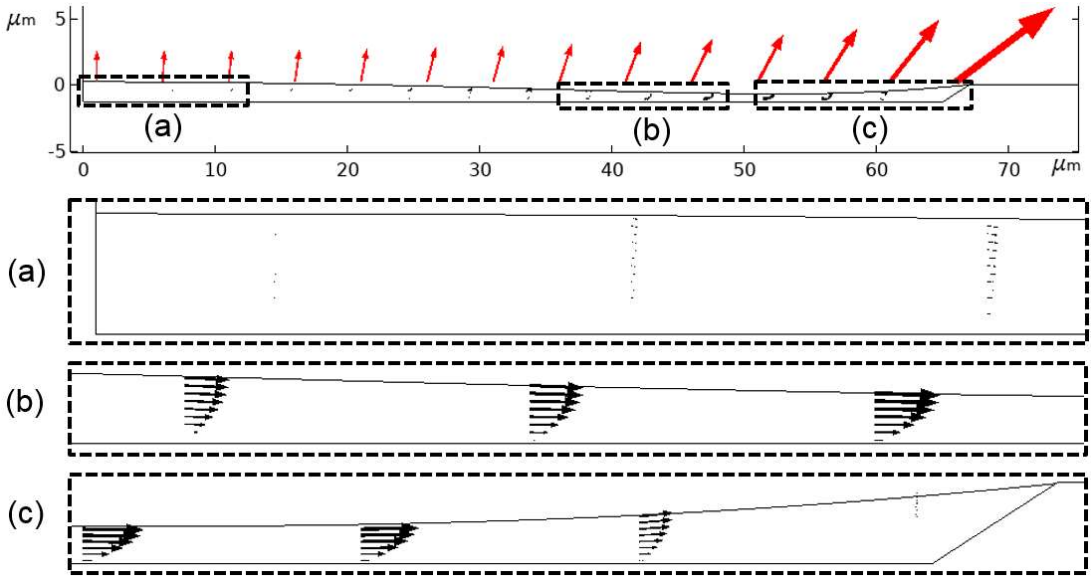

Figure 5.16: Plot of the velocity field in black and the evaporative flux in red for E=60 at t=0.017s.

Once the free surface breaks at the touchdown point, which cannot be modelled by the method used here, the droplet will split to form two droplets, one at the bank and the other with a rapidly receding contact angle towards the centre of the well. However, in a real OLED application when a polymer is suspended in the liquid, it will solidify before the split occurs.

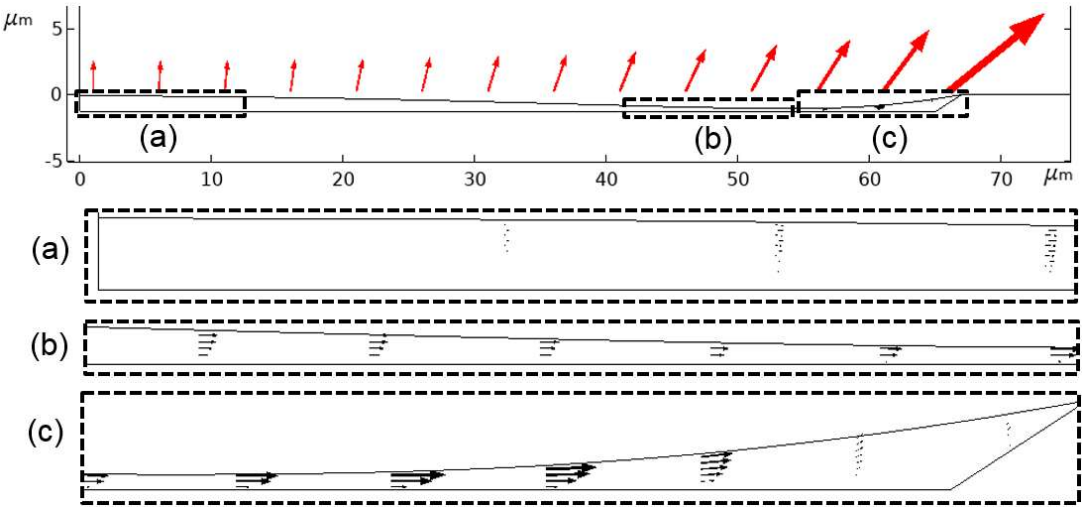

Figure 5.17: Plot of the velocity field in black and the evaporative flux in red for E=60 at t=0.0174s.

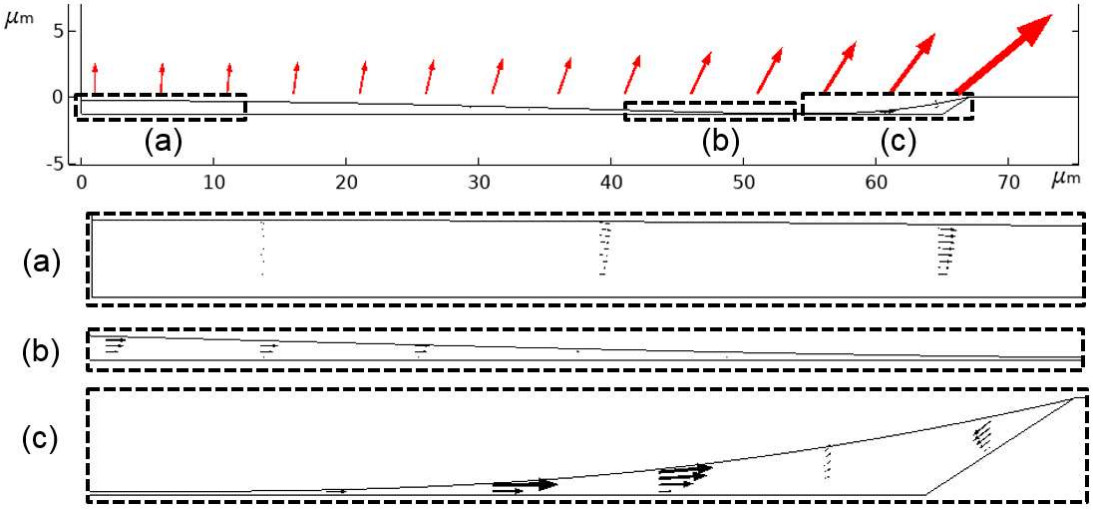

Figure 5.18: Plot of the velocity field in black and the evaporative flux in red for E=60 at t=0.0176s.

This section has shown that a higher evaporation rate leads to a W-shaped profile, as high radial outwards flows mean that liquid is drawn from the intermediate region faster than it can be replenished from the centre of the droplet, causing that region to thin, and leaving a protuberance of liquid remaining at the centre of the droplet.

5.2.3 Analysis of Surface Tension Effects

In order to study how varying surface tension affects the droplet drying profiles, the evaporation rate was set as water with E=1, and the surface tension was ranged from 7.28×10^{-5} to 7.28N/m, with this value kept constant regardless of temperature. Clearly, this wide range of surface tensions is not realistic, with no liquids having surface tensions this low, but is instead used to test the effect of surface tension of droplet drying profiles rather than reflecting something that can be tested experimentally.

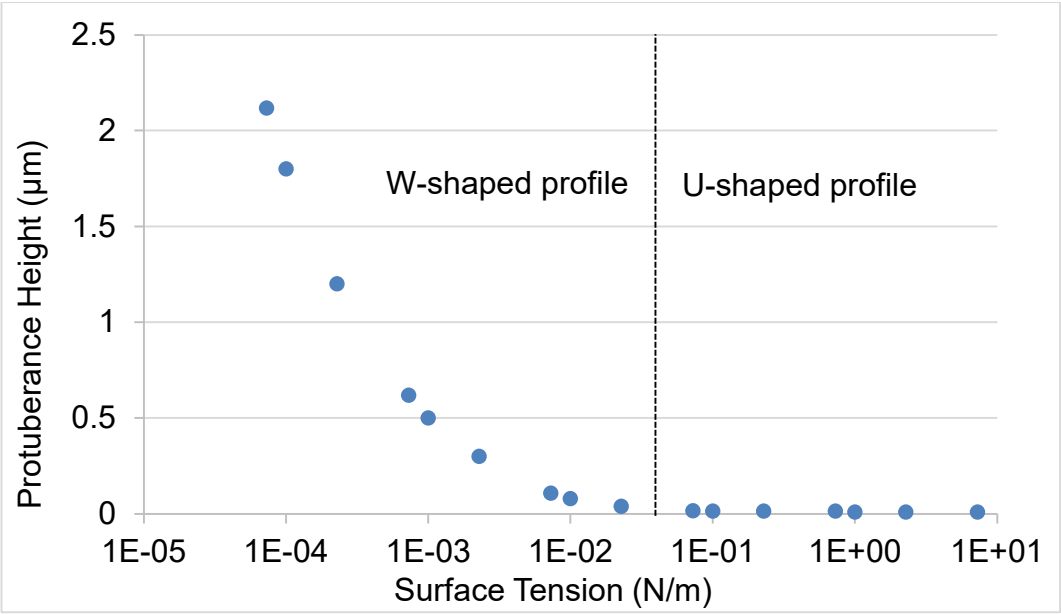

Figure 5.19: Plot of protuberance height against surface tension.

As would be expected, simulations with a lower surface tension produced W-shaped profiles, and higher surface tension models generated U-shaped profiles, as seen in Figures 5.13 and 5.14. This is due to higher surface tension being more able to maintain a spherical cap.

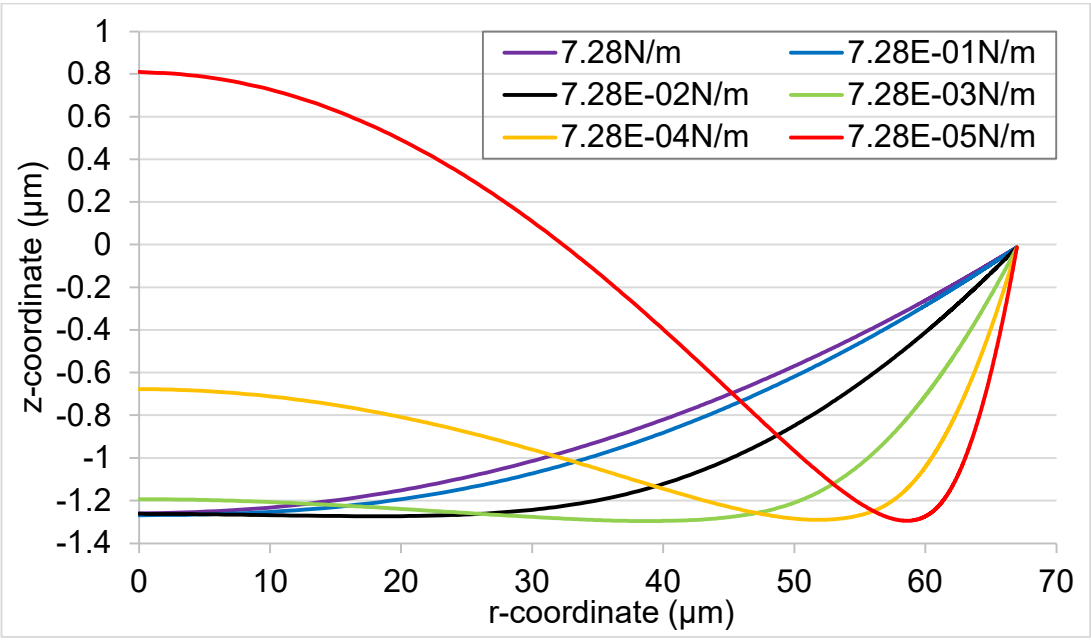

Figure 5.20: Plot of the droplet profile at final output for various surface tension values.

This section has shown that not only a high evaporation rate can cause a W-shaped profile, but also a low surface tension value, as the ability to maintain a spherical cap is diminished.

5.2.4 Viscosity Effects

Viscosity was not initially considered by Kazmierski [2018] as a decisive factor in forming droplet profiles, but as the internal flows within the droplet are clearly critical to how the profile develops, it was seen as an area of interest for the model to explore.

The viscosity was varied from 1Pa.s to 1 x 10^{-5}Pa.s, with these values selected purely for investigative purposes, and do not represent realistic viscosity values. The surface tension was constant at 7.28 x 10^{-2}N/m and E=1.

Figures 5.21 and 5.22 clearly show that increasing viscosity causes increases in the protuberance height. This is due to the increased viscosity not allowing the fluid to flow as freely from the centre of the droplet to the contact line, leading to insufficient drainage into the intermediate region and hence a W-shaped profile being produced. Simulations with viscosity values of less than approximately 1 x 10^{-3}Pa.s generated U-shaped profiles, though it is recognised that such viscosities are artificially low.

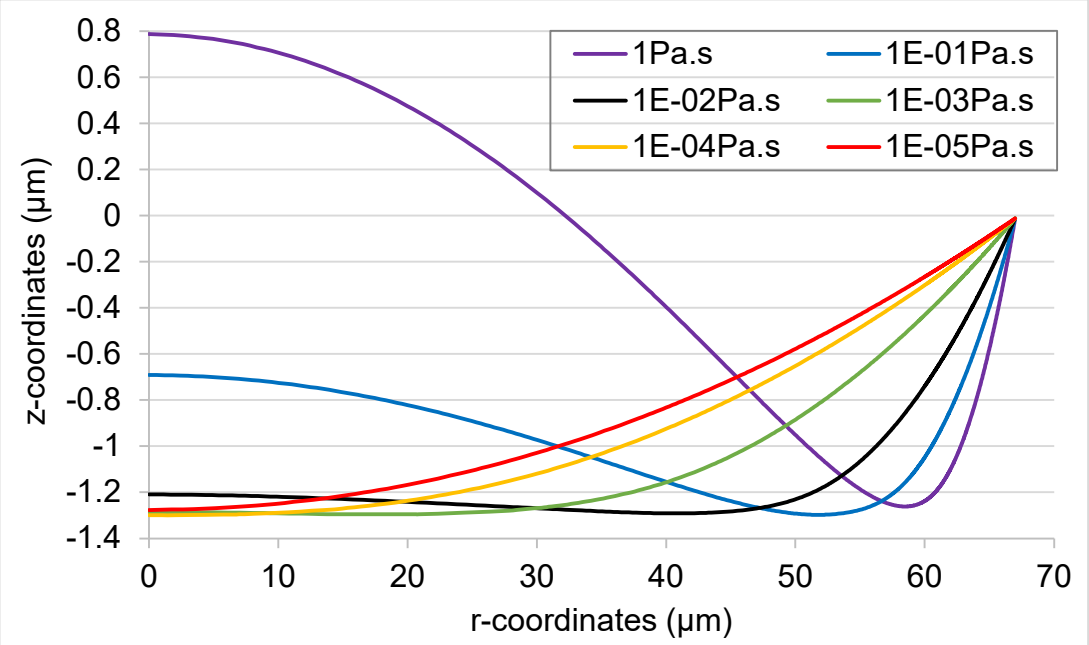

Figure 5.21: Plot of the droplet profile at final output for various viscosity values.

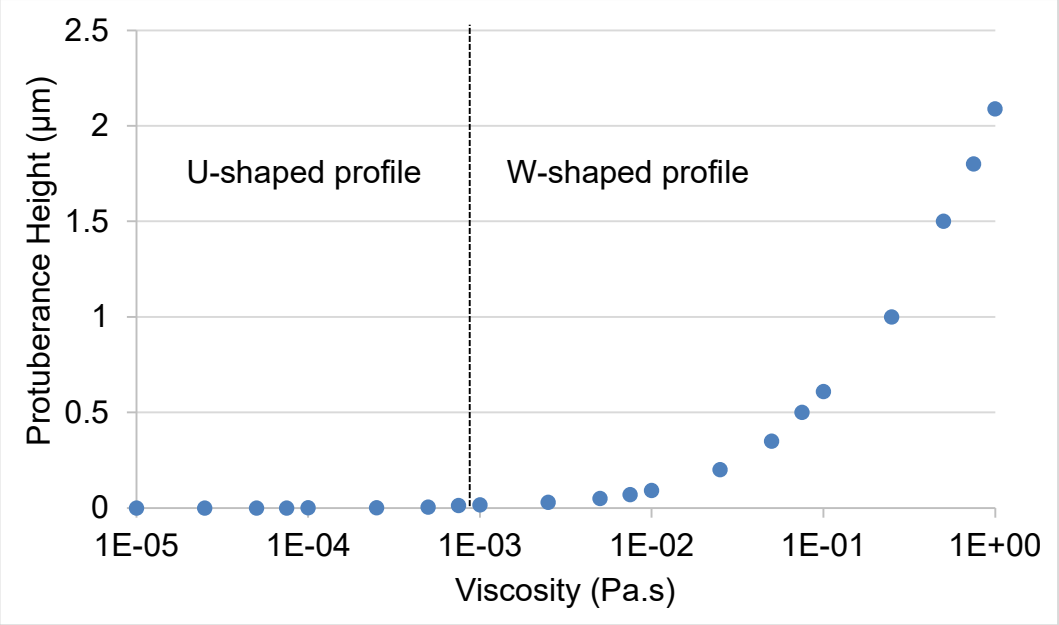

Figure 5.22: Plot of protuberance height against viscosity.

This section has shown that increasing the viscosity of the solvent increases the likelihood of a W-shaped droplet profile developing due to the restriction of flow through the intermediate region of the droplet.

5.2.5 Thermocapillary Effects

Now that the individual impacts of evaporation rate and surface tension on droplet drying profile have been established, the thermocapillary effect will be studied with the surface tension dependent upon the surface temperature, which depends in turn on cooling induced by the evaporation rate. This will be carried out by implementing eq. (3.26).

Theoretically, a higher evaporation rate will lead to greater evaporative cooling and therefore a greater surface tension gradient along the free surface, which will generate flows from the lower surface tension at the summit of the droplet towards the higher surface tension at the contact line, particularly in the intermediate region where the droplet thins due to lack of flow from the centre, promoting the generation of W-shaped drying profiles.

The thermal boundary conditions remain the same as in Sections 4.3.1 and 4.4.1, with a constant temperature at the substrate in this case of 295.15K, the same as the ambient air temperature.

As can be seen from Figure 5.23, the increased evaporation rate leads to a shift to W-shaped profiles as expected, however Figure 5.24 demonstrates

the introduction of thermocapillary flows marginally decreases the protuberance height for a given relative evaporation rate compared to results for a constant surface tension of 7.28 x 10^{-2}N/m, although the overall trend is very similar for both, suggesting that thermocapillary effects do not play a pivotal role in determining the overall drying profile of the droplet.

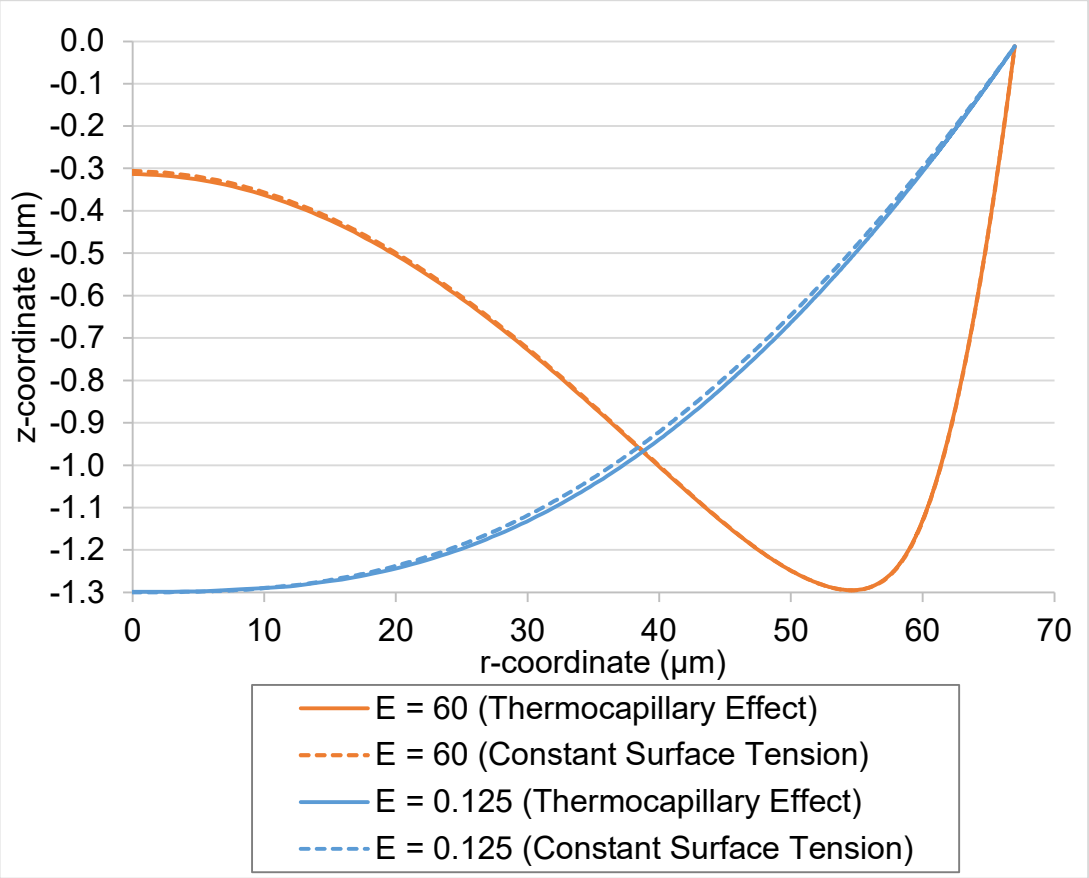

Figure 5.23: Plot of droplet profile at final output for E values of 0.125 and 60 with the thermocapillary effect.

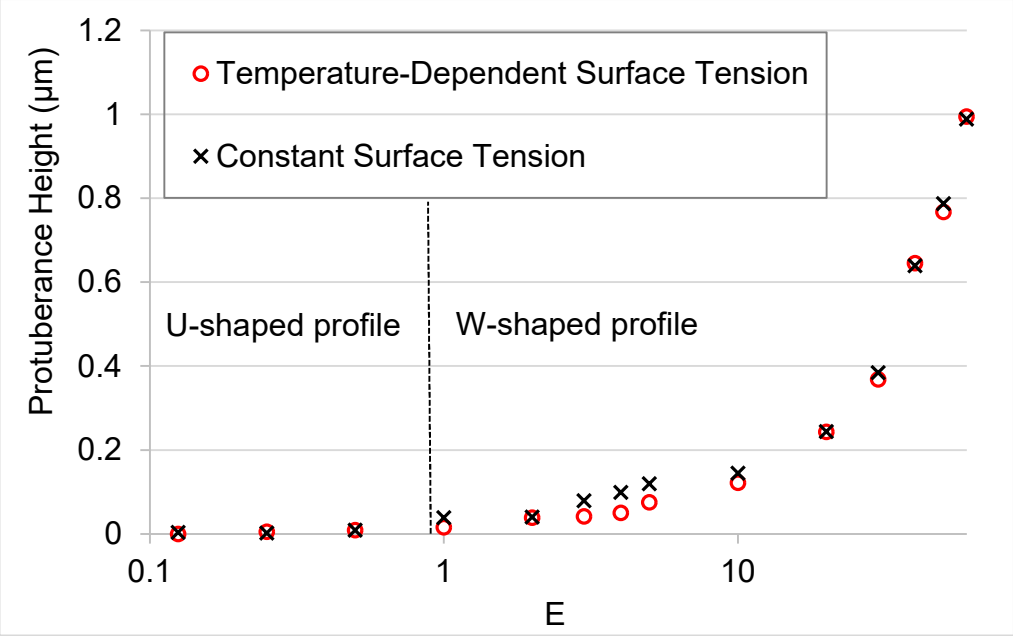

Figure 5.24: Plot of protuberance height against E for temperature-dependent and constant surface tension values.

For a slowly evaporating droplet, with E=0.125, the initial stages showed very little radial outwards flows with internal flows from the contact line towards the summit of the droplet dominating the majority of the bulk flow, with the flows converging at approximately 9μm from the droplet centre, as seen in Figure 5.25.

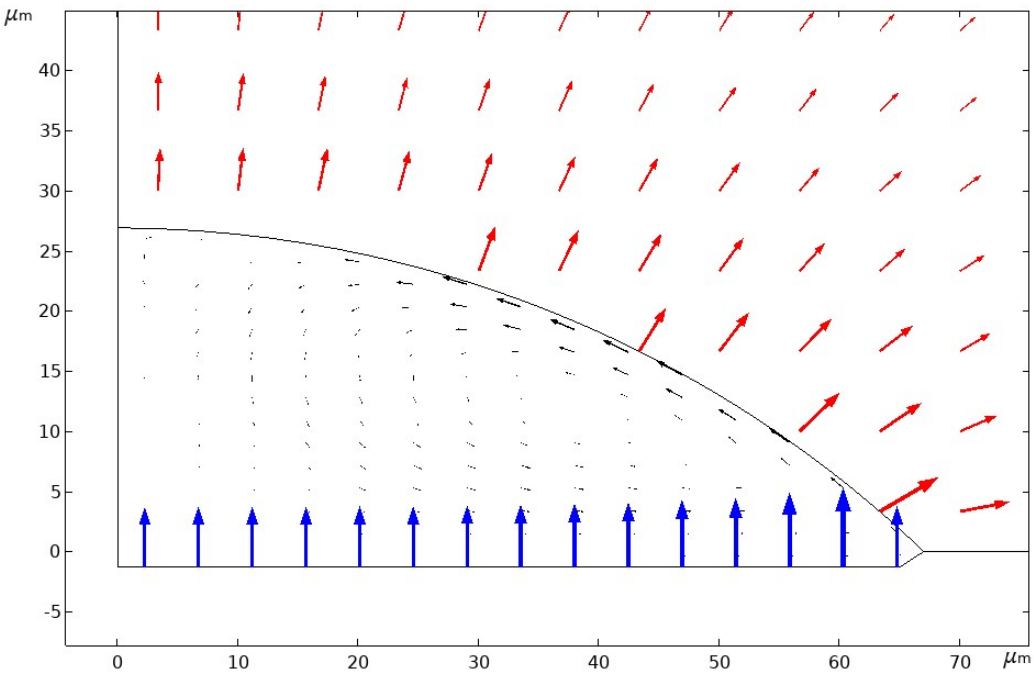

Figure 5.25: Plot of the velocity field in black, the evaporative flux in red and the heat flux from the substrate in blue for E=0.125 at t=1s.

This was due to the low evaporation rate not being able to generate substantial outwards flows and also the thermocapillary effect inducing flow from a high temperature, low surface tension region at the contact line towards the summit of the droplet, which is a low temperature, high surface tension region, as demonstrated by Figures 5.26 and 5.27.

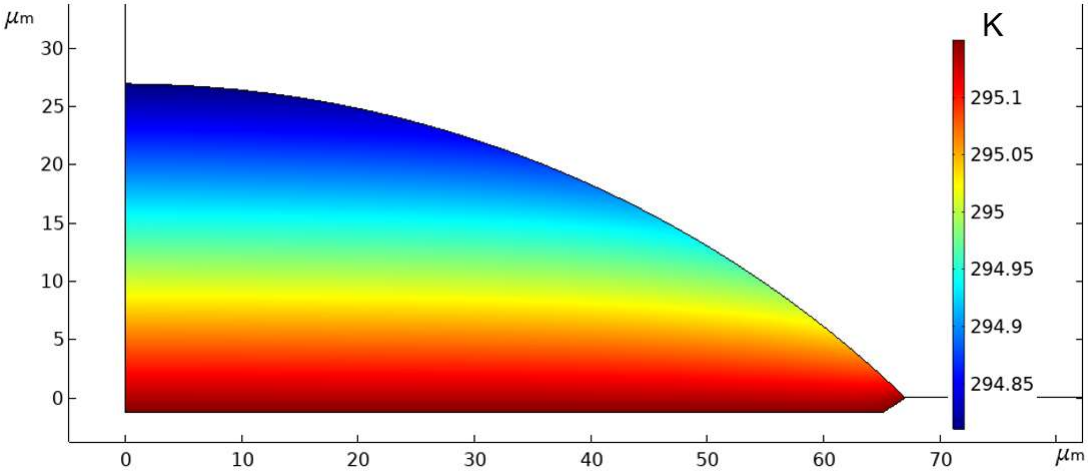

Figure 5.26: Plot of the temperature field for E=0.125 at t=1s.

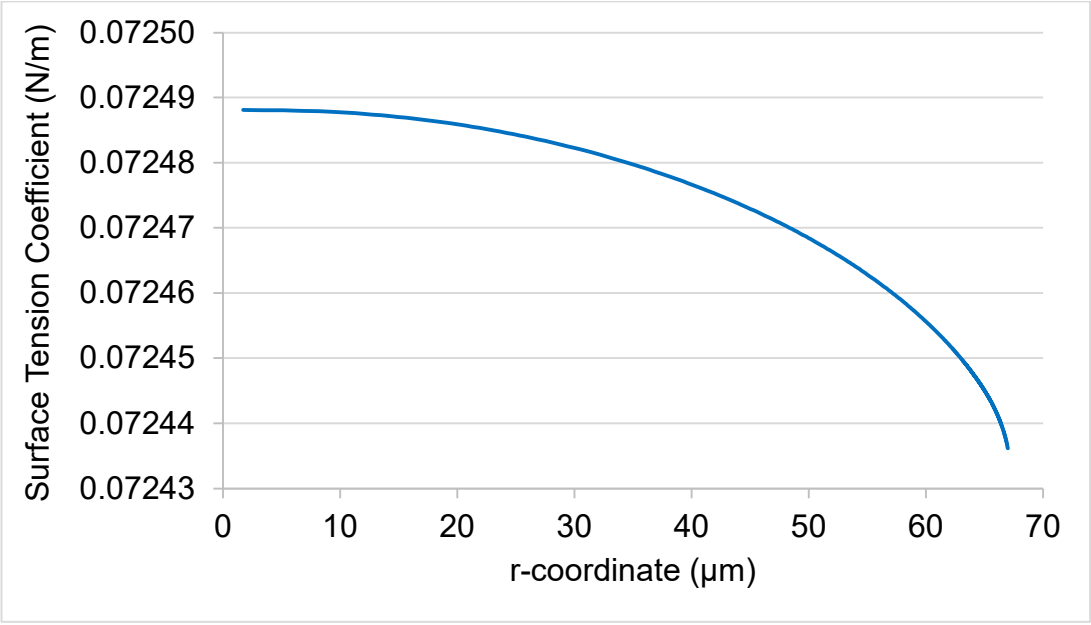

Figure 5.27: Plot of the surface tension coefficient for E=0.125 at t=1s.

As the simulation progressed, the thermocapillary effect continued to dominate the weak outwards flows, maintaining a spherical cap throughout, as seen in Figures 5.28 and 5.29.

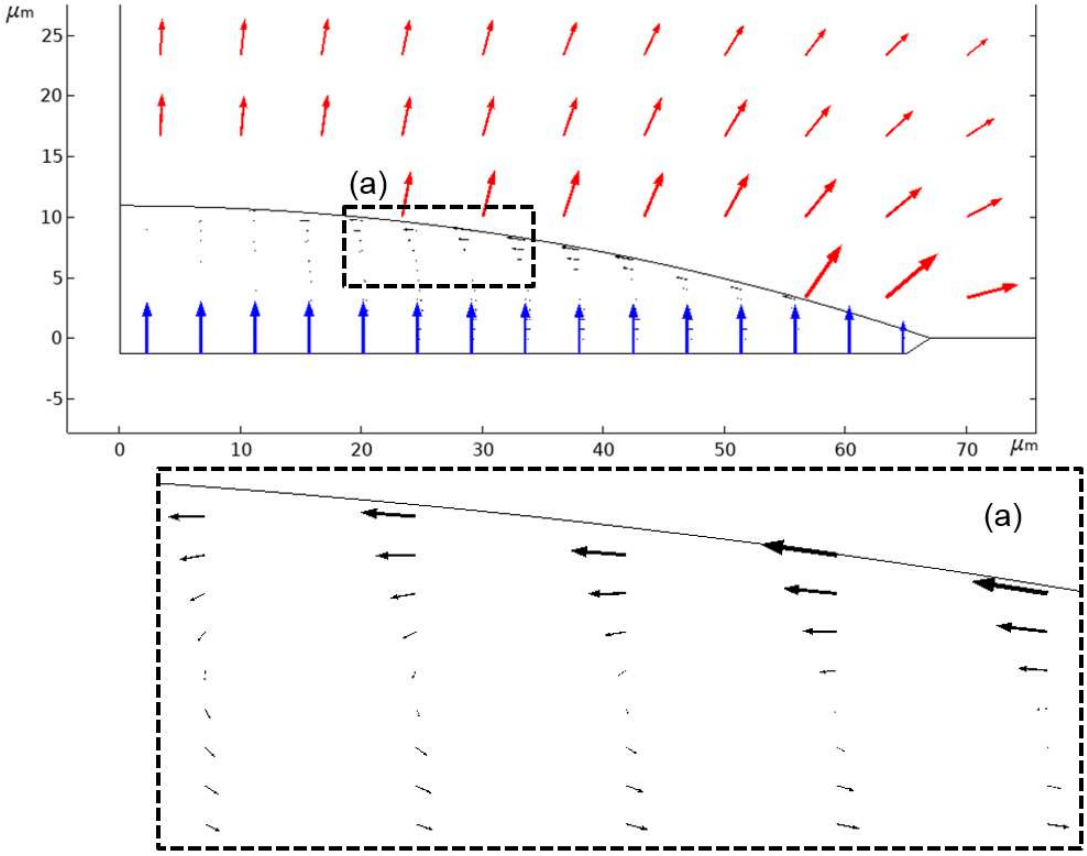

Figure 5.28: Plot of the velocity field in black, the evaporative flux in red and the heat flux from the substrate in blue for E=0.125 at t=22s.

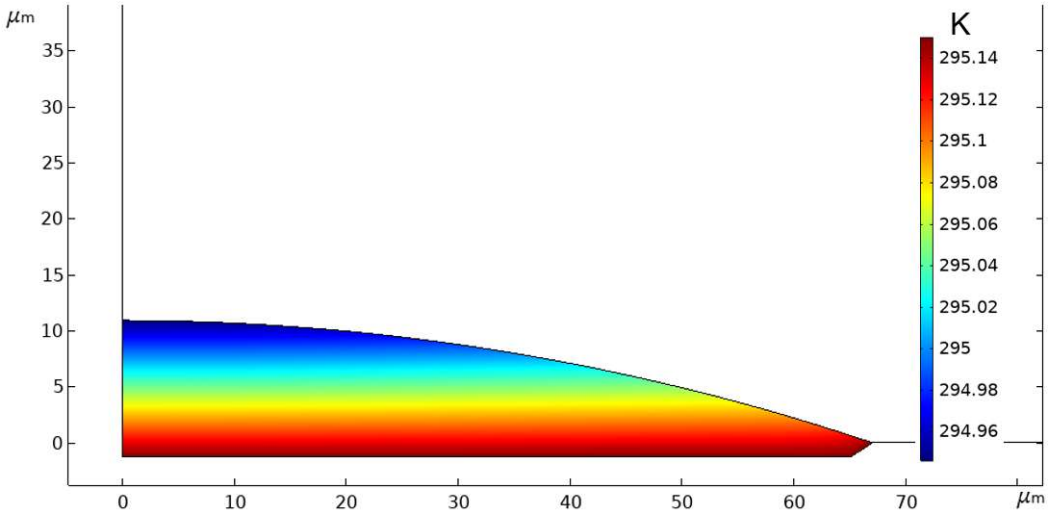

Figure 5.29: Plot of the temperature field for E=0.125 at t=22s.

When the droplet surface passes the height of the bank structure at t=44s, the temperature variation throughout the droplet is only 0.02K, due to the heat transfer from the substrate and the high aspect ratio of the droplet. Coupled with the very weak radial outwards flows, this means there is

almost no flow in the bulk of the droplet, except for a slight circulatory flow near the contact line, attributable to the thermocapillary effect being induced by the heating effect of the angled section of the bank structure, as seen in Figures 5.30, 5.231 and 5.32.

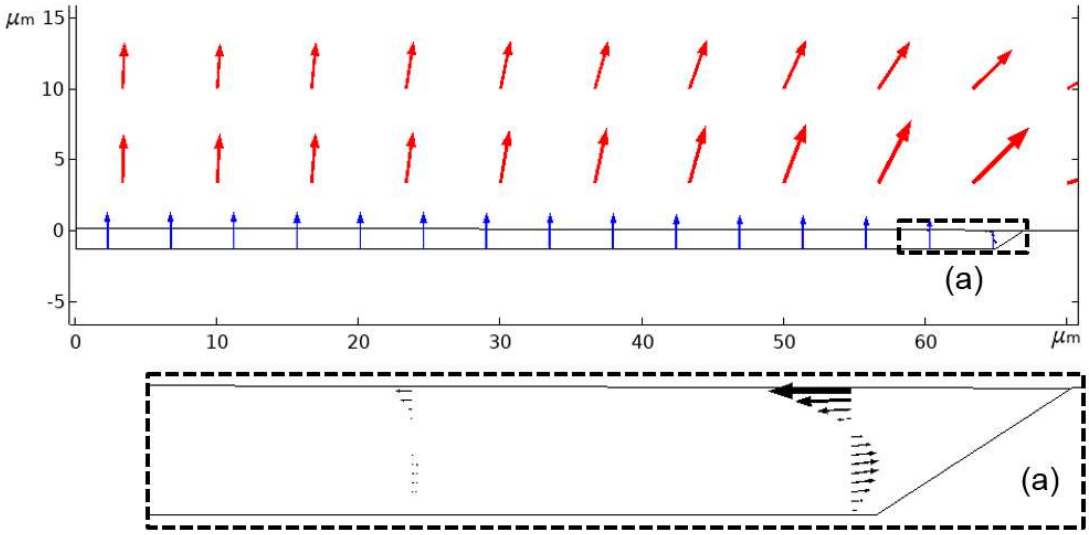

Figure 5.30: Plot of the velocity field in black, the evaporative flux in red and the heat flux from the substrate in blue for E=0.125 at t=44s.

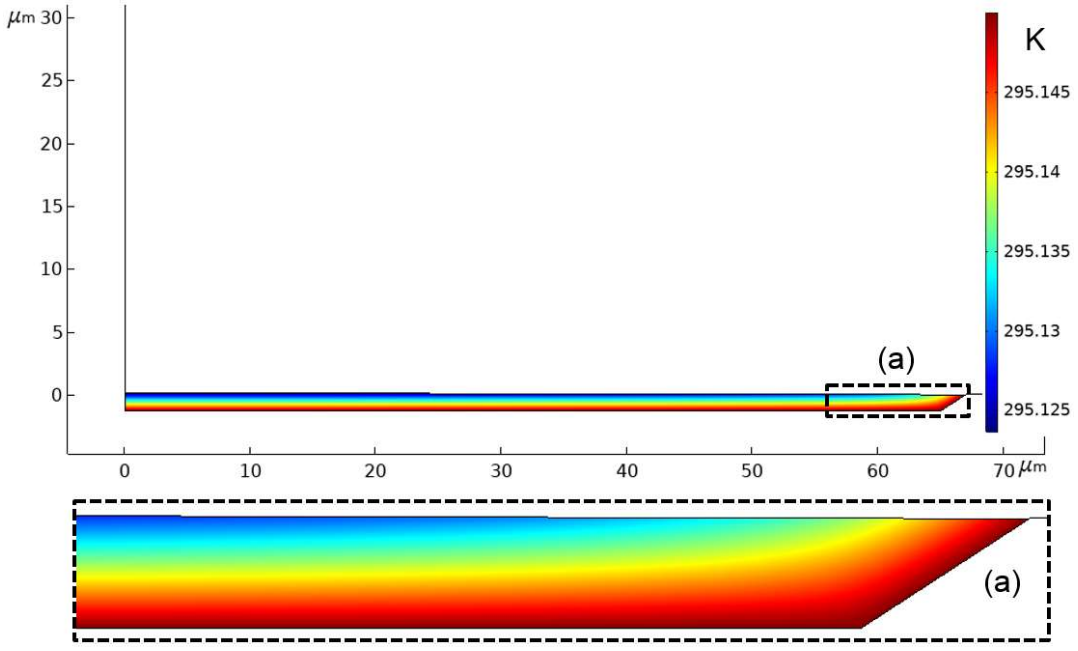

Figure 5.31: Plot of the temperature field for E=0.125 at t=44s.

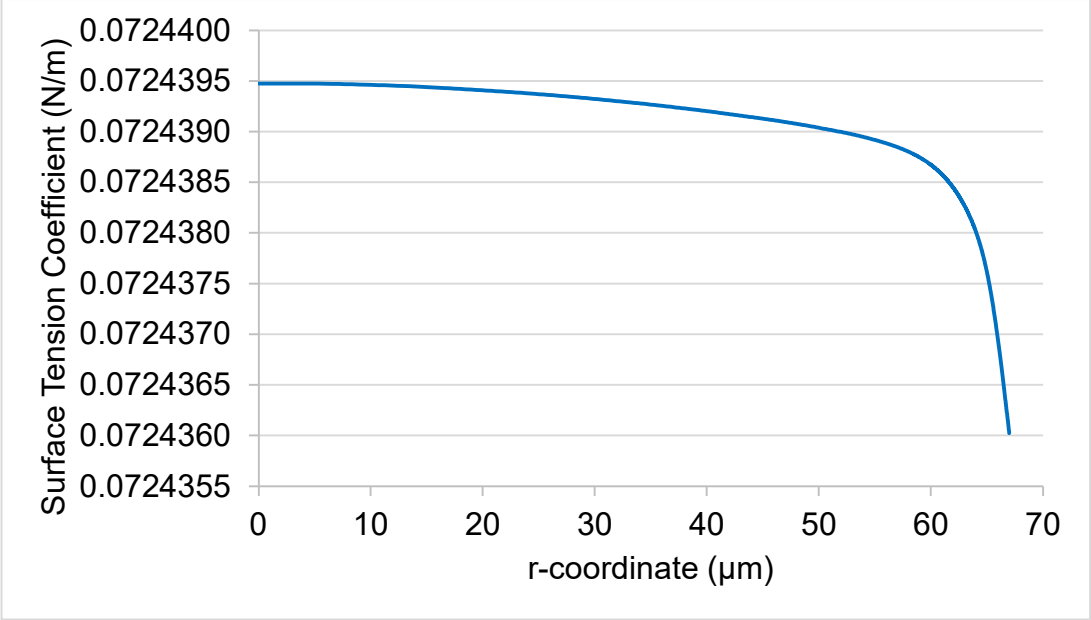

Figure 5.32: Plot of the surface tension coefficient for E=0.125 at t=44s.

As the simulation continues to touchdown at t=46.14s, there continues to be little flow in the bulk of the droplet except for a slight outwards flow due to the negative curvature of the surface and a circulatory flow near the contact line due to the heat transfer from the substrate leading to a thermocapillary flow in this region, as shown by Figures 5.33 and 5.34.

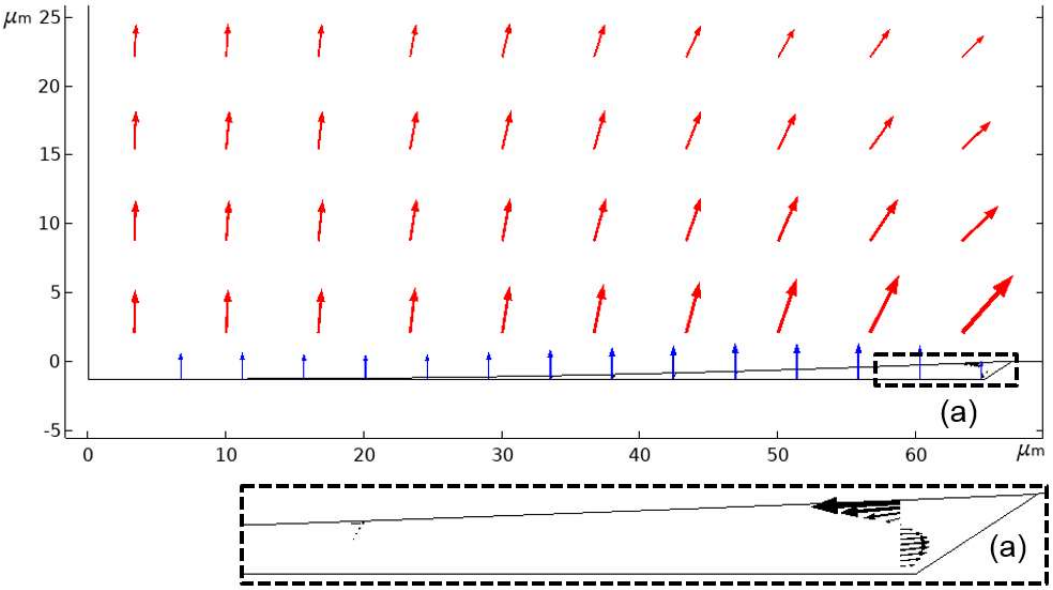

Figure 5.33: Plot of the velocity field in black, the evaporative flux in red and the heat flux from the substrate in blue for E=0.125 at t=46.14s.

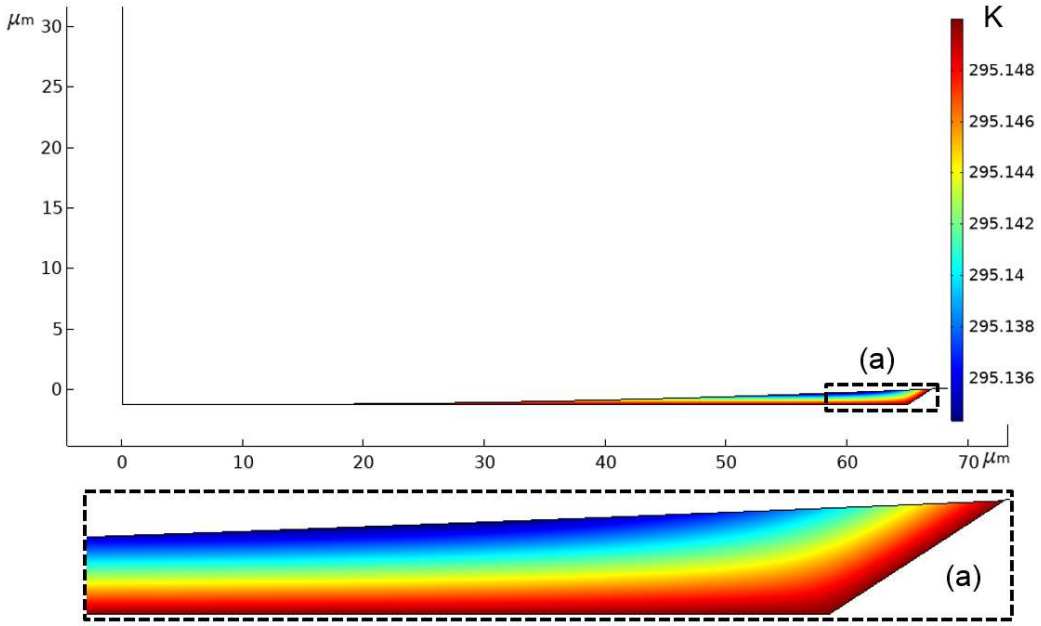

Figure 5.34: Plot of the temperature field for E=0.125 at t=46.14s.

The above analysis has shown that a slowly evaporating droplet generates low radial outwards flows, and therefore there is no opportunity under normal conditions for the flow to be restricted through the intermediate region of the droplet, so a U-shaped profile is produced.

A simulation incorporating the thermocapillary effect in a fast evaporating droplet, with E=60, again showed strong radial outwards flows from the very early stages of drying at t=0.0001s, as seen in Figure 5.35, due to the higher mass flux near the contact line. However, the heat transfer from the angled section of the substrate has increased the temperature of the droplet near the contact line, reducing the surface tension, as seen in Figures 5.36 and 5.37. This leads to thermocapillary flows back towards the centre of the droplet in the region nearest to the contact line, seen in Figure 5.36.

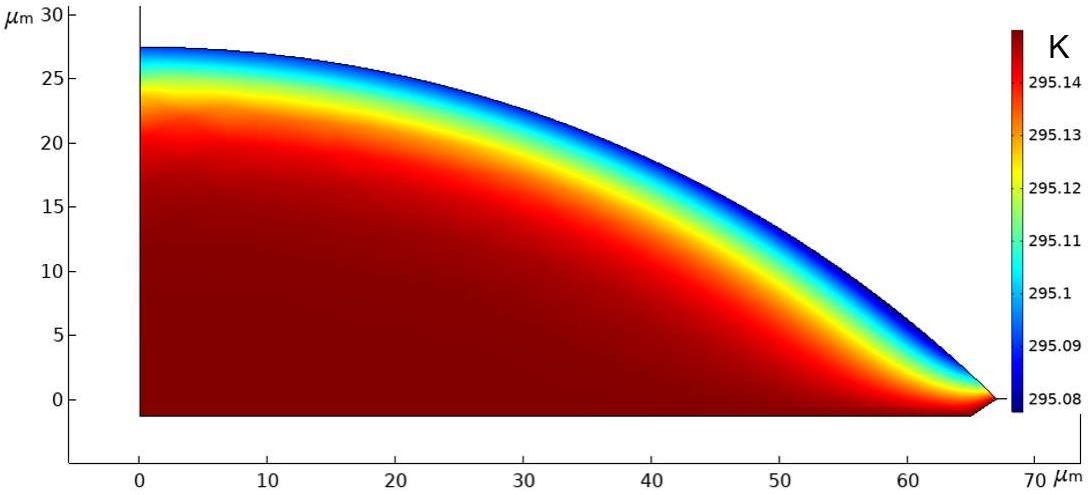

Figure 5.35: Plot of the temperature field for E=60 at t=0.0001s.

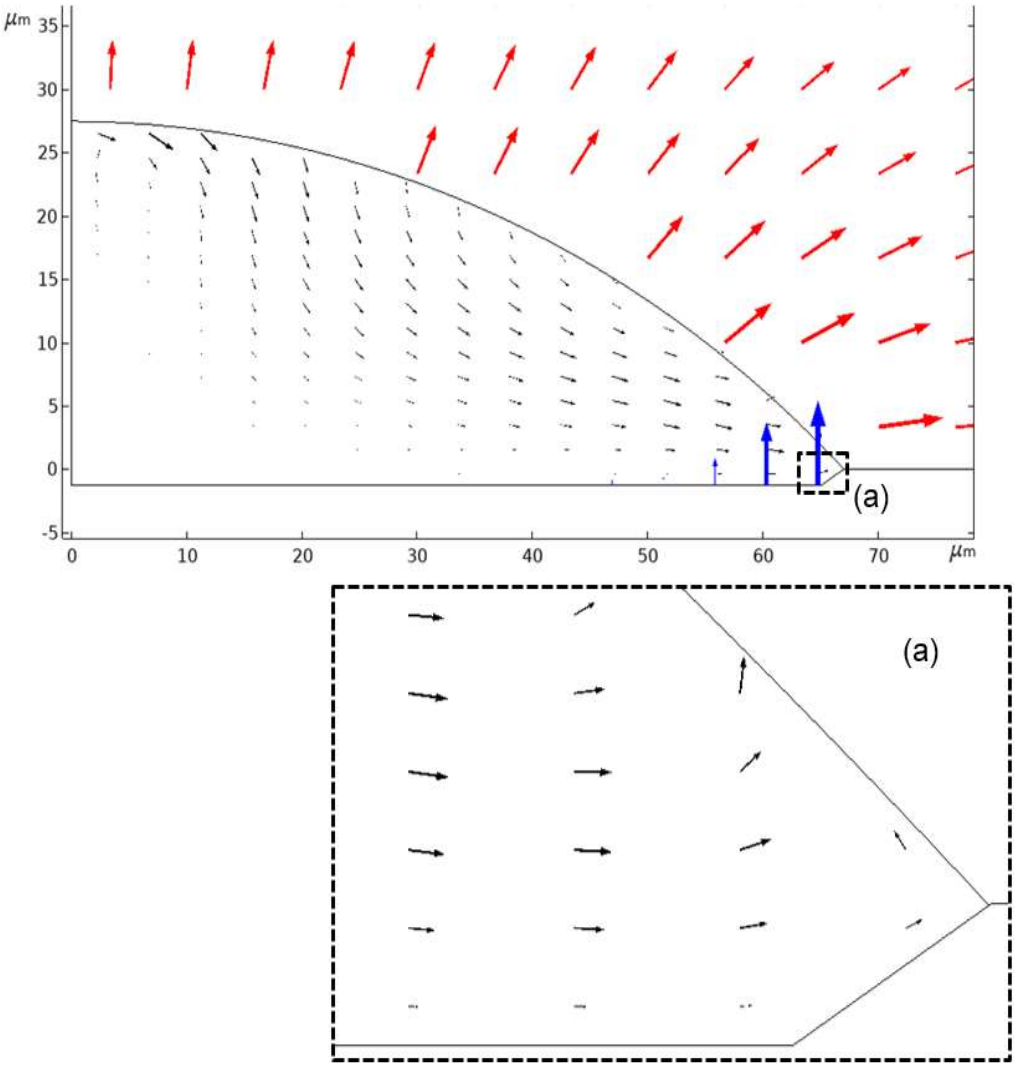

Figure 5.36: Plot of the velocity field in black, the evaporative flux in red and the heat flux from the substrate in blue for E=60 at t=0.0001s.

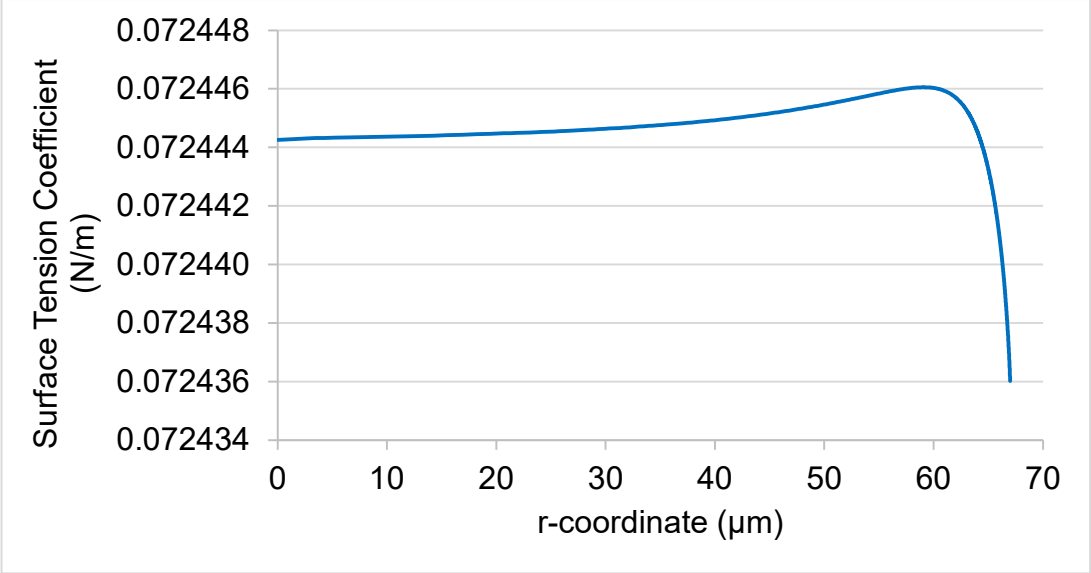

Figure 5.37: Plot of the surface tension coefficient for E=60 at t=0.0001s.

When the simulation reaches t=0.013s, the radial outwards flows are now entirely dominant over the thermocapillary flows, with strong flows towards the contact line throughout the droplet, as seen in Figures 5.38 - 5.40.

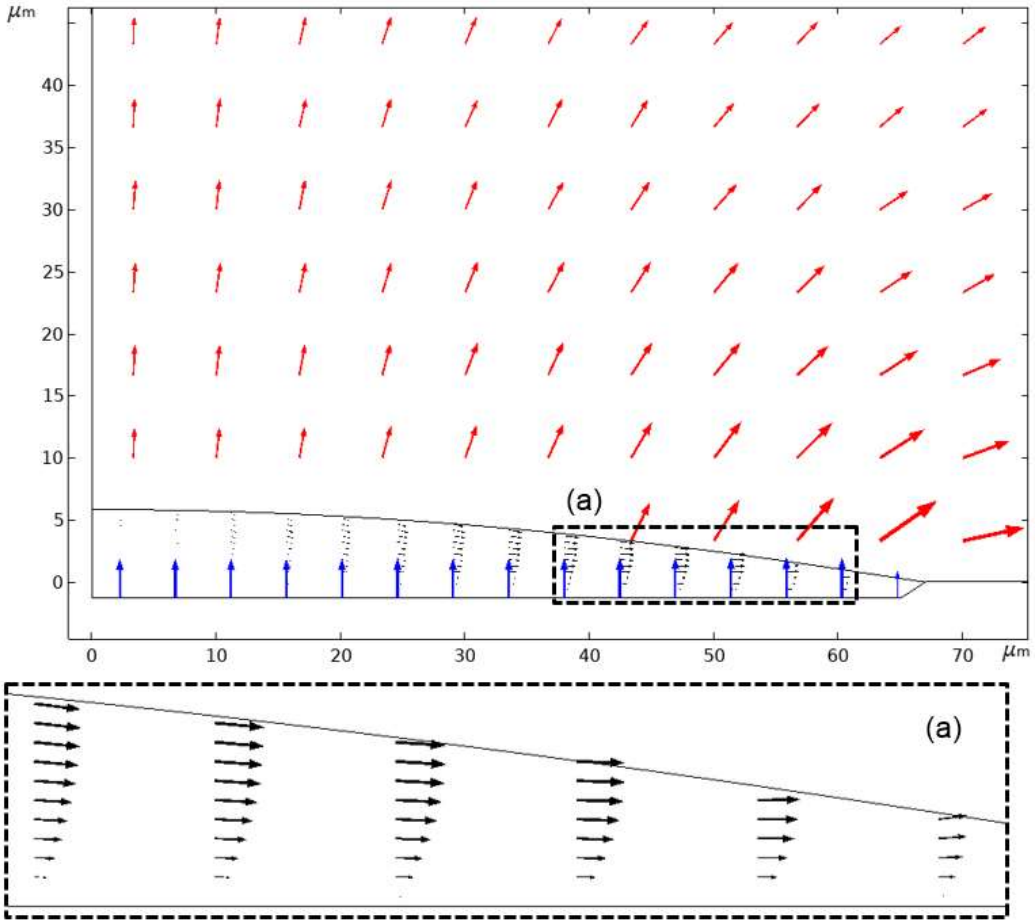

Figure 5.38: Plot of the velocity field in black, the evaporative flux in red and the heat flux from the substrate in blue for E=60 at t=0.013s.

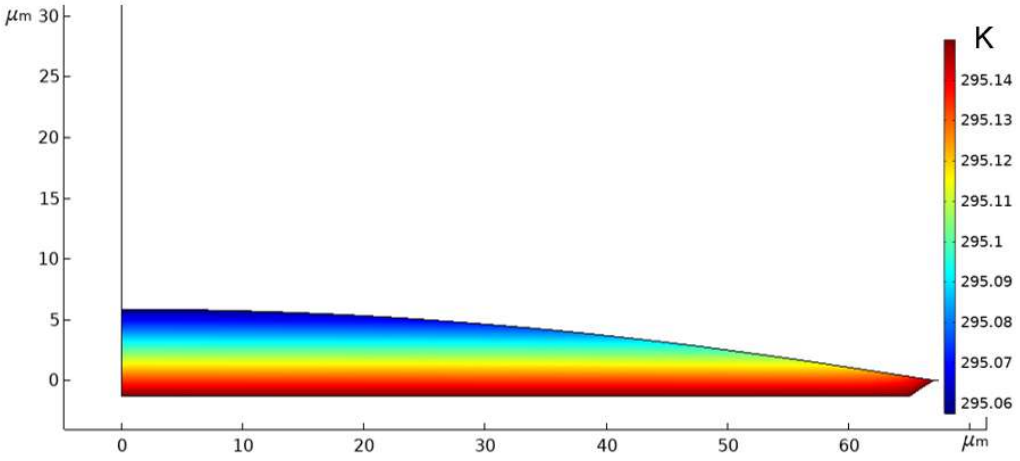

Figure 5.39: Plot of the temperature field for E=60 at t=0.013s.

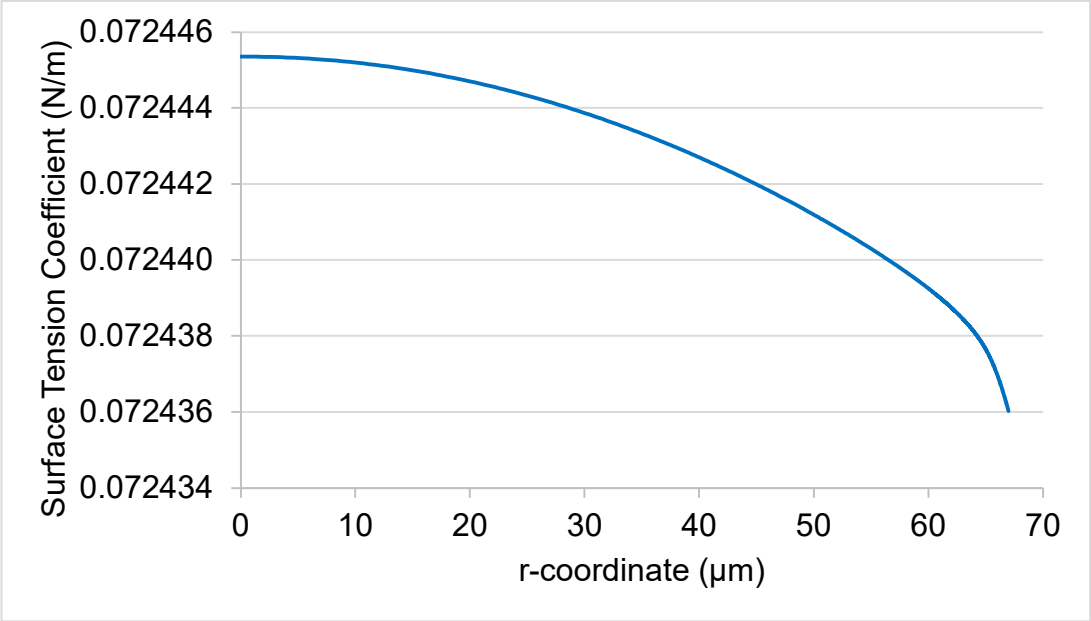

Figure 5.40: Plot of the surface tension coefficient for E=60 at t=0.013s.

The evaporation-driven outwards flows continue to dominate the thermocapillary flows as the droplet surface passes the top of the bank structure at t=0.017s, as seen in Figures 5.41 - 5.43, despite the heat transfer from the substrate now being much more effective in heating the droplet due to the high aspect ratio of the droplet at this time. A W-shaped profile was also beginning to develop.

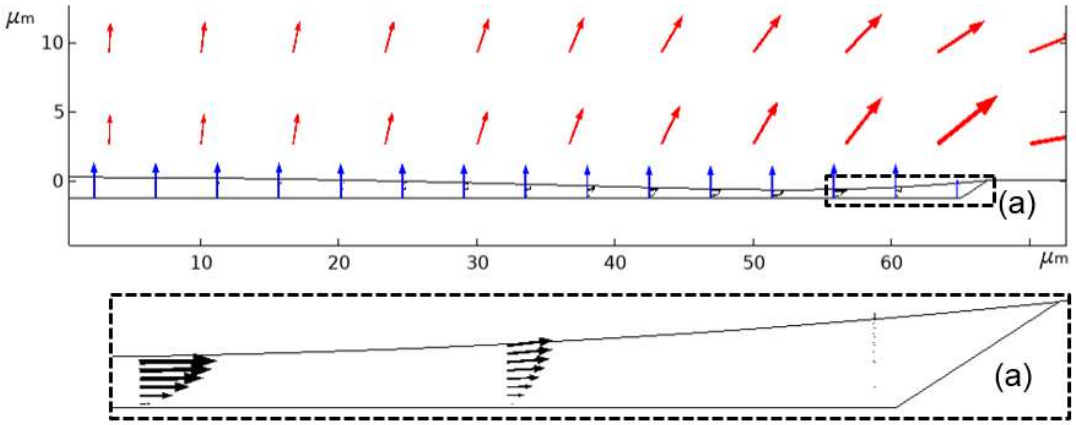

Figure 5.41: Plot of the velocity field in black, the evaporative flux in red and the heat flux from the substrate in blue for E=60 at t=0.017s.

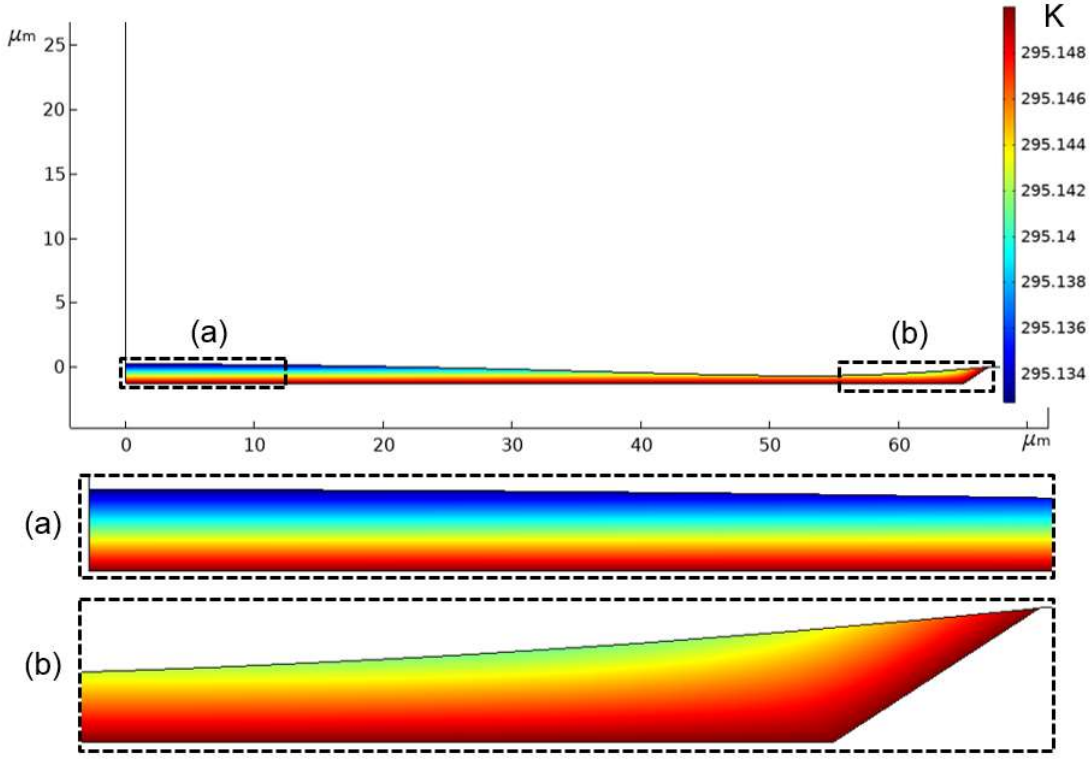

Figure 5.42: Plot of the temperature field for E=60 at t=0.017s.

Figure 5.43 shows that the higher temperature of the thinned intermediate region of the droplet reduces the surface tension in this region.

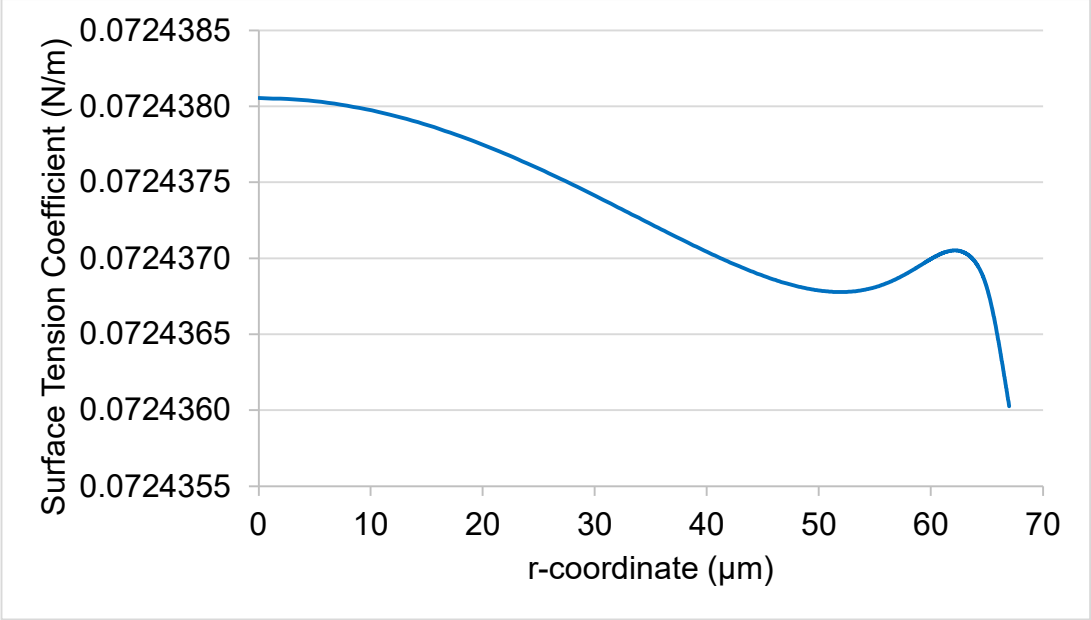

Figure 5.43: Plot of the surface tension coefficient for E=60 at t=0.017s.

As the droplet reached the touchdown point at t=0.0176s, there was a distinct W-shaped profile, caused by the drainage from the centre of the droplet not being sufficient to replenish the fluid lost to the atmosphere in the region approximately 50-60μm from the centre of the droplet, as seen in Figures 5.44 and 5.45. Near the contact line, the radial outwards flows reduced, allowing the thermocapillary effect induced by the substrate near the bank wall to generate a flow back towards the droplet centre, however this is not capable of preventing a W-shaped profiles as touchdown has already occurred.

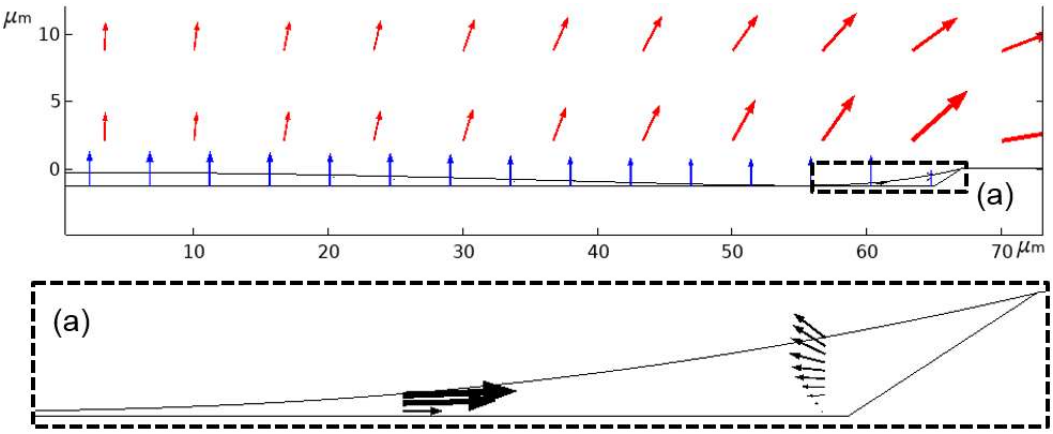

Figure 5.44: Plot of the velocity field in black, the evaporative flux in red and the heat flux from the substrate in blue for E=60 at t=0.0176s.

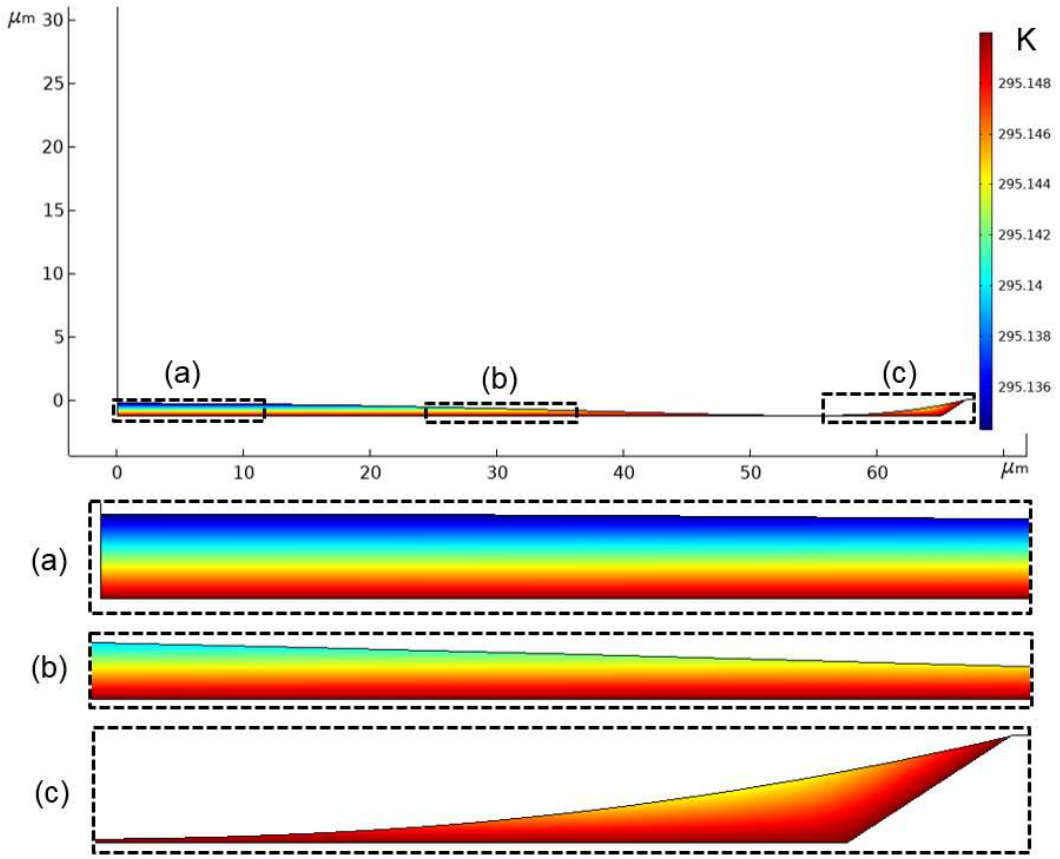

Figure 5.45: Plot of the temperature field for E=60 at t=0.0176s.

From the above analysis, it was shown that the thermocapillary effect has little effect on the final droplet profile with a heated substrate, as seen in Figure 5.23. This was due to the temperature difference across the droplet typically being in the range of 0.1 - 0.2K, which will not produce strong thermocapillary flows that can affect the shape of the free surface.

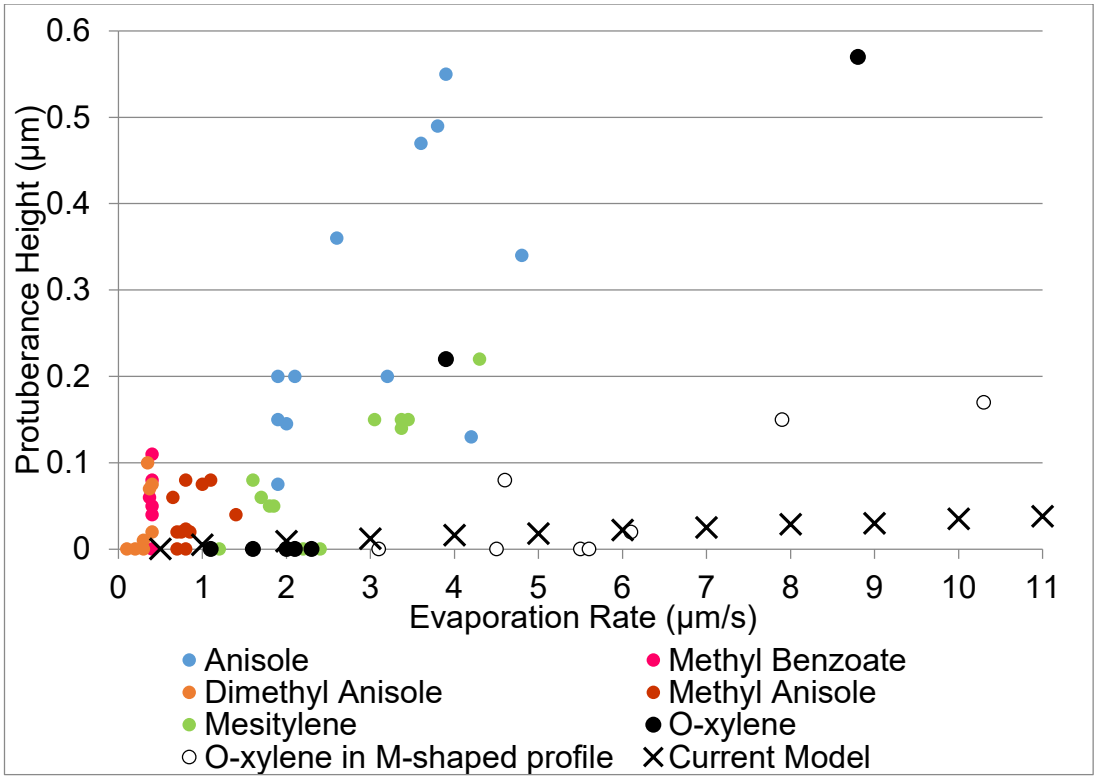

Figure 5.46: Plot of protuberance height against evaporation rate attained experimentally for various solvents [Kazmierski, 2018] and from the current model with temperature-dependent surface tension.

From Figure 5.46, it is clear that the increasing protuberance height with increasing evaporation rate from the current model has a similar trend to the o-xylene from experimental results by Kazmierski [2018], however the current model shows a near linear progression, whereas the experimental results show no such relationship. This may be due to the increased opportunity for inconsistencies in experimental work, as very small variations in temperature, solvent purity or debris on the substrate could affect results at such a small scale.

In addition, the equation used to determine the relationship between temperature and surface tension was attained experimentally for water, not the solvents listed above, and these would have to be inputted for each different solvent along with the gas phase vapour pressure (colloquialised in COMSOL as ‘humidity’). It is therefore required that a parametric study of this relationship be carried out in order to determine the effect this may have on final protuberance height, and therefore overall droplet profile, which was shown in Section 5.2.5. Other potential sources of error are the viscosity, which was set for water, and the constant temperature of the substrate at the

ambient temperature of the air. In reality, the substrate would cool slightly due to the lower temperature of the droplet.

5.2.6 Influence of Temperature-Dependent Surface Tension Variables

To study the effect of changing the relationship between temperature and surface tension, eq. (3.26) was again used in the form

$$\sigma = B\left[\frac{T_c - T}{T_c}\right]^{\mu}\left[1 + b\left(\frac{T_c - T}{T_c}\right)\right] \tag{3.26}$$

where values B = 0.2358N/m, b = -0.625, μ = 1.256 and T_c is a critical temperature of 647.15K. There is no physical meaning of B, b and μ, as they are values used to fit a curve to experimental data analysed to produce eq. (3.26). The initial temperature was set to be 295.15K.

For the first parametric sweep of surface tension, the B value was tested in the range of 0.001 to 0.95 with the effect this had on the surface tension and the resulting change in the protuberance height shown in Figure 5.47.

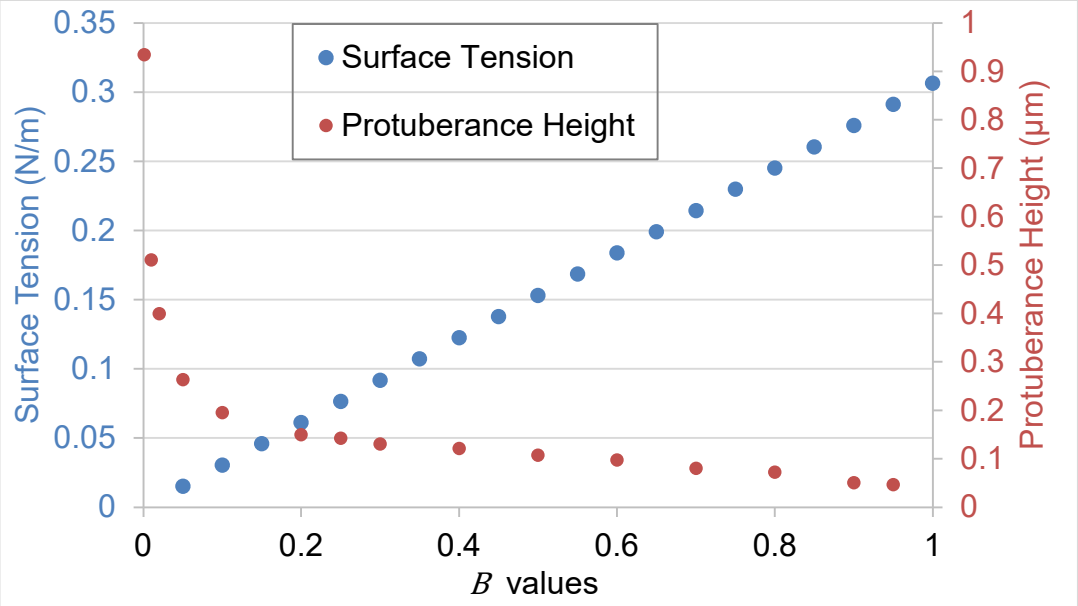

Figure 5.47: Plot of B values against surface tension and protuberance height.

The surface tension increased linearly with increasing B values, with the higher surface tension causing a lower protuberance height, as previously established in Section 5.2.3.

For the next parametric sweep, the b value was tested in the range of -1.83 to -0.01, and the impact this had on surface tension and protuberance height plotted in Figure 5.48. Any simulation with a b value less than -1.83 would not achieve touchdown due to excessive surface curvature.

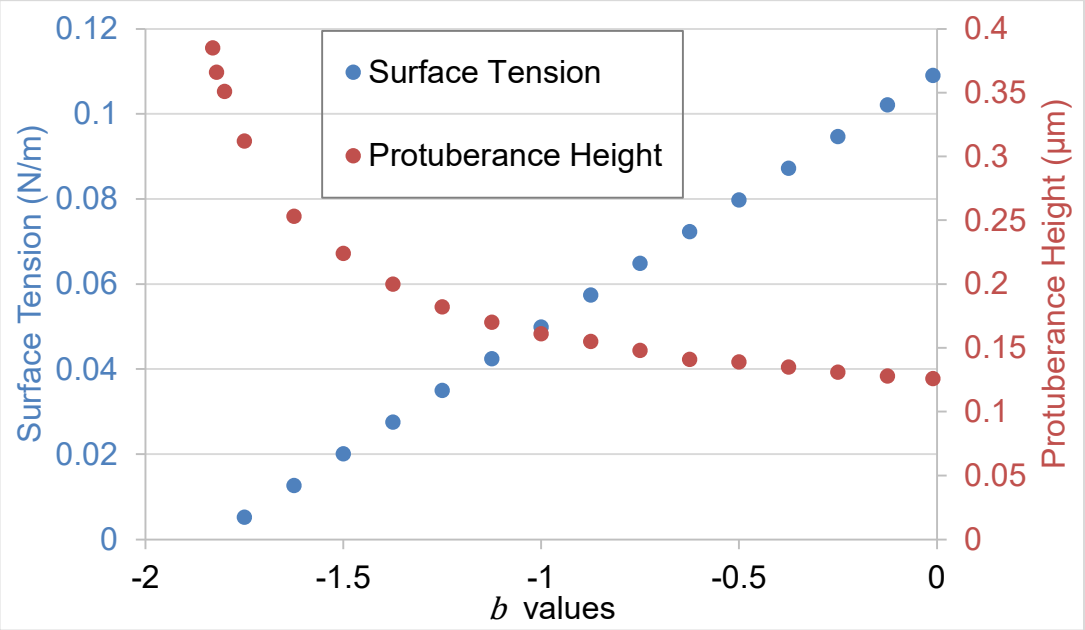

Figure 5.48: Plot of b values against surface tension and protuberance height.

As the value of b tends towards 0, the surface tension for a given temperature increases linearly, however this does not relate to a linear change in protuberance height, with decreasing b values producing a higher and higher protuberance in the centre of the droplet.

Next, the μ value was tested in the range of 0.1 to 10 and the results for surface tension and protuberance height plotted in Figure 5.49.

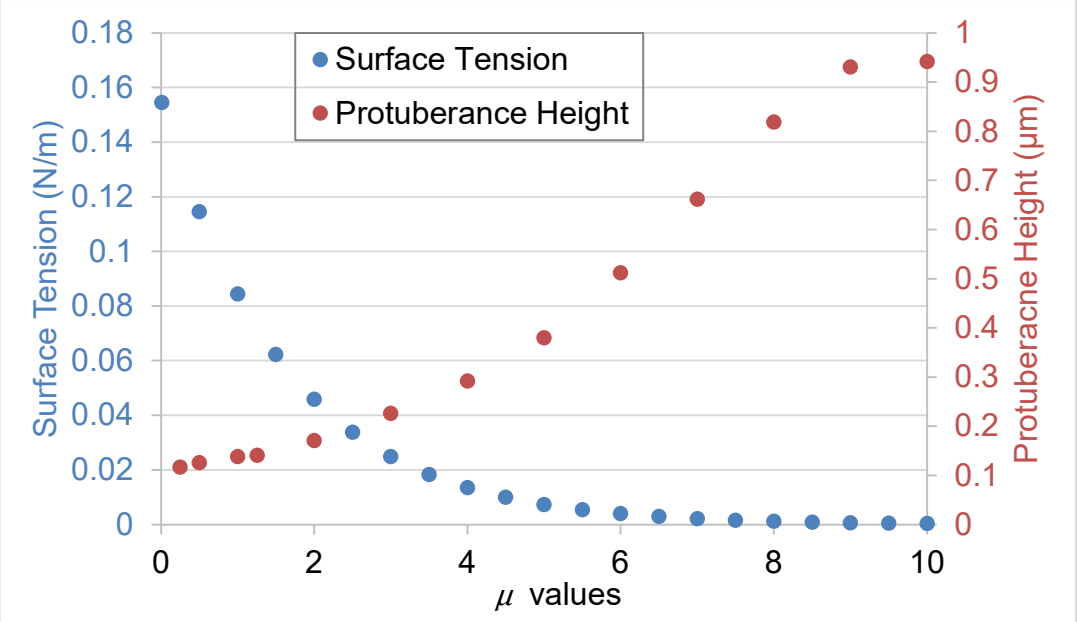

Figure 5.49: Plot of μ values against surface tension and protuberance height.

Increasing the μ value lead to increasingly lower surface tension and to an increase in protuberance height up to the maximum height achievable at 0.95µm at μ = 10.

Finally, the T_c value was tested in the range of 300K to 1000K and the results for surface tension and protuberance height plotted in Figure 5.50, which shows that as the T_c value increases, the surface tension increases, leading to a lower protuberance height

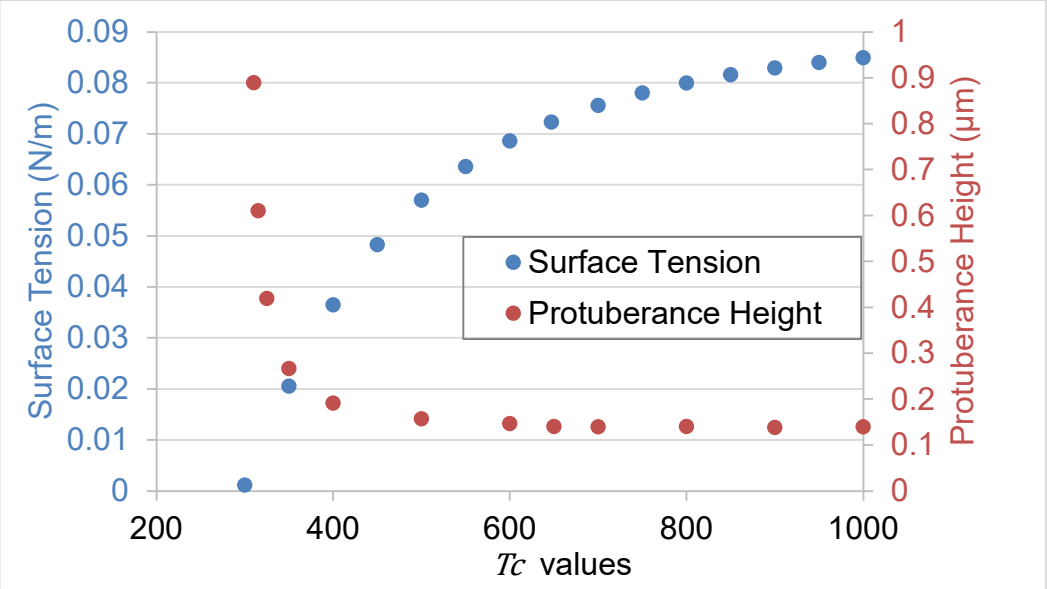

Figure 5.50: Plot of T_c values against surface tension and protuberance height.

This study has found that altering the parameters b, B, μ and Tc has a considerable effect on the surface tension and the final protuberance height, but no combination of these values was able to produce an M-shaped drying profile.

5.2.7 Effect of Surface Tension Gradient to Represent the Solutocapillary Effect

The model inputs were modified to artificially apply a surface tension that is low in the centre of the droplet and high near the contact line, in an attempt to produce an M-shaped profile. This would represent the potential effects of a solutocapillary effect occurring, which was identified by Kazmierski [2018] as the potential cause of the M-shaped profiles recorded experimentally.

The surface tension was determined by the equation

$$\sigma = \alpha(1 + r) \tag{5.1}$$

where α is an arbitrary surface tension value at the axis of symmetry (N/m) and r is the distance from the axis of symmetry (μm). All other parameters, such as evaporation rate and viscosity were set as for water at 22°C and a standard bank structure geometry for the Kazmierski [2018] study, with a radius of 67μm and a depth of 1.3μm. The surface tension values along the droplet surface are shown in Figure 5.51, with the corresponding droplet profiles shown in Figure 5.52. These values are purely. For investigative purposes, and are not intended to represent actual values produced by the solutocapillary effect.

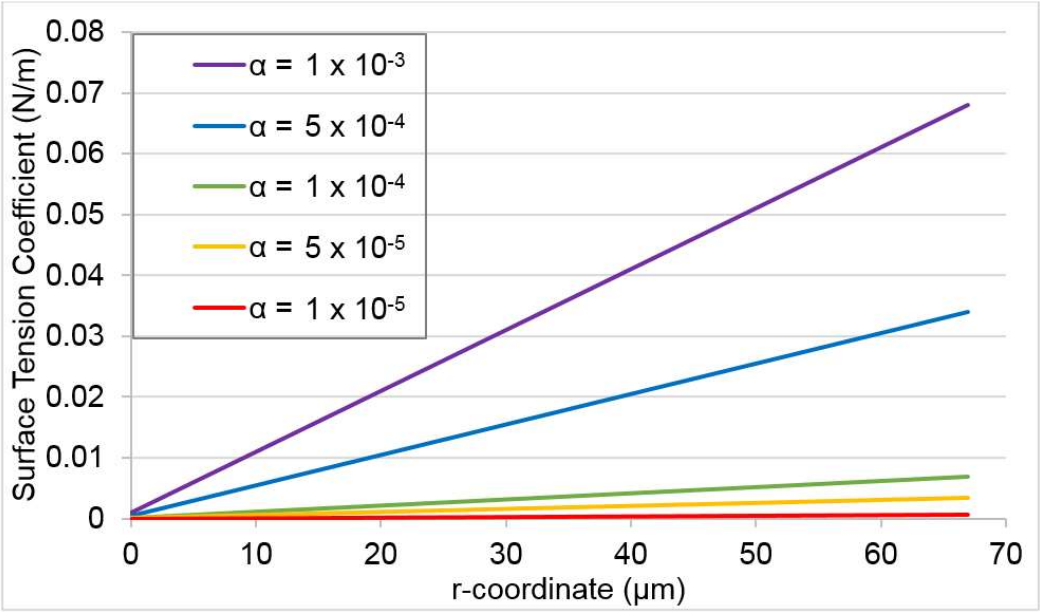

Figure 5.51: Plot of surface tension along the free surface at various α values.

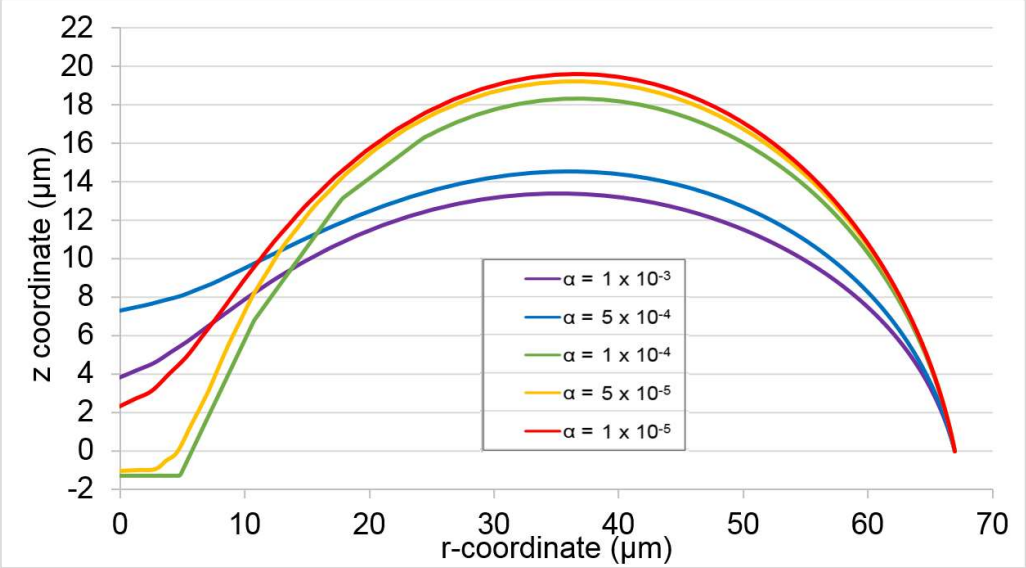

Figure 5.52: Plot of droplet profiles generated at various α values at final output.

The mechanism for the development of an M-shaped profile appears to be the extreme surface tension induced flows towards the contact line near the free surface. Figure 5.53 demonstrates the flow along the free surface for a model where α = 1 x 10^{-5}N/m in the very early stages of evaporation. The spatial frame is coloured green and the original droplet geometry remains shown throughout the plots to give reference for the changing profile shape.

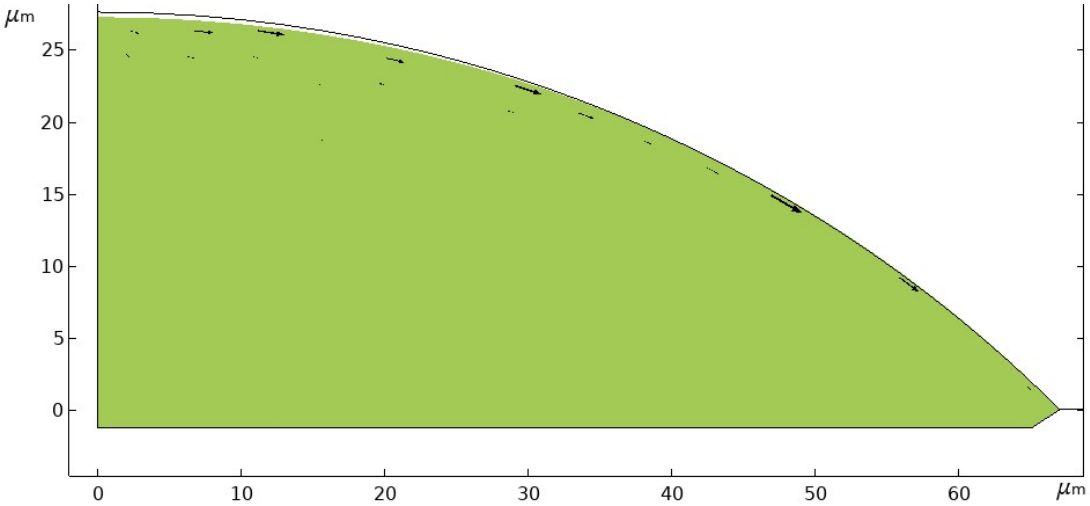

Figure 5.53: Plot of the velocity field for a droplet where α = 1 x 10^{-5}N/m at t=0.0001s.

As evaporation continues, shown in Figure 5.54, this rapid outwards flow causes the droplet to begin to 'bow' out of the original droplet shape as the low surface tension at the centre of the droplet cannot maintain a spherical cap.

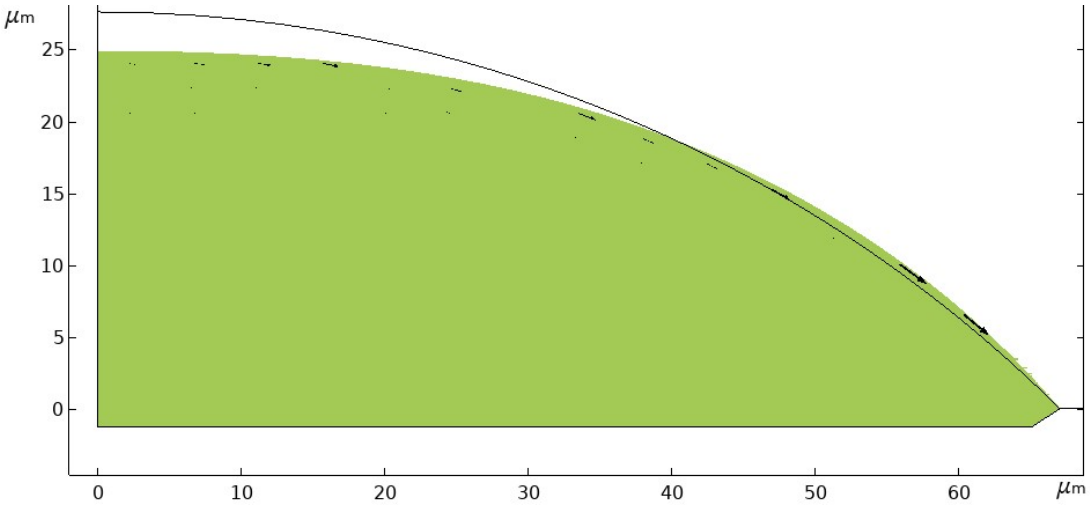

Figure 5.54: Plot of the velocity field for a droplet where α = 1 x 10^{-5}N/m at t=0.0003s.

The flow starts recirculating towards the centre of the droplet soon after this, as shown in Figure 5.55, but it is insufficient to recover the spherical cap in light of the extreme surface tension gradient.

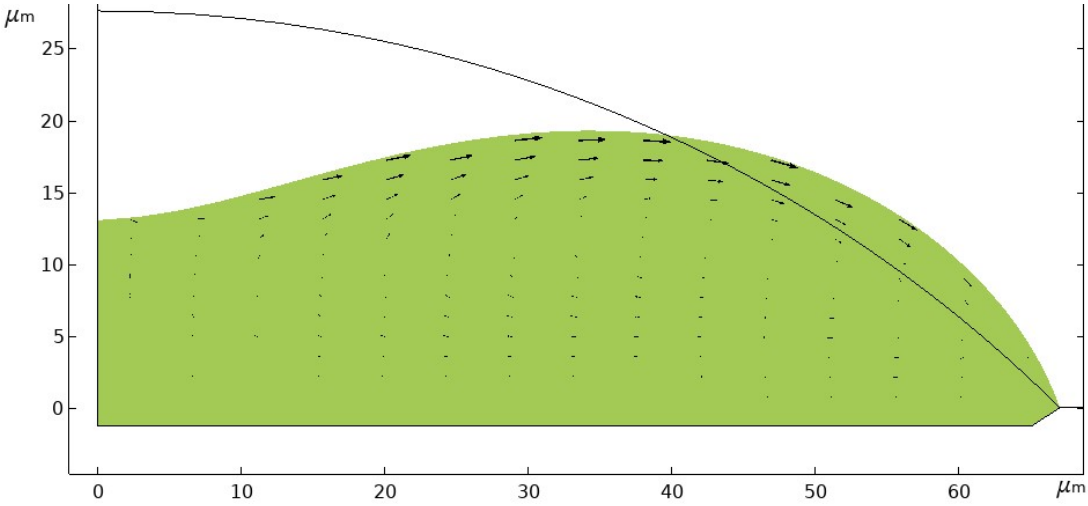

Figure 5.55: Plot of the velocity field for a droplet where α = 1 x 10^{-5}N/m at t=0.001s.

This flow pattern continues until the end of the simulation, with the profile achieving a more pronounced M-shape until the free surface curvature is too great for the computational mesh, as seen in Figure 5.56.

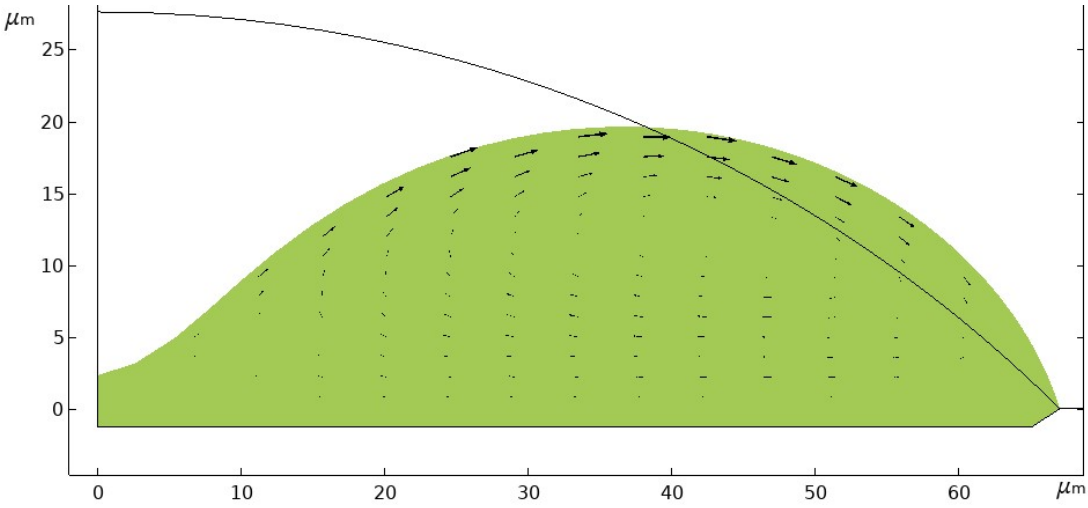

Figure 5.56: Plot of the velocity field for a droplet where α = 1 x 10^{-5}N/m at t=0.003s.

This series of simulations suggests that the theory proposed by Kazmierski [2018] that the intermittent M-shaped profiles were potentially caused by solutocapillary effects induced by contamination of the solvent is indeed plausible.

However, a more detailed model incorporating a binary liquid droplet and the accompanying effects this would have on surface tension, viscosity and

other parameters would be needed to definitively prove this notion. Such a model is outside the scope of this study.

5.3 Effects of Bank Structure Depth, Aspect Ratio and Angle

Now that the influence of evaporation rate, surface tension, thermocapillary effects and viscosity on drying profiles have been addressed, the focus of this work will now shift to the bank structure itself. Kazmierski [2018] noted several effects of well shapes on drying profiles and so this area of interest will now be expanded to cover both the depth and angle of the bank itself.

5.3.1 Bank Depth

To study the effect of changing the bank depth on the drying profile of the droplet, a series of simulations were run for bank depths ranging from 0.25µm to 5µm, all with a bank angle of 45°, at a radius of 67µm. All other parameters, such as evaporation rate, viscosity and surface tension were set as for water at 22°C. The final profiles of the droplets are shown in Figure 5.57, with the protuberance height plotted against bank depth inn Figure 5.58.

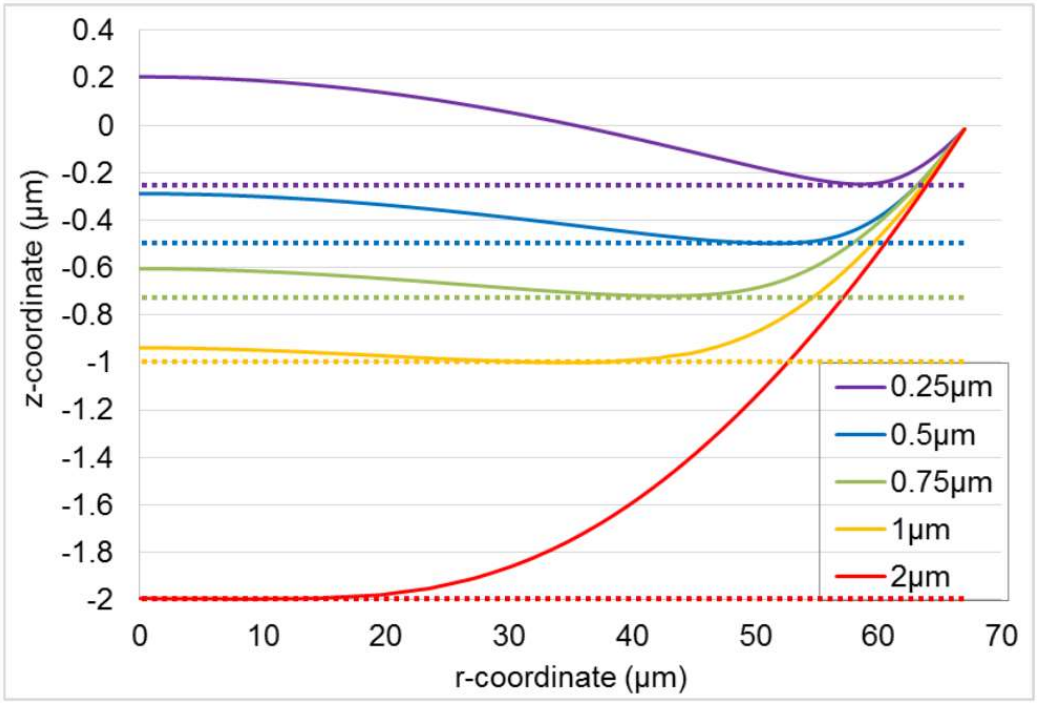

Figure 5.57: Plot of droplet drying profiles at final output for various bank depths at final output, with the respective bank depth marked with a dotted line.

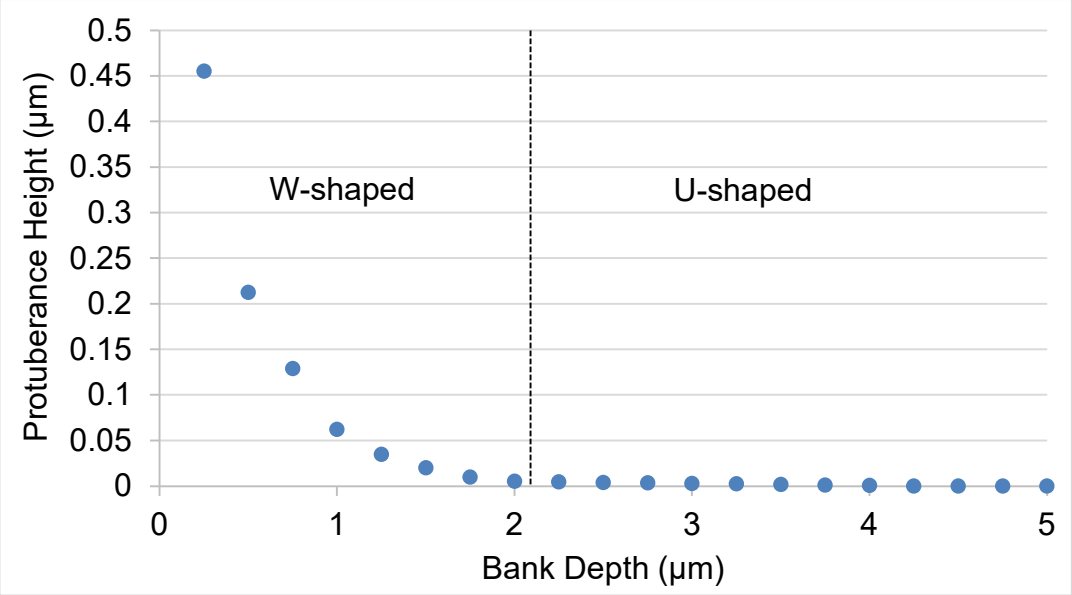

Figure 5.58: Plot of protuberance height at final output for various bank depths.

At bank depths greater than 2μm, only U-shaped profiles are seen, due to the depth allowing flow through the intermediate region of the droplet towards the contact line. As the free surface travels through this greater distance, there is never a time where the outwards flow is inhibited, and therefore a W-shaped profile cannot develop.

Banks of depth less than 2μm do produce W-shaped profiles, as the free surface approaches the substrate before the liquid in the centre can pass through the intermediate region, and is therefore trapped in a central protuberance.

5.3.2 Aspect Ratio

As the bank depth clearly has a substantial effect on the drying profile of the droplet, an investigation into the aspect ratio of the bank was performed. This will generate more general findings that can be applied to different droplet sizes, not only those with a radius of 67μm.

In order to investigate the impact of the aspect ratio, the bank depth was kept constant at 2μm, as this seemed to be a transition point between U- and W-shaped profiles at a radius of 67μm, and the well radius was varied from 20μm to 400μm. The bank angle remained at 45° and all other parameters, such as evaporation rate, viscosity and surface tension were set as for water at 22°C. The aspect ratio was calculated as the bank width divided by the depth (2μm).

It is very clear from Figure 5.59 that as the aspect ratio increases, as does the protuberance height, with the transition from U- to W-shaped profiles occurring at an aspect ratio of 30. This equates to a bank depth of 2.23μm for a bank radius of 67μm, which matches the data in Figure 5.58.

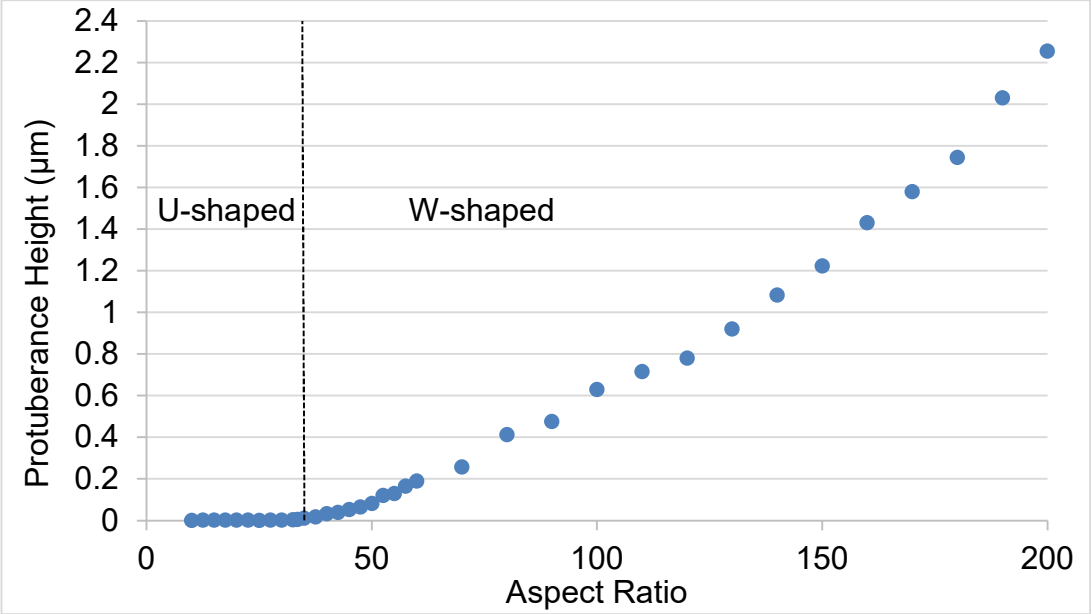

Figure 5.59: Plot of protuberance height at final output for various bank aspect ratios.

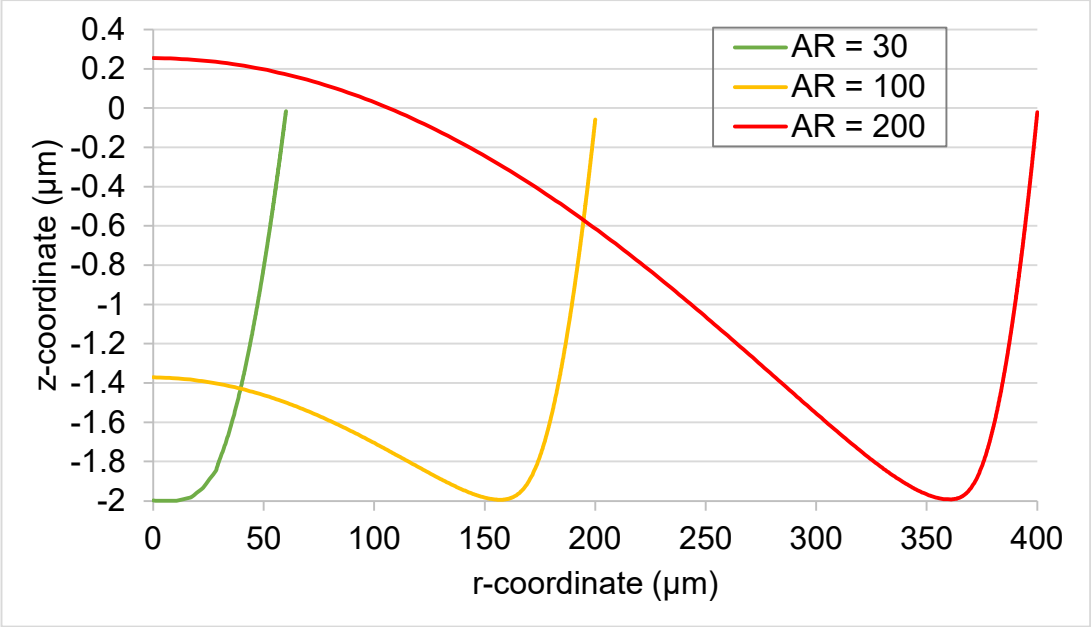

Figure 5.60: Plot of droplet drying profiles at final output for various bank aspect ratios.

Figure 5.60 clearly indicates the effect of increasing the aspect ratio on protuberance height. In a high aspect ratio well, the distance the liquid has to travel from the centre of the droplet to the bank wall is simply too far, leading to a loss of liquid from the intermediate region that cannot be sustained by flow from the centre, leading to a W-shaped profile and touchdown, as shown in Figure 5.61.

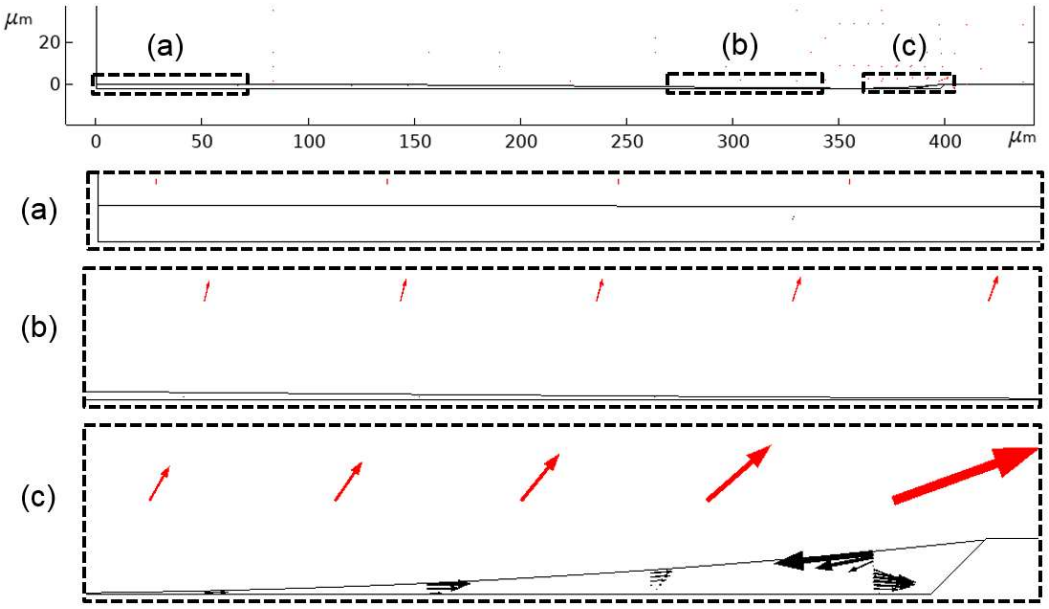

Figure 5.61: Plot of the velocity field in black and the evaporative flux in red for an aspect ratio of 200 at touchdown.

This section has shown that increasing the aspect ratio, increases the likelihood of generating a W-shaped profile, with a critical aspect ratio of around 30.

5.3.3 Bank Angle

To study the effect of changing the bank angle on the drying profile of the droplet, a series of tests were conducted on bank angles ranging from 5° to 55°, all at a bank depth of 2μm. The bank angle was defined as shown in Figure 5.62. All other parameters, such as evaporation rate, viscosity and surface tension were set as for water at 22°C.

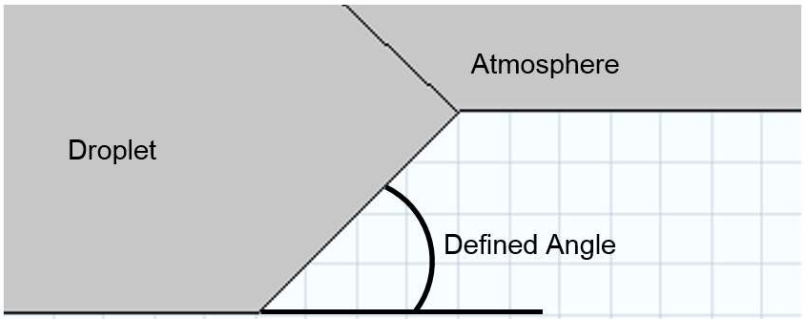

Figure 5.62: Schematic diagram showing the definition of the bank angle.

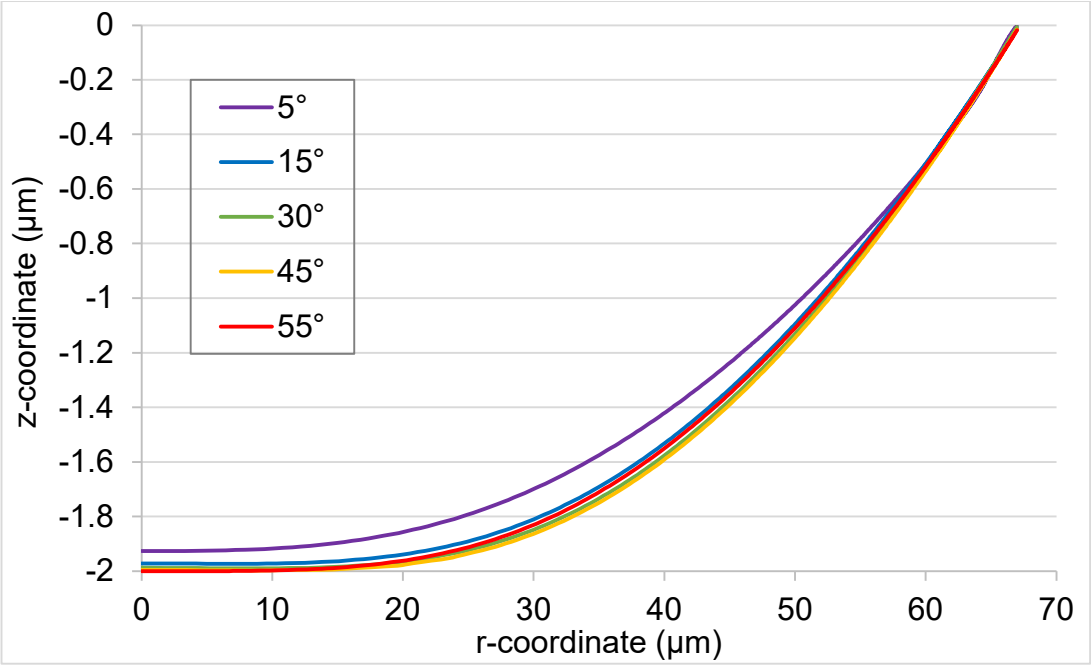

Figure 5.63: Plot of droplet drying profiles at various bank angles.

From Figures 5.63 and 5.64, it is clear that the angle of the bank has very little effect on the final height, with angles of 20° to 55° generating very similar protuberance heights, all within a 0.02µm range. All bank angles showed U-shaped profiles, showing that profile shape is much more dependent on the depth of the bank than the angle.

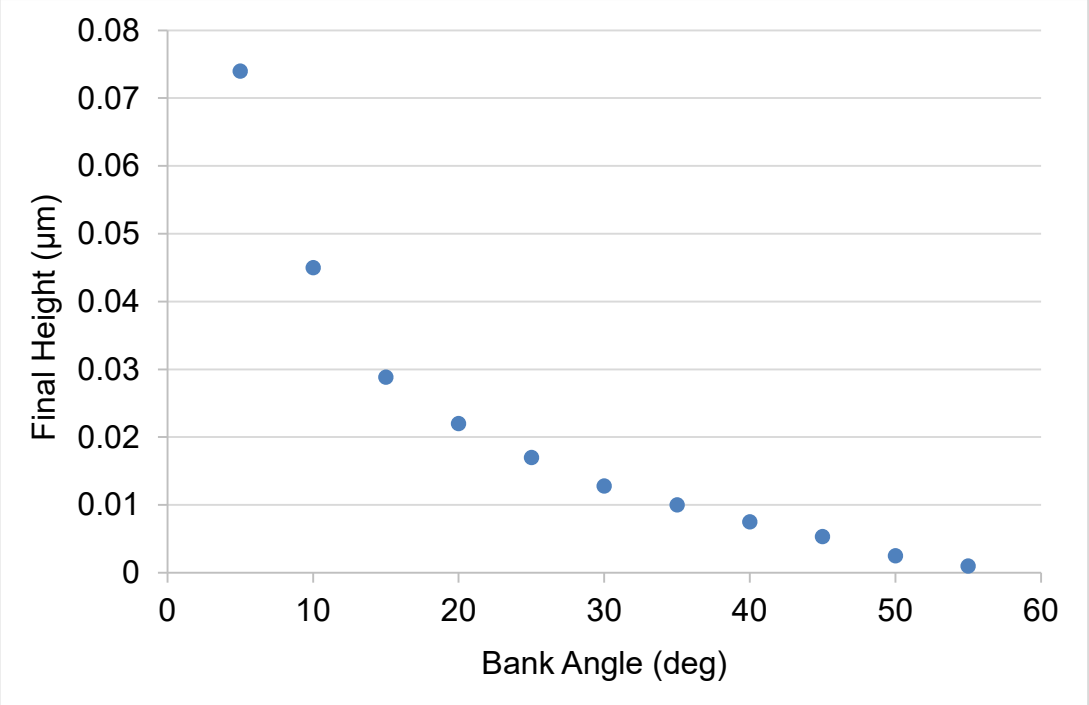

Figure 5.64: Plot of height at final output for various bank angles.

The final height for a bank angle of 5° was considerably higher than the others due to the very shallow angle causing the droplet surface to touchdown on the bank wall rather than at the bottom of the well, leading to the simulation failing and a U-shaped profile being shown.

Simulations of bank angles greater than 55° did not achieve touchdown due to the distortion of the computational mesh at the contact line.

5.4 Investigation of Curved Bank Structures

This section will investigate the impact on drying profile of more complex, curved bank structures, as these more closely resemble the actual banks used in OLED manufacture.

5.4.1 Simple Curved Bank Structures

As an introduction to curved bank structures, a simple curve was added in place of the straight bank wall, as shown in Figure 5.65. This curve was a 90° arc of the same radius as the bank depth. The contact point was positioned just below the top of the bank structure to reduce meshing errors in this region. Bank depths in the range 0.25μm to 5μm were tested at a droplet radius of 67μm, and as before all other parameters were for water at 22°C.

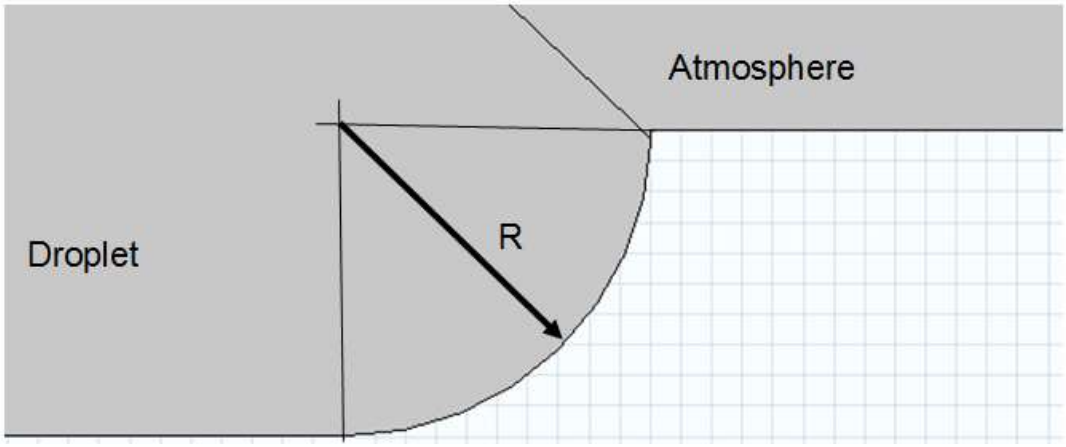

Figure 5.65: Schematic diagram of the geometry of a curved bank structure, where R is the bank depth.

Figures 5.66 and 6.67 show that the impact of having a simple curved, rather than a straight, bank structure on the final profile of the droplet is slight. The protuberance height for a given bank depth is marginally higher for a curved bank structure, but only by approximately 0.02μm, and so can be considered negligible when compared to the impact of the bank depth on droplet profile.

As with the straight bank walls, any bank depth greater than 2μm produced U-shaped profiles, with banks less than 2μm deep generating W-shaped profiles.

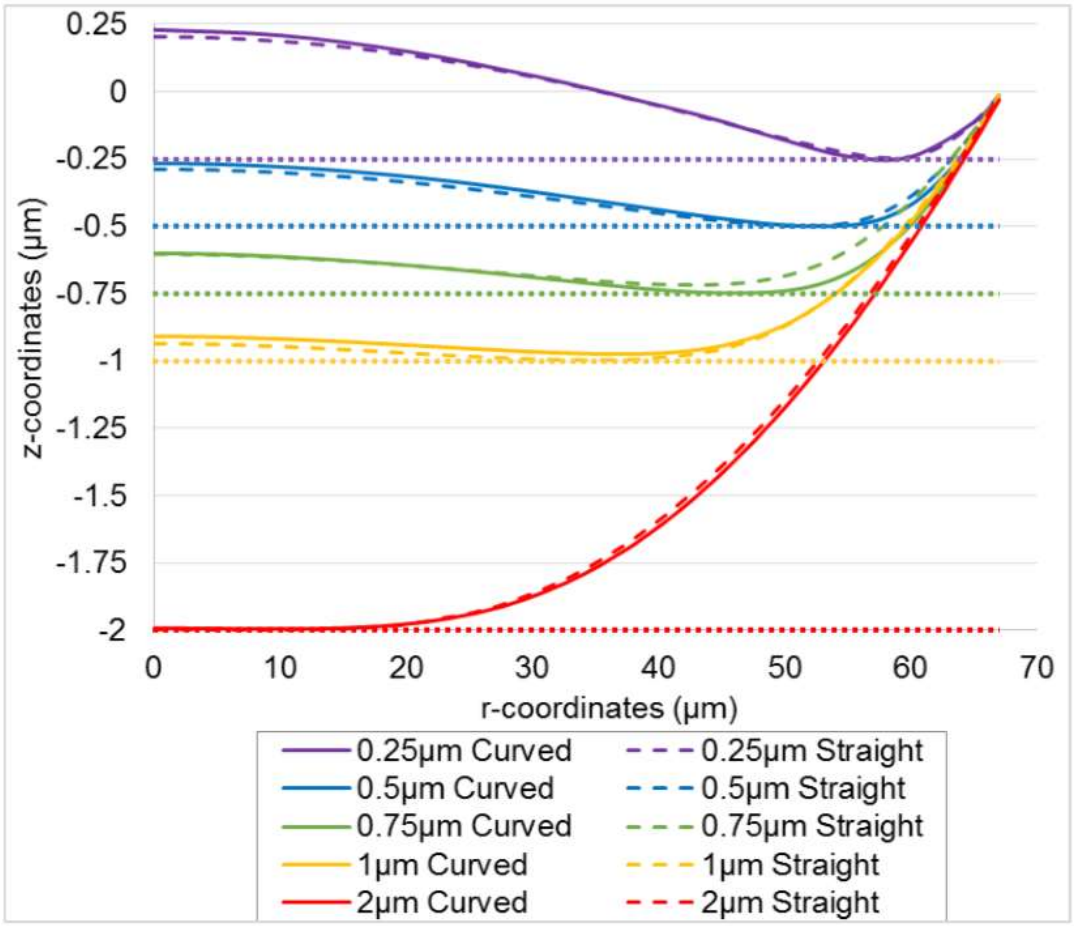

Figure 5.66: Plot of droplet drying profiles in various curved banks, with the respective bank depth marked with a dotted line.

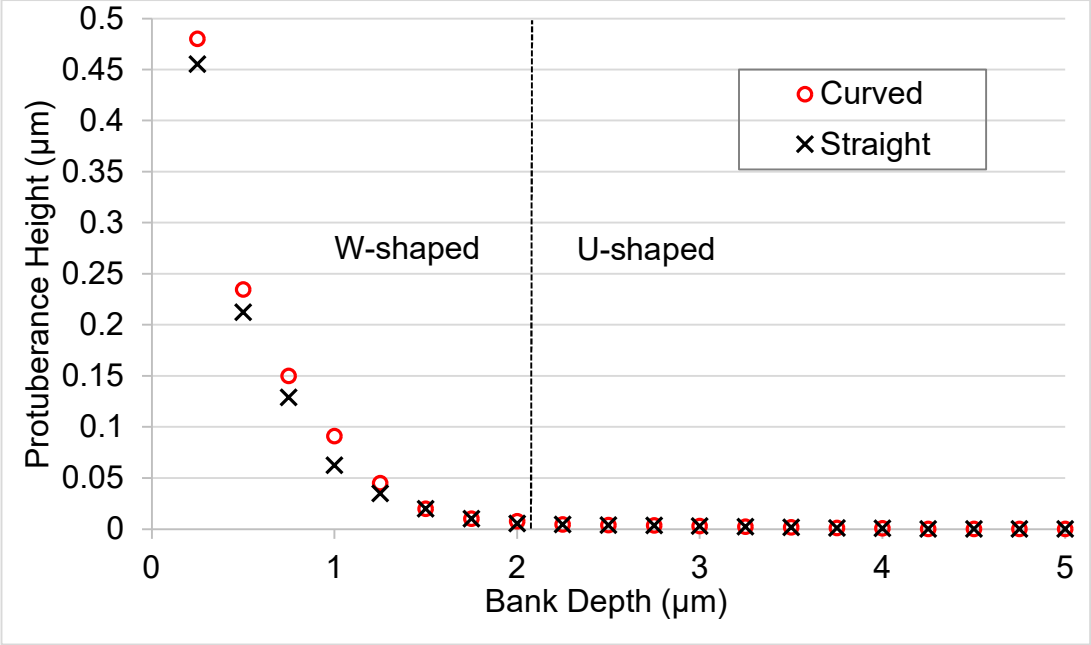

Figure 5.67: Plot of protuberance height at various bank depths for straight and curved banks.

This section has shown that the inclusion of a simple curved bank structure has little effect on the bank depth at which there is a transition from W- to U-shaped profiles or the protuberance height produced at a given bank depth.

5.4.2 'S-shaped' Bank Structures

This section will expand on the previous work done on simple curved bank structures to now include more complex 'S-shaped' banks more similar to those actually used in OLED production, as seen in Figure 5.68. The contact point was established approximately half way around the top curve, as this allowed for the greatest range of motion for the droplet surface to travel through whilst allowing the top curve to influence the drying profile. The change in contact point location in the z-direction is clearly visible in Figure 5.69.

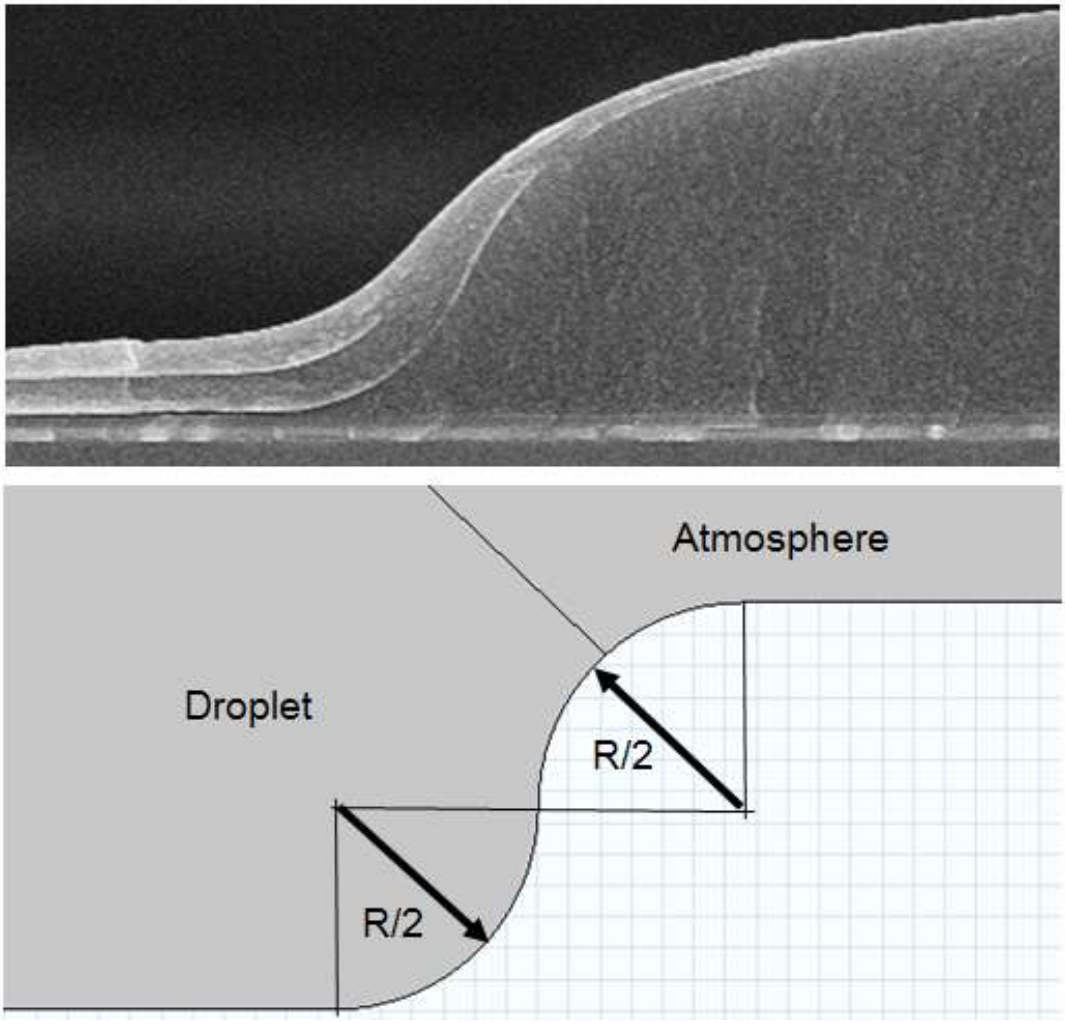

Figure 5.68: Comparison of an actual OLED bank structure [Tan, 2016] and the modelled geometry of an S-shaped bank structure, where R is the bank depth.

As can be seen in Figure 5.69, the S-shaped bank structure causes the droplet profile to remain closer to the base of the well for a greater proportion of the droplet radius than the straight bank walls. This translates to a lesser protuberance heights at deeper well depths, as shown in Figure 5.70.

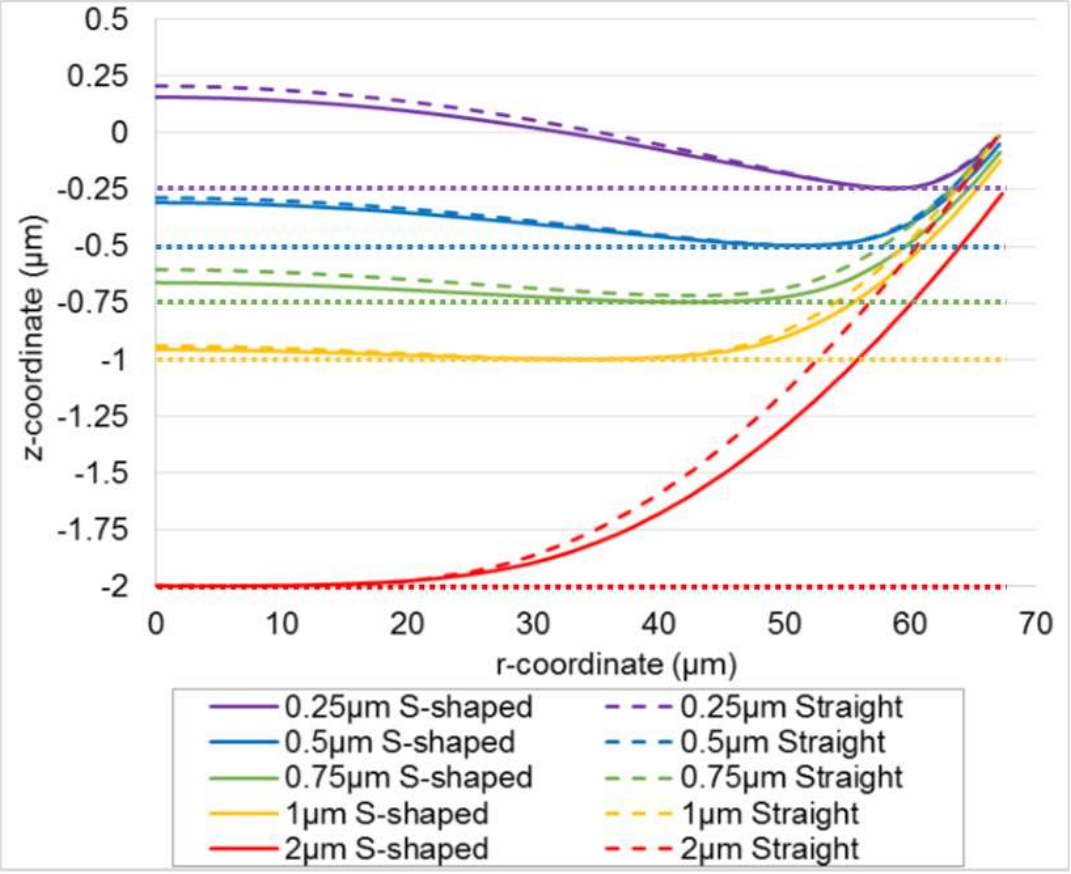

Figure 5.69: Plot of droplet drying profiles at various bank depths with an 'S-shaped' bank structure, with the respective bank depth marked with a dotted line.

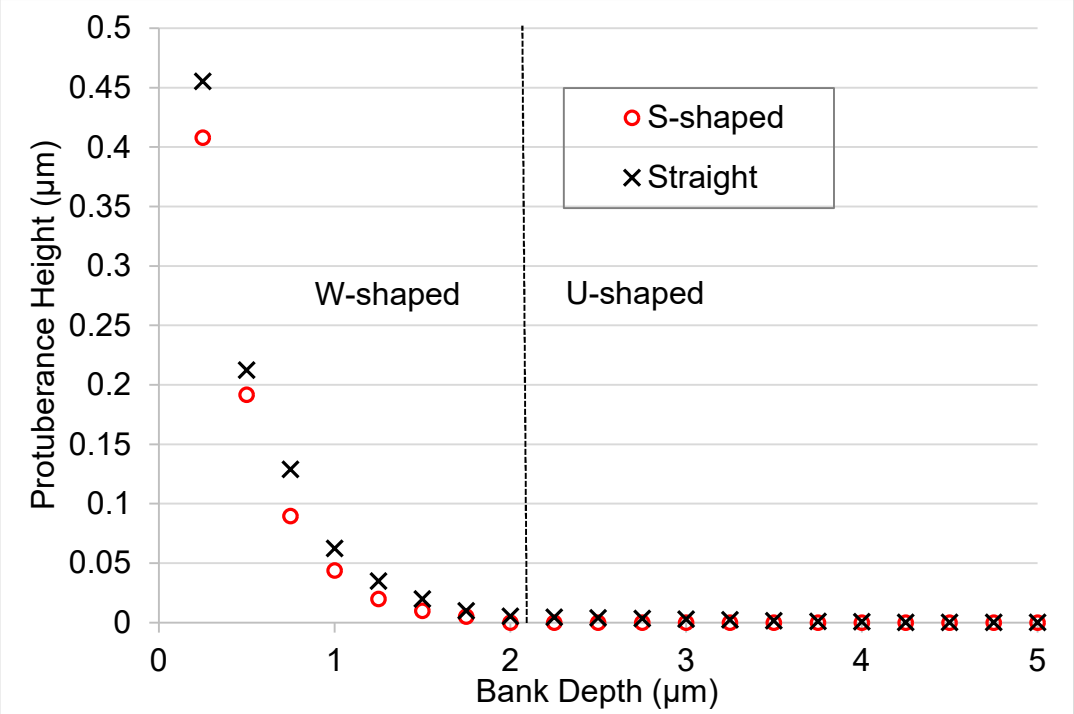

Figure 5.70: Plot of protuberance height at various bank depths for straight and 'S-shaped' banks.

For comparison against the results gathered for Section 5.3.2, an investigation in to the aspect ratio of the well was conducted for an S-shaped bank structure. The depth of the bank was set to be 2µm below the intersection of the free surface and the mid-point of the upper curve of the S-shaped wall, as seen in Figure 5.68, with the radius of the bank being altered to change the overall aspect ratio. All parameters, such as evaporation rate, viscosity and surface tension were set as for water at 22°C.

The protuberance height at the final output for the S-shaped bank structure is plotted against the results from Section 5.3.2 for a straight-sided bank structure in Figure 5.71, with the S-shaped banks clearly producing a lower protuberance height at the same aspect ratio, which corresponds to less pronounced W-shaped profiles, as seen in Figure 5.72.

Despite producing lower protuberance heights at equivalent aspect ratios, the critical aspect ratio for the transition from U- to W-shaped profiles remains the same at 30. This suggests that this is a value that is independent of the bank structure shape, and that the shape of the walls only effect the severity of the W-shape rather than whether or not it occurs.

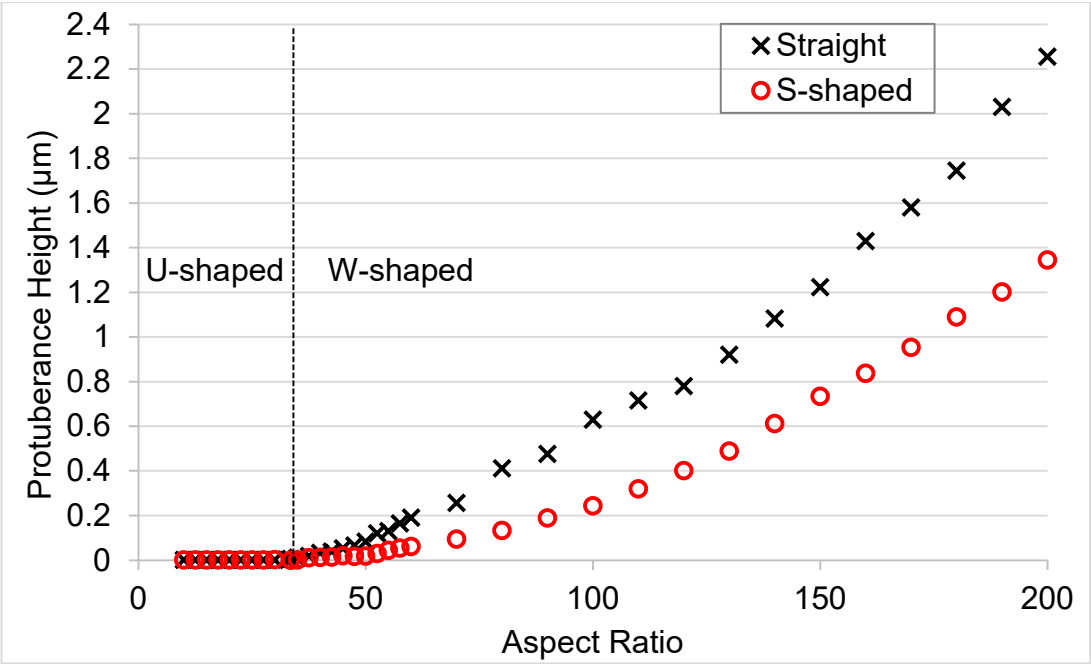

Figure 5.71: Plot of protuberance height at final output for various bank aspect ratios for S-shaped and straight bank structures.

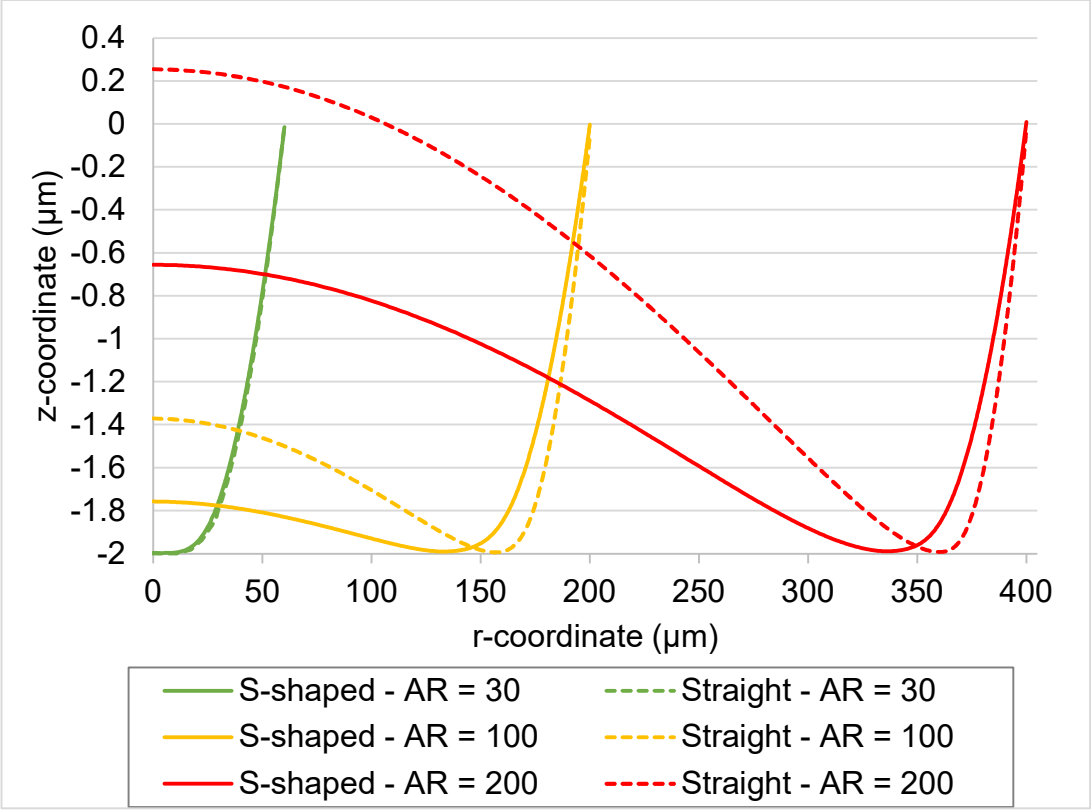

Figure 5.72: Plot of droplet drying profiles at final output for various bank aspect ratios for S-shaped and straight bank structures.

This section has shown that S-shaped banks will produce lower protuberance heights at a given bank depth or aspect ratio than a straight bank, therefore representing an advantage for the use in OLED applications where the protuberance height should be minimised as far as possible. In addition, it was found that the critical aspect ratio for the transition from a U- to a W-shaped profile remains at 30, the same as the straight bank structure. This suggests that the bank shape has far less effect on whether a droplet develops a W-shaped profile than the aspect ratio.

5.5 Conclusions

This chapter began by demonstrating that the current model is broadly capable of replicating the experimental results generated by Kazmierski [2018]. There were issues with the experimental data containing asymmetric droplet profiles, data only recorded at set times and not at touchdown, and the use of overly thick lines in the images which could potentially lead to inaccurate readings, however the general trend for all solvents modelled was clear: increasing evaporation rate leads to increasing protuberance height.

This chapter has also covered a wide range of factors that affect the drying profile of a droplet in a bank structure, and has found some interesting conclusions with regard to mitigating the formation of a central protuberance. A droplet has a high likelihood of generating a U-shaped profile under one or more of the following conditions:

- Low evaporation rate, below approximately 2μm/s.
- High surface tension, above approximately 0.07N/m.
- Low viscosity, below approximately 0.001Pa.s.
- An aspect ratio of the well of less than 30 for straight or S-shaped bank structures.

Clearly, no liquid exists with all these properties and an OLED pixel well should be as shallow as possible to allow light to pass through with as little distortion as possible.

Despite this, it seems reasonable to recommend that OLED solutions should be deposited in wells with S-shaped banks, as this provides the lowest protuberance height at typical OLED pixel well geometries, and the slower the solvent is evaporated away, the less likely a W-shaped profile is to occur, as the drainage from the intermediate region should be sufficient for a U-shaped profile to be maintained.

Of these considerations, the evaporation rate is by far the most important factor for generating a U- or W-shaped profile, followed by the aspect ratio of the well.

When the surface tension was set to be artificially low at the centre of the droplet and high near the contact line the model was able to generate an M-shaped profile, suggesting that the results showing M-shaped profiles in experimental work by Kazmierski [2018] could have been caused by a solutocapillary effect between the solvent and some unknown contaminant.

Chapter 6:
Effect of Concentration-Dependent Viscosity

6.1 Introduction

As a solvent containing OLED material evaporates away, the concentration of the suspended material will increase, thereby increasing the viscosity of the solution and eventually leading to the fluid becoming immobile, where the viscosity becomes sufficiently high to resist fluid flow, as well as the evaporation rate decreasing considerably.

This chapter will aim to incorporate concentration-dependent viscosity into the current model to determine the effect on the droplet drying profile.

The computational model is the same as that described in Chapter 3, but with an enhanced treatment of the viscosity described in Section 6.2.

6.2 Modelling Methodology

Modelling the increasing viscosity of the droplet as the concentration of solute increased was based upon the inclusion of the mixture-averaged diffusion equations

$$\rho \frac{\partial \omega_i}{\partial t} + \nabla \cdot \mathbf{j}_i + \rho(\mathbf{u} \cdot \nabla)\omega_i = R_i \tag{6.1}$$

$$\mathbf{j}_i = -\left(\rho D_i^m \nabla \omega_i + \rho \omega_i D_i^m \frac{\nabla M_n}{M_n} - \mathbf{j}_{c,i} + D_i^T \frac{\nabla T}{T}\right) \tag{6.2}$$

$$D_i^m = \frac{1 - \omega_i}{\sum_{k \neq i} \frac{x_k}{D_{ik}}} \tag{6.3}$$

$$M_n = \left(\sum_i \frac{\omega_i}{M_i}\right)^{-1} \tag{6.4}$$

$$\mathbf{j}_{c,i} = \rho \omega_i \sum_k \frac{M_i}{M_n} D_k^m \nabla x_k \tag{6.5}$$

where $\mathbf{j_i}$ (kg/(m^2.s)) is the mass flux relative to the mass averaged velocity, $\mathbf{u}$ (m/s) is the mass averaged velocity of the mixture, ω_i is the mass fraction of species i, R_i (kg/(m^3.s)) is the rate expression describing the production or consumption of species i, D_i^m and D_k^m are the mixture-averaged diffusion coefficients for species i and k, M_n (kg/mol) is the mean molar mass of the mixture, M_i (kg/mol) is the molar mass of species i, D_i^T (kg/m.s) is the thermal diffusion coefficient of species i, x_k is the mole fraction of species k, and D_{ik} is the multicomponent Maxwell-Stefan diffusivities of species i and k.

The mixture-averaged diffusion model was selected as it is less computationally expensive than the fully-comprehensive Maxwell-Stefan model, and is designed to be used when variations in the partial pressures and temperature can be assumed to not affect the multicomponent diffusion, as in this case. It is also considered much more computationally robust than the Maxwell-Stefan equations [COMSOL, 2019].

The flux at the droplet surface was accounted for by the equation

$$-\mathbf{n} \cdot \mathbf{j}_i = M_f \tag{6.6}$$

and a no flux boundary condition was applied at the interface between the droplet and the substrate by the equation

$$-\mathbf{n} \cdot \mathbf{j}_i = 0 \tag{6.7}$$

As a test case, the solute modelled here was sucrose, as the relationship between concentration and viscosity, and the diffusion when dissolved in water is well established in the literature. Martinez [2019] measured the viscosity of a water-sucrose solution at different mass fractions, as seen in Figure 6.1. In order to provide a functional form that could be incorporated into the numerical model, this data can be well fitted by the polynomial expression

$$\mu = 0.0927\omega_{sucrose}{}^{3} - 0.0003\omega_{sucrose}{}^{2} - 0.0004\omega_{sucrose} + 0.0012 \qquad (6.8)$$

where $\omega_{sucrose}$ is the mass fraction of sucrose. The corresponding curve is also shown in Figure 6.1.

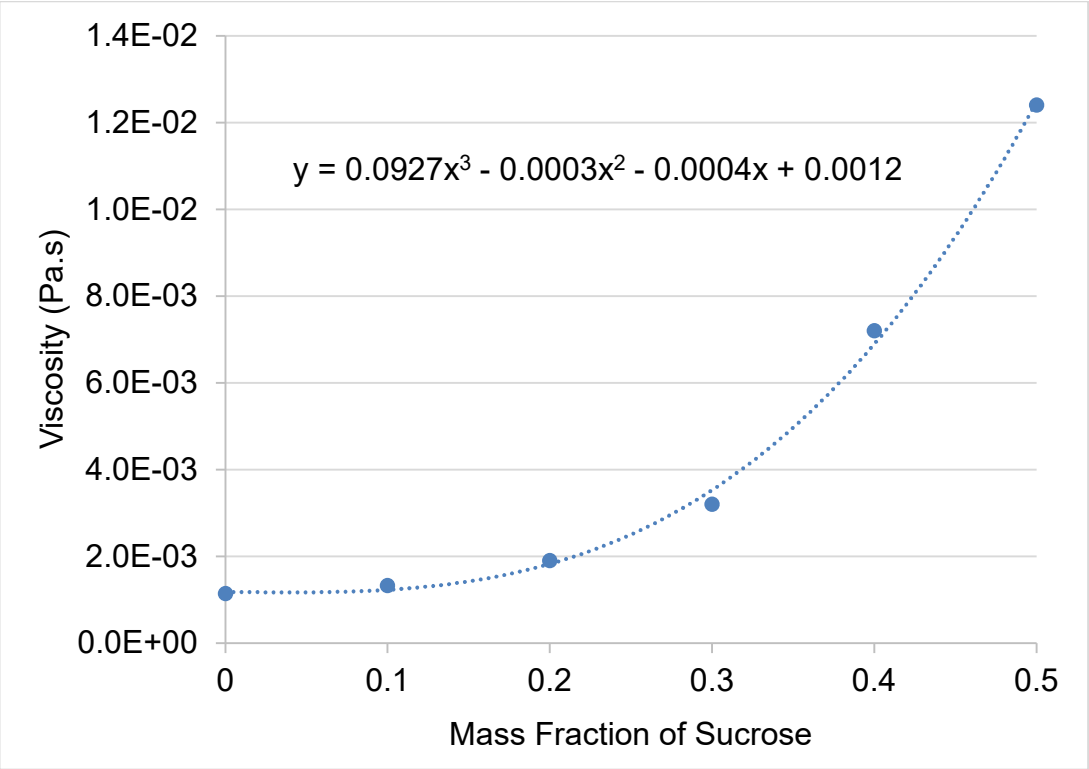

Figure 6.1: Plot of viscosity at various mass fractions of sucrose in water as measured by Martinez [2019], with a fitted trend line.

The effect of the increasing concentration of sucrose on the surface tension of the droplet was also considered through the equation

$$\sigma = 0.0093\omega_{sucrose} + 0.073 \qquad (6.9)$$

based upon experimental work by Fessenden [1928] and shown in Figure 6.2. However, as the effect of sucrose on the surface tension of water is very slight, especially when compared to the effect of the increased viscosity at higher sucrose concentrations, it was not included in the model, but for

future works involving different solvents and complex OLED solutes, this would be an important consideration in the overall drying profile of the droplet.

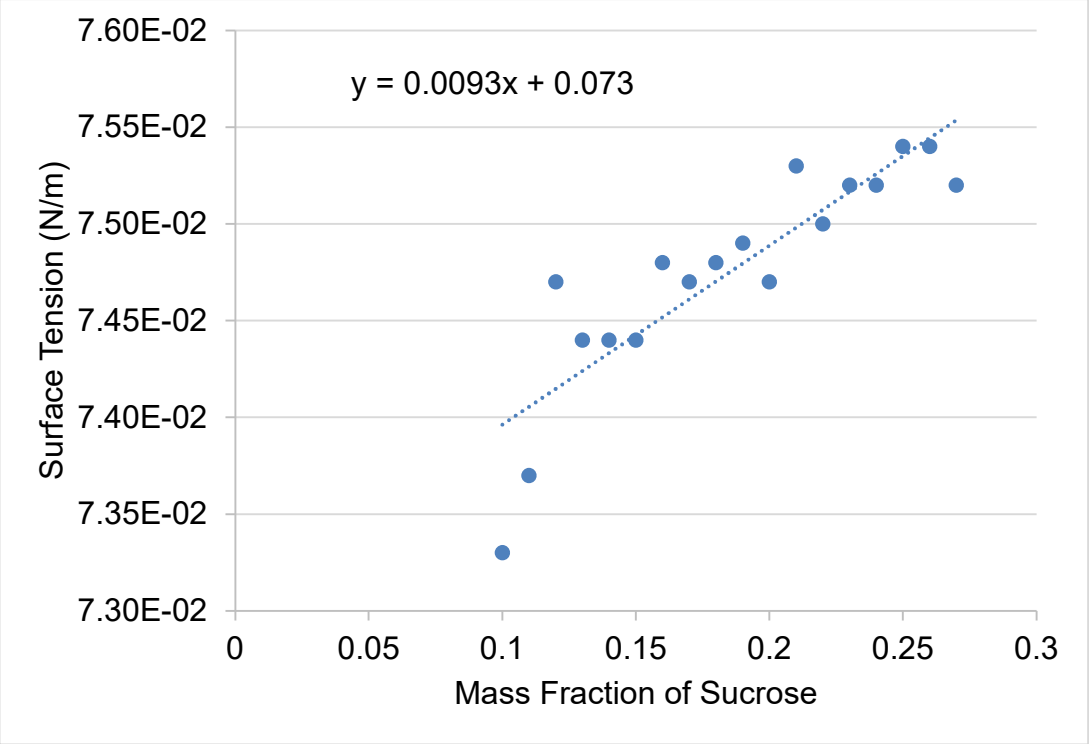

Figure 6.2: Plot of surface tension at various mass fractions of sucrose in water as measured by Fessenden [1928], with a fitted trend line.

The mass flux calculation was modified to include the impact of increasing sucrose concentration, as this will inhibit the water molecules from reaching the free surface in order to contribute to the mass flux. The mass flux equation, eq. (3.25), was modified to

$$M_f = S_F\,(1-\omega_{sucrose})(g_{evap,r}\mathbf{n}_r + g_{evap,z}\mathbf{n}_z) \tag{6.10}$$

so as the mass fraction of sucrose increased, the mass flux would tend towards zero. This is a simple way of mimicking the effect of a solute being present without having to introduce complex particle-tracking models to model the local composition of the solution at the free surface, which is outside the scope of this study.

6.3 Investigation of Initial Concentration

The equations outlined in Section 6.2 for the concentration-dependent viscosity were applied to the geometry used in Section 5.2, with a droplet radius of 67μm, a droplet initial height of 27.5μm, a bank depth of 1.3μm and a straight bank at an angle of 33°. The starting curvature of the droplet was based upon a spherical cap that intersected the axis of axisymmetry and the bank structure in the locations described. The geometry is shown in Figure 5.2. A variety of initial mass fractions (IMF) for sucrose were simulated, ranging from 1 x 10^{-5} to 0.1.

In Figure 6.3, the final height at the axis of symmetry, defined as the z-coordinate at $r = 0$ at the final output, of the droplet is plotted against the IMF and compared to the protuberance height, which is defined as the difference between the final height and the lowest point on the droplet surface. The final output was taken either when the computational mesh was so deformed that the time step had been reduced to below 1 x 10^{-6}s (typically in cases where the free surface approaches a touchdown) or when the droplet has solidified and hence no further change in free surface occurs. This therefore gives a visual representation of which IMF of sucrose values generated W-shaped profiles, namely those with a non-zero protuberance height value, and those which do not achieve touchdown due to the IMF being too high and therefore maintain a U-shaped profile, namely those with a final height far greater than the protuberance height.

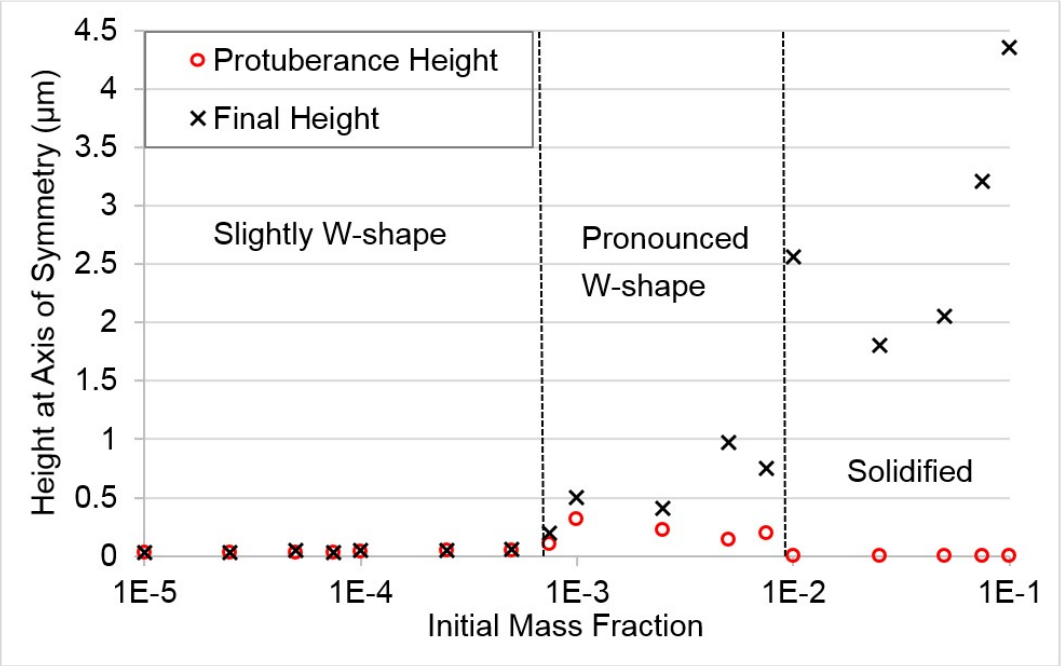

Figure 6.3: Plot of protuberance and final heights for various IMF of sucrose.

An interesting phenomenon occurs with increasing IMF of sucrose, whereby values less than 7.5×10^{-4} generate very slight W-shaped profiles, IMF between 7.5×10^{-4} and 1×10^{-2} generate pronounced W-shaped profiles, and all simulations with an IMF of sucrose larger than 1×10^{-2} do not pass the top of the bank structure.

This relationship is due to low IMF of the solute having little effect upon the viscosity and mass flux from the free surface until the droplet has almost completely dried, and so the droplet behaves very much like a pure water droplet until the final stages of evaporation when the mass fraction of sucrose becomes much greater and the related increase in viscosity causes a very slight protuberance in the centre of the well, as seen in Figure 6.4. this is consistent with previous findings in Section 5.2.4.

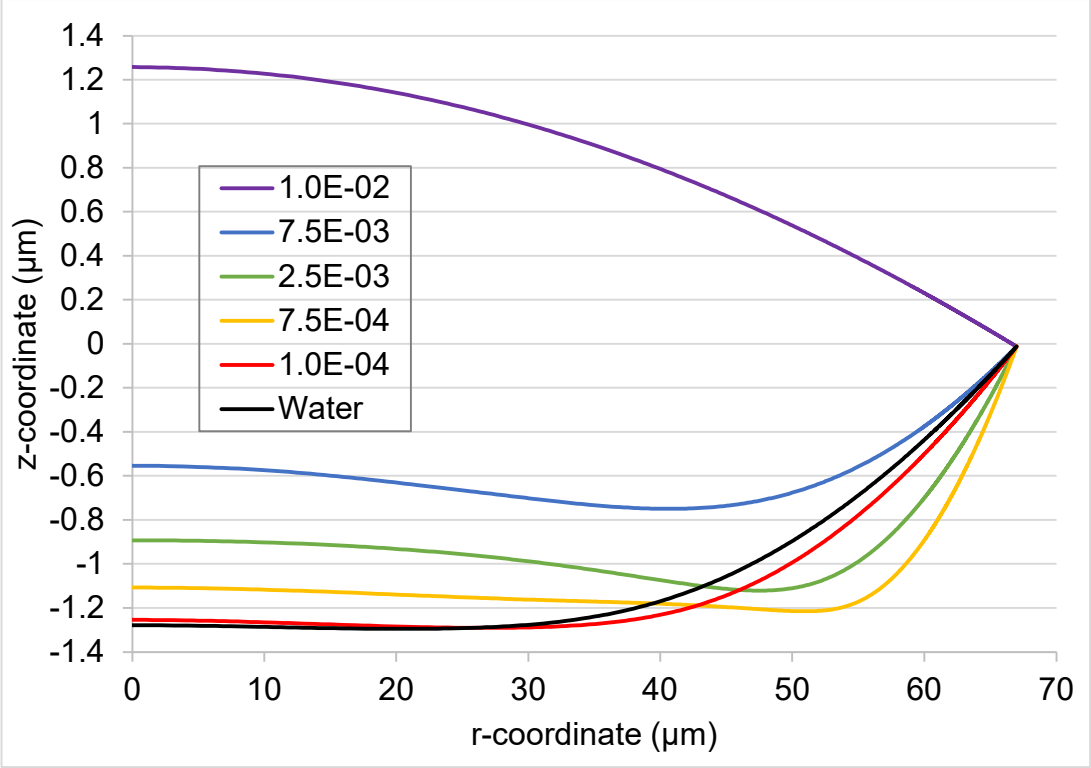

Figure 6.4: Plot of droplet drying profiles for various IMF of sucrose.

IMF between 7.5 x 10^{-4} and 1 x 10^{-2} generates very pronounced W-shaped profiles due to the viscosity increasing earlier in the drying process, due to the higher concentration of sucrose, and therefore inhibiting flow through the intermediate region, which has been previously identified a contributing factor to W-shaped profile development. The final droplet height of these simulations is proportional to the IMF of sucrose, as the volume of solute is large enough to reduce the mass flux to essentially zero.

Figure 6.5 shows the volumes of both the solute and the droplet at the final time step, and it is clear that low IMF of sucrose causes the simulation to fail due to the free surface contacting the substrate, as in previous chapters, but higher IMF of the solute means that essentially all of the water has evaporated away by the end of the simulation and the remaining volume is almost completely sucrose. This is the reason why high IMF of solute do not pass the height of the bank structure, because there is more volume of sucrose than there is available inside the well.

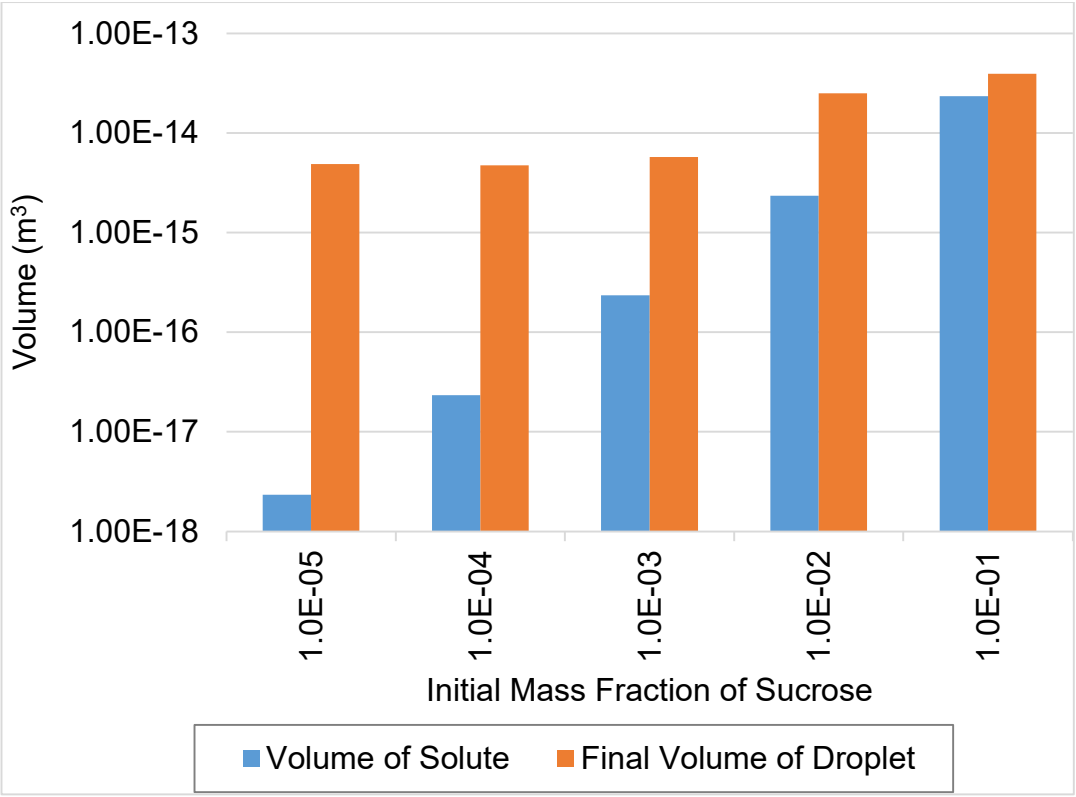

Figure 6.5: Plot of the volume of the solute and the volume of the droplet at the final output.

6.4 Effect of Bank Structure Depth

In order to study the impact of a concentration-dependent viscosity value, simulations were run in a variety of depths of S-shaped bank structures, 67μm in radius, for comparison against work from Chapter 5. The S-shaped banks were selected for this investigation as they are the most similar to actual OLED pixel bank geometries and produced slightly less protuberance height then either the straight or simple curved banks. The bank depths tested ranged from 0.25μm to 9μm for IMF of sucrose of zero (pure water), 1 x 10^{-5}, 1 x 10^{-4} and 1 x 10^{-3}.

Figures 6.6 and 6.7 show that very shallow banks, less than approximately 1μm, generate strong W-shaped profiles at all IMF values, which is due to the enhanced evaporation at the contact line causing a radial outwards flow that cannot maintain a spherical cap due to insufficient flow through the intermediate region, as with pure water.

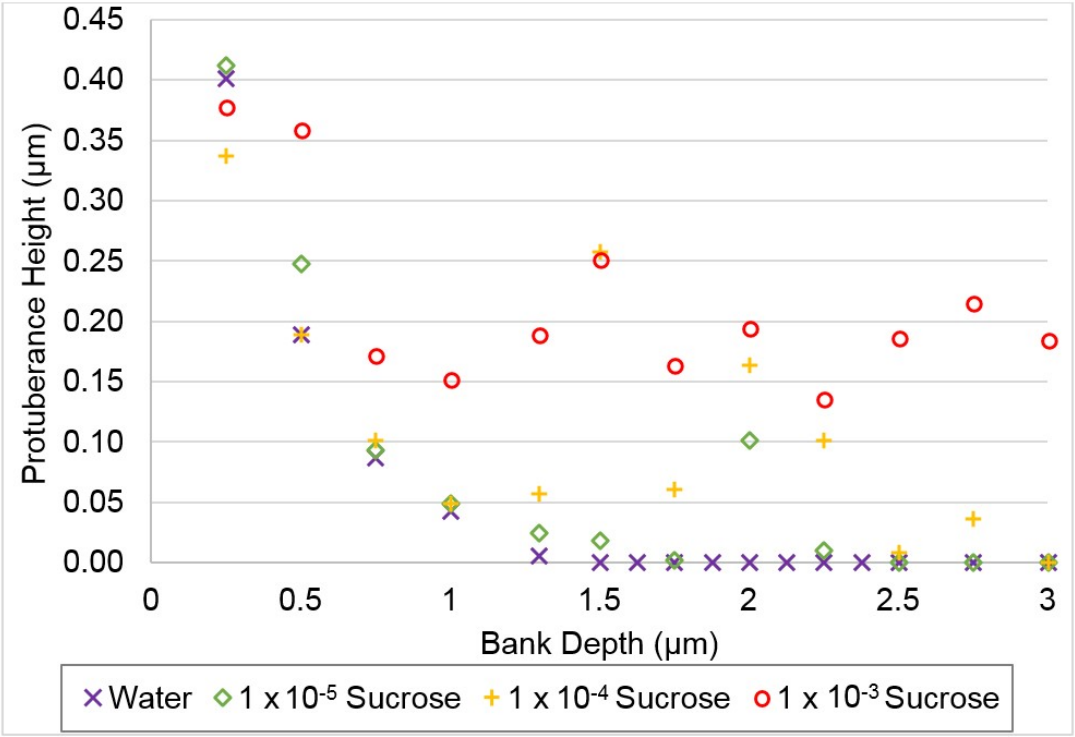

Figure 6.6: Plot of protuberance heights for various initial mass fractions of sucrose at different bank depths up to 3μm at final output.

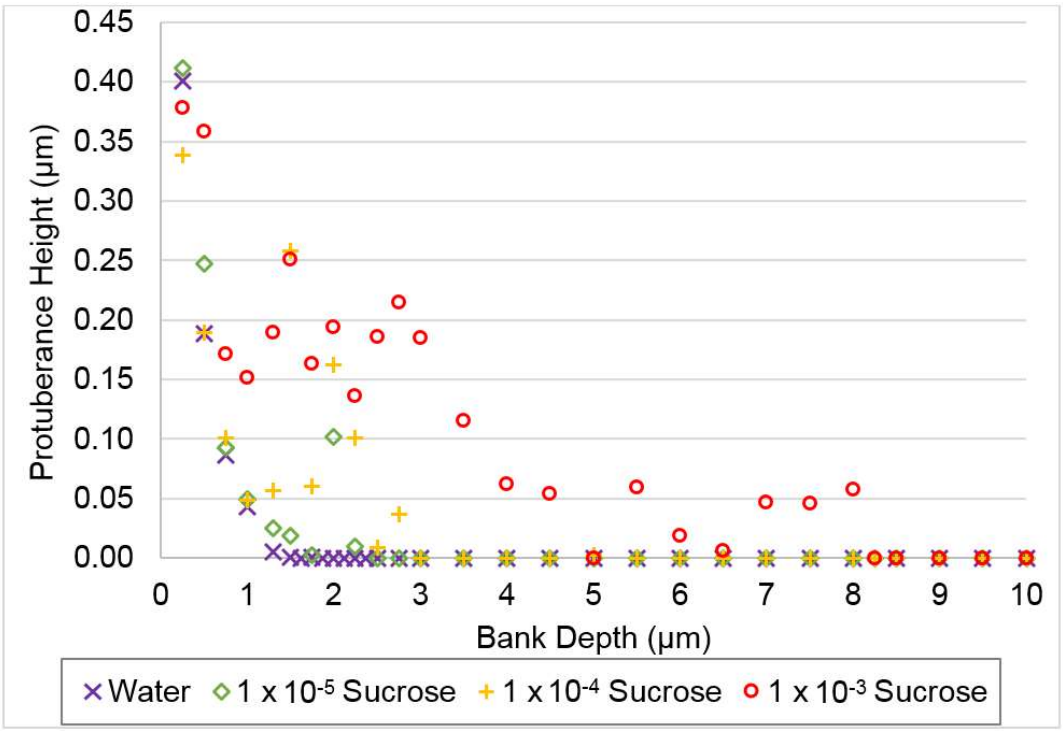

Figure 6.7: Plot of protuberance heights for various initial mass fractions of sucrose at different bank depths up to 10µm at final output.

Figure 6.6 exhibits what appears to be an oscillatory response for an IMF of 1×10^{-3}. As this is a result that has not been previously observed in any other literature, further investigations were conducted to ensure that these results were independent of solver parameters, and did not represent an artefact of the time-step or mesh size.

In order to do this, studies were conducted for an IMF of 1×10^{-3} at a bank depth of 1.5µm, as this represents the peak of one of the potential oscillations. The time-based stop condition was varied from 1×10^{-5} s to 1×10^{-9} s, with 10625 mesh elements, with the results shown in Figure 6.8.

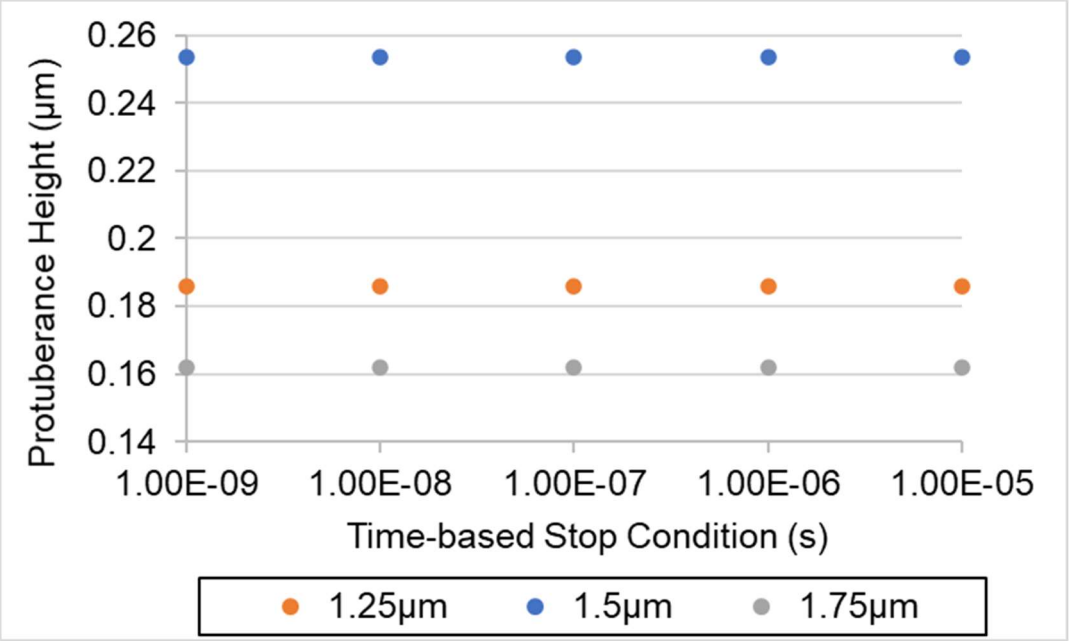

Figure 6.8: Plot of protuberance heights at different time-based stop conditions for an IMF of 1 x 10^{-3} at a bank depths of 1.25µm with 10112 mesh elements, 1.5µm with 10625 mesh elements and 1.75µm with 10943 mesh elements.

As is seen in Figure 6.8, varying the time-based stop condition between 1 x 10^{-5} s and 1 x 10^{-9} s had no effect whatsoever on the protuberance height generated, with all simulations resulting in the same protuberance height as when these combinations of IMF and bank depth were simulated for Figure 6.6.

The mesh size was then varied to generate between 5000 and 20000 mesh elements, at a time-based stop condition of 1 x 10^{-6} s, with the results shown in Figure 6.9.

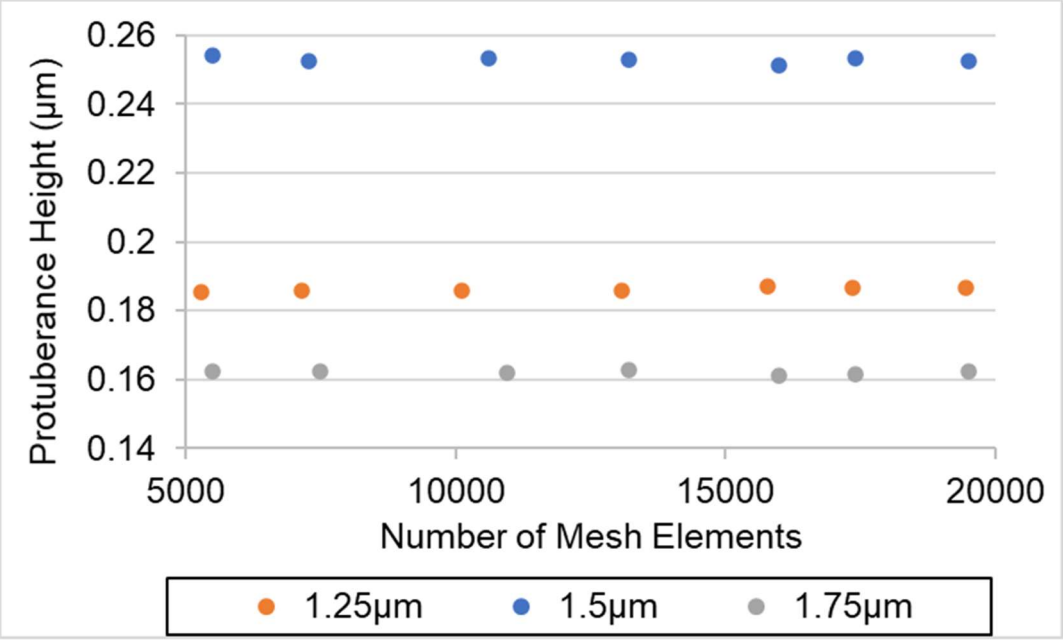

Figure 6.9: Plot of protuberance heights at different mesh resolutions for an IMF of 1 x 10^{-3} at bank depths of 1.25µm, 1.5µm and 1.75µm, with a time-based stop condition at 1 x 10^{-6} s.

Figure 6.9 shows a total variance range of only around ±0.002µm from the protuberance height previously seen at all three bank depths tested, with the majority of results falling in the ±0.001µm range.

The results presented in Figures 6.8 and 6.9 clearly show that the results shown in Figure 6.6 for the protuberance height generated with an IMF of 1 x 10^{-3} at bank depths of 1.25µm, 1.5µm and 1.75µm is independent of solver parameters. It is therefore logical and reasonable to infer that the other results that show oscillatory behaviour demonstrated in Figure 6.6 are also independent of solver parameters, and do not represent an artefact of the computational mesh or the time-based stop condition.

As this oscillatory behaviour is an entirely novel phenomena, it represents an excellent opportunity for further work to investigate the potential causes. Based on previous studies carried out in Chapters 4, 5 and 6 of this work, the author postulates that this behaviour is likely due to a confluence of evaporation rate, viscosity and surface tension affecting the drainage of fluid from the centre of the droplet towards the periphery, and culminating in this unusual correlation between bank depth and protuberance height. Further detailed investigations into this phenomena are outside of the scope of this work, but a more in-depth study of the relationship between bank depth and protuberance height with the above parameters, particularly with bank depths in the 0-8µm range, could yield very interesting future studies.

Figures 6.6 and 6.7 show that an IMF of 1 x 10^{-5} generated only U-shaped profiles at bank depths above 1µm, except at depths of 2µm (shown in Figure 6.10) and 2.25µm, where the profile was slightly W-shaped. This was due to the relationship between the depth of well available for flow through the intermediate region and the increasing viscosity of the solution coalescing in such a way that flow through the intermediate region was restricted, as seen in Figures 6.11 and 6.12.

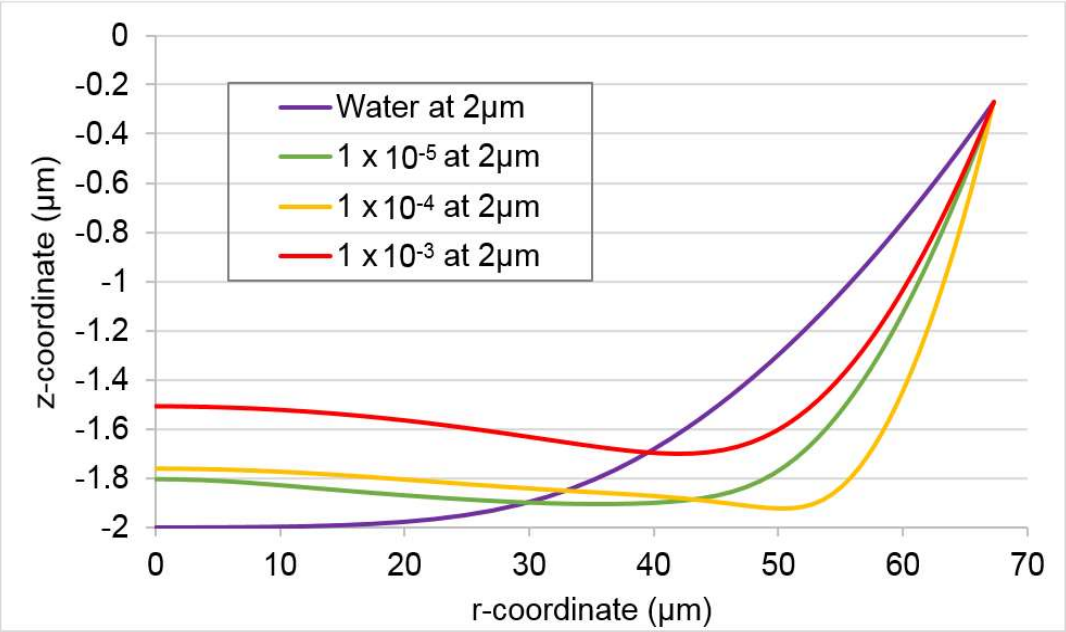

Figure 6.10: Plot of droplet drying profiles for various initial mass fractions of sucrose at a bank depth of 2µm.

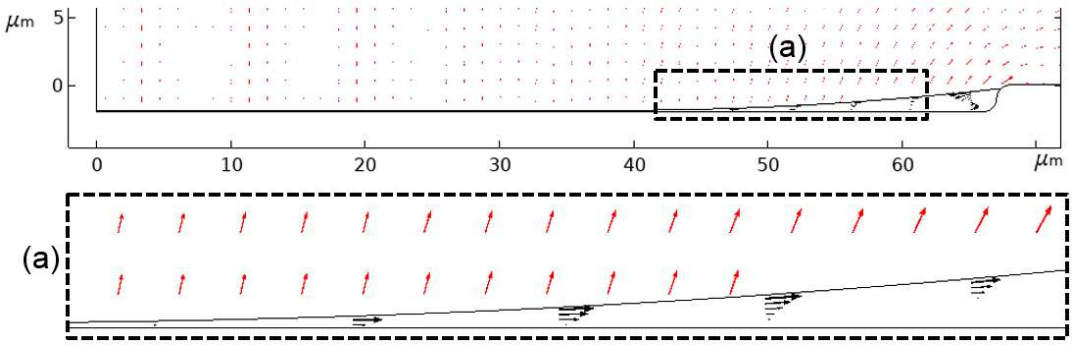

Figure 6.11: Plot of the velocity field in black and the evaporative flux in red for a bank depth of 2µm and an IMF of 1 x 10^{-5} at final output.

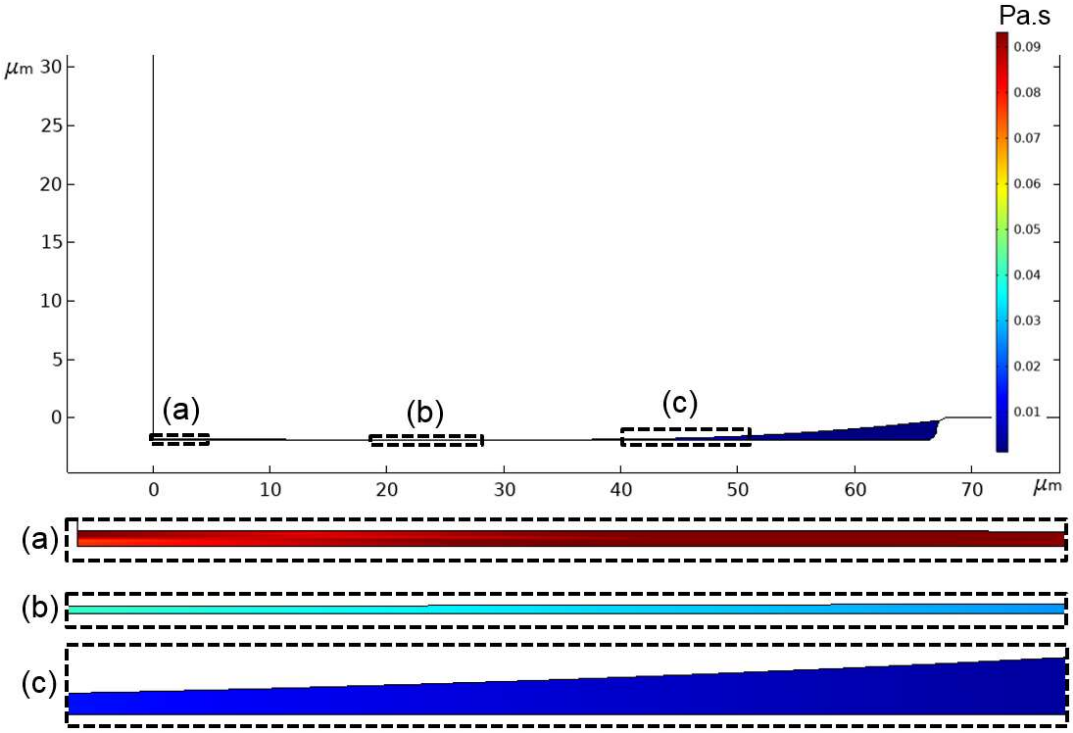

Figure 6.12: Plot of the dynamic viscosity for a bank depth of 2μm and an IMF of 1 x 10^{-5} at final output.

For bank depths greater than 2.25μm and less than 2μm (but above 1μm), this relationship did not create any restrictions to flow through the intermediate region and therefore produced U-shaped profiles, as seen in Figures 6.13 and 6.14.

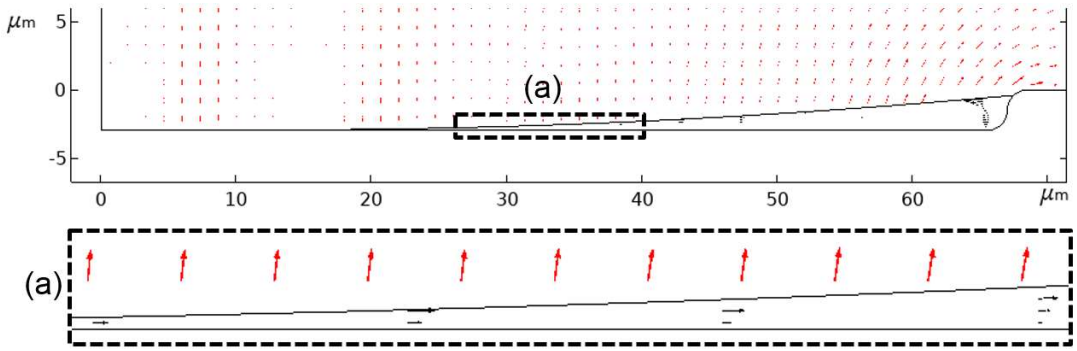

Figure 6.13: Plot of the velocity field in black, evaporative flux in red and the dynamic viscosity for a bank depth of 3μm and an IMF of 1 x 10^{-5} at final output.

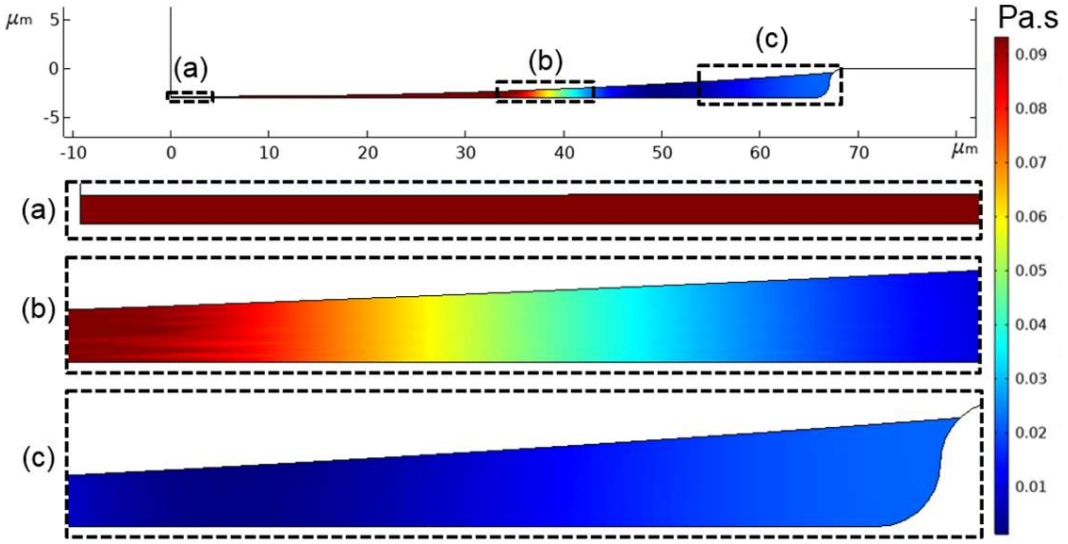

Figure 6.14: Plot of the dynamic viscosity for a bank depth of 3μm and an IMF of 1 x 10^{-5} at final output.

A similar phenomenon occurred with an IMF value of 1 x 10^{-4}, where W-shaped profiles were generated between bank depths of 1.3μm and 2.5μm, but not at greater bank depths. The W-shape of the droplet surface was more pronounced and over a greater bank depth range in this case, as the higher IMF meant that the viscosity changed over time to a far greater extent. This was made even more extreme for an IMF value of 1 x 10^{-3}, where a W-shaped profile was always seen up to a bank depth of 9μm, where the profile became U-shaped, as seen in Figure 6.15.

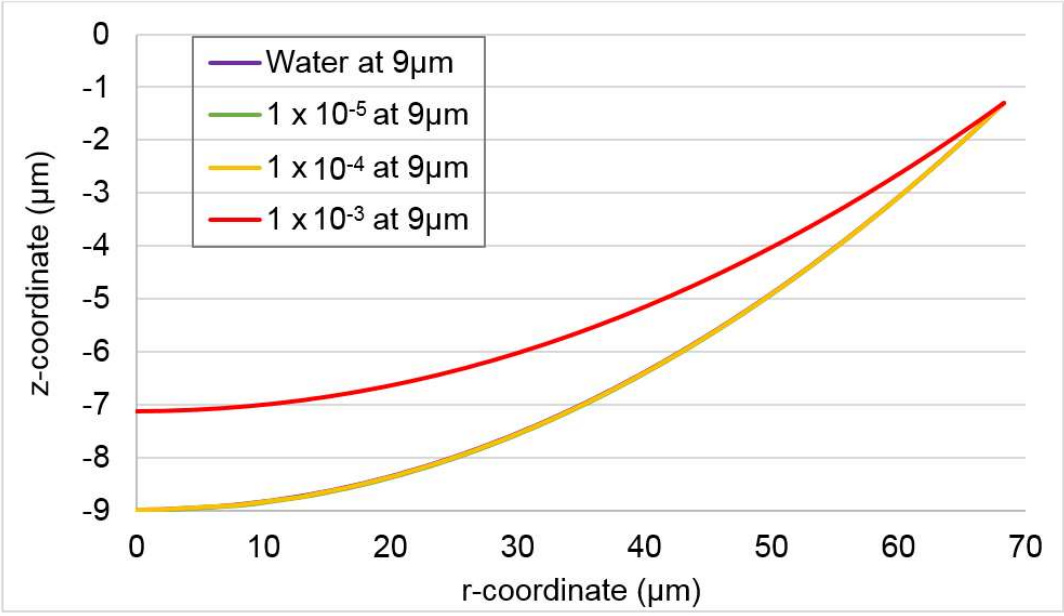

Figure 6.15: Plot of droplet drying profiles for various initial mass fractions of sucrose at a bank depth of 9μm.

This section has shown that the bank structure depth, and by extension the aspect ratio, is still an important factor in determining profile shape when a concentration-dependent viscosity is applied, with deeper bank being more likely to produce U-shaped profiles, which is consistent with results shown in Chapter 5.

6.5 Effect of Evaporation Rate

In order to study the effect of changing evaporation rates on the protuberance height generated in droplets with a concentration-dependent viscosity, the E value was varied in the range of 0.5 to 20 for a droplet with an IMF of sucrose of 1 x 10^{-4} in a 5μm deep S-shaped bank structure.

This bank structure was selected due to the chosen IMF value producing a U-shaped profile at E=1 (i.e. the evaporation rate of water), and so any changes would be attributable solely to the increased evaporation, whereas a bank depth that produced a W-shaped profile at a given IMF of sucrose may be impacted by other variables and so conclusions may become unclear.

Figure 6.16 shows the relationship between the relative evaporation rate and the protuberance height, and it is clear that there is a sudden shift from U-shaped to W-shaped profiles at E=10, with similar protuberance heights being seen up to E=20.

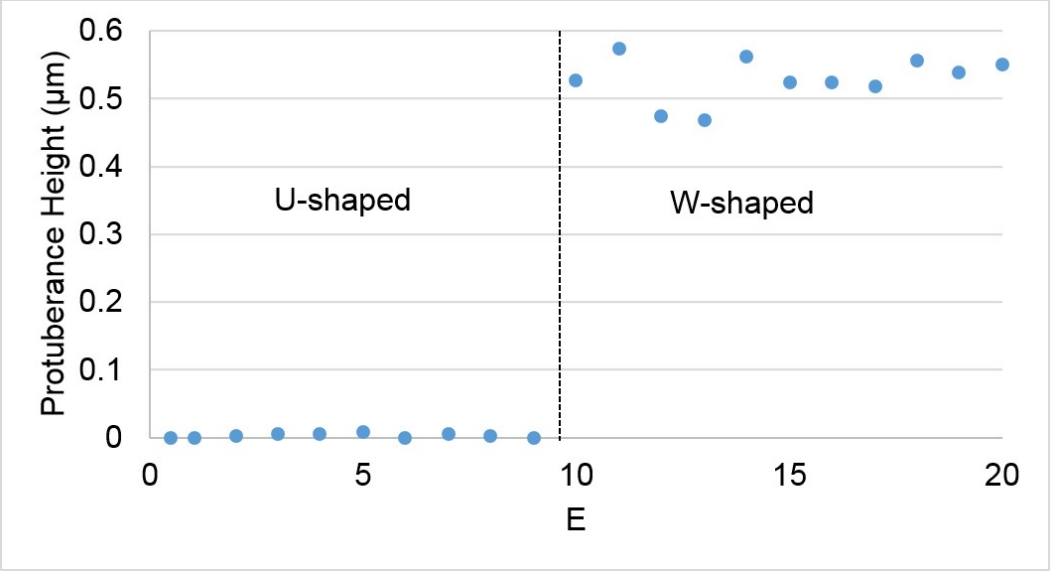

Figure 6.16: Plot of protuberance height against E for a droplet with concentration-dependent viscosity.

This is the first time in this thesis that a ‘snap’ change from U- to W-shaped profiles has been seen, with all other transitions occurring somewhat gradually.

In order to understand this phenomena, the droplet profiles were plotted in Figure 6.17, where the difference in profile shape is also of a kind that is previously unseen.

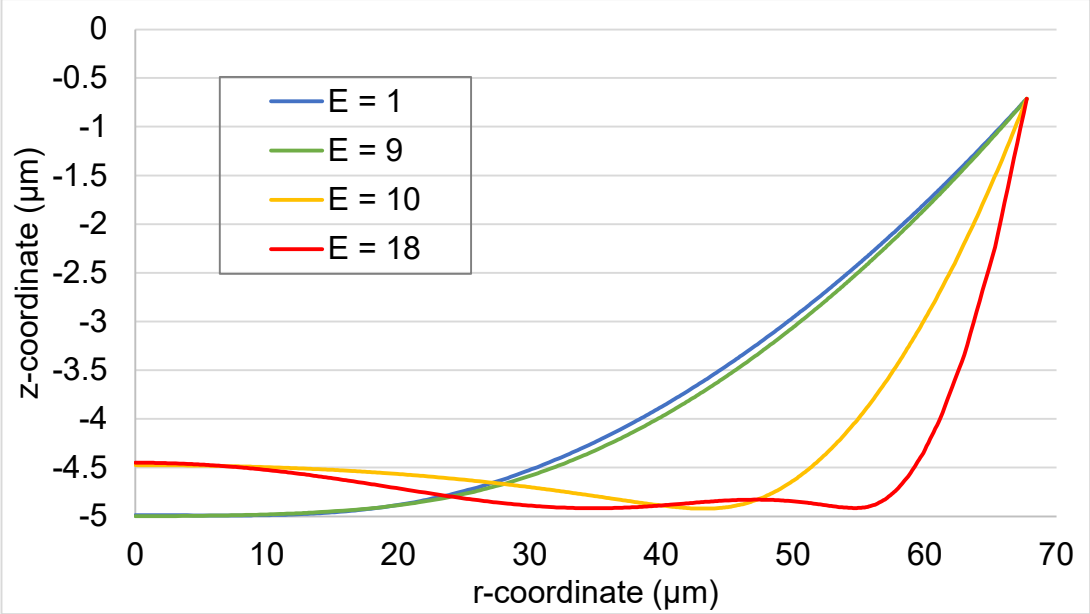

Figure 6.17: Plot of droplet drying profiles for various E values for a droplet with concentration-dependent viscosity.

An E value of 1 produces a U-shaped profile at this bank depth and radius, as studied in Section 6.4, as does E=9, however E=10 produces a protuberance height of approximately 0.5μm. This was due to the higher evaporation rate crossing the threshold at which the radial outwards flows can be maintained by flow from the centre of the droplet. Figure 6.18 clearly shows that the flow from the centre sustains the radial outwards flows at E= 9, but Figure 6.19 shows that E=10 cannot sustain the outwards flows and so leads to a W-shaped profile beginning to occur, with the final profile being shown in Figure 6.20.

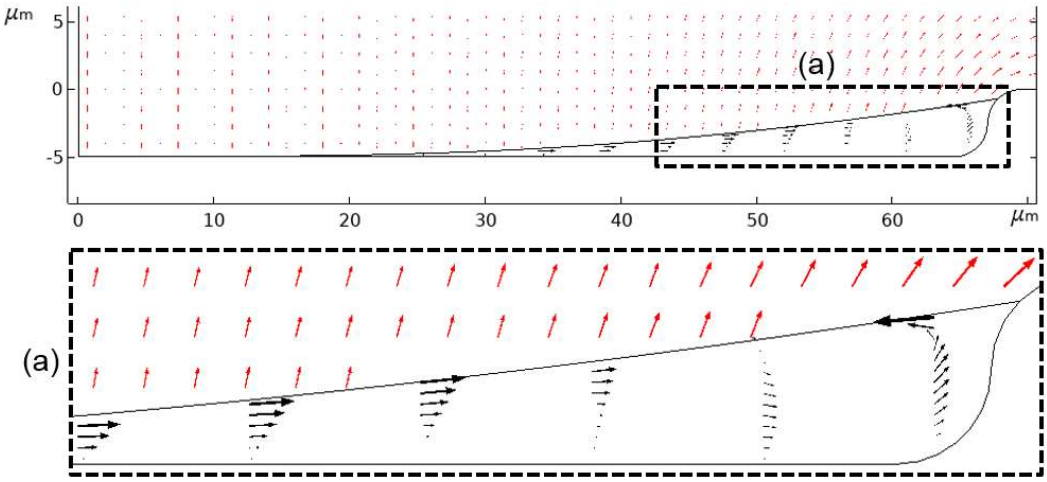

Figure 6.18: Plot of the velocity field in black and the evaporative flux in red for E=9 at t=0.483s.

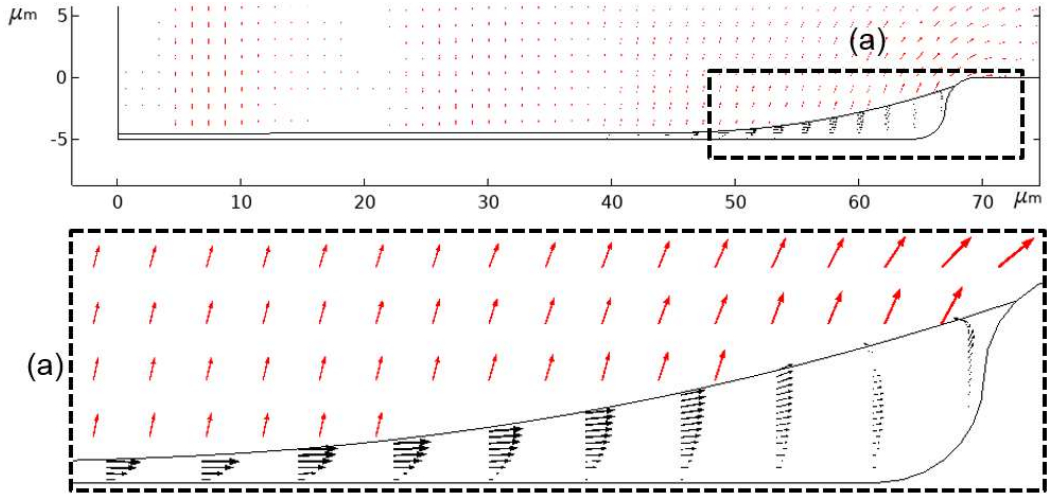

Figure 6.19: Plot of the velocity field in black and the evaporative flux in red for E=10 at t=0.483s.

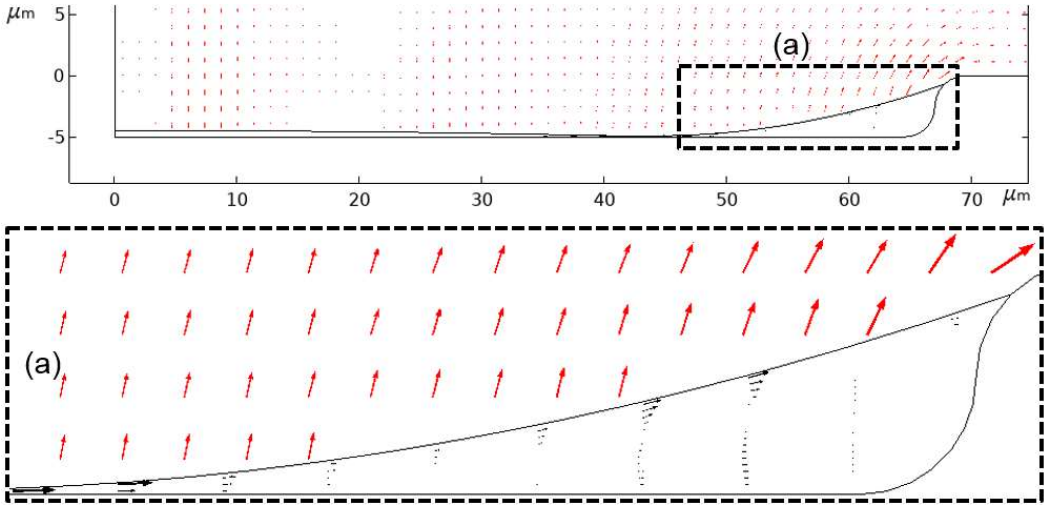

Figure 6.20: Plot of the velocity field in black and the evaporative flux in red for E=10 at t=1.655s.

At E values above 18, as seen in Figure 6.17, there is a 'double-dip' profile, where the droplet could conceivably achieve touchdown at two separate points. This was caused by a combination of the fast radial outwards flows generated by the higher evaporation rate and the increasing viscosity with increasing sucrose concentration. At t=0.22, as seen in Figure 6.21, the profile very much resembles that of a droplet with E=10, as seen in Figure 6.19, except with considerably higher outwards flows.

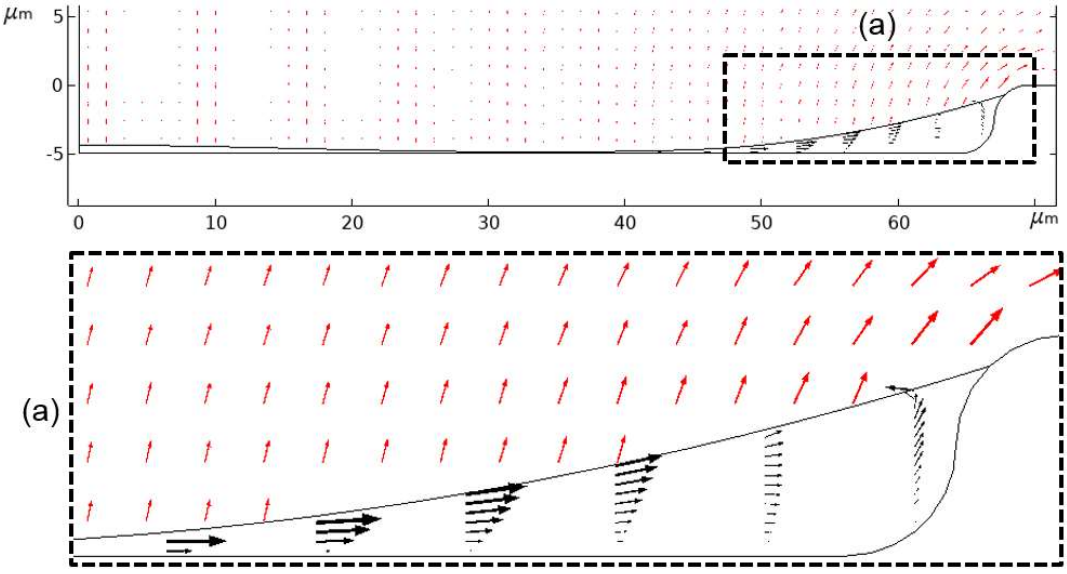

Figure 6.21: Plot of the velocity field in black and the evaporative flux in red for E=18 at t=0.22s.

However, the increasing viscosity in the region that will produce a double-dip profile, shown in Figure 6.22, creates a second region where the flow cannot

sustain the outwards flows, as with the fluid at the centre of the droplet when a standard W-shaped profile develops. This leads to the velocity field at t=0.25s shown in Figure 6.23, which clearly shows the flow from the double-dip region not being sustained from the higher viscosity region, and to the final profile at t=0.375s shown in Figure 6.24.

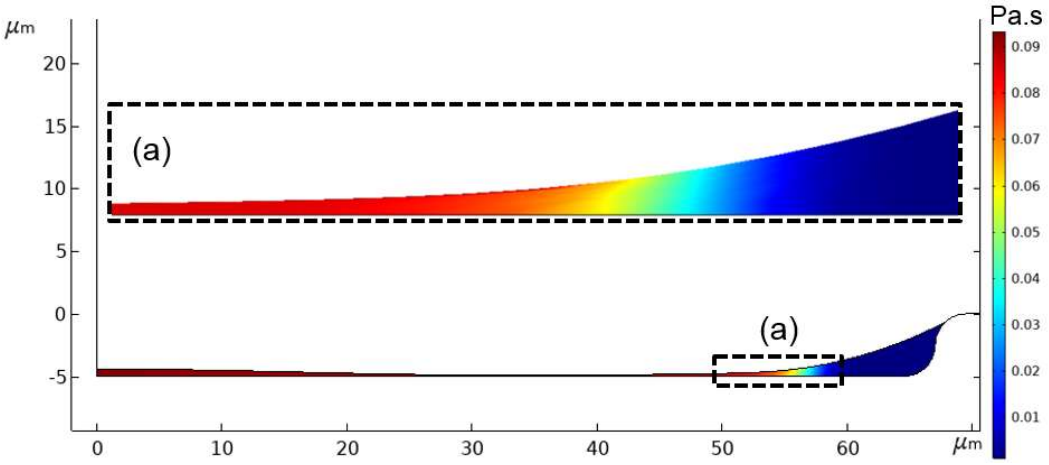

Figure 6.22: Plot of the dynamic viscosity for E=18 at t=0.22s.

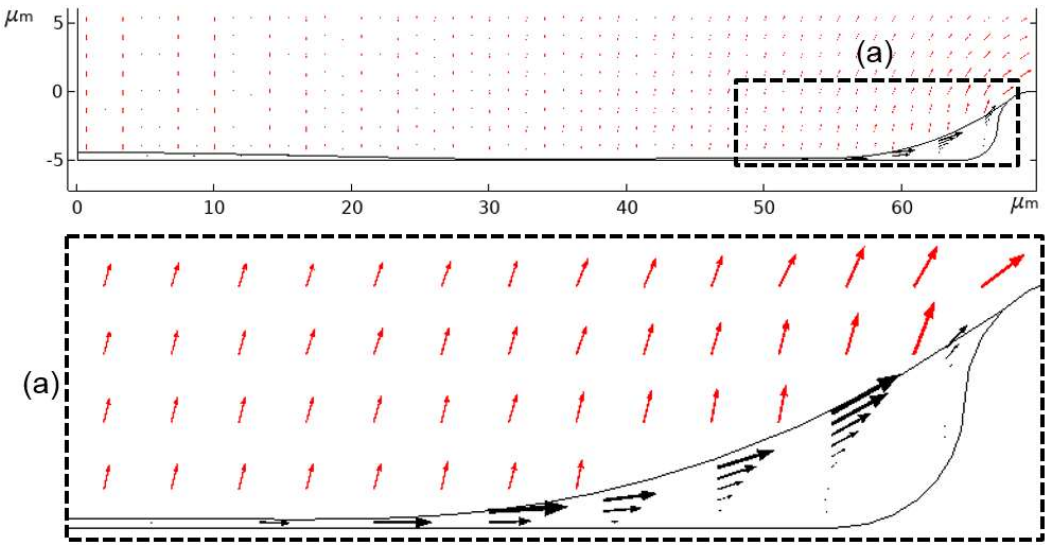

Figure 6.23: Plot of the velocity field in black and the evaporative flux in red for E=18 at t=0.25s.

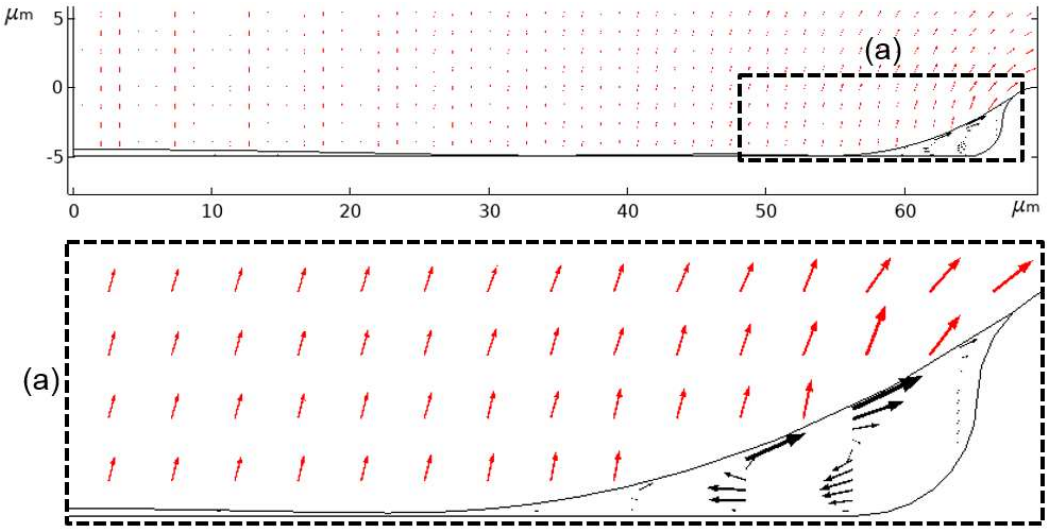

Figure 6.24: Plot of the velocity field in black and the evaporative flux in red for E=18 at t=0.375s.

This section has shown that an increased evaporation rate is more likely to produce a W-shaped profile, consistent with the findings in Chapter 5, however rather than there being a gradual transition from U- to W-shaped, there is now a step change at around E = 10. This was due to the combination of increased radial outwards flow and rapidly increasing concentration-dependent viscosity meaning that flow from the centre could no longer sustain a spherical cap, and the intermediate region thinned to produce a W-shaped profile. Also, above E = 18, a double-dip profile was seen, where this process occurred again on the side of the thinned region closest to the contact line, due to the very high evaporation rate, outwards flows and increase in viscosity.

6.6 Conclusions

This chapter has explored the effects of introducing a concentration-dependent viscosity, based on published data for sucrose, into the current model.

It has been found that increasing the initial mass fraction (IMF) of sucrose increases the final droplet height, as the volume of the solute becomes the vast majority of the droplet volume in the final stages of drying with higher IMFs. It has also been found that at IMFs between 7.5×10^{-4} and 1×10^{-2}, pronounced W-shaped profiles are generated, with IMFs lower than this range having little effect upon the viscosity and mass flux from the free surface until the droplet has almost completely dried, so the droplet behaves essentially like pure water. Above this range, the free surface does not pass the height of the bank structure due to the volume of the solute present.

Investigation into the effect of bank structure depth showed that bank depths of less than approximately 1μm generate W-shaped profiles at all IMFs, due to flow from the centre of the droplet not being able to sustain the radial outwards flows, as with pure water. Different IMFs produce W-shaped profiles at different bank depths, but there seems to be a consensus among the IMF values that a bank depth of around 2μm will generate the largest protuberance height, with deeper banks more likely to produce U-shaped profiles, and all profiles being U-shaped for the tested IMFs by a bank depth of 9μm. The deeper bank depths produce U-shaped profiles due to the lower aspect ratio of the well allowing flow from the centre of the droplet to the contact line with little restriction.

Investigation was conducted into whether the novel oscillatory behaviour seen with an IMF of 1×10^{-3} was an artefact of the numerical method applied, and through studying the variation in protuberance heights at various mesh sizes and time-based stop conditions, it was concluded that they indeed were independent of solver parameters. It was postulated that this behaviour is likely due to a confluence of evaporation rate, viscosity and surface tension impacting the drainage of fluid from the centre of the droplet towards the periphery, as has been seen in previous Chapters of this work, and that this presents a very interesting opportunity for future investigations.

Studying the impact of changing the evaporation rate, it was found that E values below 10 will produce U-shaped profiles in a bank depth of 5μm, and E values above 10 will generate a protuberance height. Above an E value of

18 however, a unique ‘double-dip’ profile is seen, with two potential touchdown points. This was attributed to the high velocity of the outwards flows combined with the rapidly increasing viscosity in the double-dip region restricting flow and leading to that region having a dip by the same mechanism that a W-shaped profile appears - being unable to sustain the outwards flows.

Comparing the effects of applying a concentration-dependent viscosity on the droplet drying profile seen in current model to changes that may occur in an actual OLED system is very difficult at this time. No experimental data was available for comparison, and it was not possible to acquire any data from the industrial sponsor of this work, as they closed their UK-based OLED research facility during the course of this project. The industrial supervisor for this project, along with all the other staff at the facility, was made redundant, and so there was no possibility of further contact or collaboration. Clearly this was a major inconvenience in terms of this project, but does offer substantial scope for future works to perform these experiments for comparison to the phenomena seen here.

Chapter 7:
Conclusions and Future Work

7.1 Conclusions

The aim of this research was to understand the dynamics of interface deformation of a drying OLED droplet in a bank structure, by way of numerical modelling, to predict the behaviour of drying OLED solutions and the deposits left behind.

In order to achieve this, a numerical model was developed that contained several advantages over most previous models, such as a local evaporative flux coupled to a free surface to represent droplet profile shapes other than spherical caps and considerations for the internal flows and thermal characteristics and other variable parameters throughout.

The use of the ALE approach, implemented through the Finite Element Method, gave the current model several notable advantages over other numerical methods, such as the interface being precisely defined at all times, the easy application of complex boundary conditions and the avoidance of spurious currents. In addition, the zero-thickness interface is a much closer approximation to a real interface than other methods, and there are no difficulties in having large density ratio between the liquid and air domains.

The main issue with using the ALE approach was the inability to deal with the free surface coming into contact with the substrate, however, as the current research was chiefly concerned with the behaviour of the droplet up to the point of touchdown, the impact of this was minimal.

The model developed was very much akin to the model proposed by Yang, Hong and Cheng [2014], with the novel addition of a bank structure to represent an OLED pixel geometry.

The model was verified and validated on a flat substrate against numerical and experimental work by Hu and Larson [2002], which proved it capable of delivering accurate results for the concentration gradients in the gas domain and the deformation of the free surface, while comparison against Yang, Hong and Cheng [2014] validated the ability of the current model to predict evaporation-driven radial outwards flows to an accuracy of 1-1.5%, evaporative cooling to within 0.13-0.26K, and thermocapillary flows to within 3.5%.

The model was compared against numerical and experimental works for solvents other than water, namely anisole [Fukai, 2014] and ethanol [Nguyen and Nguyen, 2012], showing that the current model can accurately replicate the evaporation of other solvents, if the correct data for parameters such as diffusion coefficient, density, surface tension and viscosity are known.

Experimental work by Kazmierski [2018] into the evaporation of droplet from bank structures had shown that different solvents produce either U-, W- or M-shaped drying profiles, with U- and W-shaped profiles being attributed to slower or faster drying solvents respectively. M-shaped profiles were only seen sporadically with o-xylene, with the introduction of thermal or solutal Marangoni flows seen as the only possible cause, but without direct evidence.

The presence of a bank structure was added into the geometry of the model, which was shown to be is broadly capable of replicating the experimental results generated by Kazmierski [2018] for anisole, methyl anisole, mesitylene and o-xylene. There were issues with the experimental data containing asymmetric droplet profiles, data only recorded at set times and not at touchdown, and the use of overly thick lines in the images which could potentially lead to inaccurate readings, however the general trend for all solvents modelled was clear: increasing evaporation rate leads to increasing protuberance height.

Upon detailed parametric sweeps of evaporation rate, surface tension, viscosity and the well aspect ratio, it was found that a droplet has a high likelihood of generating a U-shaped profile under one or more of the following conditions:

- Low evaporation rate, below approximately 2μm/s.
- High surface tension, above approximately 0.07N/m.
- Low viscosity, below approximately 0.001Pa.s.
- An aspect ratio of the well of less than 30 for a straight bank or S-shaped bank structures.

It was also found that, of these considerations, the evaporation rate is by far the most important factor for generating a U- or W-shaped profile.

When the surface tension was set to be artificially low at the centre of the droplet and high near the contact line, the model was able to generate an M-shaped profile, suggesting that the results showing M-shaped profiles in experimental work by Kazmierski [2018] could have been caused by a solutocapillary effect between the solvent and some unknown contaminant.

A concentration-dependent viscosity was then added to the model to represent the immobilisation of the fluid that occurs when a droplet containing a solute, in this case sucrose, has lost solvent through evaporation.

It was found that increasing the initial mass fraction (IMF) of sucrose increases the final droplet height, as the volume of the solute becomes the vast majority of the droplet volume in the final stages of drying with higher IMFs, and that intermediate IMF values generated pronounced W-shaped profiles, with lower IMFs having little effect upon the viscosity and mass flux from the free surface until the droplet has almost completely dried.

During investigations into the effect of the IMF on protuberance heights, a novel oscillatory behaviour was observed. Studies into the mesh and time-based stop condition indicated that this was not an artefact of the numerical method applied, and was in fact a realistic simulation of the droplet under those conditions. To the best knowledge of the author, this is the first time this phenomena has been observed, and it is postulated that this behaviour is likely due to a confluence of evaporation rate, viscosity and surface tension impacting the drainage of fluid from the centre of the droplet towards the periphery, as has been concluded in the rest of this work. This revelation opens up very interesting opportunities for future investigations into the exact cause of these oscillations on protuberance height with increasing evaporation rates.

Investigation into the effect of bank structure depth showed that shallow bank depths, all IMFs produced W-shaped profiles, but different IMFs produced W-shaped profiles at different bank depths, with deeper banks more likely to produce U-shaped profiles.

Studying the impact of changing the evaporation rate, it was found that an evaporation rate, E (where E=1 is the evaporation rate of water) below 10 will produce U-shaped profiles in a bank depth of 5μm, and E values above 10 will generate a protuberance height, with very little transition between the two profile types. Above an E value of 18 however, a unique ‘double-dip’ profile is seen, with two potential touchdown points. This was attributed to the high velocity of the outwards flows combined with the rapidly increasing viscosity in the double-dip region restricting flow and leading to that region having a dip by the same mechanism that a W-shaped profile appears - being unable to sustain the outwards flows.

As the stated aim of this research was to understand the dynamics of interface deformation of a drying OLED droplet in a bank structure by way of numerical modelling, and to predict the behaviour of drying OLED solutions and the deposits left behind, this study can be deemed to have been mostly successful. There is now a firm understanding of the various parameters that will lead to U- or W-shaped drying profiles, and a likely reason for the generation of M-shaped profiles has been presented. However, the inability of the model to achieve a final, fully ‘dried’ state is a major shortcoming, and the overall progress of the work was severely hampered by the closure of Merck’s OLED research facility and the redundancy of my industrial supervisor, which made acquiring realistic data on OLED droplets essentially impossible.

7.2 Future Work

There are several shortcomings of the model applied in this work that could be improved upon in future iterations.

One such shortcoming is the lack of a detailed model to represent the solutocapillary effect, with it instead being represented by a function applied to the surface tension. If multiple solvents could be modelled in the same droplet, with fully coupled, but independent, viscosity, surface tension, evaporation rate, density and other values, a more realistic and diverse representation of the solutocapillary effect would be achieved. This would also imbue the model with the ability to reproduce other experimental works by Kazmierski [2018] into the evaporation of binary droplets from OLED bank structures.

Another future improvement would be the inclusion of some sort of particle-tracking model to represent the immobilisation of the fluid resulting from ever-increasing viscosity, rather than a concentration-dependent viscosity, as this would allow for a greater level of detail in analysis and could also enable the complex OLED compounds to be modelled realistically. Additionally, the change in surface tension with regards to increasing mass fraction of a solute could be incorporated.

Future investigation should also explore the possibility of modifying the model to allow for a fully ‘dried’ final state. This may be possible through the use of a re-meshing function upon touchdown, which then treats the centre of the droplet and the outer ring as separate fluid domains. This would alleviate the primary shortcoming of the ALE approach.

The newly observed oscillatory behaviour of the protuberance height with increasing evaporation rate in the presence of a concentration-dependent viscosity could also be the subject of future works.

The heat transfer between the substrate and the droplet could be made more realistic with a conjugate heat transfer model, where the temperature of the droplet, substrate and atmosphere are fully coupled.

The inclusion of a vacuum drying model, in which a pump-down function is applied at the outer boundary of the atmosphere domain, would enable the model to represent the effect of an actual OLED production environment, where the array of OLED pixels is subjected to a low, variable atmospheric pressure to increase evaporation rate and increase production throughput.

The availability of data on the exact composition and properties of actual OLED material in suspension within a solvent would be a considerable help to any future studies in this area, and would allow for far more in-depth, far-reaching analysis.

The final, and potentially most valuable, improvement that could be made to the model would be to make it fully 3D. Whilst this would drastically increase the complexity and computational load of the model, OLED pixels are not axisymmetric, and therefore the most accurate and realistic way to model them is in full 3D, especially if an array of pixels is to be studied.

References

AP Physics. (n.d.). *Evaporation.* Retrieved from <http://ap-physics.david-s.org/evaporation/> [Accessed 24/06/2019].

Bennacer, R., & Sefiane, K. (2014). *Vortices, dissipation and flow transition in volatile binary drops.* Journal of Fluid Mechanics, Vol. 749, pp. 649–665.

Benziger Group. (n.d.). *Organic Vapour Phase Deposition for Optoelectronic Devices.* Department of Chemical and Biological Engineering, Princeton University, USA. Retrieved from <https://www.princeton.edu/~benziger/OVPD.pdf> [Accessed 14/06/2019].

Berthier, J. (2013). *Micro-Drops and Digital Microfluidics.* 2nd ed. Elsevier, Oxford, UK.

Birdi, K. S., Vu, D. T., & Winter, A. (1989). A Study of the Evaporation Rates of Small Water Drops placed on a Solid Surface. Journal of Physical Chemistry, Vol. 93, No. 9, pp. 3702-3703.

Breinlinger, T. (n.d.). *Inkjet Example.* Retrieved from <http://www.simpartix.com/fileadmin/_migrated/pics/inkjet_example_470_01.jpg> [Accessed 21/06/2019].

Brutin, D., & Starov, V. (2018). *Recent advances in droplet wetting and evaporation.* Chemical Society Reviews, Issue 2, Vol. 47, pp. 558-585.

Burrows, P. E., et al. (1995). *Organic vapour phase deposition: a new method for the growth of organic thin films with large optical non-linearities.* Journal of Crystal Growth 156, pp. 91-98.

Bush, J. (2010). *Marangoni Flows.* Lecture Slides from Interfacial Phenomena, Department of Mathematics, MIT, USA. Retrieved from <http://ocw.mit.edu/courses/ mathematics/18-357-interfacial-phenomena-fall-2010/lecture-notes/MIT18_357F10_ Lecture9.pdf> [Accessed 23/06/2019].

Castrejón-Pita, J. R., et al. (2013). *Future, Opportunities and Challenges of Inkjet Technologies.* Inkjet Research Centre, University of Cambridge, UK. Atomisation and Sprays, Begell House, Inc.

Chen, S., & Raad, D. B. (1997). *The surface marker and micro-cell method*. International Journal for Numerical Methods in Fluids, Vol. 25, No. 7, pp. 749–778.

Chen, S., & Doolen, G. D. (1998). *Lattice Boltzmann Method For Fluid Flows.* Annual Review of Fluid Mechanics, Vol. 30, No. 1, pp.329-364.

Chen, Y. H., et al. (2017). *Transient effects and mass convection in sessile droplet evaporation: The role of liquid and substrate thermophysical properties.* International Journal of Heat and Mass Transfer, Vol. 108, pp. 2072-2087.

Chesterfield, R., et al. (2011). *Solution-Coating Technology for AMOLED Displays*. DuPont Displays, California, USA. Retrieved from <http://www.dupont.com/content/ dam/dupont/products-and-services/display-and-lighting-materials/oled-technology/ documents/DEC-frontline_technology_AMOLED.pdf> [Accessed 15/06/2019].

Chon, C.H., et al. (2007). *Effect of Nanoparticle Sizes and Number Densities on the Evaporation and Dryout Characteristics for Strongly Pinned Nanofluid Droplets.* Langmuir, Vol. 23, No. 6, pp. 2953-2960.

COMSOL. (n.d.). *BDF, Generalized Alpha, and Runge-Kutta Methods.* COMSOL 5.4 Documentation.

COMSOL. (2017/a). *The Marangoni Effect*. COMSOL 5.4 Documentation.

COMSOL. (2017/b). *The Finite Element Method (FEM).* COMSOL 5.4 Documentation.

COMSOL. (2017/c). *About Frames.* COMSOL 5.4 Documentation.

COMSOL. (2017/d). *Smoothing Methods.* COMSOL 5.4 Documentation.

COMSOL. (2019). *The Transport of Concentrated Species Interface.* COMSOL 5.4 Documentation.

COMSOL. (2021). *About the Phase Field Method.* COMSOL 5.4 Documentation.

Costa, B. (2015). *Tears of Wine and the Marangoni Effect.* Retrieved from <https://www.comsol.com/blogs/tears-of-wine-and-the-marangoni-effect/> [Accessed 23/06/2019].

CPI (Centre of Process Innovation). (n.d.). *OLED/PLED/OPV Markets.* MBRAUN. Retrieved from <http://www.mbraun.com/markets/oled-pled-opv/> [Accessed 24/06/2019].

Crafton, E. F., & Black, W. Z. (2004). *Heat transfer and evaporation rates of small liquid droplets placed on a solid surface.* International Journal of Heat and Mass Transfer, Vol. 47, pp. 1187-1200.

Cui, L., et al. (2012). *Suppression of the coffee ring effect by hydrosoluble polymer additives.* ACS Applied Materials and Interfaces, Vol. 4, No. 5, pp. 2775-2780.

Dan, B., et al. (2011). *Templating of Self-Alignment Patterns of Anisotropic Gold Nanoparticles on Ordered SWNT Macrostructures.* ACS Applied Materials & Interfaces, Vol. 3 No. 9, pp. 3718-3724.

Darwich, S., et al. (2011). *Nanobubble and nanodroplet template growth of particle nanorings versus nanoholes in drying nanofluids and polymer films.* Nanoscale, Vol. 3, No. 3, pp. 1211-1217.

David, S., Sefiane, K., & Tadrist, L. (2007). *Experimental investigation of the effect of thermal properties of the substrate in the wetting and evaporation of sessile drops.* Journal f Colloids and Surface A: Physiochemical and Engineering Aspects, Vol. 298, pp. 108-114.

Derby, B. (2010). *Inkjet Printing of Functional and Structural Materials: Fluid Property Requirements, Feature Stability, and Resolution.* Annual Review of Materials Research, Vol. 40, pp. 395-414.

Dhavaleswarapu, H. K., et al. (2007). *Experimental Investigation of Steady Buoyant-Thermocapillary Convection Near an Evaporating Meniscus.* Physics of Fluids, Vol. 39, No. 8, Article 082103.

De Coninck, J. (2016). *Wetting Statics.* Wetting Fundamentals: Statics, MicroMAST 2016 Spring School on the Fundamentals of Surface Tension and Wettability, ULB, Belgium.

Deegan, R. D., et al. (1997). *Capillary Flow as the Cause of Ring Stains from Dried Liquid Drops*. Letters to Nature, Nature 389, pp. 827-829. Macmillan Publishers Ltd.

Deegan, R. D. (2000/a). *Pattern Formation in Drying Drops*. Physical Review E, Vol. 61, No. 1, pp. 475-485. The American Physical Society.

Deegan, R. D., et al. (2000/b). *Contact Line Deposits in an Evaporating Drop*. Physical Review E, Vol. 62, No. 1, pp. 756-765. The American Physical Society.

Diddens, C. (2017). *Detailed finite element method modelling of evaporating multi-component droplets.* Journal of Computational Physics, Vol. 340, pp. 670-687.

Diddens, C., et al. (2017/a). *Modelling the evaporation of sessile multi-component droplets.* Journal of Colloidal and Interface Science, Vol. 487, pp. 426-436.

Diddens, C., et al. (2017/b). *Evaporating pure, binary and ternary droplets: thermal effects and axial symmetry breaking.* Journal of Fluid Mechanics, Col. 823, pp. 470-497.

Dobson, K., Grace, D., & Lovett, D. (2008). *Physics (Third Edition).* Collins Advanced Science, Collins, London, UK.

Doust, A. (2011). *Polymer OLED Materials and Device Operation.* Cambridge Display Technology OLED100 Summer School, Cambridge, UK. Retrieved from <https://www.cdtltd.co.uk/pdf/p-oled-materials-device-operation.pdf> [Accessed 15/06/2019].

Dunn, G. J., et al. (2009). *The strong influence of substrate conductivity on droplet evaporation.* Journal of Fluid Mechanics, Vol. 623, pp. 329-351.

Eales, A. D., et al. (2015/a). *Evaporation of Pinned Droplets Containing Polymer – An Examination of the Important Groups Controlling Final Shape*. American Institute of Chemical Engineers. Wiley Publishing.

Eales, A. D., et al. (2015/b). *The Impact of Trough Geometry on Film Shape. A Theoretical Study of Droplets Containing Polymer, for P-OLED Display Applications.* Journal of Colloid and Interface Science, Vol. 458, pp. 53-61.

ECHA. (2021). *4-methylanisole.* Retrieved from <https://echa.europa.eu/registration-dossier/-/registered-dossier/5990> [Accessed 26/06/2021].

Engineering Toolbox. (2021/a). *Dynamic Viscosity of some common Liquids.* Retrieved from <https://www.engineeringtoolbox.com/absolute-viscosity-liquids-d_1259.html> [Accessed 26/06/2021].

Engineering Toolbox. (2021/b). *Liquids - Densities.* Retrieved from <https://www.engineeringtoolbox.com/liquids-densities-d_743.html> [Accessed 26/06/2021].

Enright, D., et al. (2002). *A hybrid particle level set method for improved interface capturing.* Journal of Computational Physics, Vol. 183, pp. 83–116.

Eral, H. B., et al. (2013). *Contact Angle Hysteresis: A Review of Fundamentals and Applications*. Colloid Polymer Science 291, No. 2, pp. 247–260.

Erbil, H. Y. (2012). *Evaporation of pure liquid sessile and spherical suspended drops: A review.* Advances in Colloid and Interface Science, Vol. 170, pp. 67–86.

Fessenden, R. W. (1928). *The viscosity and surface tension of dispersions of sucrose, lactose, skim milk powder and butterfat.* Master's Thesis, University of Massachusetts Amherst. Retrieved from <https://scholarworks.umass.edu/theses/1503> [Accessed 08/08/2019].

Fukai, J. et al. (2014). *Numerical Simulation on Drying Process of an Inkjet Droplet using Lagrangian FEM.* 10th International Conference on Heat Transfer, Fluid Mechanics and Thermodynamics. Orlando, Florida, USA.

Gelderblom, H. (2013). *Fluid Flow in Drying Drops.* PhD Thesis, Physics of Fluids Group, Faculty of Science and Technology, University of Twente, The Netherlands.

Girard, F., Antoni, M. & Sefiane, K. (2008). *On the effect of Marangoni flow on evaporation rates of heated water drops.* Langmuir, Vol. 24, pp. 9207-9210.

Gurrala, P., et al. (2021). *A Review on the Evaporation Dynamics of Sessile Drops of Binary Mixtures: Challenges and Opportunities.* Fluid Dynamics and Material Processing, Vol. 17, No. 2, pp. 253-284.

Hamer, J. W. (2014). *Innovative High-Performance Deposition Technology for Low-Cost Manufacturing of OLED Lighting: Progress Review.* OLED Works LLC, USA.

Handrigan, J. P. (2011). *Vacuum Thermal Evaporation*. Retrieved from <http://www.johnpaulhandrigan.net/vacuum-thermal-evaporation/> [Accessed 14/06/2019].

Holyst, R., Litniewski, M., & Jakubczyk, D. (2015). *A Molecular Dynamics Test of the Hertz-Knudsen Equation for Evaporating Liquids.* Journal of Soft Matter, Vol. 11, pp. 7201-7206.

Hu, H., & Larson, R. G. (2002). *Evaporation of a Sessile Droplet on a Substrate.* Journal of Physical Chemistry, Vol. 106, pp. 1334-1344.

Hu, D., & Wu, H. (2015). *Numerical study and predictions of evolution behaviours of evaporating pinned droplets based on a comprehensive model.* International Journal of Thermal Sciences, Vol. 96, pp. 149-159.

Jacqmin, D. (1999). *Calculation of Two-Phase Navier–Stokes Flows Using Phase-Field Modelling.* Journal of Computational Physics, Vol.155, No. 1, pp. 96-127.

Jena, S., & Das, H. (2007). *Modelling for Vacuum Drying Characteristics of Coconut Presscake.* Journal of Food Engineering, Vol. 79, Issue 1, pp. 92-99.

Johnson, C. (2009). *Numerical Solution of Partial Differential Equations by the Finite Element Method.* Dover Publications Inc., Mineola, New York, USA.

Kadanoff, L. P. (1986). *On two levels.* Physics Today, Vol. 39, pp. 7–9.

Katam, N. K., et al. (2014). *Effect of Chemical Treatments on ITO and OLED Device*. Advanced Materials Research, Vol. 849, pp. 387-390.

Kazmierski, B.K. (2018). *The Drying of Inkjet Printed Drops on Patterned Substrates*. PhD Thesis. Department of Chemistry, Durham University, UK.

Kreis, J., et al. (2012). *Organic Vapour Phase Deposition (OVPD (R)) for efficient OLED manufacturing: The specific advantages and possibilities of carrier-gas enhanced vapour phase deposition for the manufacturing of organic thin film devices.* Proc. of SPIE, Vol. 8476.

Laplace, P-S. (1802). *Traite de Mécanique Céleste*. Tome III.

Lebedev, N. N. (1965). *Special Functions and Their Application.* Prentice-Hall, Englewood Cliffs, New Jersey.

LEDinside. (2013). *The "Seven Deadly Sins" of OLED TV.* Retrieved from <http://www.ledinside.com/news/2013/8/the_seven_deadly_sins_of_oled_tv > [Accessed 08/06/2019].

Liza, A. (2013). *Organic Vapour Phase Deposition.* Retrieved from <http://image. slidesharecdn.com/oledtechnology-130802023919-phpapp01/95/oled-technology-seminar-ppt-13-638.jpg?cb=1375411214> [Accessed 14/06/2019].

Long, M., et al. (2006). *New Capabilities in Vacuum Thermal Evaporation Sources for Small Molecule OLED Manufacturing.* Eastman Kodak Company, New York, USA. SID '06 Digest, pp. 1474-1476.

Lopes, M. C., et al. (2013). *Influence of the substrate thermal properties on sessile droplet evaporation: Effect of transient heat transport*. Journal of

Colloids and Surfaces A: Physiochemical and Engineering Aspects, Vol. 432, pp. 64-70.

Lugg, G. A. (1968). *Diffusion Coefficients of Some Organic and Other Vapors in Air.* Analytical Chemistry, Vol. 40. No. 7, pp. 1072-1076.

Madigan, C., Van Slyke, S., & Vronsky, E. (2015). *Inkjet Printing Equipment for Organic LED Mass Production.* Retrieved from <http://spie.org/newsroom/5940-inkjet-printing-equipment-for-organic-led-mass-production> [Accessed 24/06/2019].

Maleki, H., & Bertola, V. (2020). *Recent advances and prospects of inkjet printing in heterogeneous catalysis.* Catalysis Science & Technology, Vol. 10, pp. 3140-3159.

Martinez, I. (2019). *Properties of some particular solutions*. Retrieved from <http://webserver.dmt.upm.es/~isidoro/bk3/c07sol/Solution%20properties.pdf> [Accessed 06/08/2019].

Matheson, R. (2015). *Tackling the "Achilles' Heel" of OLED Displays*. MIT News Office. Retrieved from <http://news.mit.edu/2015/mass-produced-inkjet-printed-oled-displays-0212> [Accessed 14/06/2019].

Meggs, L. (2011). *The Marangoni Effect: A Fluid Phenom.* International Space Station Program Science Office, NASA, USA. Retrieved from <http://www.nasa.gov/mission_pages/station/research/news/marangoni.html> [Accessed 23/06/2019].

Merklein, L. et al. (2019). *Comparative Study of Printed Multilayer OLED Fabrication through Slot Die Coating, Gravure and Inkjet Printing, and Their Combination.* Colloids and Interfaces, Vol. 3, Issue 1, Article 32.

Mokeba, M. L., Salt, D. W., Lee, B. E., & Ford, M. G. (1997). *Simulating the Dynamics of Spray Droplets in the Atmosphere using Ballistic and Random-Walk Models Combined.* Journal of Wind Engineering and Industrial Aerodynamics, Vol. 67-68, pp. 923-933.

Morrison, N.F., & Harlen, O.G. (2010). *Viscoelasticity in inkjet printing*. Rheologica Acta, Vol. 49, pp. 619–632.

Nakajima, K., et al. (2003). *Marangoni Convection Driven by Thermocapillary and Solutocapillary Forces in the Fe-O Alloy Pool during the Solidification or Remelting Process.* Metallurgical and Materials Transactions B, Vol. 34, Issue 1, pp. 37-49.

Nave, R. (2016). *Surface Tension.* Hyper Physics, Department of Physics and Astronomy, Georgia State University, USA. Retrieved from <http://hyperphysics.phy-astr.gsu.edu/hbase/surten.html> [Accessed 21/06/2019].

Nguyen, T. A. H. & Nguyen, A. V. (2012). *On the Lifetime of Evaporating Sessile Droplets.* Langmuir, Vol. 28, pp. 1924-1930.

Olsson, E., & Kreiss, G. (2005). *A conservative level set method for two phase flow.* Journal of Computational Physics, Vol. 210, No. 1, pp.225-246.

Ozawa, K., et al. (2005). *Modelling of the Drying Process of Liquid Droplet to Form Thin Film.* Japanese Journal of Applied Physics, Vol. 44, pp. 4229-4234.

Patil, N. D., et al. (2016). *Effects of Substrate Heating and Wettability on Evaporation Dynamics and Deposition Patterns for a Sessile Water Droplet Containing Colloidal Particles.* Langmuir, Vol. 32, No. 45, pp. 11958–11972.

Picknett, R. G., & Bexon, R. (1977). *The Evaporation of Sessile or Pendant Drops in Still Air.* Journal of Interface Science, Vol. 61, No. 2, pp. 336-350.

Pradhan, T. K., & Panigrahi, P. K. (2015). *Deposition Pattern of Interacting Droplets.* Colloids and Surfaces A: Physiochemical and Engineering Aspects, Vol. 482, pp. 562-567.

Pradhan, T. K., & Panigrahi, P. K. (2016). *Influence of an adjacent droplet on fluid convection inside an evaporating droplet of binary mixture.* Journal of Colloids and Surfaces A: Physiochemical and Engineering Aspects, Vol. 500, pp. 154-165.

Raghupathi, P. A., & Kandlikar, S. G. (2016). *Contact Line Heat Transfer Mechanisms for an Evaporating Interface.* International Journal of Heat and Mass Transfer, Vol. 95, pp. 296-306.

Raznjevic, K. (1995). *Handbook of Thermodynamic Tables.* 2nd ed. Begell House, New York, USA. p.85.

Robbliard, N. (2015). *OLEDs: Theory and Fabrication.* Retrieved from <http://study lib.net/doc/9908521/oleds---theory-and-fabrication> [Accessed 08/06/2019].

Rowan, S. M., et al. (1995). *Evaporation of Microdroplets and the Wetting of Solid Surfaces.* Journal of Physical Chemistry, Vol. 99, No. 35, pp. 13268-13271.

Sáenz, P. J. et al. (2017). *Dynamics and universal scaling law in geometrically-controlled sessile drop evaporation.* Nature Communications, Vol. 8, Article 14783.

Sastry, S. S. (2017). *Introductory Methods of Numerical Analysis.* (5th ed.). PHI Learning Private Ltd., Delhi, India.

Schwambera, M. (2006). *Optimising OVPD technology towards lowest OLED manufacturing cost.* Organic Semiconductor Technologies, AIXTRON AG, Germany. Proc. of ASID ’06, 8-12 Oct, New Delhi.

Sefiane, K., et al. (2009). *On the Effect of the Atmosphere on the Evaporation of Sessile Droplets of Water.* Physics of Fluid, Vol. 21, Article 062101.

Sefiane, K., & Bennacer, R. (2009). *Nanofluids droplets evaporation kinetics and wetting dynamics on rough heated substrates.* Advances in Colloid and Interface Science, Vol. 147, pp. 263-271.

Sefiane, K. (2010). *On the Formation of Regular Patterns from Drying Droplets and Their Potential Use for Bio-Medical Applications.* Journal of Bionic Engineering, Vol. 7, pp. S82-S93.

Serras-Pereira, J. et al. (2008). *Characteristics of Ethanol, Butanol, Iso-Octane and Gasoline Sprays and Combustion from a Multi-Hole Injector in a DISI Engine.* SAE International, 2008-01-1591.

Shin, S., Jacobi, I., & Stone, H. A. (2016). *Bénard–Marangoni instability driven by moisture absorption*. Europhysics Letters, Vol. 113, pp. 24002.

Sobac, B., & Brutin, D. (2012). *Thermal effects of the substrate on water droplet evaporation.* Physical Review E, Vol. 86, No. 021602.

Solvay. (n.d.). *Infographics: OLED.* Retrieved from <http://www.solvay.cn/zh/binaries/Infographic-Oleds-221957.png> [Accessed 15/06/2019].

Starov, V., & Sefiane, K. (2009). *On Evaporation Rate and Interfacial Temperature of Volatile Sessile Drops.* Journal of Colloids and Surfaces A, Vol. 333, pp. 170-174.

Strasser, E. (2014/a). *OLED Inkjet Printing*. Retrieved from <http://ww3.oled-display.net/wp-content/uploads/2014/11/oled-inkjet-printing.jpg> [Accessed 16/06/2019].

Strasser, E. (2014/b). *Printable OLED-TVs*. Retrieved from <http://ww3.oled-display.net/printable-oled-tvs> [Accessed 16/06/2019].

Sussman, M., & Puckett, E. (2000). *A coupled level set and volume-of-fluid method for computing 3D and axisymmetric incompressible two-phase flows.* Journal of Computational Physics, Vol. 162, pp. 301–337.

Takei, A. (2013). *Capillary Micro Motor.* Surface Tension in Microsystems: Engineering Below the Capillary Length, pp. 199-209. Springer, Heidelberg, Germany.

Tan, H., et al. (2016). *Evaporation triggered microdroplet nucleation and the four life phases of an evaporating Ouzo drop*. Proceedings of the National Academy of Sciences, USA, Vol. 113, No. 31, pp. 8642–8647.

Tan, L. W. (2016). *Private Correspondence.* Merck KGaA, Darmstadt, Germany. Received 18/03/2016.

Tanguy, S., & Berlemont, A. (2005). *Application of a level set method for simulation of droplet collisions*. International Journal of Multiphase Flow, Vol. 31, No. 9. pp.1015-1035.

Tantec. (n.d.). *The Basics of Plasma Treatment.* Retrieved from <http://www .tantec. com/the-basics-of-plasma-treatment.html> [Accessed 11/07/2019].

Tarasevich, Y. Y., et al. (2011). *Desiccating colloidal sessile drop: Dynamics of shape and concentration.* Journal of Colloidal Polymer Science, Vol. 289, pp. 1015-1023.

Tornberg, A. K., & Enhquist, B. (2000). *A finite element based level set method for multiphase flow applications.* Computing and Visualisation in Science, Vol. 3, pp. 93–101.

Trokhymchuk, A., et al. (2001). *A Simple Calculation of Structural and Depletion Forces for Fluids/Suspensions Confined in a Film.* Langmuir, Vol. 17, No. 16, pp. 4940-4947.

Trusler, J. P. M. (2011). *Knudsen Number.* Retrieved from <http://www. thermopedia .com/content/908/> [Accessed 16/03/2019].

Tsujimura, T. (2012). *OLED Displays: Fundamentals and Applications.* Wiley-SID Series in Display Technology. John Wiley & Sons, Inc. Hoboken, NJ, USA.

Uno, K., et al. (1998). *Particle adsorption in evaporating droplets of polymer latex dispersions on hydrophilic and hydrophobic surfaces.* Colloid and Polymer Science, Vol. 276, No. 9, pp. 810-815.

Vafaei, S., et al. (2006). *Effect of nanoparticles on sessile droplet contact angle.* Nanotechnology, Vol. 17, No. 10, pp. 2523.

Vargaftik, N. B., Volkov, B. N., & Voljak, L. D. (1983). *International Tables of the Surface Tension of Water.* Journal of Physical Chemistry Reference Data, Vol. 12, No. 3, pp. 817-820.

Varioptic. (2010). *The Liquid Lens Technology*. Retrieved from <http://www.varioptic.com/media/uploads/publication/varioptic_liquid_lens_technology_2010_12_02.pdf> [Accessed 21/06/2019].

Villani. F,. et al. (2009) *Inkjet Printed Polymer Layer on Flexible Substrate for OLED Applications.* Journal of Physical Chemistry, Vol. 113, pp. 13398-13402.

Ward, C. A., & Duan, F. (2004). *Turbulent Transition of Thermocapillary Flow Induced by Water Evaporation.* Physics Review E, Vol. 69, Article 056308.

Wasan, D., Nikolov, A., & Moudgil, B. (2005). *Colloidal dispersions: Structure, stability and geometric confinement.* Powder Technology, Vol. 153, No. 3, pp. 135-141.

Weast, R. C., & Astle, M. J. (1982). *CRC Handbook of Chemistry and Physics*. 62nd ed. CRC Press, Boca Raton, Florida, USA.

Weon, M. B., & Je, J. H. (2013). *Self-Pinning by Colloids Confined at a Contact Line.* Physical Review Letters, Vol. 110, 028303.

What HIFI? Magazine. (2015). *OLED TV: Everything you need to know.* Retrieved from <http://www.whathifi.com/advice/oled-tv-everything-you-need-to-know> [Accessed 08/06/2019].

Wray, A.W., et al. (2014). *Electrostatic Suppression of the "Coffee Stain Effect".* Langmuir, Vol. 30, No. 20, pp. 5849-5858.

Wray, A.W., et al. (2015). *Electrostatic Suppression of the "Coffee-stain Effect".* Procedia IUTAM, Vol. 15, pp. 172-177.

Wu, C. C., et al. (1997). *Surface Modification of Indium Tin Oxide by Plasma Treatment: An Effective Method to Improve the Efficiency, Brightness, and Reliability of Organic Light Emitting Devices.* Applied Physics Letters, Vol. 70, Issue 17, pp. 1348-1350.

Yang, K., Hong, F., & Cheng, P. (2014). *A fully coupled numerical simulation of sessile droplet evaporation using Arbitrary Lagrangian-Eulerian*

formulation. International Journal of Heat and Mass Transfer, Vol. 40, pp. 409-420.

Yaws, C. L. (1999). *Chemical Properties Handbook*. McGraw-Hill.

Yaws, C. L. (2009). *Transport properties of chemicals and hydrocarbons: viscosity, thermal conductivity, and diffusivity of Cl to Cl 00 organics and Ac to Zr inorganics*. William Andrew Inc.

Yoxall, B. E., et al. (2012). *Rotary Liquid Drop Microbearing.* Journal of Microelectromechanical Systems, Vol. 21, Issue 3, pp. 721-729.

Yu, S-Y., et al. (2012). *Approaching Charge Balance in Organic Light-Emitting Diodes by Tuning Charge Injection Barriers with Mixed Monolayers.* Langmuir, 2012, Vol. 28, pp. 424-430.

Yu, S-Y., et al. (2014). *Effect of ITO Surface Modification on the OLED Device Lifetime.* Langmuir 2014, Vol. 30, pp. 7369-7376. American Chemical Society.

Zhang, D., et al. (2019). *Evaporation of a Droplet: From physics to applications.* Physics Reports, Vol. 804, pp. 1-56.

Zhang, Z., & Chen, Q. (2007). *Comparison of the Eulerian and Lagrangian methods for predicting particle transport in enclosed spaces.* Atmospheric Environment, Vol. 41, No. 25, pp. 5236-5248.

Zhong, X., Crivoi, A., & Duan, F. (2015). *Sessile nanofluid droplet drying*. Advances in Colloid and Interface Science, Vol. 217, pp. 13-30.

Zhong, X., Xie, H., & Duan, F. (2016). *Deposition patterns from evaporating sessile droplets with suspended mixtures of multi-sized and multi-species hydrophilic and non-adsorbing nanoparticles*. Applied Thermal Engineering, Vol. 111, pp. 1565-1572.

Zhong, X., & Duan, F. (2016). *Flow regime and deposition pattern of evaporating binary mixture droplet suspended with particles.* The European Physical Journal E, Soft matter and biological physics, Vol. 39, No. 2, pp. 1-6.

Zhou, Q. (2006). *Microhandling using Robotic Manipulation and Capillary Self-Alignment*. Proc. of IEEE/RSJ International Conference on Intelligent Robots and Systems, 9-15 Oct, Beijing, China, pp. 5883-5888.

Zhou, Z. (2007). *Combinatorial Fabrication & Studies of Small Molecular Organic Light Emitting Devices (OLEDs) and Structurally Integrated OLED-*

based Chemical and Biological Sensors. PhD Thesis, Paper 13944, Retrospective Theses and Dissertations, Iowa State University, USA.